SYNTHESIS OF METAL OXIDES NANOSTRUCTURES FOR THE REMOVAL OF TOXIC RESIDUES

Ph.D. THESIS

by

MONU

DEPARTMENT OF CHEMISTRY
INDIAN INSTITUTE OF TECHNOLOGY ROORKEE
ROORKEE – 247 667 (INDIA)

APRIL, 2016

SYNTHESIS OF METAL OXIDES NANOSTRUCTURES FOR THE REMOVAL OF TOXIC RESIDUES

A THESIS

Submitted in partial fulfilment of the requirements for the award of the degree

of

DOCTOR OF PHILOSOPHY

in

CHEMISTRY

by

MONU

DEPARTMENT OF CHEMISTRY
INDIAN INSTITUTE OF TECHNOLOGY ROORKEE
ROORKEE – 247 667 (INDIA)

APRIL, 2016

INDIAN INSTITUTE OF TECHNOLOGY ROORKEE
ROORKEE

CANDIDATE'S DECLARATION

I hereby certify that the work which is being presented in the thesis entitled **"SYNTHESIS OF METAL OXIDES NANOSTRUCTURES FOR THE REMOVAL OF TOXIC RESIDUES"** in partial fulfilment of the requirements for the award of the degree of Doctor of Philosophy and submitted in the Department of Chemistry of the Indian Institute of Technology Roorkee, Roorkee is an authentic record of my own work carried out during a period from December, 2011 to April, 2016 under the supervision of Dr. Vinod Kumar Gupta, Professor, Department of Chemistry and Dr. Ramesh Chandra, Professor, Institute Instrumentation Centre, Indian Institute of Technology Roorkee, Roorkee.

The matter presented in the thesis has not been submitted by me for the award of any other degree of this or any other Institute.

(MONU)

This is to certify that the above statement made by the candidate is correct to the best of our knowledge.

(Vinod Kumar Gupta)
Supervisor

(Ramesh Chandra)
Supervisor

Date:

ACKNOWLEDGEMENTS

The completion of my doctoral thesis has been a long journey which was a memorable, unforgettable, enlightening and learning experience for me. The research presented in this doctoral thesis has been carried out at the Department of Chemistry and Institute Instrumentation Centre (IIC), Indian Institute of Technology-Roorkee. The path towards this thesis spans three years of research work that involves help, support and mentorship from several individuals both from within the institute and outside of it. This is the instance and my immense pleasure to show my gratification to all of them.

My utmost gratitude goes to my research supervisor, Dr. Vinod Kumar Gupta for allowing me to join his team, for his expertise. I would like to express my heartfelt thanks and earnest deference to him for his encouragement, supervision and support from the preliminary to the concluding level of this research work. This thesis would not have been possible without his constant monitoring, advice, unsurpassed knowledge and invaluable direction provided by him in the topic which was essential in every step I took to complete this work. He always provided his valuable time for probing and finalizing the research papers regardless of his enormous academic activities. His gracious approach and motivation were the major strength in successfully overcoming tough times during my research work. The critical remarks, propositions and elucidations from him regarding experimental and technical part played a vital role to the progress of my research work. His patience, flexibility, genuine caring and concern, and faith in me enabled to successfully complete my research work. The unflinching courage, conviction and ideology of his will always inspire me throughout my life to continue the work with his noble thoughts.

I am also extremely indebted to my supervisor, Dr. Ramesh Chandra for picking me up as a student and was fortunate to be one of the members of his Nano Science research group. He has helped me to see life and science in their full depth, and taught me how to appreciate the good scientific work that helps other researchers to build on it. He remained a supporter and provided insight and direction-right from the start up to the end in defining the objectives of research work and fulfilling it. His smiling face persona, frank and friendly temperament provided a stimulating and fun filled environment in the laboratory for pursuing the research work. The scientific zeal

and vast materials science knowledge of his has been invaluable on both academic and experimental level to accomplish my research work. The enthusiasm and dedication of his to develop new experimental and research facilities will forever encourage me to emulate it as much I can in future.

I am thankful to the members of my doctoral student research committee (SRC), Dr A.K. Singh (Chairman), Dr. Anil Kumar Maheshwari (Internal member) and Dr. Sashi (External member) for their useful suggestions and critical evaluation of the progress of my thesis.

I am thankful to Prof. M.R. Maurya, Head of the Department, and other faculty members of the department for their support in this work. I am highly obliged and express my sincere thanks to the official & technical staff of the Department of Electrical Engineering and Institute Instrumentation Centre, IIT Roorkee. Also, special thanks go to Mr. S.D. Sharma, Mr. Anil Kumar Saini, Mr. Shiv kumar, Mr. Mukesh Tripathi, Mr. Birendra Dutt, Mr. Shiv Kumar, Mr. Kamal Singh Gotyan, Mr. Madan Singh, Mr. Mahaveer Singh, Mr. Duli Chand Meena, and Mr. Yashpal Singh for their kind support during my research. It would be impossible what I am today without my family and relatives. I am grateful to my father Mr. Subhash and my mother Smt. Manju for their apprehension and steady persuasion that played a foremost part in my commencement of studies at appropriate time. I am heartily thankful to my half breath Sandhya Deshwal, for their love, affection, caring and magnanimous nature, for never letting me feel alone and their emotional support during my stay at IIT Roorkee. I am grateful to my brothers Amit Verma and Rajeev Verma and my sister Neetu Verma for timely help and loveable support. I am grateful to my uncle Mr. Krishana Pal Singh, his wife Mrs. Suresha and her childs Mega, Chutki and Vatsal for their constant support and motivation.

I had a great time and benefited a lot working with my lab mates Dr. Paritosh Dubey, Dr. Yogendra Kumar Gautam, Dr. Rajan Waliya, Dr. Vikaramaditya Dave, Dr. Amit Chawala, Samta Chouhan, Amit Kumar Singh, Dr. Saurabh Srivastava, Inderjeet Tyagi, Archana Mishra, Ashwani Kumar, Jyoti, Satyendra Kumar Maurya, Gaurav Malik and Arvind kumar, at Nano Science laboratory and Indeerjeet Singh in water treatment lab. I am thankful to all these mates for their assistance and help all through my work and being like a family enjoying, partying, playing, pursuing research and having fun together.

I will always cherish my friendship with Rupam, Ravi, Amit Kalbandhae, Naresh, Syam, Goverdhan, Naveen, Sauraj, and Amit, whose humorous and comic behavior allowed me to laugh at tough times. Thank you buddies.

I would like to thank to Dr. Ashish Selokar and Dr. Akash Katoch, as my senior as my seniors-cum-friend for providing lively company and motivation for the completion of my work.

At the outset, let me thank the almighty God, who is the most graceful and generous for his blessing that has given me courage, strength to face any adverse situation, wisdom to make wise decisions and pleasant, memorable moments of my life.

Our work greatly improved thanks to the comments of the anonymous reviewers and editors of the articles published with contributions of this thesis.

I would like to thanks everybody who was important to the successful realization of thesis, as well as expressing my apology that I could not mention personally one by one.

(Monu)

ABSTRACT

From the last few decades, decontamination of chemical warfare agents (CWA) in the battlefield conditions and removal of heavy metal ions from the polluted water are the major challenges for the scientific community for the national security and human health interest. Among different CWA, sulphur mustard (HD) and sarin (GB) are well identified CWA and have been effectively employed in the World Wars (WW-I and WW-II) followed by its usage in several other incidents such as in Gulf War and in Japan by terrorist. HD affects several organs of the human including skin, mucous membrane which causes blisters. It also alkylates guanine nucleotide in DNA and causes fatality to the cells. GB attacks on nervous transmission and block it permanently by binding with the acetylcholinesterase enzyme, causing paralysis and mortality. On the other hand, presence of heavy metal ions such as lead, mercury, chromium, nickel, iron and other metals has a potentially harmful effect on human physiology and biological system. Hence, search for the technique and materials having high adsorption capacity to adsorb the CWA and removal of metal ions from water is essential. A number of adsorbent and techniques have been so far used to minimize the above problem and finally stops onto metal oxides nanostructures. Metal oxides structures synthesized at nanoscale demonstrate superior ability for the safety of human from CWA and heavy metal ions by mean of their remarkable capability including high adsorbing power and reactivity. These nanostructures can adsorb and degrade them through hydrolysis, elimination or oxidation reaction to convert them into non-toxics form. Also, heavy metal ions such as Cr (VI) and Pb (II) adsorb and removed from water by their preferential adsorption at highly reactive sites available in nanostructures. The reactivity and adsorption power of metal oxides nanostructures mainly because of their high surface area, large number of highly reactive edges, corner defect sites and unusual lattice planes.

The main objective of the present work was to synthesize metal oxides based nanostructures including nanoparticles of copper oxide (CuO), tungsten oxide (WO_3), zirconium oxide (ZrO_2) and mixture of nanoparticles and nanorods of manganese oxide (MnO_2) using reactive magnetron sputtering technique to investigate the decontamination ability for the degradation of CWA and removal of heavy metal ions from water. The effect of particle size on aforementioned issues was thoroughly investigated. The sputtering parameters were successfully controlled to analyse effect on structural, morphological and thermal properties of different metal

oxides as well as to get the optimum particle size to minimize the above mentioned issues. A chapter wise summary of the thesis is given below.

Chapter 1 gives an overview about the CWA, used by ambitious countries and terrorist to affect the environment and human life (in the first part) and another part gives about water related problem. The first part discusses the different type of CWA and their mechanism to affect the human health. Different type of decontaminant that was used to degrade these CWA was also discussed in this chapter. The mechanism of CWA degradation was also described using some important decontaminants such as bleaching powder, DS2 solution and some different metal oxides nanostructures and discussed their ability to degrade them. In the other part, discussion about the water pollutants was carried out, followed by different technologies and methods effective in minimizing the water related problem. Among them, absorption technology and adsorbents of different category are thoroughly discussed.

After discussion of the problem and different treatments related to CWA and water pollution, we moves towards technology dependence over nanoscale materials that gives much better results towards decontamination of CWA and removal of heavy metal ions. Different synthesis techniques were discussed for preparation of the metal oxide nanostructures that were used in the CWA degradation and removal of heavy metal ions from water through adsorption technique. The usage of different nanostructures using adsorption technique were found effective solution of the above mentioned problems.

Chapter 2 presents the details of synthesis and characterization techniques employed for the present work. **Section 2.1** gives description about the nanoparticles formation. **Section 2.2** discusses the process description and mechanistic details of DC reactive magnetron sputtering technique used for the preparation of nanostructures in the present work. **Section 2.3** discusses the methodology used for the characterization of nanoparticles by different techniques such as X−Ray Diffraction (XRD) for the phase identification and grain size, Raman spectroscopy for the confirmation of structural phase. Field Emission Scanning Electron microscope (FE−SEM) and Transmission Electron Microscope (TEM) were used for the surface morphology analysis and electron diffraction scattering (EDS) for elemental composition analysis. N_2−BET analysis was used for surface area and pore size distribution, Thermogravimetric (TG) analysis for the water content onto the surface of nanoparticles. Gas Chromatograph equipped with Flame

Ionization Detector (GC–FID) was used for the kinetics measurement. Gas Chromatograph equipped with Mass Spectrometer (GC–MS) and Fourier transform infrared spectroscopy (FT–IR) were used for the characterization of the reaction products. Atomic adsorption spectroscopy (AAS) was used for the identification of elements concentration.

Chapter 3 describes the synthesis and characterization of copper oxide nanoparticles at different sputtering parameters. **Section 3.1** gives a brief introduction about the copper oxide nanoparticles followed by discussion on the work of different research groups contributed in the field of CWA degradation. **Section 3.2** includes discussion on the temperature effect on the structural, morphological and thermal properties of the sputtered deposited copper oxide nanoparticles and their ability to degrade 2-chloro ethyl ethyl sulphide (CEES), well known simulant of sulphur mustard. The characterization of the nanoparticles was carried out by powder XRD, TEM, FE–SEM, N_2–BET, FT–IR and TGA and the degradation kinetics was obtained by using GC–FID. The reaction products was characterized by GC–MS and then confirmed through FT–IR technique. The average particle size of CuO nanoparticles calculated using XRD analysis was varied from 7 to 86 nm for as–deposited and annealing at different temperatures up to 900 °C. It was found that as the particle size increased as a function of annealing temperature and the rate of CEES degradation decreases from 0.434 to 0.134 h^{-1}. The results indicates the role of hydrolysis reaction in the decontamination of CEES. The **Section 3.3** discussed the structural, morphological and thermal properties of CuO nanoparticles as sputtering power is varied from 30–80 W. The enhancement in sputtering power results the increase in size of particle with spherical type morphology from 10, 12 and 15 nm, respectively. The TG results indicate decreases in water content as a function of the sputtering power. **Section 3.4** discusses about the effect of sputtering pressure (10-50 mTorr) on different properties of CuO nanoaprticles. The particles size increases from 6 to13 nm with enhancement of the sputtering pressure. TG pattern indicates that the nanoparticles are purely hydrous and weight loss was inversely correlated to the particle size.

Chapter 4 presents the details of synthesis and characterization of tungsten oxide nanoparticles in relation to the different sputtering parameters. **Section 4.1** gives a brief introduction about the tungsten oxide nanoparticles and the work performed by the different research groups contributed in the decontamination of CWA. **Section 4.2** discusses the

temperature effect on the structural, morphological and thermal properties of the sputter deposited tungsten oxide nanoparticles. The annealing temperature was varied from 200–500 ºC. XRD result confirmed formation of monoclinic phase and was further confirmed by the Raman spectroscopy technique. It was found that as the temperature increase, average crystallite size increases from 2–47 nm. On the other hand, the surface area and pore volume values decrease from 63.22 to 33.28 m^2/g and 0.128 to 0.082 ml/g, respectively. These nanoparticles were used in the decontamination of 2-chloro ethyl ethyl sulphide (CEES) and dimethyl methylphosphonate (DMMP), well known simulants of sulphur mustard (HD) and sarin (GB), respectively. It was found that rate of degradation decreased from 0.143 to 0.109 h^{-1} and 0.018 to 0.010 h^{-1}, for CEES and DMMP, respectively with increase in annealing temperature. Results indicates the role of hydrolysis reaction in the decontamination of CEES and DMMP. **Section 4.3** exhibited the structural, morphological and thermal properties of WO_3 nanoaprticles synthesized at 40, 60, 80 and 100 W power. The TG curve shows that the nanoparticles are purely hydrous with weight loss 10.9 % up to 300 ºC.

Chapter 5 details the synthesis and characterization of zirconium oxide nanoparticles. **Section 5.1** deals with the properties ZrO_2 nanoparticles and highlights the work done by the various research group on their properties and their role to minimize the environmental problems. **Section 5.2** describe the temperature effect on their structural, thermal and morphological properties using Powder XRD, FE–SEM, TEM, Raman spectroscopy, N_2–BET, TGA and FT–IR techniques of ZrO_2 nanoparticles and their efficiency for the decontamination of 2–choro ethyl ethyl sulphide (CEES) and dimethyl methyl phosphonate (DMMP). XRD patterns indicate that the as–deposited nanoparticles are amorphous in nature and as the annealing temperature was increased from 300, 450 & 600 °C, they transform from tetragonal to monoclinic phase. The decontamination reactions exhibits pseudo first order kinetic behaviour with rate constant and half life values 0.178–0.107 h^{-1} and 3.87-6.43 h for CEES and 0.034–0.015 h^{-1} and 20.024-45.127 h for DMMP, respectively. The degradation occur through hydrolysis and elimination reactions. **Section 5.3** describes the effect of sputtering power on structural, morphological and thermal properties at room temperature. The sputtering power was varied from 40 to 100 W followed by annealing at 350 ºC to obtain the crystalline properties.

Chapter 6 details the synthesis and characterization of mixture of MnO_2 nanoparticles and nanorods for the detoxification of 2−choro ethyl ethyl sulphide (CEES) and dimethyl methyl phosphonate (DMMP). It gives a short discussion about the MnO_2 nanoparticles and nanorods for the degradation of different type of CWA. It also highlighted the work of different research group over MnO_2 synthesis. Thereafter, analysed was carried out by different techniques such as powder XRD, Raman spectroscopy, FE−SEM, TEM, BET, FT−IR and Thermogravimetry (TG). The FE−SEM and TEM analysis confirms the formation of aggregates MnO_2 nanoparticles and nanorods. Powder XRD and Raman results confirm the formation of pure tetragonal phase of MnO_2 nanoparticles and nanorods. XRD and Raman spectroscopy confirms the formation of tetragonal phase. The decontamination reactions exhibited the formation of hydrolysis and surface bound products on the surface of nanoparticles and nanorods. The value of rate constant and half life was found to be 0.267 h^{-1} and 2.58 h for CEES and 0.068 h^{-1} and 10.10 h for DMMP, respectively.

Chapter 7 details the synthesis and characterization of copper oxide nanoparticles. **Section 7.1** gives introduction about the water pollution due to the presence of heavy metal ions in the water. Thereafter, discusses about different treatment and technology to minimize the water related problems. **Section 7.2** deals with the copper oxides nanoparticles synthesis and their characterization for the adsorptive removal of Cr (VI) ions from aqueous solution. Different batch adsorption parameters such as solution pH, adsorbent dose, initial metal ion concentration, equilibrium contact time and temperature were used for the removal of Cr (VI) ions. The maximum adsorption capacity of Cr (VI) ion is 15.625 mg/g which was calculated using Langmuir isotherm model. The positive value of ΔH indicates the endothermic nature of adsorption process whereas negative value of Gibbs free energy (ΔG) indicates the spontaneous nature of Cr (VI) ions adsorption. The adsorption kinetics followed pseudo second order kinetic behaviour nature. **Section 7.3** deals with the adsorptive removal properties of Pb (II) ions from aqueous solution. The characterization was carried out using powder XRD, FT-IR, Raman, FE-SEM, EDS, TEM, SAED, BET surface area, AAS techniques for the structural, morphological and adsorption properties. The optimum parameters were found to be pH 6, contact time 3 hours, adsorbent dose 2 g/L for 50 mg/L Pb (II) ion concentration. The adsorption kinetics follows pseudo second-order kinetic model which indicates that the adsorption controlled through chemisorption process. The adsorption isotherm follows Langmuir isotherm with maximum

adsorption capacity 37.027 mg/g. The ΔS and ΔH values were found to be positive which indicate the endothermic nature of adsorption process whereas negative value of Gibbs free energy (ΔG) indicates the spontaneous nature of Pb (II) adsorption.

Chapter 8 presents the summary and conclusion of the entire work presented in the thesis and also proposes the future directions in which these studies can be extended.

PUBLICATIONS

1. **Monu Verma,** Vinod Kumar Gupta, V. Dave, Ramesh Chandra, G.K. Prasad, Synthesis of sputter deposited CuO nanoparticles and their use for decontamination of 2-chloroethyl ethyl sulfide (CEES), J. Colloid Interface Sci. 438 (2015) 102–109. Impact factor: **3.368**
2. **Monu Verma,** Ramesh Chandra, Vinod Kumar Gupta, Synthesis of magnetron sputtered WO_3 nanoparticles-degradation of 2-chloroethyl ethyl sulfide and dimethyl methyl phosphonate, J. Colloid Interface Sci. 453 (2015) 60–68. Impact factor: **3.368**
3. **Monu Verma,** Ramesh Chandra, Vinod Kumar Gupta, Synthesis and characterization of magnetron sputtered ZrO_2 nanoparticles: Decontamination of 2-choloro ethyl ethyl sulphide and dimethyl methyl phosphonate, Journal of Environmental Chemical Engineering 4 (2016) 219–229, Impact factor: **awaited**
4. **Monu Verma,** Ramesh Chandra, Vinod Kumar Gupta, Decontamination of 2-chloro ethyl ethyl sulphide and dimethyl methyl phosphonate from aqueous solutions using manganese oxide nanostructures, J. Mol. Liq. 215 (2016) 285–292 Impact factor: **2.515**
5. **Monu Verma,** Ramesh Chandra, Vinod Kumar Gupta, Removal of Pb (II) ions from aqueous solution using magnetron sputtered CuO nanoparticles, J. Mol. Liq. 215 (2016) 285–292 (Accepted) Impact factor: **2.515**
6. **Monu Verma,** Ramesh Chandra, Vinod Kumar Gupta, CuO nanoparticles: An effective adsorbent for Cr (VI) removal from water, J. Colloid Interface Sci. (Under Review). Impact factor: **3.368**
7. CuO nanoparticles: sputtering based synthesis and its structural thermal and optical studies, **Monu Verma**, Samta Chauhan, V.K. Gupta, Ramesh Chandra, Materials Advanced Materials Latters (Under Review). Impact factor: **1.99**

CONFERENCES AND WORKSHOPS ATTENDED AND PRESENTATIONS GIVEN

1. International Conference on optoelectronic materials and thin films: OMTAT 2013, January 3 to 5, 2013 in Kochi, India

Poster Presentation: Structural and thermal properties of nanocrystalline CuO synthesized by reactive magnetron sputtering

2. International Conference on Emerging Materials and Processes, 26-28 Feb. 2014 in Bhubaneshwar, Odisha,

Oral Presentation: Structural and Thermal Properties of Nanocrystalline WO3 Synthesized using Reactive Magnetron Sputtering

3. International Conference on Condensed Matter and applied Physics, October 30-31, 2015, Bikaner, India

ZrO_2 nanoparticles: reactive magnetron sputtering based synthesis and its structural, morphological and thermal studies

4. Nanocon 2014, international conference on Nanotechnology, 14-15 Oct. 2014

Oral Presentation: Power effect on structural and thermal properties of magnetron sputtered WO_3 Nanoparticles

5. ICMTech 2016, International Conference on Materials Science & Technology, 1-4 March 2016

Oral Presentation: Study of structural, thermal and optical properties of magnetron sputtered CuO nanoparticles.

6. Workshop on "Nano Drug Delivery Systems (Industry-Academia Interaction)", Centre of Excellence: Nanotechnology, IIT Roorkee, January 10, 2015.

Dedicated

To

My Parents and Friends

CONTENTS

LIST OF FIGURES

LIST OF TABLES

CHAPTER 1

INTRODUCTION AND LITERATURE REVIEW

1.1 Chemical warfare agents

The term Chemical warfare agents (CWA) is used to define any chemical substance whose toxic properties are utilised to kill, injure or incapacitate a humans, livestock, or plants. These agents are different from explosive chemicals in which the destructive effects are caused by shear force and are localized. The roots of these toxic agents were started from 600 B.C. when Athenians used to contaminate the water supply during the siege of Kirrha. Thereafter, time to time CWA were applied in the battlefield, but modern CWA were used during the First World War (WWI). These toxic agents in the form of chlorine, phosgene, hydrogen cyanide, diphenylchlorarsine, ethyl-and methyldichloroarsine, lewisites and sulphur mustard created 100,000 deaths and nearly 1.2 million casualties **[1]**. During Second World War (WWII), Germany used nerve agents such as sarin (GB), soman (GD), tabun (GA) and HCN gas by which millions of innocent civilians were killed. After the WWII, the major use of CWA occurred in the Iran-Iraq war of 1980 in which 5000 people were killed by Iraqi nerve agent **[2]**. Several terrorist groups have been used sarin in Japanese cult in Matsumoto city (1994) and the Tokyo subway system (1995) in which 12 killed and 5,000 casualties **[3]**.

Thus, due to highly destructive and non-discriminating nature of CWA, Chemical Weapons Convention (CWC) came into force in 1997 stated the outlaws of production, stockpiles and use of CWA. Also, stated to destroy the chemical weapons within next 10 years up to the "levelling out principle". Still after that, some countries especially those have not nuclear power posses these deadly CWA as they are cheap, easy to synthesize and have devastating effects. Moreover, these CWA can be used by small scale terrorist attack as an effectively weapons.

1.1.1 Classification of CWA

The CWA posses various class of compounds having different physicochemical, physiological and chemical properties **[4]**. These are classified in many ways but more

acceptable classification is based on physiological effects created by the CWA on human's health. The classification of CWA is given below.

- Nerve agents
- Blister/vesicants agents)
- Bloods agents (cyanogenic agents)
- Choking agents (pulmonary agents

1.1.1.1 Nerve agents

As name indicate that they affect the functioning of the nervous system. These are the amide or ester derivatives of phosphonic acid and are structurally related to organophosphate (OP) insecticides. These agents were further classified into G and V series. G series includes GA (tabun), GB (sarin), GD (soman) and GF (cyclohexyl methylphosphonofluoridate) and V series includes VX (Methylphosphonothioic acid S–(2–(bis(1-methylethyl)amino)ethyl) O–ethyl ester), VE (Phosphonothioic acid, ethyl–, S–(2–(diethylamino)ethyl) O–ethyl ester), VG (amiton) and VM (Phosphonothioic acid, methyl–S–(2–(diethylamino)ethyl) O-ethyl ester). The chemical structures and important physical/toxicological properties of highly powerful nerve agents are listed in **Fig. 1.1** and **Table 1.1**, respectively.

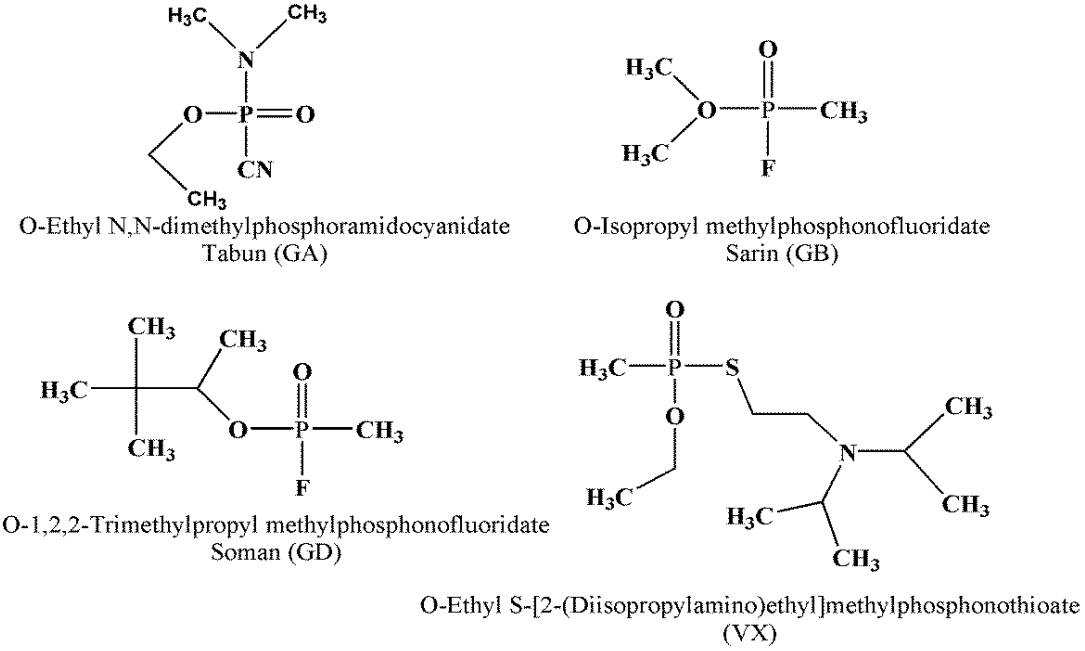

Fig. 1.1 Chemical structures of common chemical warfare agents.

The mechanism of nerve agent action is well reported in the previous literature **[5, 6]**. The primary mechanism of toxicity of nerve agents is related to inhibition of the acetyl cholinesterase (AChE) enzyme which is responsible for hydrolysing the acetylcholine (ACh), a neurotransmitter liberated at the nerve synapse, neuromuscular (nerve muscle) junction and nerve–gland junction. In a normal individual, a small quantity of ACh is continuously liberated and hydrolyzed by AChE enzyme. AChE has two active sites i.e. anionic and esteratic. Inactivation of AChE occurs irreversibly by alkyl phosphorylation of a serine hydroxyl group at the esteratic site of the enzyme. This inactive phosphorylated enzyme is highly stable and the spontaneous hydrolysis of nerve agent intermediately does not occur. This intermediate loses non-enzymatically alkyl side chain which enhanced the stability of enzyme-nerve agent complex. This process is known as aging. The harmful effects of nerve agents are the results of the action on muscarinic and nicotinic receptors within the central nervous system. The harmful effects include constriction of meiosis (pupil), increased production of saliva, running nose, increased perspiration, defecation, urination, bronchosecretion, bronchoconstriction, decrement the heart rate, blood pressure, muscular twitches and cramps, cardiac arrhythmias, tremors and convulsions. The toughest effect is the paralysis of the respiratory muscles and inhibition of the respiratory centre which gives death results.

Table 1.1 Physical and toxicological properties of common nerve agents.

Properties	**Tabun (GA)**	**Sarin (GB)**	**Soman (GD)**	**VX**	**Dimethyl methyl phosphonate (DMMP)**
Molecular weight (g/mol)	162.12	140.09	182.19	267.40	124.08
Melting point (ºC)	–50	–56	–42	–51	–50
Boiling point (ºC)	248	158	198	240	181
Vapor density (air = 1)	5.63	4.86	5.60	7.29	–
Liquid density (g/cm^3, 25 ºC)	1.07	1.10	1.02	1.062	1.14
Vapor pressure (mmHg, 25 ºC)	0.037	2.9	0.40	0.0007 at 20 ºC	0.962

Volatility (mg/m^3, 25 °C)	610	22,000	39,000	75	–
LD_{50} (skin, mg/kg)	1–1.50	0.10	0.045	0.077–0.128	> 2000
LCt_{50} (inhalation, mg-mg/m^3)	135–400	70–100	70–400	30	–

1.1.1.2 Blistering agents

Blistering agents or vesicants are the toxic chemicals that produce severe blisters during contact with the skin **[7]**. On inhalation, they affect to the upper respiratory tract as well as to the lungs which produce pulmonary edema. These agents can also damage the eyes, mucous membranes, respiratory tract, and internal organs. During eye contact fast pain, lachrymation, conjunctival oedema and blepharospasm occur. When these agents exposed over skin then skin burns which cause oedema, extreme pain and intense pruritus. During high dose exposed on skin completely burns with spreading vesication follows, required immediately surgical debridement and antibiotics. These agents are two types i.e. arsenicals (lewisite) and mustards. The nitrogen mustard includes to HN1, HN2 and HN3 classes and lewisite includes to L1, L2 and L3 classes as representing in the **Fig. 1.2.** Sulphur mustard is the most important chemical in this class of blistering agents and is known as king of CWA. It is highly toxic and has the power to divide the cells. Mustards easily penetrate the skin, rubber and most textiles due to lipophilic nature. When mustard passes through the cellular membrane, it converted into the sulphonium ion which is highly reactive intermediate. This intermediate alkylates to the DNA, RNA and protein, causing death of the cells; especially to DNA **[8–10]**. Another theory of mustard reactivity was given by Gross et al. according to which it depletes the cell of Glutathione which leads to oxidative damage and death of cell **[10]**. Nitrogen mustard and lewisite also reacted in a similar way like sulphur mustard **[8]**.

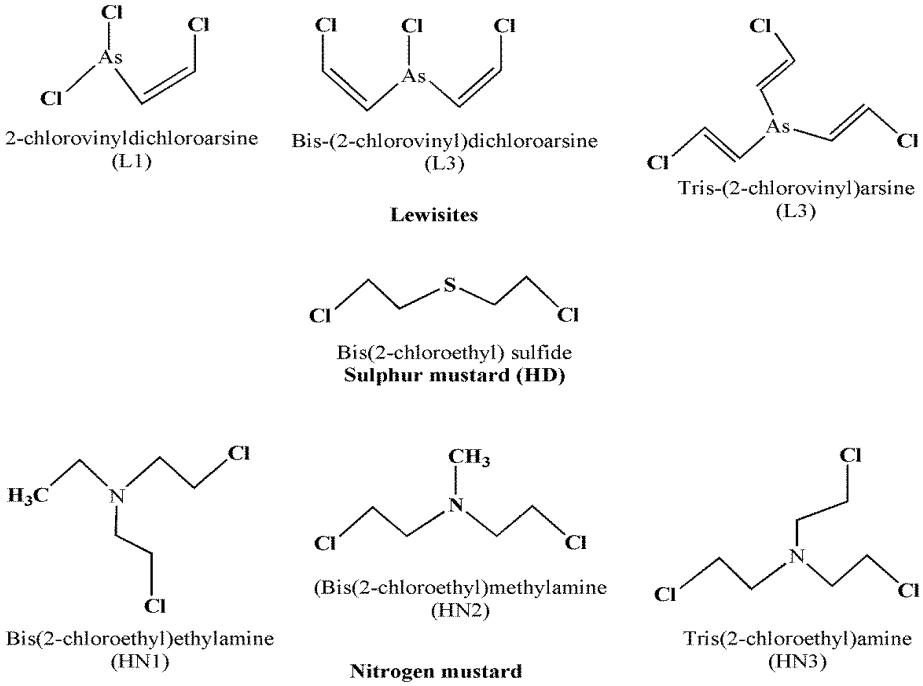

Fig. 1.2 Chemical structures of blister agents.

1.1.1.3 Blood agent

These are the metabolic poisons having cyanide group which affect to the bodies functions by stopping the normal utilization of oxygen by body tissues. These agents include cyanogens chloride (CNCl) and hydrogen cyanide (HCN) types which exerts their toxicity at the cellular level by interrupting the electron transport chain in the inner membranes of the mitochondria. Cyanide (CN^-) has much affinity towards Fe^{3+} ion. When CN^- enter into the biological system, it reacts readily with the Fe^{3+} ion of cytochrome oxidase enzyme of cellular respiration chain and forms complex, thereby stops the impartation of oxygen in the tissues. Eventually, death occurs as a result of respiratory failure **[11]**. The concentration of the inhaled toxic vapour duration of exposer exhibits the how much symptoms are? At low dose of HCN exposer, weakness, headache, confusion, giddiness, nausea and vomiting occur in the form of illness. At higher level of exposer, lack of coordination of movement, rapid and painful respiration, hypoxic convulsions, cardiac irregularities, coma and respiratory failure culminating in death. Some specific properties of these agents are listed in **Table 1.2.**

Table 1.2 Physical and toxicological properties of common blood agents.

Properties	Hydrogen cyanide (AC)	Cyanogen chloride (CNCl)
Molecular weight (g/mol)	27.03	61.48
Melting point (ºC)	−13.4	−6.91
Boiling point (ºC)	25.7	12.8
Vapor density (air = 1)	1.007	2.10
Liquid density (g/cm^3, 25 ºC)	0.687	1.18
Vapor pressure (mmHg, 25 ºC)	742	1000
Volatility (mg/m^3, 25 ºC)	$1.08*10^6$	$2.6*10^6$
LD_{50} (skin, mg/kg)	100 (liq.)	Data not available
LCt_{50} (respiratory, mg-mg/m^3)	2000	11000

1.1.1.4 Choking/pulmonary agent

These are the chemical agents that inflict injure an individual mainly on the respiratory tract, i.e. they irritate the nose, throat and especially the lungs. On inhalation in large scale, these cause swell on membrane, filled the lungs with liquid which results in death due to lack of oxygen. Thus, these agents are defenceless individually. These agents referred to as "dry land drownings" due to fatality nature. This CWA include chlorine and phosgene as the best class agents. Also, nitric acid, perfluoroisobutylene (PFIB) and diphosgene belongs to this group. Both chlorine and phosgene widely used in chemical industries. The mechanism of toxicity of these agents towards human health is reported earlier **[12]**. According to which, when it comes in contact with the moist tissues such as throat, eyes and lungs, it combines with the –SH, $–NH_2$ and –OH groups of biological macromolecules, including enzymes, and this may account for its toxic effects. During combining, it behaves as oxidising agent and form hydrochloric acid, hypochlorous acid and oxygen free radicals that directly damage lung tissue resulting in an inflammatory response that damages the alveolar-capillary membrane of the human lung. Some specific properties of these agents are listed in **Table 1.3.**

Table 1.3 Physical and toxicological properties of common choking agents.

Properties	Chlorine (CL)	Phosgene (CG)	Diphosgene (DP)
Molecular weight (g/mol)	70.9	98.9	197.8
Melting point (ºC)	-101	-128	-57
Boiling point (ºC)	-34	7.6	128
Vapor density (air = 1)	2.5	3.4	6.8
Liquid density (g/cm^3, 25 ºC)	1.393	1.38	1.65
Vapor pressure (mmHg, 25 ºC)	5168	1180	4.2
Volatility (mg/m^3, 25 ºC)	21.9×10^6	4.3×10^6	4.5×10^4
LCt_{50} (respiratory, mg-mg/m^3)	Data not available	3200	3000

In all different types of CWA, we have chosen 2–chloro ethyl ethyl sulphide (CEES) and dimethyl methyl phosphonate (DMMP) to carry out the research, which are well known simulants of sulphur mustard (HD) and sarin (GB), respectively. The HD and GB are banned by UN for the experiments due to their highly toxic nature. Hence, study the adsorptive removal kinetics of these simulants was carried out in the thesis. Before going to discuss about these simulants, first some discussion related to these important agent is urgent.

1.1.2 Sulphur Mustard (HD)

It is also known as blistering agent (vesicant) or yperite agent or tissue–injuring agents that cause severe, delayed burns of the skin, eyes and respiratory tract during contact of body through skin, inhalation, or ingestion or by eyes. It is highly reactive bifunctional compound due to which it behaves as antimitotic, mutagenic, carcinogenic, teratogenic and cytotoxic agent **[13]**. The adverse effects of HD depends upon the route of exposure, how much people exposed and length of the time that people were exposed. It affects to the skin, eyes and respiratory tract principally but most importantly target is deoxyribose nucleic acid (DNA). When it comes into the contact of skin, it become redness with fully etching within 4–48 h after exposure and may change eventually yellow blistering on the skin. In eyes irritation, swelling, pain tearing occurs within 1–2 hours of exposure and severe pain and blindness reached up within 2–10 days. On inhalation, runny nose, sneezing, hoarseness, bloody nose, sinus pain,

shortness of breath, and cough problems creates within 12 to 24 hours of a severe exposure. In bone narrow, decrement in formation of blood cells (red or white cells and platelets) occur which leads to weakness, bleeding and infection.

1.1.2.1 Synthesis of HD

It was prepared by the reaction of sulphide chloride **[14]**:

$$SCl_2 + 2\ C_2H_4 \rightarrow (Cl–CH_2CH_2)_2S$$

1.1.2.2 Physical and chemical properties

It is colourless and odourless liquid in pure state but yellow or brown colour having garlic, onions or sulphur like smell due to impurity. It is water insoluble and has the solubility 1 g/l at room temperature. The physical properties are listed in **Table 1.4.**

The chemical properties of the HD were due to presence of sulphur atom at centre having free lone pair of electron as well as by side chains. Due to presence of this lone pair of electron, it is subjected to the electrophilic attack leading to production of sulphone and sulphoxides. Also, HD gives hydrolysis reaction by forming heterocyclic onium ion formation between the interaction of nucleophile centre atom and negatively inductive effect of the chlorine atom. The kinetics and mechanism of the hydrolysis reaction have been proposed earlier in literature **[15, 16]**. The oxidation of HD occurs by the addition of one or two oxygen atoms to the centred sulphur atom in presence of different oxidising agents. The mechanism of oxidation reactions is reported in earlier literature **[17, 18]**. The toxicity reaction of HD with DNA is already discussed shortly in blistering agent section.

Table 1.4 Physical and toxicological properties of common blistering agents.

Properties	Sulphur Mustard (HD)	Nitrogen Mustard (HN3)	Lewisite (L1)	2-chloroethyl ethyl sulphide
Molecular weight (g/mol)	159.08	204.54	207.32	124.632
Melting point (ºC)	14.0	-3.7	-18 (trans/cis mix)	27.2
Boiling point (ºC)	228 (decompose)	256 (decompose)	190 (trans/cis mix)	156
Vapor density	5.40	7.10	7.1	4.27

(air = 1)				
Liquid density (g/cm^3, 25 °C)	1.27	1.234	1.89	1.066 at 20 °C
Vapor pressure (mmHg, 25 °C)	0.11	0.010	0.35	3.4
Volatility (mg/m^3, 25 °C)	900	121	4480	16.57 mg/l at 20 °C
LD_{50} (skin, mg/kg)	100	10	30	1425
LCt_{50} (respiratory, mg-mg/m^3)	1000-1500	1500	1400	Data not available

1.1.2.3 Simulants of HD

To understand the chemistry of agent, a number of simulants are exist such as $RSCH_2CH_2Cl$ (R= methyl, ethyl or phenyl) and $RSCH_2CH_2X$ (X= tosylate, brosylate, Br^-, I^-, or other leaving group) which react in the same way as HD but give much simpler reaction products and kinetic rate expressions. 2–chloroethyl ethyl sulphide (CEES) (chemical formula C_4H_9ClS) is the well known surrogate of HD which has similar structure. It is widely used in the research field due to less toxic nature and involves a low risk human health in comparison to HD. Therefore, in the present thesis, we have used CEES agent instead of HD in all decontamination experiments. The physical properties of the CEES are listed in **Table 1.4.** The chemical properties of CEES are same as HD.

1.1.3 Sarin

Sarin (GB) is a man–made CWA, classified as nerve agent. It is an organophosphorus compound that produces potent and irreversible inhibition of cholinesterase. It is highly toxic for the nervous system. Firstly, it was produced by Germany as a pesticide during the Second World War in 1938. The people can expose it through skin contact, eye contact or through inhalation of the contaminated air. After exposer, symptoms occur within few seconds of vapour form and few minutes of liquid form. These symptoms are in the form of headache, weakness, confusion, diarrhea, cough, eye pain, small pinpoint pupils, watery eyes low or high

blood pressure. With contact of skin, sweating and twisting occur at the touched skin place. In case of large amount of exposer, extremely harmful effects occur in the form of loss of consciousness, convulsion, paralysis and respiratory failure results of death.

1.1.3.1 Synthesis of sarin

Sarin (chemical formula, $CH_3–P(=O)(–F)(–OCH(CH_3)_2)$ is a chiral molecule and is prepared by the mixture of methylphosphoryl difluoride and isopropyl alcohol.

$$CH_3P(O)F_2 + (CH_3)_2CHOH \rightarrow [(CH_3)_2CHO]CH_3P(O)F + HF$$

1.1.3.2 Physical and chemical properties

It is colourless, odourless and tasteless liquid that can evaporate into the vapour state and can become toxic to the environment. It is highly soluble in water. The physical properties of the sarin are listed in **Table 1.1**. The chemical properties of sarin occur due to presence of P atom as well as P–X bond. The P–X bond easily broken by the nucleophilic reagents such as water or –OH group and give the non–toxic hydrolysis product i.e. phosphoric acid. In hydrolysis reaction, the complex form as intermediate which give nucleophilic reaction with water or –OH group. The toxicity reaction of sarin is called anticholinesterases because they phosphoryl to the enzyme acetylcholinesterase (AChE), which plays a significant role in the nervous system. Before going into the details of how nerve agents inhibit this enzyme, it is important to understand the role of this enzyme in the nervous system, which is explained in **Fig. 1.3 (a).** The AChE helps in the hydrolysis of neurotransmitter acetylcholine which transmits the signals between neurons from central nervous system to the muscle as also discussed in the earlier section.

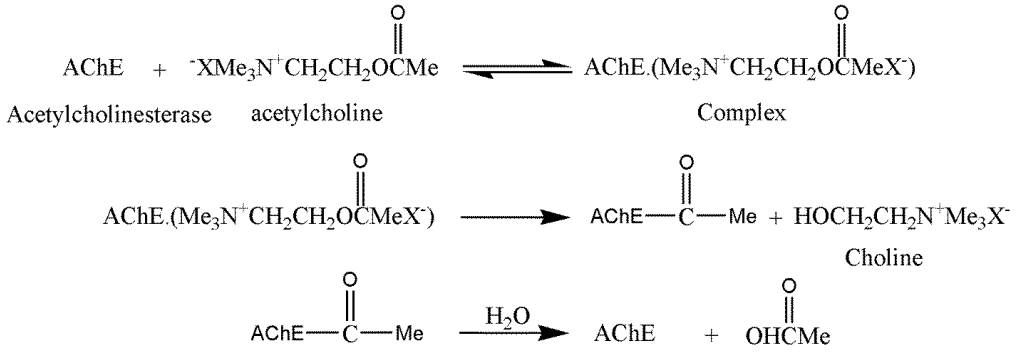

Fig. 1.3 (a) Catalytic action of the enzyme acetylcholinesterase.

Sarin inhibits the AChE by phosphorylation and make it inactive which forbids the transmission of nerve impulse, leading to failure of muscle movement. This results increase the uncontrolled acetylcholine concentration at cholinergic synapses, leading to a variety of cholinergic effects, such as myosis, salivation, hypotension, muscle tremors, convulsions and respiratory depression. The mechanism of inhibition of AChE by sarin is given in the **Fig. 1.3 (b).**

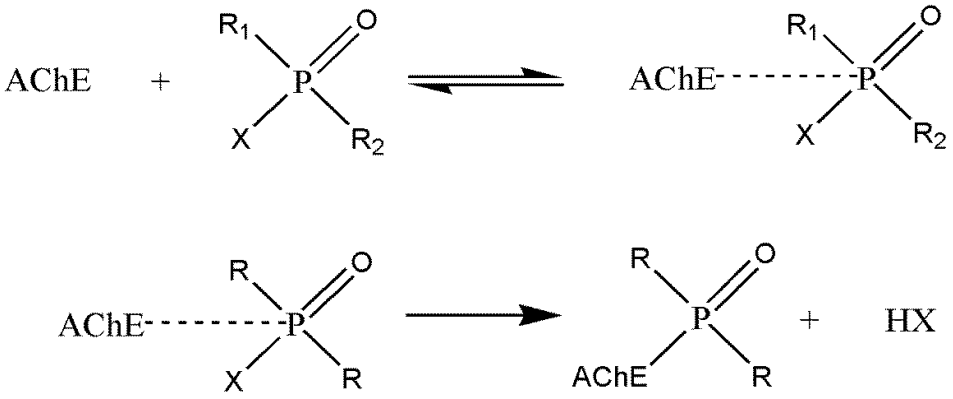

Fig. 1.3 (b) Inhibition of acetylcholinesterase by sarin.

All the nerve agents having form $R_1R_2(O/S)X$ where R_1 and R_2 are alkyl or alkoxy groups and X is a good leaving group are good phosphorylating agents due to X group. They form stable complex as shown in **Fig. 1.3 (b),** causing phosphorylation of the AChE enzyme and hence inhibit enzyme action **[19, 20]**.

On the basis of chirality, the (S)–(–) configuration was proposed to be more toxic and more reactive enantiomer due to greater binding affinity to anticholinesterases **[21]**. In this enantiomer, P–F bond easily broken by nucleophilic agents.

1.1.3.3 Simulants of GB

A series of simulants such as DMMP (dimethyl methylphosphonate), DIMP (diisopropyl methylphosphonate), MDCP (methyl dichlorophosphate), DFP (diisopropyl phosphorofluoridate), TCP (trichlorophosphate) and NPDP or PNPDPP (p-nitrophenyl diphenylphosphate)] of GB have been extensively investigated as model substrates. However, TCP, MDCP are more dangerous for the health than DMMP, and therefore less frequently studied. DMMP (chemical formula $CH_3PO(OCH_3)_2$) is a well known colourless simulant of sarin and has similar structure. It is widely used in the preparation of CWA and in the research field due to less toxic nature and involvement at low risk for human health in comparison to

sarin. Moreover, DMMP exhibits many of the group frequencies associated with the actual agents in infrared spectroscopy. Therefore, in the present study, we have used DMMP instead of GB agent in all decontamination experiments. The physical properties of the DMMP are listed in **Table 1.1**. The chemical properties of DMMP are same as sarin and gives hydrolysis product.

1.2 Background of water

Water is a valuable environmental source which requires special attention of the entire world. Although, water cover 71% of the earth but only 2.5% limited quantity is available as fresh water. Out of which 1.75% in glaciers, ice and snow, 0.5-0.75% as fresh ground water and soil moisture. Therefore, search for clean, potable and fresh water has always been one of the important mankind's priorities. However, due to fast industrialization and modern methods of agricultural and domestic activities, the demand of fresh water increased tremendously and this has resulted in the generation of large amounts of wastewater containing a number of pollutants that are harmful to both human and animal life **[22]**. According to the United Nations World Water Development Report, nearly two million tonnes of waste per day were disposed into the receiving waters including industrial wastes and chemicals, human wastes agricultural wastes which include fertilizers, pesticides and pesticide residue **[23]**. In addition to this, according to the World Water Council and the World Health organization (WHO) **[24]** there is already more waste water generated and dispersed today than any time of the history of the whole world and more than one out of six people lack access to safe drinking water. Also, according to the report of WHO, nearly 2.63 billion people have not proper sanitation facilities and ~1.1 billion people do not have not access to any type of improved drinking water facility. It is also estimated that in the middle of this century, at worst seven billion people in sixty countries and at best 2 billion people in the forty-eight countries will be water-scarce **[23]**.

1.2.1 Pollutant

In a broad sense, the term "pollutant" refers to a substance or material that have the ability to change the natural quality of the environment by physical, chemical or biological process. The three main activities that mankind indulges in are domestic, agricultural and industrial. In all of these activities, a large amount of fresh water is used which discharged in the form of waste water containing different pollutants. These may be inorganic and organic chemicals and

biological agents as well as heat and radiations **[25, 26]**. Some major pollutants on the basis of chemical nature are given below in shortly.

1.2.1.1 Biological agent

Such as *Vibrio comma, Salmonella typhosa, Escherichia coli, Yersinia enterocollitica and Shigella dysenteries* may be present in domestic and sewage water and, hence, need to be removed **[25]**.

1.2.1.2 Heat

The high temperature of the waste water creates many chemical, bacteriological reactions such as the formation of trihalomethane (THM) high corrosion which affect the human life, hence, need to be removed **[27]**.

1.2.1.3 Dissolved and non-dissolved chemicals

During the course of domestic, industrial and agricultural operations, a number of chemicals are used which discharged as waste water and mixed with fresh water. The chemicals may be dissolved or non–dissolved. The non–dissolved solid substances are generally settled down with the formation silt.

The common dissolved chemicals in the waste water are heavy metals, dyes, phenols, detergents, pesticides, polychlorinated biphenyls (PCBs) and a host of other inorganic and organic substances **[25]**.

1.2.1.3.1 Heavy metals

The waste water generated from many industries may contain a number of heavy metals which have significant toxic effect and therefore considered as toxic pollution **[28]**. The various industries such as tanning, plumbing fixtures, cable coverings, batteries, glassware, ceramics, electroplating, pigments and paints, mining and photographic generate such type of waste water. This waste water contain different heavy metals such as chromium, lead, arsenic, copper, iron, cadmium, vanadium, manganese, cobalt, nickel, mercury, molybdenum, bismuth and among others. The amount and the number of metals exist in the water are correlated directly with the operations that carried out in the industries. For e.g. chromium discharge in waste water from tanneries; chromium, copper, zinc and cadmium generate from metal plating industries and lead generates from a number of industrial and mining sources. In most waste

waters, the presence of the heavy metal concentration is much larger than the safe acceptable limits and therefore, they need to be removed.

1.2.1.3.2 Dyes

Dyes are mainly used in textile, dying, paper and pulp, tannery and paint industries. These industries dye are considered to be an objectionable type of pollutant because of the two reasons; firstly they impart colour to the water which is not acceptable on aesthetic grounds, and secondly they are toxic adversely affect to the human life **[29]**.

1.2.1.3.3 Pesticides

Depending on their function, these are sub-divided as insecticides, nematicides, molluscides, rodenticides, fungicides, avicides, piscides, bactericides, slimcides, algicides and herbicides **[30]**. These also considered as toxic pollutants which not arise only due to agricultural operations but also from pesticide manufacturing plants.

1.2.1.3.4 Phenols

Like metals and dyes, phenols are also considered priority elements as they impart bad taste and odour to the water and also toxic, even at low concentration **[31]**. Therefore, removal of these from water is important. These are present in waste waters generated from pulp and paper, chemical, paints, resin, gas, coke manufacturing, pesticides, tanning, rubber, plastics, textile, pharmaceutical and petroleum industries.

1.2.1.3.5 Detergents

These are the phosphate based which are major water pollutants and responsible for 42% diseases in the human and animals.

1.2.1.3.6 PCBs and PBDEs

Polychlorinated biphenyls (PCBs) are different chemicals used for the lubrication and insulation in electrical equipments and are generated in the manufacturing of glass ceramics, brake linings, grinding wheels, different type of coatings, varnishes, sealants, flame proof paints, sealants, electrical equipments and plastic coatings etc. PCBs are considered the most dangerous of life threatening substances created by humans. Many studies showed that PCBs are capable to disrupt the endocrine and are associated with reproductive failure, immune system disorders, behavior and learning disorders cancers **[29]**.

Polybrominated diphenyl ether (PBDE) is the flame retardant, sub-family of brominated flame retardant group and used in the households' products such as fabrics, furniture and electronics.

1.2.1.3.7 PAHs

Polycyclic aromatic nuclear hydrocarbons (PAHs) are the chemicals that consist of fused aromatic rings and not contain any heteroatom or other substituent. Toxicity of PAHs depends on their structure (same formula but different number of rings). These are formed by the incomplete combustion of carcon containing fuels, such as coal, wood, fat, diesel and tobacco etc. **[31]**.

1.2.1.3.8 Dioxins

The toxicity of these chemicals due to their chemical structure mimics that of hormones which create cancer.

1.2.1.3.9 Radioactive substances

These are harmful due to their harmful radiations emitted by them. These materials are found in research laboratories, hospitals, nuclear power plants, and ore processing industries, military and natural sources.

1.2.1.3.10 Other organic chemicals

A number of organic chemicals includes trihalomethane (chloroform, bromoform), trichloroethylene, aromatic hydrocarbons such as benzene, toluene, xylene, and biphenyls, halogenated aromatics such as dichlorobenzene, chlrotoluene and choloroxylene, halogenated aliphatic compounds such as bromochloromethane, dibromomethane, and tetrachloromethane, fluorine, aldehydes, esters, alicyclic hydrocarbon and ketones that are generated from different industries also affect the quality of water. The present of the chemicals above a certain concentration level in water are toxic and therefore, considered as pollutants. In view of general awareness, it has become impressive part of the government, industries and municipal authorities to work out on the methods for pollution control. A number of methods are available but cost factors, efficiency of removal are important to control the pollution. Therefore, search for the effective technology for safe and effective treatment is important and has been discussed in the literature review section.

1.3 Literature review

Literature review is related to development of material technology to decontaminate the CWA and removal of heavy metal ions from water through adsorption process. The first part of the literature gives some briefly description related to the decontamination of CWA and second part gives the description of water treatment methods and technology.

1.3.1 Decontamination of CWA

Decontamination is a method which involves the conversion of toxic chemicals into non–toxic (harmless) products by degradation. Decontamination includes one or more of the following principles:

- To destroy the CWA by chemical modification
- To remove the CWA by physical process i.e. through absorption, washing or evaporation,
- To physically screen-off the CWA so that these cause no damage.

Most of the CWA can be destroyed by using chemicals but such chemicals may be unsuitable since their use corrode, etch or erode on the surface. Ideally, a decontamination must have the given requirements **[32]**.

- It should be compatible with, and non-corrosive to, equipment used in its application as well as to the equipment to be decontaminated.
- It should not soften nor damage paints, coatings, polymeric seals or gaskets or transparencies such as windscreens.
- It should not interfere with in-service monitoring equipment used to verify the effectiveness of the decontamination or to locate residual contamination.
- It should be easy to prepare, easy to apply and remove, and remain stable for a reasonable length of time after preparation.
- It is highly desirable that it adhere to and coat vertical surfaces for sufficient periods of time for agent desorption from the surface and detoxification, yet be easy to remove by evaporation or by rinsing. If used in combination with a surfactant, the decontamination formulation should not compromise the integrity of the foam.
- It should be of low toxicity, be non-flammable and have a low impact on the environment in order that training can be realistically and frequently performed.

The kinetics and mechanism of the decontamination reactions are strongly affected by the solvent property, decontamination medium. A best medium is one, which dissolved the both agents and promotes the desired reaction. As the reactive decontaminants are more effective in comparison to the non−reactive decontaminants because agent removal is more complete at increased speed. However, depending on the resources available on the battlefield, decontamination can also be accomplished by physical methods such as mechanical forces, dissolution, evaporation, or absorption in the absence of any chemical conversions. In physical methods, the contaminated surface can become decontaminated by scrubbing, spraying with a soap solution, spraying with a steam jet, or covering with carbonaceous materials.

1.3.1.1 Background of decontamination system

After the Second World War in which HD was used by Germany on Allied troops at Ypres, France, hence, requirement of decontaminating agents was must and necessary. For this, bleaching powders was the first decontaminant that was used in decontamination and to a lesser extent, potassium permanganate (**Table 1.5**) **[33]**. With excess amount of bleach, CWA strongly converted into non−toxic or less toxic products in few minutes of liquid−liquid (bleach solution) or liquid−solid (bleach powder) interaction. In the presence of bleach solution, HD is converted into a series of oxidation and elimination products (**Scheme 1.1**). As it was believed that firstly oxidation product formed (sulfoxide and then sulfone) and then elimination product viz. monovinyl and divinyl sulfoxides and sulfones formed in strongly basic solution **[34]**. But due to some disadvantages such as (i) stability of active chlorine content of the bleach which gradually decrease (ii) amount of bleach for oxidation and importantly (iii) corrosive nature of bleach. As results, buffered solutions of bleach as shown in **Table 1.5** and less alkaline N−chloro compounds (Chloramine−B, trichloroisocyanuric acid, sodium N, N−dichloroisocyanurate, chloramine−T) were used as decontaminants to overcome the above difficulties.

Table 1.5 Decontaminants Composed of Hypochlorite.

Decontaminant	Composition	Applications
bleach	2-6 wt % NaOCl in water	skin and equipment
HTH (high test hypochlorite)	Ca(OCl)Cl+ Ca(OC1)Z as a solid powder or a 7% queoua slurry	equipment and terrain
STB (super tropical bleach	Ca(OC1)z + CaO as a solid powder or aa 7,13,40, and 70 wt % aqueous slurries	equipment and terrain
Dutch powder	Ca(OC1)Z + MgO	skin and equipment
ASH (activated solution of hypochlorite)	0.5% Ca(OC1)Z + 0.5% sodium dihydrogen phosphate buffer +0.05% detergent in water	skin and equipment
SLASH (self-limiting activated solution of hypochlorite)	0.5% Ca(OC1)2 + 1.0% sodium citrate + 0.2% citrate acid + 0.05 % detergent in water	skin and equipment

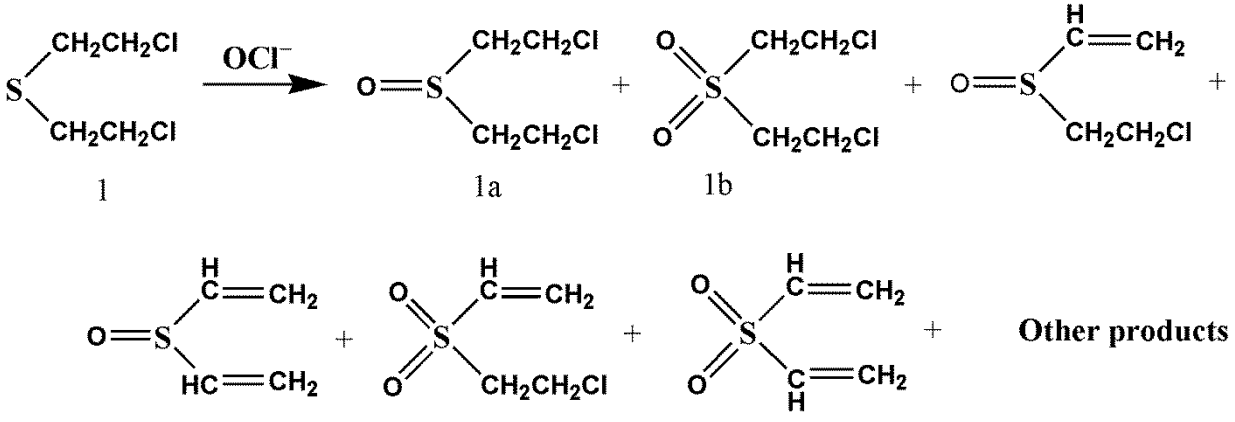

Scheme 1.1 Reaction products from HD and hypochlorite anion.

During the Second World War, G agents were used which were rapidly convert into non-toxic form in the alkali salts (e.g., Na_2CO_3, NaOH, or KOH) solution by converting them into

their phosphonic acid **[35]**. Also, these nerve agents could be detoxify rapidly in the bleach solution through hypochlorite anion which behaved as a catalyst **Scheme 1.2 [36]**.

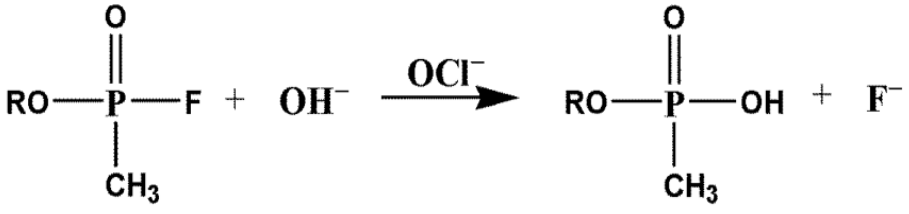

2, 3 3a, 4a

2 $R = (CH_3)_2CH$ **3** $R = (CH_3)_3CCH(CH_3)$

Scheme 1.2 Reaction products from nerve agents and hypochlorite anion.

Due to stability drawback of bleaching powder, the search for a new decontaminant was started and finished on DS2 in 1951 after Second World War. This was an effective decontaminant with long term storage stability in a large operating temperature (–26 to 52 ºC). It is a mixture of 70% diethylenetriamine ($H_2NCH_2CH_2NHCH_2CH_2NH_2$), 28% ethylene glycol monomethyl ether (**a,** $CH_3OCH_2CH_2OH$), and 2% sodium hydroxide (NaOH). The reactive compound in DS2 was found to be $CH_3OCH_2CH_2O^-$, conjugate base of **a**. It reacts with HD as shown in **Scheme 1.3**. Reaction was completed within one min and after reaction only one product 1d was formed, **1c** was an intermediate **[37]**.

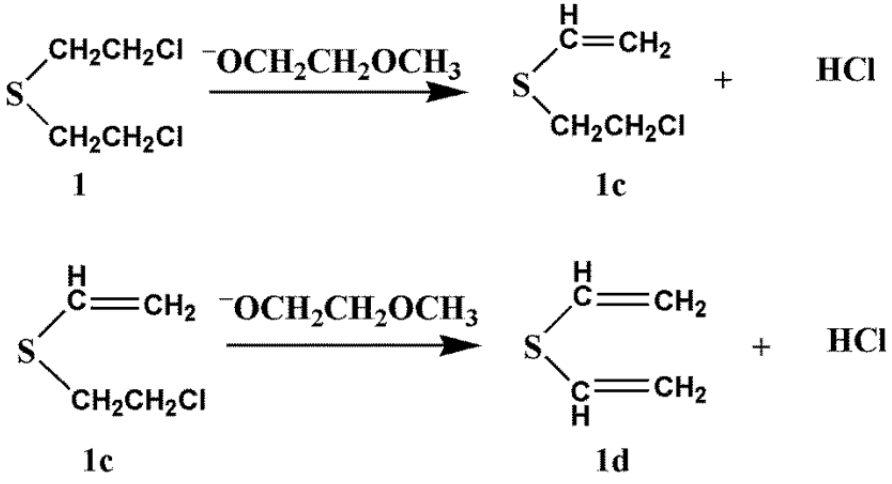

Scheme 1.3 Reactions of HD with DS2 solution.

Nerve agent 2, 3, and 4 also react with conjugate base to form diesters 2c, 3b and 4b and the products are listed in **Scheme 1.4.** After some time, these diesters products further decompose in DS2 via slower secondary reaction to form 2a, 3a and 4a other final products **[37]**. The agents have been already detoxified by primary reaction due to which these reactions are not so important.

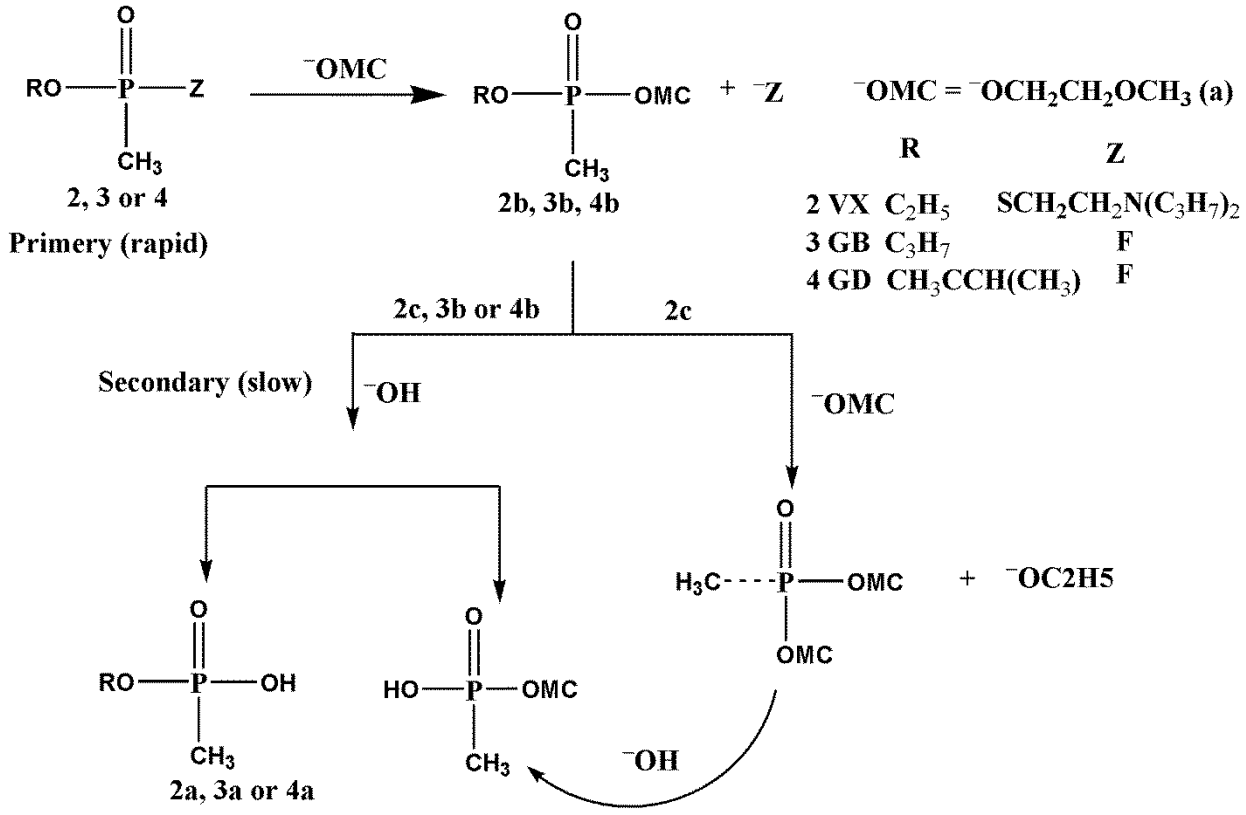

Scheme 1.4 Reactions of VX, GB, and GD with DS2 solution.

Although, DS2 easily decontaminate to the toxic agents but it has corrosive nature and damage to the paints as well as plastics, rubber and leather materials. Personal handling also required highly protective gloves with eye shields and chemically protective gloves in order to avoid skin contact. To avoid these problems, need of searching the new decontaminating solution which is stabile, non−corrosive, non−toxic and environmentally safe. American decontamination kit called M258A1 and M280 that contain the ethanol (72%), phenol (10%), NaOH (5%), ammonia (0.2%) and water (12%) and German emulsion C8 that was composed of tetrachloroethylene (15%), water (76%), anionic surfactant (1%) and calcium hypochlorite (8%) have used as decontaminating solvents. Along with, microemulsion

based multi-purpose chemical, biological decontaminant (MCBD) system contains water (60%), tetrachloroethylene (7%), n−cetyl trimethyl ammonium chloride (28%) and traces of cosurfactant, (n−Bu)4 NaOH was used as decontaminating solvent. To this microemulsion, Fichlor (4%), sodium 2−nitro−4−iodoxybenzoate (0.1%) and sodium borate are added for reactions with the agents. The MCBD system was superior to the C8 system because it is a more stable emulsion at a lower pH of 10, contains less tetrachloroethylene and is partially catalytic. These are non-corrosive and physically stable which can penetrate into paint to dissolve and react with the imbedded agent without damaging the paint.

The above solvents haves good decontamination property but the lack of solubility with CWA, inability to work in colder environment are also problem, hence, search for solid sorbent decontaminants instead of liquid decontaminants. The solid sorbent decontaminants such as resin mixture (XE−555), fuller's earth and metal oxides particles such as SiO_2, Al_2O_3, $\alpha-Fe_2O_3$, La_2O_3 which have larger size, convert these toxic CWA into non−toxic products. But due to larger size of the particles, the reactions rate was very slow and only a small amount of CWA agent convert into non−toxic products even after several days **[38–41]**. From the foregoing discussion, it is clear that each technique has some drawbacks. Hence, new effective method is required to detoxify the CWA which provide high rate constant value with non-corrosive, non-toxic, non−flammable and environment friendly nature. A ray of hope arises with the advent of nanotechnology. Hence, moving towards nanotechnology which provides higher surface area, strong adsorbability and potential reactivity to the sorbent based decontaminants for the CWA. The nanoparticles remove the agents rapidly from the contaminated surfaces and degrade it in−situ and render the agent non−toxic.

1.3.2 Wastewater treatment technology

Water treatment is an important issue due to which scientist are looking for suitable and inexpensive technologies. In present, unit operations and processes are combined together and called primary, secondary and tertiary treatment. Primary treatment includes primary purification process of physical and chemical, while secondary treatment deals with the biological treatment. In tertiary treatment, water treated by primary and secondary process is converted into the high quality water that can be used in different use e.g. in drinking, industrial, medicinal etc. From the last treatment, 99% impurities removed from waste water.

Despite the development of different technologies for the water treatment, effective and rapid treatment and reclamation at commercial level is still a challenging task. The management of removed pollutants (sludge) is also a big problem. The systematic approach of water treatment recycling process involves the understanding of the technology that includes construction and operational cost, maintenance and management of removed pollutants. Water treatment and recycling technologies have been classified by

I. Primary water treatment technologies

II. Secondary water treatment technologies

III. Tertiary water treatment technologies

1.3.2.1 Primary water treatment technologies

In this category, water is treated at primary level by using screening, filtration **[42]**, centrifugation **[43]**, sedimentation **[31]**, coagulation **[44]**, and flotation **[10]**, methods. Generally, these methods are applied at highly polluted water.

1.3.2.2 Secondary water treatment technology

In this category, biological routes were applied for the removal of soluble and non-soluble pollutants from water through microprobe. During treatment, microprobe (bacterial and fungal stains) converts the organic maters into water, CO_2 and NH_3 gases **[45]**. The disadvantage of this method is the production of large quantity of biosolids which require further costly management.

1.3.2.3 Tertiary water treatment technologies

This is the most important technology for the waste water treatment as used to get safe water for human consumption. The techniques distillation **[46]**, evaporation **[47]**, crystallization **[48]**, solvent extraction **[49]**, chemical oxidation that was carried out using chlorine, potassium permanganate, Fenton's reagent (H_2O_2 and Fe catalyst), H_2O_2, ozone, and chlorine dioxides **[50], [51]**, advanced oxidation methods using ozone **[52]**, combined ozone and peroxides **[53]**, ultra violet enhanced oxidation such as UV/Fenton or photo-Fenton **[54]**, UV/hydrogen peroxide, UV/ozone **[55]**, UV/air wet air oxidation and catalytic wet air oxidation, photocatalysis using oxides such as ZnO, TiO_2, CeO_2 etc. or sulphides such as ZnS, CdS etc. **[56], [57]**, reverse osmosis **[58]**, precipitation **[59]**, ion exchange **[60]**, sonolysis **[61]**, micro

and ultra filtration **[31]**, adsorption **[62]**, electrolysis **[63]**, and elecrodialysis **[64]** were used in this category.

From the above methods, a particular method is not effective in removing all pollutants and in such cases, a number of processes may be used in the conjunction so that all types of pollutants can be tacked. Under such situation adsorption process is considered to be a better method as compared to the other convenience, simplicity of design, ease of operation and universal in use. Additionally, this process can remove/minimize to the different type of pollutants and thus has a wide applicability in pollution control. As a part of this thesis deals with the removal of heavy metal ions such as Cr (VI) and Pb (II) from aqueous water, that why a survey is desirable for adsorption method as given in the below section.

1.3.3 Adsorption technology

The excess of resources and wider applicability of adsorption to control the pollution have been recognized **[65]**. The importance of adsorption in the chemical, petroleum, pharmaceutical and food industries is also well established **[66]**.

The term "adsorption" refers to a process in which a material is concentrated at the solid surface from its liquid or gaseous surrounding. It is considered to be two types. Firstly, if the attraction occurred between the solid surface and adsorbed molecules is physical in nature then it referred to as physical adsorption. Generally, in physical adsorption the attractive forces are Vander Waals forces, as they are weak, resulting adsorption is reversible in nature. Secondly, if the attraction forces between adsorbed molecules and the solid surface arise due to chemical bonding, the adsorption process is called chemisorption. It is due to higher strength of bonding in chemisorptions, it is difficult to remove the chemisorbed species from the solid surface and hence irreversible adsorption. The strength of bonding in physical adsorption and chemisorption is manifested in the values of enthalpy of adsorption which are much lower ($\leq$ 25kJ/mol) for the former as compared to later (200 kJ/mol). The solids that adsorb to the materials are called adsorbents whereas the substances that adsorbed on the solid surfaces are called adsorbates.

The first quantitative phenomena related to the adsorption were studied by C.W. Scheele **[11]** in 1773 on the uptake of gases on charcoal and clays. This was followed by the observations of Lowitz who used charcoal for the decolonization of tartaric acid solutions. Again, Larvitz in 1792 and Kehl in 1793 observed similar phenomenon with the vegetable and

animal charcoals, respectively. However, the term "adsorption" was proposed by Bois-Reymond but introduced in the literature by Kayser **[66]**. Ever since then, the adsorption process has been widely used for the removal of solutes from the solutions and gases from air atmosphere. The extent of adsorption is found to depend on the nature of adsorbent especially its porosity and surface area. A number of adsorbents have been developed by various workers and some of these discussed below.

1.3.4 Adsorbents

The important characteristics of good adsorbent are their high porosity and consequently large surface area with specific adsorption sites **[67]**. Most adsorbents which have been used in pollution control tend to have porous structure. The porous structure not only increases the surface area and adsorption but also affects the kinetics of adsorption. A good adsorbent is one which has high surface area with less time of adsorption equilibrium. Thus for the removal of pollutants, one look to the adsorbent is the higher surface area and high faster kinetic. A number of adsorbents have been developed time to time by the researchers for the waste water treatments. Some of them are given below in short description

1.3.4.1 Silica gel

It is an important amorphous adsorbent having stable chemical properties and highly complicated porous structure. Both siloxane (–Si–O–Si–) and silanol (–Si–O–H–) bonds are presence in the gel structure. These are classified as three types: regular, intermediate and low density gels which show surface areas 750 m^2/g, 300–350 m^2/g and 100–200 m^2/g, respectively. It is used in many industries for drying liquid and gases, purification of hydrocarbons etc. **[68]**.

1.3.4.2 Activated alumina

It comprises a series of non–equilibrium forms of partially hydroxylated alumina, Al_2O_3. In general, as the hydrous alumina precursor is heated, hydroxyl groups are driven off leaving a porous structure of activated alumina. They have the surface area in the range of 200–300 m^2/g and used to remove water from organic liquids **[69]**.

1.3.4.3 Activated carbon

It is the most popular and widely used adsorbent in the waste water treatment throughout the world. Its random imperfect structure gives highly porosity over a wide range of pore sizes from visible cracks and crevices to molecular dimensions. Activated carbon generally exists into two forms (i) powdered activated carbon (PAC) (ii) granular activated carbon (GAC). GAC is more adaptable due to continuous contacting and no need to separate the carbon from the bulk fluid; hence most of the work of removal of water pollutants was done on GAC. On the other hand, PAC faced the problem of separation but acceptable due to low cost and lesser contact time of requirement. Currently, hundreds of brands of activated carbon are manufactured for a large variety of purpose such as for the removal of metal ions **[70]**, phenols **[71]**, Dyes **[72]**, pesticides **[73]**, detergents **[74]**, chlorinated hydrocarbons **[75]**, human substances **[76]**, and many other chemicals and organism **[77]**.

Also, modified activated carbon has been prepared by chemical treatment at the time of activation during manufacturing activated carbon which enhanced the adsorption capacity **[53]**. This modification was carried out mainly by oxidation methods to produce a more hydrophilic structure with a large number of oxygen-containing groups.

1.3.4.4 Agricultural wastes as low–cost adsorbents

Agricultural materials particularly those contain cellulose show potential sorption capacity for various pollutants. In the last few decades, some of the agricultural wastes such as nuts **[78]**, apricots stones **[79]**, tea and coffee wastes **[80]**, coconut wastes **[81]**, almonds **[82]**, olive wastes **[83]**, wastes resulting from the production of cereals such as rice **[84]**, wheat **[85]**, corn **[86]**, maize **[87]**, sugar cane bagasse **[88]** and coir pith **[89]** etc. These agricultural wastes have been used in their natural form or after some physical or chemical modifications.

1.3.4.5 Natural materials as low cost adsorbents

The accumulation and concentration of pollutants from aqueous solution by the biological materials is known as biosorption. In this instance, biological materials such as chitin and chitosan **[90]**, yeast, fungi or bacterial biomass **[91]** and peat **[92]** etc. were used as sorbents.

The above mentioned adsorbents have their own disadvantages such as cost, excessive time and adsorption efficiency and reproducibility etc., then moves to search newer adsorbents that provide high adsorption capacity within a short contact time. Nanotechnology gives new hope

to obtain these properties. Recently, nanostructures materials developed by various chemical routes have been used for the adsorptive removal of water pollutants especially metal ions from the water. The unique properties of nanostructure adsorbents provide unexpected opportunities for the removal of heavy metals in highly efficient and commercial approaches and for that a number of metal oxides nanoparticles have been used for this purpose. Nanoparticles possess higher surface area and large number of active sites due to which great adsorption efficiency occur.

1.4 Nanotechnology

Nanoscience and technology is a broad and interdisciplinary area of research and development activity that has been growing explosively from late 1990s **[93]**. The investigation of low dimensional metal oxide structures, such as nanoparticles, nanowires, nanorods and nanocrystalline thin films have attracted much attention in recent years, because they not only demonstrate electronic and optical properties, but also show promise for their application to degradation of persistent chemical warfare agents and in water purification **[94– 96]**.

The regulation of nanostructures requires a widely agreed definition of such particles. Nanoparticles are routinely defined as particles with sizes (at least one dimension) between about 1 and 100 nm that show properties that are not found in bulk samples of the same material. Here, we argue that evidence for novel size–dependent properties alone, rather than particle size, should be the primary criterion in any definition of nanoparticles when making decisions about their regulation for environmental, health and safety reasons.

During the last decade, nanostructure materials have shown an unprecedented growth because such materials/metal oxides possess unique physical, chemical and biological features that are superior those of conventional large grained polycrystalline materials **[97–99]** for examples

- Large surface area to volume ratio
- Large reactive edges
- Large corner defects and unusual lattice planes
- Higher electrical resistivity
- Lower thermal conductivity
- Greater specific heat
- Higher thermal expansion coefficients

- Superior soft magnetic properties

According to above advantages material oxide nanostructures have been used in different fields of applications such as such as electrochromic or photochromic devices, gas sensors, solar energy transformation, semiconductors, and solar cells, catalysis and biotech industries [100]–[106]. Also, metal oxides nanoparticles exhibits better ability to adsorb and decompose CWA in comparison to the bulk metal oxides and pure metal surfaces. This extraordinary ability occur due to high surface area, large number of highly reactive sides, corner defect sites, unusual lattice planes and high surface area to volume ratio. **Fig. 1.4** exhibits the reactive sites, such as Lewis acid (metal cations), Lewis base (oxide anions) and defect sites (Frenkel & Schottky) available on the surface of metal oxides, particularly on nanoparticles, which contribute to their reactivity towards CWA. Extremely porous solids or fine powders composed of nanoparticles usually have high surface area and pore volume which assists strong adsorption due to inherent large adsorption capacity towards CWA. The active sites become more in number in the nanomaterials in comparison to the bulk materials and as the size of the nanomaterial decreases for a material, surface chemistry changes. For e.g. if the nanoparticle is a cube with corners cleaved off, edge ions are 20% to total surface ions, whereas in larger hexagonal microcrystal, edge ions to surface ions are 0.5%. Thus there is a large portion of edge sites in nanocrystals **[107]**. Hence, metal oxide nanoparticles possess enhanced reactivity towards chemical warfare agents and in the water purification and were successfully tested for the decontamination and adsorption applications **[38, 39, 108–110]**.

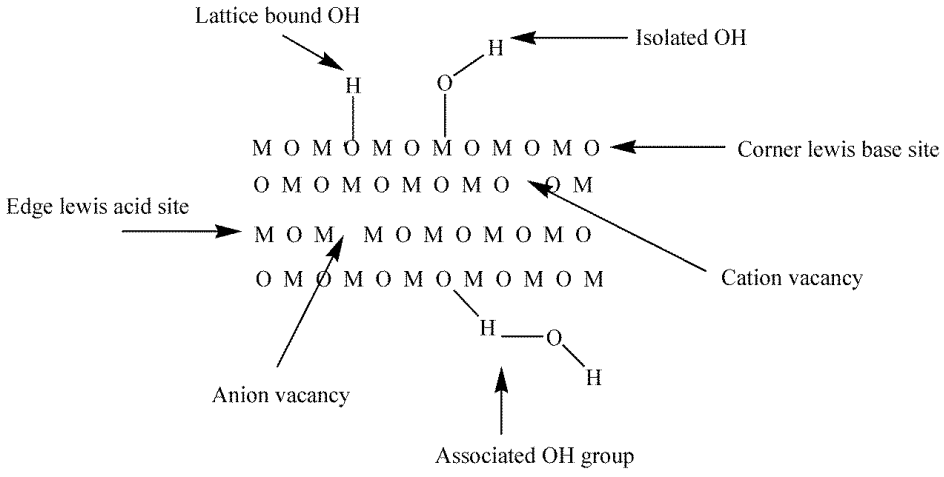

Fig. 1.4 Reactive sites on the surface of metal oxides.

1.4.1 Nanomaterials synthetic techniques

A wide verity of nanostructures metal oxides may be broadly synthesized using chemical vapour deposition (CVD), physical vapour deposition (PVD), inert gas condensation, various aerosol techniques, precipitations from the vapour, and supersaturated liquids or solids (both crystalline and amorphous) techniques and some of the technique are given below

1.4.1.1 Sol-gel method

From this method, a number of metal oxide nanoparticles such as ZnO, WO_3, CuO, MnO_2 ZrO_2, TiO_2 etc. have been synthesized for application of different fields related to degradation of toxic chemicals, photocatalyst, sensors etc. **[97, 111, 112]**. In this method, nitric acid was used to adjust the pH and for restrain the hydrolysis process of the solution.

1.4.1.2 Hydrothermal process

In this method, metal oxides nanoparticles were synthesized by hydrothermal-ion exchange method **[113]**.

1.4.1.3 Microwave irradiation

In this method, ethanolic solution of metal acetate was mixed with the specific amount of ethanolic solution containing NaOH of specific molarity. Thereafter, Polyethylene glycol-19000 (PEG) was mixed into the solution and put into the microwave reflux system for some time **[114]**.

1.4.1.4 Thermal decomposition of precursors

In this method, nanoparticles of metal oxides was prepared using precursor of metal **[98]**.

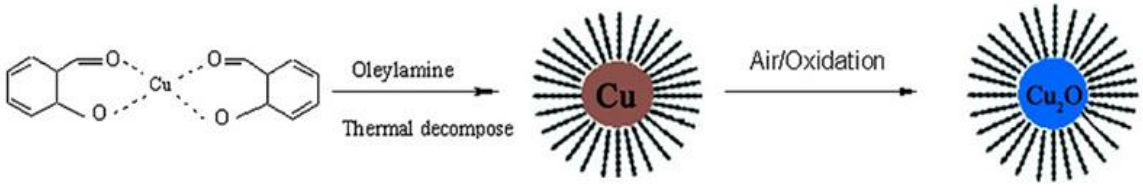

1.4.1.5 Alkoxide based preparation

In this method, the reaction occurs during the precipitation of metal oxides is given below **[115]**.

$$CuCl_2 + 2NaOH \rightarrow Cu(OH)_2 + 2NaCl$$

$$Cu(OH)_2 \rightarrow CuO + H_2O$$

$$NiCl_2{\cdot}6H_2O + 2NaOH \rightarrow Ni(OH)_2 + 2NaCl + 6H_2O$$

$$Ni(OH)_2 \rightarrow NiO + H_2O$$

1.4.1.6 Sonochemical preparation

In this method controlled crystal growth of metal oxides nanoparticles has been studied by composite **[116]**.

The reaction steps for the formation of CuO nanoparticles are as follows:

$$Cu^{2+}(aq) + H_2O(l) \xrightarrow{))))))} CuO(s) + 2H^{+}(aq)$$

1.4.1.7 Wet chemical route

In this method, production of dielectrics and other functional ceramics including complex functional and ion conducting materials was prepared **[117]**.

1.4.1.8 Variety of methods including chemical plasma synthesis

In this method, Iron nano powders as an additive to motor oil, pigments for fraud protection (yttria-iron garnet, >5 nm), BN nano powders for use in protective film for reflecting microwave radiation and UO_2 powders of nuclear fuel have been prepared **[118]**.

1.4.1.9 Wet chemical precipitation and low temperature synthesis, also plasma generation and aerogel recitation in liquid metals

In these methods, oxide ceramic powders including multicomponent oxides of Pu, Th and U with Mg, Y, Gd, Ca etc., for use in high density nuclear fuels, production of very small nanoparticles of a wide range of functional materials using plasma erosion have been prepared **[119]**.

1.4.1.10 Microwave plasma chemical synthesis

In this method, production of high purity metal, oxide, nitride and carbide powders (<100 nm) including functional materials e.g. PZT have been synthesized.

1.4.1.11 Flame synthesis

From this method, high purity nano active carbon having size in the range of 3–5 nm and surface area 1,000 m^2/g occur **[120]**.

1.4.1.12 Direct wet chemical precipitation and low temperature synthesis

From these methods, oxides of ZrO_2, TiO_2, LaSr, MnO_3, $LaBGeO_5$, etc. having particle size 5-50 nm were prepared. Ultrasonic processing was used to disperse and prevent agglomeration **[121]**.

1.4.1.13 Plasma arc synthesis

From this method, high purity oxide ceramic nanopowders, such as Al_2O_3, Y_2O_3, ZrO_2 and the mixtures with dopants having size in the range of 10 to 30 nm have been synthesized **[122]**.

1.4.1.14 Mechano-chemical technique

From this method**, c**arbides, hydrides, oxides, etc. have been synthesized for the use in ion conductors, hydrogen storage, explosives, hardening additions etc. **[123]**.

1.4.1.15 Solid and gas phase self propagating high temperature (combustion) synthesis followed by mechanical crushing

From this method, metal oxides and carbide ceramics such as ZrO_2, Al_2O_3, TiC having particle size in the range 10–20 nm have been synthesized. Also, nitrides, carbides and oxides, eg. AlN, BN, Si_3N_4, SiC have been synthesized with a range of sizes. Other materials can be produced using several stages of processing **[124]**.

1.4.1.16 Aero–gel process

From this method, a number of metal oxide nanoparticles and nanocomposites such as $MgAl_2O_4$ have been synthesized having particle range 12–32 nm and used as adsorbent in the destructive of paraoxon and acid-base adsorption **[125]**.

1.4.1.17 Sputter deposition

From this technique a number of various metal oxides nanoparticles such as CuO, Cu_2O, WO_3, ZrO_2 etc. have been synthesized which have particle size range 1–10 nm for the application of degradation of CWA **[126]**.

1.4.1.18 Laser ablation technique

From this technique a number of various metal oxides nanoparticles such as In_2O_3, SnO_2, ZnO etc. have been synthesized for the purpose of different applications such as catalysis, energy-related materials, photothermal therapy fields etc. **[127]**.

1.4.2 Uses of metal oxides for the decontamination of CWA

During decontamination, some important keys such as decontamination efficiency, speed of degradation, equipment friendness, ecofriendness, and versatility (ability to decontaminate wide range of CWA) are required for the best decontaminant **[128]**. A number of metal oxides nanostructures such as MgO **[129]**, CaO **[130]**, Al_2O_3 **[131], [132]**, TiO_2 **[133]**, ZnO **[111**], **[134]**, MnO_2 **[97], [113], [135]**, ZrO_2 **[136]**, CuO **[137]**, V_2O_3 **[138]**, SrO, BaO, Fe_2O_3 **[139]**, mixed metal oxides such as V_2O_5–TiO_2 **[140]**, CuO-ZnO **[141]**, Al_2O_3-Fe_2O_3, Al_2O_3-V_2O_5 and Al_2O_3–CuO **[142]** have been proved the above advantages and therefore used for the decontamination of CWA and their simulants. The decontamination of CWA occur through hydrolysis, elimination, nucleophilic substitution, oxidation and surface complexation reactions which involves the C–X or P–X bond or H–X (X=Cl, F, and CN), –C–S– or –P–OR bond. These metal oxides exhibits unusual destructive chemisorption capability towards acid gases and CWA due to Lewis acid/base sites of varying the coordination number (M^{n+}), i.e. metal cations, oxide anions. Also, the metal oxides contain rich surface chemistry due to residual surface –OH group. It was observed that ~7–9 –OH group exist within the 1 nm^2 surface of a nanocrystal, however, the concentration of this –OH group decreases with increasing temperature. The –OH groups mainly concentrated on the edge and corner sites and more isolated, whereas on the larger particles, they found to be on flat planes in closer proximity to each other. If the surface –OH groups on the nanostructures are situated edge/corner sites, then it may be expected that Bronsted acidity would be lower since O^{2-} would be lower coordination and therefore have more basic character **[139, 143]**. The GC–MS and FT–IR spectroscopy have been widely used to explore the interaction and reaction mechanism which facilitate the decontamination of CWA and their simulants with above sites. Authors Templeton and Weinberg found the adsorption of DMMP onto both Bronsted and Lewis acid sites through the binding with phosphoryl oxygen. At room temperature, interaction with Bronsted acid sites occur resulted in the molecular adsorption. Dissociative adsorption at Lewis acid sites led to the formation of an adsorbed methyl methylphosphonate (MMP). Another methoxy group is

presumably converted into methanol either directly through reaction with a surface –OH group or through two step process with a surface methoxy group as an intermediate **[144]**.

Also, the interaction of DMMP with the surface of metal oxide clearly indicates the involvement of –OH group due to loss of –OH group concentration, relative to before adsorption of DMMP onto metal oxides. The frequency of –OH group involved in the binding exhibits the most acidic proton nature, which are not hydrogen bond. The interaction of DMMP with metal oxides indicates the chemisorption due to involvement of Lewis acid metal sites binding to the phosphoryl oxygen at room temperature **[144–146]**. As the temperature increases up to 200 ºC, a clear loss of intensity is displayed by bands, which corresponding to the methoxy methyl groups. The intensity of stretching vibrations at 2956 cm^{-1} and 2853 cm^{-1}, decreased up to 50% on heating up to 200 ºC while the intensities of methyl modes associated with phosphorous bound methyl groups at 2996 and 2930 cm^{-1} remain constant. This is due to the loss of methoxy group from DMMP molecules and formation of surface bound MMP. The frequency of P=O adsorption shift towards lower side and is consistent with the interaction between phosphoryl oxygen and Lewis acid aluminium sites on the surface. As the temperature increases, the bond formed between M–O and P=O is breaking and taking on more single bond character, the frequency of P–O stretch adsorption decreases by 60 cm^{-1}, which can be of associated MMP. Below the mechanism of the CWA degradation onto the surface of some metal oxides nanostructure materials have been explained.

1.4.3 Decontamination mechanism and reactions of CWA on metal oxides nanostructures

Some metal oxides reaction mechanism of the decontamination of CWA was given below.

1.4.3.1 Decontamination of HD, GB, GD and VX with AP–MgO, AP–CaO and AP–Al_2O_3

Wagner and co–workers have deeply studied the decontamination of HD, GB, GD and VX over the surface of aero gel produced MgO, CaO and Al_2O_3 nanoparticles using solid-state Magic Angle Spinning (MAS) NMR technique. They give the elimination and hydrolysis product ratio 50:50, 80:20 and 17:83 with the AP–MgO, AP–CaO and AP–Al_2O_3, respectively **[39, 130, 147]**. The reaction mechanism of the above mentioned CWA on the surface is given in **Fig. 1.5** (in case of CaO and Al_2O_3, only put Ca and Al instead of Mg) which shows the hydrolysis and elimination reactions over the surface of metal oxides nanoparticles and quite

similar to those observed in solution **[33]**. In the case of HD decontamination, the hydrolysis and elimination reactions were characterized by ^{13}C NMR and preferred hydrolysis process. In the former part of the reaction, thiodiglycol (TG) was obtained whereas in the latter, elimination product 2-chloroethyl vinyl sulphide (CEVS) was obtained via HCl removal initially. CEVS product subsequently gives another elimination product divinyl sulphide (DVS) via removal of again HCl. The final product obtained in the ratio of 50% TG and 50% DVS, which are not surface bound due to lack of any binding interaction with the surface and remain volatile. During decontamination of HD, cyclic sulphonium ion was formed as intermediate, being in the form of (non-volatile) salt, which gives hydrolysis and elimination products. In the case of product distribution of HD, MgO gives 50:50 and CaO gives 80:20 ratios of products DVS and TG and/or sulfonium ions (CH-TG) which apparently reside as surface alkoxides. On partially hydrated CaO, a rather fast steady−state elimination of HCl was observed owing to acid-catalysed surface reconstruction (to regenerate fresh surface) and the formation of $CaCl_2$, which is known to be more reactive than CaO.

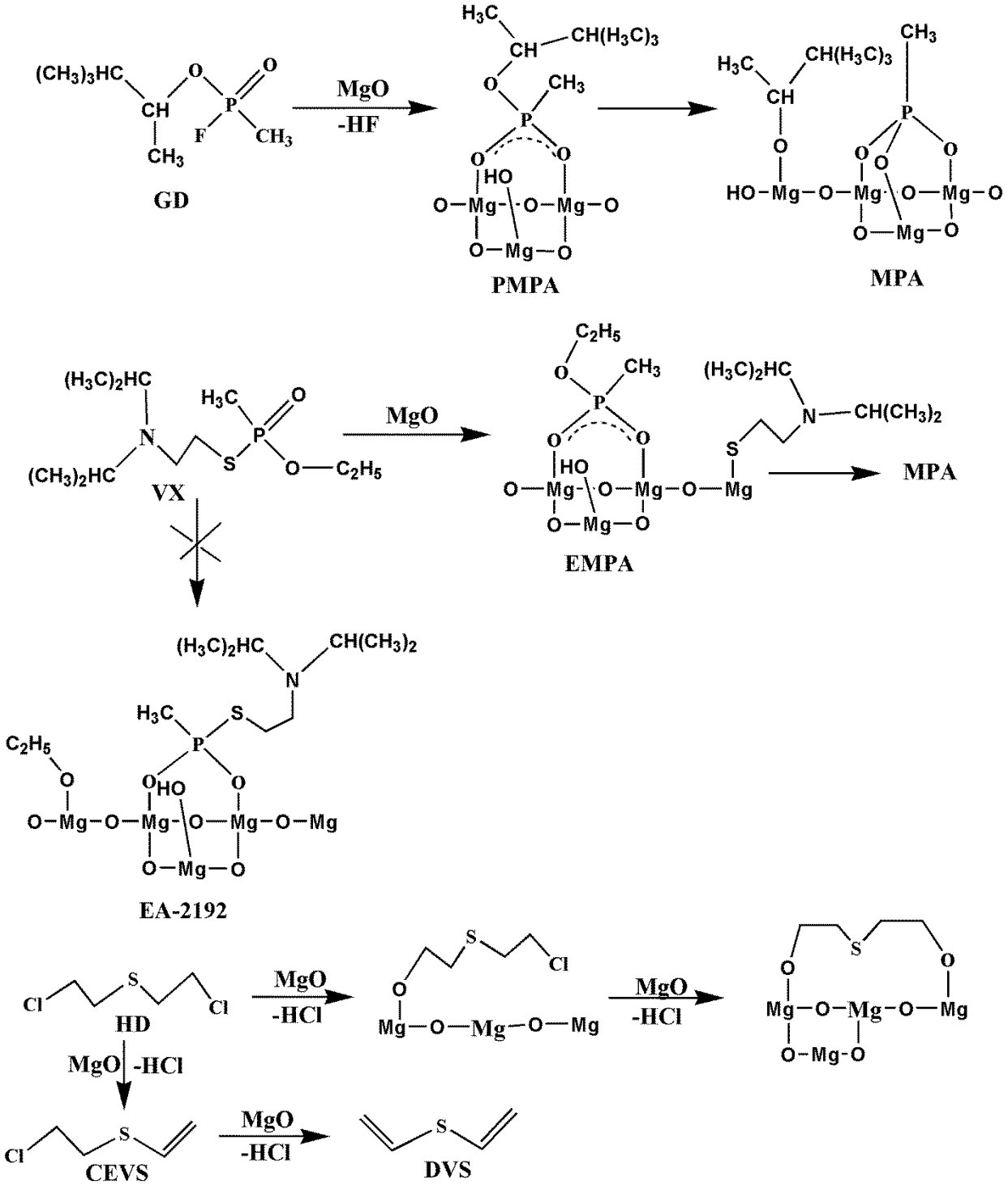

Fig. 1.5 Reactions of GD, VX & HD on MgO nanoparticles.

In the case of decontamination of organophosphorus compounds VX and GD, the non–toxic surface–bound metal phosphonate and hydrolysis product formed. Due to presence of surface hydroxyls and physisorbed water on the surface of above mentioned metal oxides

nanoparticles, VX gives ethyl methylphosphonic acid (EMPA) and methylphosphonic acid (MPA), but toxic S−(2−diisopropylamino) ethyl methylphosphonothioate (EA−2192) was not observed which was occur during basic hydrolysis of VX in solution **[148, 149]**. GD gives the pinacolyl methyl phosphonic acid (PMPA) and MPA. For the VX and GD, broad ^{31}P NMR lines were observed for their products which are consistent with the formation of surface bound magnesium phosphonate or calcium phosphonate or aluminium phosphonate. The reactivity of Al_2O_3 nanoparticles for the CWA degradation was found to the more in comparison to the MgO and CaO because the reactions are not only surface limited and continued to the core of the Al_2O_3 particles. The above mentioned metal oxides surfaces confirmedly contain the surface hydroxyl groups as understood by IR spectroscopy.

Saxena el al. reported the decontamination and kinetics adsorption of different CWA such as HD and GB using Al_2O_3 nanoparticles impregnated with different chemicals **[132, 147]**. The degradation occurs through hydrolysis and elimination reactions.

1.4.3.2 Decontamination of HD, GD and DMMP on the surface of ZnO nanorods

ZnO has been used as a catalyst, toxic sensors and promising adsorbent in the degradation of environmental pollutants in the both normal and light irradiated conditions. It shows unexpected reactivity towards toxic chemicals under normal conditions due to presence of Lewis acid and base sites, Bronsted acid sites of different coordination and due to surface bound hydroxides. Due to these properties, it attracted for the research for the detoxification of CWA over the ZnO nanoparticles and nanorods **[111, 150]**.

Prasad et al. reported the ZnO nanorods (100−500 nm) for the degradation of CWA. Although ZnO did not find much difference in the respective surface areas but show higher rate of detoxification reactions due to having large number of reactive sites in the form of defects and surface bound hydroxyls group, although they have less moisture content than the bulk. In the case of HD decontamination, these molecules interacted with unreactive sites of ZnO nanorods due to higher reactivity as shown in **Fig. 1.4.** The decontamination products of HD were identified by Gas chromatography−Mass spectroscopy (GC−MS) which shows the formation of sulphur mustard, thiodiglycol (TG), confirming the role of the hydrolysis reaction (**Fig. 1.6 (a)**), and chloroethyl vinyl sulfide (CEVS), divinyl sulfide (DVS) and hydroxyethyl vinyl sulfide (HEVS), confirming the role of the elimination (**Fig. 6 (b)**). The IR spectrum

gives adsorption band at 1222 cm^{-1}, 905 cm^{-1} and 720 cm^{-1} indicated the formation of surface bound complexes **[39]**.

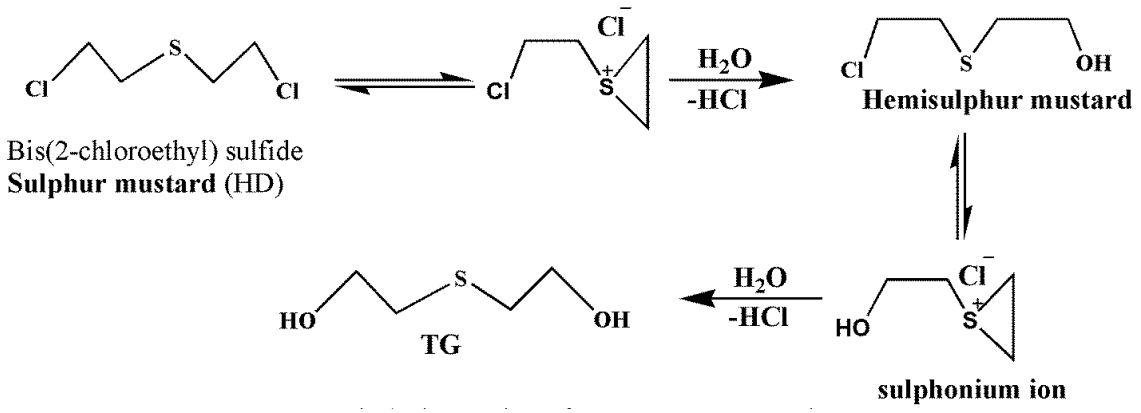

Fig. 1.6 (a) Hydrolysis reaction of HD on the ZnO nanorods.

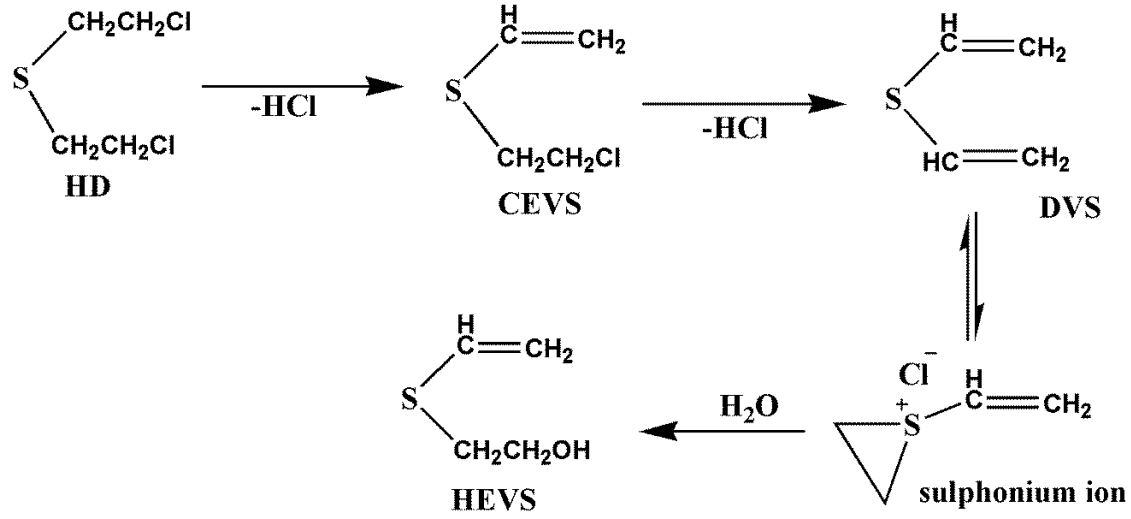

Fig. 1.6 (b) Elimination reactions of HD occurring on the surface of ZnO nanorods.

Inspired by these results, Mahato et al. studied the decontamination of GB on the surface of sol–gel synthesized ZnO nanorods and products were identified by GC–MS and FT–IR spectroscopy. They obtained the similar results regarding the higher rate of decontamination on the surface of the nanomaterials as compared to the bulk. The rate constant and half life value of the detoxification reaction of GB on the surface of nanocrystalline ZnO surface was found to be 4.12 h^{-1} and 0.16 h while 0.1017 h^{-1} and 6.81 h on the bulk ZnO surface. The high rate constant and low half life value of the nanomaterials ZnO exhibited better decontamination

reactivity than bulk due to presence of large number of reactive sites and high surface area in ZnO nanomaterials. The data matches well with the previously reported **[39, 147, 151]**.

The surface hydroxyls present in ZnO nanomaterials attacks on the P–F bond and GB is converted initially into to isopropyl methylphosphonic acid (IMPA) and further into methyl phosphonic acid (MPA) which exists both in surface bound and free states (**Fig. 1.7**). Degradation of GB and accumulation of free MP were experimentally detected. The rate of GB degradation was seemed to be higher than the rate of accumulation of free MPA, which indicates that the degraded GD was collected either in the form of IMPA or MPA. The rate of accumulation of MPA was limited by either transformation rate of IMPA into MPA or desorption rate of MPA. The final product MPA exists both in the form of surface bound and free states as per IR and GC data. Formed MPA seemed to bind with basic groups existing on ZnO. FT–IR data revealed that, bands at 1255 cm^{-1} (P–O), 1020 cm^{-1} (C–O–P) and at 840 cm^{-1} (P–F) those are typical of sarin changed/disappeared during the reaction thus indicating the hydrolysis of sarin.

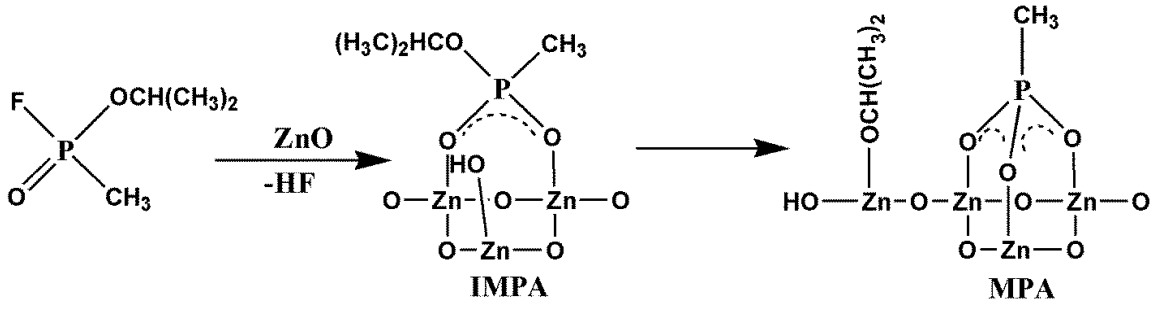

Fig. 1.7 Hydrolysis reaction of GB on the surface of ZnO nanorods.

DMMP molecules bind with ZnO surface through P=O bond; gas phase P=O stretching frequency 1276 cm^{-1} red shifts to 1242 cm^{-1} when adsorbed on ZnO, subsequently to 1210 cm^{-1} when P=O bond interacts with hydroxyls present over the surface of metal oxides. Similar shifting of phosphoryl frequency was reported for DMMP due to interaction with ZnO **[139]**.

The above experimental results exhibited that ZnO nanomaterials offer higher surface area and facilitate adsorption of sulphur mustard and sarin and then, surface hydroxyls and other basic reactive sites (edge defects, etc.), reacted with agent thereby rendering toxic agent to non-toxic products.

1.4.3.3 Decontamination of HD and GB on the surface TiO_2 nanotubes (NTs)

TiO_2 nanotubes also used in the same way as ZnO and reactions seemed to be fast in the initial stage and steady state at the later stage of the reaction with rate constant and half life value of 0.1156 h^{-1} and 5.99 h on the surface of TiO_2 nanotubes indicating the pseudo first order behaviour of decontamination reaction. The GC–MS data was obtained after silylation of reaction products by Bis(trimethylsilyl) trifluoro acetamide due to polar and non–volatile nature.

According to GC–MS and IR data, HD molecules reacted in two ways. In one way, HD molecules react with the intercalated or physisorbed water molecules, which are present on the surface of nanotubes to form thiodiglycol. Initially, the cyclic sulphonium ion seemed to be formed which being in the form (non volatile) of salt could not be extracted out and detected by GC **[33, 152]**. In another way, HD molecules react with isolated hydroxyl groups (Ti–OH) and Lewis acid (Ti^{+4}) sites to form surface bound alkoxy species. Sarin molecules also reacted in similar fashion as mustard with nanotubes. They reacted with physisorbed or intercalated water molecules to form nontoxic isopropyl methyl phosphonic acid in one way and in other they reacted with isolated hydroxyl groups (Ti–OH) groups and Lewis acid (Ti^{4+}) sites to form surface bound phosphonates.

The authors also used modified TiO_2 NT, using transition metal ions such as Ru^{3+}, Ni^{2+}, Cu^{2+}, Ag^{+}, Mn^{2+}, and Co^{2+} **[153]** for decontamination of CWA. The value of the rate constant and half life at the initial stage was found to be 0.0186 h^{-1}, 0.0760 h^{-1}, 0.049 h^{-1}, 0.179 h^{-1}, 0.0875 h^{-1}, 0.0621 h^{-1} and 37.26 h, 9.12 h, 14.14 h, 3.87 h, 7.92 h, 11.16 h, for the Ru^{3+}, Ni^{2+}, Cu^{2+}, Ag^{+}, Mn^{2+}, and Co^{2+} modified TiO_2 nanotubes, respectively. The rate of decontamination of HD was found to be increase on the surface of Ag^{+}–TiO_2 with respect to the original TiO_2 nanotube, because of the abstraction of the chloride ion by Ag^{+}. Other materials (Ru^{3+}, Ni^{2+}, Cu^{2+}, Mn^{2+}, Co^{2+}–TiO_2 NTs), however, exhibited lower rate constants than even the original TiO_2 NTs, indicating their negligible role in abstraction of the chloride ion. These results clear that Ag^{+}–TiO_2 nanotubes exhibited promising results for the decontamination of CWA i.e. HD and GB. Kleinhammes et al. reported the decontamination of 2–CEES through hydrolysis reaction on the surface of TiO_2 nanoscrolls **[154]**.

1.4.3.4 Decontamination of HD and GB on the surface V_2O_5 nanotubes (NTs)

Mahato et al. used the non-stoichiometric vanadia ($V_{1.02}O_{2.98}$) NTs for the decontamination of decontamination of HD and GB **[155]**. The reactions occur fast in the initial stage of the reactions and stead state at the later stage of the reactions with rate constant and half life values 0.11 h^{-1} and 6.30 h for HD and 0.1 h^{-1} and 6.93 h for GB, indicating first order kinetic behaviour. The reactions give similar path of the decontamination reactions as in case of TiO_2 NTs but the reaction is slower. HD give hydrolysis product TDG, oxidation product sulphoxide of HD and surface bound alkoxy species. GB gives hydrolysis product IMPA and surface bound phosphonate.

Also, Singh el al. reported the significance of porous structure of V_2O_5 nanotubes on the degradation of HD and CEES **[138]**. The degradation follow first order kinetics of HD and CEES and the rate constant and $t_{1/2}$ were calculated to be 0.026 h^{-1}, 26.6 h for CEES and 0.052 h^{-1}, 13.24 h for HD. According to GC–MS data, the decontamination of these agents occurs through hydrolysis, elimination and oxidation reactions. The percentage of products found to be 6.4%, 46%, 16.40% and 30% of vinyl ethyl sulphide, hydroxyl ethyl ethyl sulphide, vinyl ethyl sulphide and CEES sulphoxide, respectively in the CEES degradation and 09%, 1.66%, 26.42%, 3.0%, 66.36% and 1.65% of chloro ethyl vinyl ethyl sulphide, hydroxyl ethyl vinyl ethyl sulphide, chloro ethyl hydroxyl ethyl sulphide, thiodigylcol, HD sulphoxide and HD sulphone, respectively, in the HD degradation. For both the agents, percentages of products follows the order as oxidation product > hydrolysis product > elimination product. It was also observed that the percentage of oxidation products was higher for HD in comparison to CEES. This may be due to the more electropositive character of S atom of HD compared to S atom of CEES. The formation of oxidation product of CEES and HD can be explained by the reaction of sulphur atom by the metal ion at normal lattice point at V^{5+} site, i.e., V O bond. Oxidation reaction is affected by the oxidation–reduction mechanism in which the electrophilic lattice oxygen of the vanadium oxide is taken away by the sulphur atom in its d orbital leading to a hypervalent sulphur atom and subsequently sulphoxide of CEES and HD will be formed. Although, very small amount of sulphur mustard sulphone was detected for HD, for CEES only sulphoxide was detected and sulphone of CEES was not detected. The hydrolysis reaction of HD and CESS occurs through the reaction with surface hydroxyl and water molecule inside the vanadium oxide NTs. It is observed that the β elimination proceeds readily over solid acids and

bases. However, in case of vanadium oxide it is observed that elimination product is much smaller compared to CaO and MgO. It may be due to the presence of large amount of water or hydroxyl groups on vanadium oxide NTs.

1.4.3.5 Mesoporous manganese oxides nanobelts, nanotubes and nanosheets for the decontamination of HD, GB and CEES

Mesoporous Manganese oxides nanobelts, nanotubes and nanosheets demonstrate intriguing adsorption and reactive properties against CWA and environmental pollutant. Mahato et al. reported the decontamination reaction of HD, GB and CEES with mesoporous MnO2 nanobelts **[113]**. The decontamination HD, GB and CEES follow pseudo first order behaviour and the values of rate constant and half life were found to be 0.43 h^{-1} and 1.6 h for GB, 0.02 h^{-1} and 34.6 h for CEES, and 0.01 h^{-1} and 69.32 h for HD. Faster decontamination reaction of CWA with MnO_2 nanosheets can be attributed to rapid adsorption and distribution of liquid within the pores and its inter-action with accessible reactive sites. High surface area available on the adsorbent could have facilitated faster adsorption and enabled GB molecules to reach reactive acid base sites at a faster rate and finally GB molecules get decontaminated. However, surface had become poisoned thus forming strongly bound products on the surface and as a result, spreading of liquid stopped. At this stage, agent molecules could have reached fresh reactive sites by evaporation and diffusion in gas phase. Diffusion limited reactions usually exhibit pseudo first order behaviour. Rate of evaporation is usually influenced by vapour pressure of the agent. This observation was seemed to be supported by the high vapour pressure value of GB (2.9 mm Hg). Due to high vapour pressure, the rate of nanobelts. Whereas, HD has very low vapour pressure (0.07 mm Hg) due to which reactions were relatively slow and is consistent with the above rate data. On the contrary, in the case of CEES, although it has high vapour pressure (3.4 mm Hg) could not exhibit faster reaction rates. The reason could be poisoning of active sites due to release of hydrochloric acid and the results are consistent with the reported data **[39]**. The decontamination of GB, HD and CEES on mesoporous adsorbent composed of MnO_2 nanotubes and nanobelts is shown in **Fig. 1.8.**

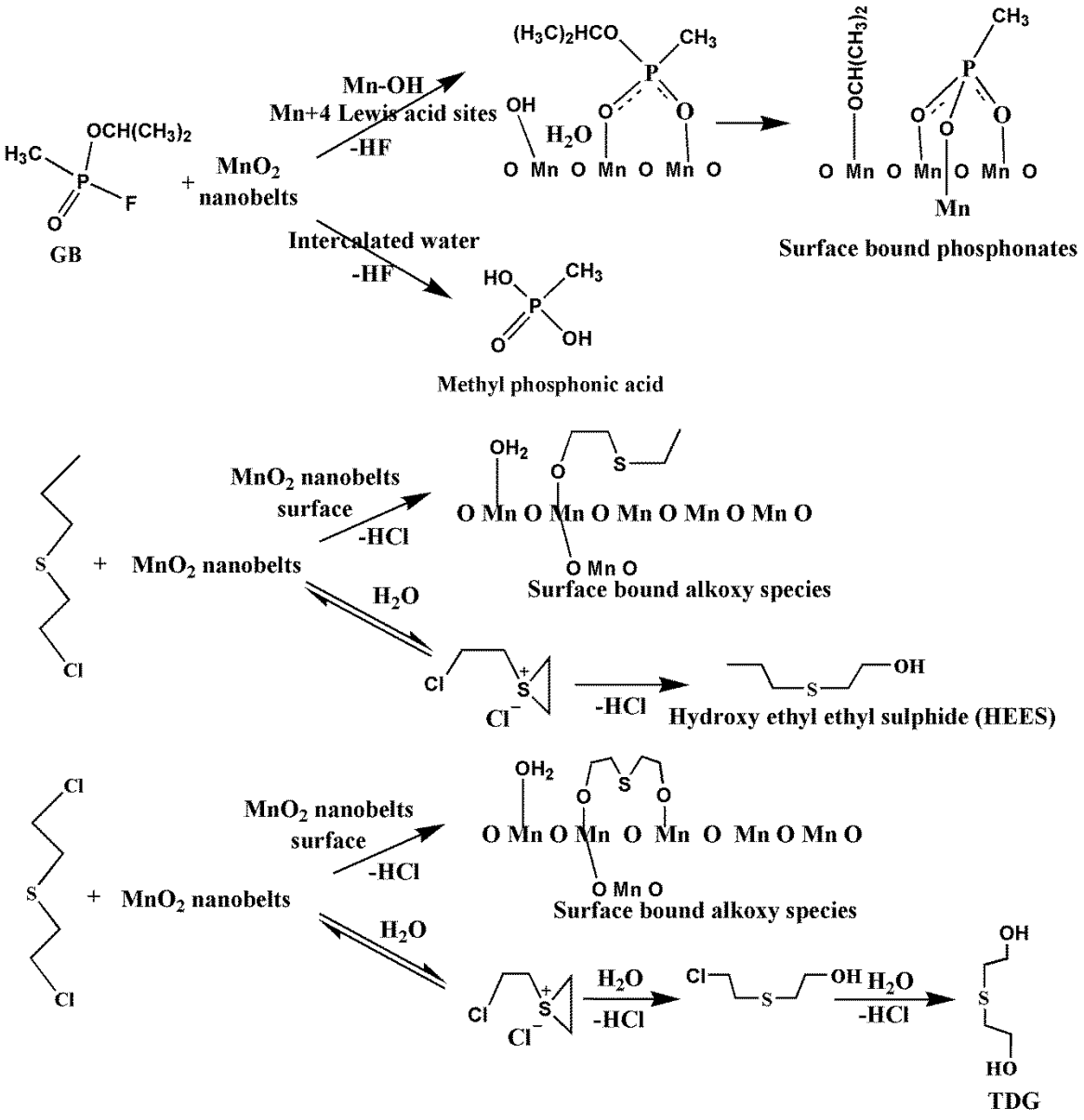

Fig. 1.8 Schematic representation of GB, HD and CEES decontamination on mesoporous MnO_2 nanotubes and nanobelts.

1.4.3.6 Decontamination of HD on CuO nanoparticles

Prasad et al. reported the CuO nanoparticles, synthesized using a traditional precipitation method and then annealed at 250, 300, 350, 550, 700, 800 and 900 °C for 4 h to yield CuO nanoparticles **[156]**. Author reported that variation in calcinations temperature brought about changes in surface structure and hence in the surface acidic and redox properties. With increase in calcinations temperature acidic sites decrease, (bronsted) or basic sites increases. With decrease in OH group as well as hydrated water were changed the path of reaction from

hydrolysis to elimination which minimize the rate of reaction. Tang and co-workers reported that the rate of degradation of HD increases in presence of water through hydrolysis reaction i.e. positive effect of water was found for degradation of HD **[157]**. Literature results also indicate that as the annealing temperature increases, the particle size increases and the surface area decreases **[158]**. Due to decrease in surface area with increase in particle size, the available active sites for adsorption and the activation of the reactant decreases which in turn reduces the rate of degradation reaction.

GC–MS data indicated that at low temperature, CuO nanoparticles react manly through hydrolysis pathway whereas the calcined at 700 ºC and above react only through elimination pathways. The change in the product distribution indicates the change in the property of the CuO nanoparticles. Literature **[158]** exhibits that with increase in the calcinations temperature, the size of the particle increases as well as surface area decreases. Also, during heating the removal of oxygen as an electrically neutral species makes CuO nanoparticles strong Lewis base which may be the cause of the increase in elimination product of HD.

1.4.3.7 Adsorption and decomposition study of DMMP

A number of authors reported the adsorption and decomposition of DMMP on the bulk metal oxides such as WO_3 **[159]**, Fe_2O_3 **[160]**, MnO_2 **[161]**, TiO_2 **[162]**, Al_2O_3 **[163]**, La_2O_3 **[164]**, SiO_2 **[165]**, and MgO **[146]**. Additionally, the interaction of DMMP with nickel, iron, copper, vanadium, and cerium oxides, supported on α–Al_2O_3 **[166]**, and on titania supported nickel and copper metal clusters **[167]** has been studied. DMMP interaction with metal-oxide nanomaterials has been studied with MgO **[168]**, CaO **[169]** and with heterogeneous CaO **[169]**, MgO **[39]**, TiO_2 **[170]**, Pt activated ZnO **[171]** and CeO_x **[172]** nanocomposites and thin films, confirming enhanced reactive properties for the nanomaterials. The adsorption chemistry of DMMP on metal oxides resembles that of the real agents. As demonstrated in **Fig. 1.9 (a)**, DMMP readily adsorbs through the phosphoryl oxygen onto most metal oxides at Lewis acid (metal atom) or at Bronsted acid (hydroxyl) sites **[164, 173]**. The decomposition of DMMP occurs onto metal oxides (excluding silica) through oxidation or hydrolysis on the surface.

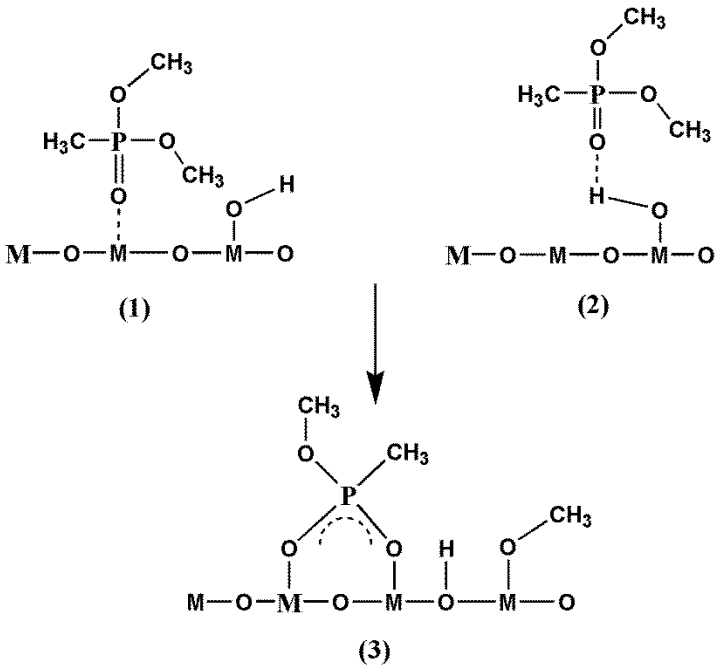

Fig. 1.9 (a) Proposed structure of **(1)** molecular DMMP adsorbed at a Lewis acid site, **(2)** molecular DMMP adsorbed at a Bronsted acid (hydroxyl) site, and **(3)** dissociated DMMP along with a surface–bound methoxy group.

The mechanism of interaction of DMMP onto MgO, Al_2O_3, Y_2O_3, La_2O_3 and WO_3 surfaces, as invisaged by the above mentioned research groups, suggested in (**Fig. 1.9 (b)**). Firstly, DMMP molecules adsorbed through the phosphoryl oxygen to the surface at an acid site (generally metal cation), followed by stepwise elimination of the methoxy group. This methoxy group subsequently combines with surface hydrogen atoms to yield methanol, which, being volatile, is evolved from the surface. Finally, a surface–bound methyl phosphonate product is observed, with the P-CH_3 bond intact. The formation of surface bound PO_x species poisons the active sites from future reaction **[174, 175]**.

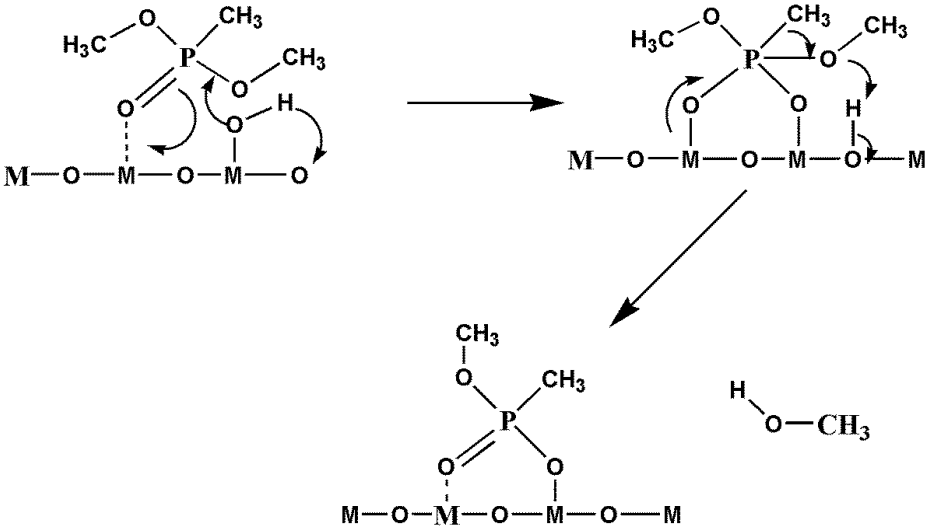

Fig. 1.9 (b) Mechanism involved in DMMP decomposition

The O–CH_3 bond is preferentially attacked, unless an alternative mechanism is available, for oxides like MgO, Al_2O_3–supported CeO_2 and Fe_2O_3, CeO_2, Fe_2O_3, SiO_2 and TiO_2 as reported above **[161, 164, 167, 176–179]**. On the other hand, the adsorption of DMMP on the surface of SiO_2 occurs in different way from that on WO_3, TiO_2 and Al_2O_3 occur **[180]**. Decomposition of DMMP occur via elimination of methoxy groups for WO_3, TiO_2 and Al_2O_3, while weak interaction via formation of two hydrogen bonds between DMMP and the surface hydroxyls on SiO_2 has been reported for high surface area SiO_2 powders. However, at sufficiently high temperatures, complete molecular desorption occurs from the SiO_2 surface. Auger electron spectroscopy (AES) has been used to analyze the interactions of DMMP with SiO_2 **[181]**. For dehydrated SiO_2, no decomposition of DMMP was observed, while on the hydrated surface about 10% DMMP decomposed into methyl phosphonate and methanol.

1.4.4 Water treatment using nanostructures metal oxides

Metal oxide nanostructures potentially offer cost effective wastewater treatment and remediation technology due to their high surface area to volume ratio and enhanced adsorption efficiency. A number of metal oxides nanostructures such as iron oxides, titanium oxides, aluminium oxides, copper oxides of different forms (such as particles, tubes and others) have been used for the removal of heavy metal ions such as arsenic, lead, mercury, copper, cadmium, chromium, nickel. The size and shape both are important factors for the better adsorption performance and synthesized by different methods which includes (1) Physical

approach: inert gas condensation, high energy ball milling, ultra sound shot penning, severe plastic deformation and (2) Chemical approach: reverse micelle (or microemulsion), chemical vapor condensation, controlled chemical co-precipitation, pulse electrode position, liquid flame spray, gas-phase reduction, liquid-phase reduction etc. **[182]**. Among these different synthesis process, co-precipitation **[183]**, thermal decomposition and/or reduction **[184]**, and hydrothermal synthesis techniques **[185]** are commonly used and are easily scalable with high yields. The characterization was carried out to find the morphology, crystallite size, structure, specific surface area and pH_{pzc} (zero point of charge). Below some metal oxides nanostructures are given below.

1.4.4.1 Hydrous manganese oxide (HMO)

Adsorption of metal ions such as Pb (II), Cd (II), and Zn (II) reported in the formation of inner-sphere complex and it can be explained by ion exchange process **[186]**. The adsorption follows Freundlich model more reasonably than Langmuir model, indicates that the active sites of HMO surface are heterogeneous for metal sorption. The adsorption follows the order Pb^{2+} > Cd^{2+} > Zn^{2+}.

Mixed–valence manganese oxides usually present as octahedral molecular sieve (OMS) and used as potentially sorbents for cations. Pakarinen et al. **[187]** reported that OMS materials showed selective adsorption of Cu^{2+}, Ni^{2+} and Cd^{2+} in the presence of Mg^{2+} and Ca^{2+}. The exchange rates were reasonably high due to the small particle dimensions. These materials show the uptake capacity in the range of 0.9–1.3 mmol/g.

1.4.4.2 Nanosized aluminum oxide

Alumina (Al_2O_3) is a traditional adsorbrent for heavy metal ions, and γ–Al_2O_3 is anticipated to be more adsorptive active than α–Al_2O_3. Modification through physical or chemical process in γ–Al_2O_3 nanoparticles with certain functional groups such as oxygen, nitrogen, sulphurs and phosphorous is expected to improve their sorption for heavy metal ions **[188]**. Also, γ–Al_2O_3 modified with 2,4–dinitrophenylhydrazine (DNPH) used as adsorbent for removal of Pb (II), Cr (III), Cd (II), Ni (II), Co (II) and Mn (II) and observed that sorption isotherms follow by Freundlich model for Mn (II), Pb (II), Cr (III) and Cd (II) ions and by Langmuir model for Ni (II) and Co (II) ions. The maximum adsorption capacity (q_m), calculated from Langmuir

equation toward Cr (III), Cd (II) and Pb (II) ions from multiple-metal solution (mixture of six metal ions) were 100.0, 83.33 and 100 mg/g, respectively **[189]**.

1.4.4.3 Nanosized zinc oxide

ZnO is an environmental friendly material and recently used to remove the heavy metal ions. The plate like nanostructures have been reported for the removal of Cu (II) ions with adsorption capacity of >1600 mg/g **[190]**. The adsorption follows Freundlich isotherm with K_F = 324.44 $(mg/g/mg)^{-n}$.

1.4.4.4 Nanosized magnesium oxides

Gao et al. **[191]** reported flower like mesoporous MgO which exhibited better adsorption capacities to Cd (II) and Pb (II) ions. With a contact time of 120 min., the concentration of Cd (II) and Pb (II) ions decreased from 100 mg/l to 0.007 and 0.05 mg/L, respectively, which are much lower than the Pollutant Dischargeable Standard in China (Cd (II) <0.01 mg/L, Pb (II) < 0.1 mg/L) and a little higher than MCLs for drinking water established by the Environmental Protection Agency (EPA) of the United States (Cd (II) <0.005 mg/L, Pb (II) < 0.015 mg/L).

1.4.4.5 Copper oxide nanostructures

Especially nanoparticles have been used to remove the heavy metal ions from water. Reddy et al., 2007 **[192]**; Reddy and Attili et al., 2005 **[193]** found as an effective adsorbent for the removal of arsenic because it did not any requirement of pH or oxidation of As (III) into As (V) and it performed well in the presence of competing ions. Martinson et al., 2009 **[109]**; used CuO nanoparticles having size 12–18 nm as adsorbent for the removal of As (III) into As (V) in the range of pH 6–10 and found maximum adsorption capacity 26.9 mg/g for As (III) and 22.6 mg/g for As (V). The presence of sulphate and silicate ions in water did not inhibit adsorption of As (V) but only slightly inhibited adsorption of As (III). High concentrations of phosphate (>0.2 mM) reduced the adsorption of arsenic onto CuO nanoparticles. X–ray photoelectron spectroscopy indicated that As (III) was oxidized into As (V) and adsorbed onto CuO nanoparticles. The nanoparticles were also used to remove arsenic (>3μg/L) from ground water. Goswami et al. **[194]** reported the removal of arsenic from water through adsorption process using CuO nanoparticles, synthesized by thermal refluxing technique. Different batch adsorption experiments were studied and found that adsorption process followed pseudo second

order kinetic and endothermic behaviour. Also, adsorption followed Langmuir isotherm and give adsorption capacity 1086.2 μg/g. Mohan et al. **[108]** synthesized CuO nanoparticles through green route using Citrus limon juice and utilized for the removal of chromium ion Cr (VI) from water through adsorption process with a different batches mode and reported the adsorption capacity 8.35 mg/g at pH 4.0. Thermodynamic study exhibited spontaneous and endothermic nature of the adsorption while adsorption kinetics followed by pseudo−second order kinetics model. Arfaoui et al. **[195]** synthesized CuO nanorods using hydrothermal method and then used as adsorbent for the Pb (II) ions. The effect of various parameters such as pH, contact time and initial concentrations was studied and found the adsorption capacity 188.67 mg/g from Langmuir isotherm at optimum pH 6. Farghali et al. **[196]** synthesized various types of CuO nanostructures (oval, cluster, leaves, small rod, and porous nanosheets) by microwave radiation technique and then used their ability to adsorb the Pb (II) ions from aqueous solution. The maximum adsorption capacity of the oval, cluster, leaves, small rod and porous nanosheets CuO nanostructures for Pb^{2+} are 125, 116, 117, 120 and 115 mg/g at pH 4 and contact time of 4 h. The adsorption process follows pseudo second−order reaction kinetics, as well as Langmuir and Freundlich adsorption isotherms.

From the above discussion, it is clear that metal oxides nanostructures have a tendency to remove the heavy metal ions from water. Also copper oxide nanoparticles, synthesized using different chemical methods give good adsorption capacity towards different heavy metal ions. However, as discussed earlier, chemical methods have also their own disadvantages and give low surface area value. That's why we moved towards a newer technique that provides high purity with narrow size distribution, reproducibility and large value of surface area and active sites that hence the adsorption capacity towards the heavy metal ions. PVD technique especially sputtering provides such properties to the synthesized materials which give much better results for the removal of metal ions.

To the best knowledge, nobody has used the physical vapour deposition (PVD) technique especially sputtering technique for the purpose of above mentioned applications.

1.5 Materials selection for the degradation of CWA and removal of heavy metal ions

The degradation of toxic chemicals through metal oxide nanoparticles and adsorptive removal of heavy metal ions from aqueous water are the most important and versatile means

for protection of human life. The metals that form easily oxides and have sufficient surface area to adsorb the toxic chemicals and heavy metals on the surface of adsorbent are used for this purpose. Thus, following transition metal oxides that have been selected for degradation of toxic chemicals are

(1) Copper oxide (CuO)

(2) Zirconium oxide (ZrO_2)

(3) Tungsten oxide (WO_3)

(4) Manganese oxide (MnO_2)

1.6 Synthesis technique for preparation of nanostructures metal oxide

The above mentioned materials have been successfully synthesised for the purpose of degradation of CWA and adsorptive removal of heavy metal ions from aqueous water. These have been synthesized by physical vapor deposition method i.e. through sputtering not using thermal evaporation, e-beam evaporation and pulse laser deposition. Among different physical vapour deposition techniques, sputtering was found to be best method for the different point of views. Hence we will develop metal oxide nanoparticles using reactive magnetron sputtering technique.

1.7 Scope and objective of the thesis

1.7.1 Scope

Transition metal oxides demonstrate superior ability in the field of chemical, industrial and engineering due to their unexpected high adsorbing power and reactivity in comparison to pure metal surfaces. This is often attributed reactive sites on the metal oxide surface through which CWA like HD and GB can adsorb and subsequently undergo hydrolysis, elimination or oxidation reactions to convert them into non–toxic form. Also, due to existing of highly reactive sites, metal ions such as Cr (VI) and Pb (II) ions were adsorb and removed from aqueous solution. The reactivity and adsorption power of metal oxides nanostructures increases due to their high surface area, large number of highly reactive edges, corner defect sites, unusual lattice planes and high surface to volume ratio. For the preparation of nanoparticles, deposition conditions like temperature, sputtering power, pressure, gas flow rate, distance

between target and substrate, deposition time etc. significantly affect the structure, morphological, thermal and other properties. Although numbers of literatures are available on their properties but application areas are different. Therefore, in the present thesis we have synthesized different metal oxide nanoparticles using reactive magnetron sputtering technique to detoxify the CWA and adsorptive removal of heavy metal ions.

1.7.2 Objectives of thesis

The main objectives of the research work are as follows:

- Synthesis of CuO, WO_3, ZrO_2 and MnO_2 nanostructures (nanoparticles and nanorods) using reactive magnetron sputtering technique for the decontamination of 2−chloroethyl ethyl sulphide (CEES) and dimethyl methyl phosphonate (DMMP), well known simulants of HD and GD, respectively.
- To synthesize CuO nanoparticles using other sputtering parameters and their use in water purification by removing Cr (VI) and Pb (II) ions.
- To investigate effect of sputtering parameters such as sputtering power and pressure on their structural, morphological and thermal properties of synthesized nanostructures.
- To analyse the morphology and size and surface area of synthesized materials by FE−SEM and TEM and N_2−BET technique.
- To analyse structural properties of synthesis nanostructures using Raman spectroscopy, XRD, FTIR and TGA techniques.
- To investigate the degradation reactions by GC−FID instrument and characterization of the products formed by GC−MS and FT−IR techniques. To study the concentrations of element in aqueous solution by AAS instrument.
- To investigate degradation reactions of CEES and DMMP on the surface of obtained nanostructures by using GC−FID, GC−MS and FT−IR techniques.

- To analysis the concentrations of element in aqueous solution by AAS instrument.

CHAPTER 2

SYNTHESIS AND CHARACTERIZATION TECHNIQUES

2.1 Introduction

In this chapter, we shall be discussed shortly about the nanomaterials synthesis using sputtering, physical vopor deposition (PVD) technique and brifly discussed about sputtering technique and then characterization techniques that were used during the work to explain their different properties. Firstly, a short discussion of the nanostructures is digen below.

2.2 Nanoparticles

As descussed in the earlier chapter that nanoparticles materials are of interest of scientist and engineers because as the particle size decreases (<100 nm) surface properties such as chemical, electrical, optical, magnetic and mechanical begin to dominate over the bulk material. Incorporation of these 'designer' structures into other materials, allows the formation of novel products with enhanced or entirely different properties. By using the nanoparticles, metal oxides can be highly used in the different field of applications.

The change in properties from bulk to surface can readily be seen in the precious metals series. Silver, bulk metals like Gold and Platinum are non reactive, but in the form of nanoparticles (<5 nm) they all are potent catalysts. The platinum reforming catalyst accounts for most of the world's gasoline (petrol) refineries and nanoparticle silver is further used as a powerful bactericide and has been commercialized as a wound dressing. Besides, there are many more applications of nanoparticles in everyday use, like scratch resistant coatings, stain resistant fibres, self-cleaning glass and sunscreens.

Materials with a nanometer-sized microstructure are called nanocrystalline materials. The synthesis, characterization and processing of such nanocrystalline materials are the part of an emerging and rapidly growing field referred to as nanotechnology. Research in this field emphasizes scientific discoveries in the development of materials with controlled microstructural characteristics, also motivates the development of processes with engineered properties and technological functions, and introduces new device concepts and manufacturing methods. Recent advances in techniques for the deposition and processing of thin films have enabled the design and manipulation of materials with unique properties that are often

unachievable in bulk materials. The different synthesic techniques have been discussed in the earlier chapter. Here, we shall be discussed shortly of PVD synthesis and then moved towards sputtering technique.

2.3 Physical vapor deposition technique

Initially Michael Faraday, without any name given for the process of physical vapor deposition (PVD), deposited the coatings as far back as the year 1838. But the term physical vapor deposition (PVD) was originally given by Powell et al. (1966) **[197]**. The PVD is a general term used to describe any of a variety of methods to deposit thin films by the condensation of a vaporized form of the material onto various surfaces (e.g. onto semiconductor wafers). The coating method involves purely physical processes such as high temperature vacuum evaporation or plasma sputter bombardment rather than involving a chemical reaction at the surface to be coated as in chemical vapor deposition. Variants of PVD include, in order of increasing novelty:

- **Evaporative deposition:** In which the material to be deposited is heated to a high vapor pressure by electrically resistive heating in "low" vacuum.
- **Electron beam physical vapor deposition:** In which the material to be deposited is heated to a high vapor pressure by electron bombardment in "high" vacuum.
- **Sputter deposition:** In which a glow plasma discharge (usually localized around the "target" by a magnet) bombards the material sputtering some away as a vapor.
- **Cathodic arc deposition:** In which a high power arc directed at the target material blasts away some into a vapor.
- **Pulsed laser deposition:** In which a high power laser ablates material from the target into a vapor.

In the present work, the nanostructures metal oxides have been synthesized using sputtering method

2.3.1 Sputtering technique

In PVD technique, the synthesis of nanostructures are usually carried out from the same material whose nanostructures are to be synthesized. It’s purity is decided by purity of the target materials, base vacuum and purity of the ambient gas atmosphere (Gohil et al. 2008)

[198]. The sputtering process which is a PVD process involves the physical vaporization of atoms from a surface by momentum transfer from bombarding energetic atomic sized particles. The energetic particles are usually ions of a gaseous material accelerated in an electric field. This PVD technique also includes thermal evaporation and pulsed laser deposition (PLD) process. The most common approach for growing thin films/nanostructures by sputter deposition is the use of a magnetron source in which positive ions present in the plasma of a magnetically enhanced glow discharge bombard the target. The target can be powered in different ways, ranging from direct current (DC) for conductive targets to radio frequency (RF) for non-conductive targets, to a variety of different ways of applying current and/or voltage pulses to the target. For the different PVD techniques, magnetron sputtering is used extensively in the scientific community. The schematic diagram of a simple DC sputtering system is shown in **Fig. 2.1** which consists of a vacuum chamber, target and a substrate holder. The target is a 2 inch diameter disc of material to be deposited which is connected to the negative terminal of a DC power supply. Target and coper cold finger as electrodes and face each other in a typical sputtering chamber.

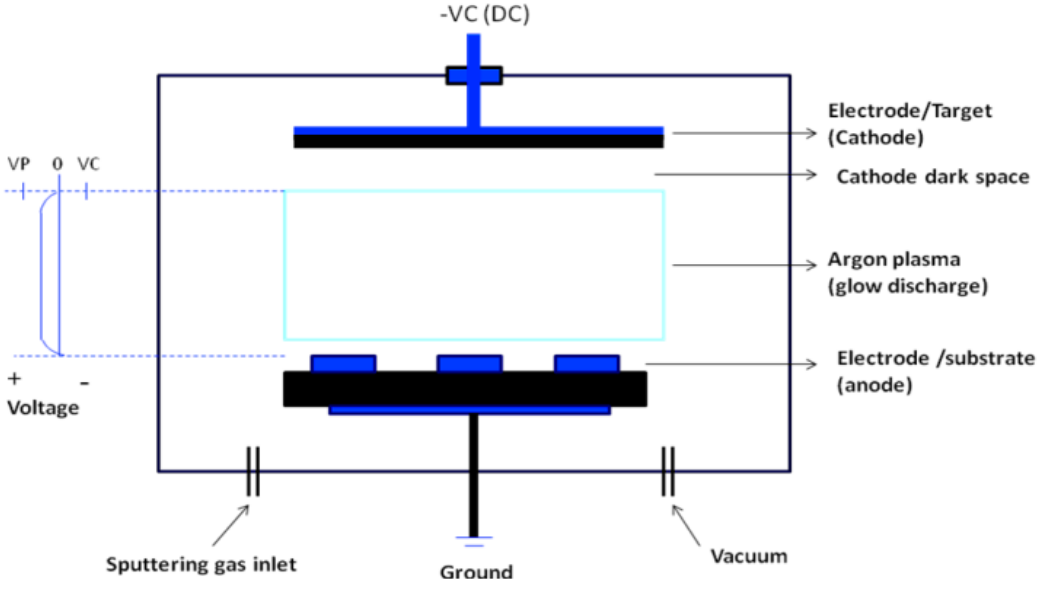

Fig. 2.1 A schematic diagram of a simple DC sputtering system and voltage distribution.

2.3.2 Process of Sputtering

The first step in the sputtering process is the pumping of the vacuum chamber to a typical base pressure of 10^{-6} Torr or more by vaccum pumps like rotary and turbo molecular pumps

etc. An inert gas, usually argon with a pressure ranging from a few to 100 mTorr depending upon the requirement, is introduced into the system as the medium to initiate the discharge and maintain the plasma once initiated. When an electric field of several kilovolts per centimeter is applied between cathode and anode, a glow discharge is initiated and maintained between these two electrodes. A very little current flows at first due to the small number of charge carriers in the system after the initial application of the voltage. Once sufficient number of charge carriers builds up, the free electrons strike the neutral Ar atoms to create Ar^+ ions and more free electrons. The newly created free electrons can now ionize additional Ar neutrals thus multiplying the number of Ar^+ ions. In this visible glow maintained between the electrodes, the Ar^+ ions in the plasma gets accelerated towards direction of the cathode and strike the target. Free electrons are accelerated by the electric field and gain sufficient energy to ionize argon atoms. So, the positive ions (Ar^+) in the discharge strike the cathode (the source target) and this bombardment creates a cascade of collisions in the target material's surface. These multiple collisions results in the ejection of neutral target (or sputter) atoms through momentum transfer from the surface into the gas phase. These atoms are then directed towards the substrate to form a thin film of the synthsized material.

Since sputtering is the result of momentum and energy transfer, the incoming argon ions should have high enough energy to break the bonds holding the target atom in place. The typical surface binding energy is 5~10 eV. With high enough energy of argon ions, the collision cascade can be 5–10 nm below the target's surface. However, the particles ejected are usually within 1nm of the surface. Only a small fraction of collisions produce sputtering. The process of sputtering has been shown schematically in **Fig. 2.2**. To measure the efficiency of sputtering, the sputter yield, S, is defined as the number of sputtered atoms per incident particle. In a practical sputtering process, the yield is from 0.1 to 10 %. During the collision with the target surface, secondary electrons are emitted. They are accelerated away from the cathode. These electrons then travel back into the argon plasma and collide with the argon atoms, ionizing some of them and sustaining the plasma.

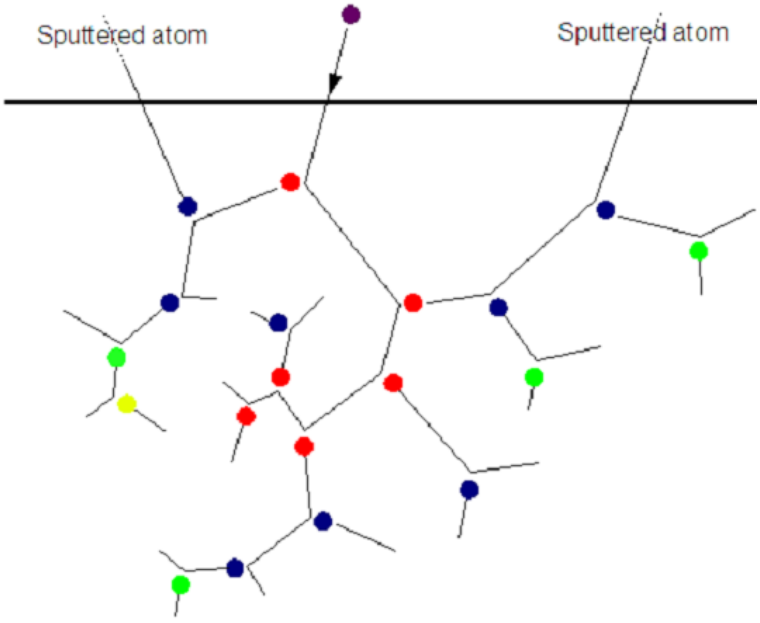

Fig. 2.2 Schematic of physical sputtering process. The thick line illustrates the position of the surface, and the thinner lines the ballistic movement paths of the atoms from beginning until they stop in the material. The purple circle is the incoming ion. Red, blue, green and yellow circles illustrate primary, secondary, tertiary and quaternary recoils, respectively. Two of the atoms happen to move out from the sample, i.e. be sputtered.

Sputtering yield depends on the chemical bonding of the target atoms and the energy transferred by collision. The sputtering yields of various materials bombarded by a variety of ion masses and energies have been determined experimentally (Laegried et al. 1961 **[199]**, Wehner et al. 1961 **[200]**) and have been calculated from first principles using Monte Carlo techniques (Yamamura et al. 1983) **[201]**. The sputtering yields for some metals and semiconductors at the indicated energy of sputtering gas have been given in **Table 2.1** (Ohring M. 1992) **[202]**. It may be mentioned that the sputtering yields are generally less than one at bombarding energies of several hundred electron volts, indicating the large amount of energy input is necessary to eject one atom.

Table 2.1 Sputtering Yields by 500eV ions **[202]**.

	Be (9)	**Al (27)**	**Si (28)**	**Cu (64)**	**Ag (106)**	**W (184)**	**Au (197)**
He^+ (4 amu)	0.24	0.16	0.13	0.24	0.2	0.01	0.07
Ne^+ (20 amu)	0.42	0.73	0.48	1.8	1.7	0.28	1.08
Ar^+ (40 amu)	0.51	1.05	0.50	2.35	2.4-3.1	0.57	2.4
Kr^+ (84 amu)	0.48	0.96	0.50	2.35	3.1	0.9	3.06
Xe^+ (131 amu)	0.35	0.82	0.42	2.05	3.3	1.0	3.01

Magnetic fields (magnetron) can also be applied to the plasma region in order to improve the sputtering performance. A magnetron uses a static magnetic field configured at the cathodelocation. The magnetic field is located parallel to the cathode (target) surface. Secondary electrons which are emitted from the cathode due to ion bombardment are constrained by this magnetic field to move in a direction perpendicular to both the electric field (normal to the surface) and the magnetic field. This is known as an E×B drift. This drift causes electrons to move parallel to the cathode surface in a direction 90 degrees away from the magnetic field. If the magnetic field is set up correctly, this E×B drift can be arranged to close on itself, forming a current loop of drifting secondary electrons (**Fig. 2.3**).

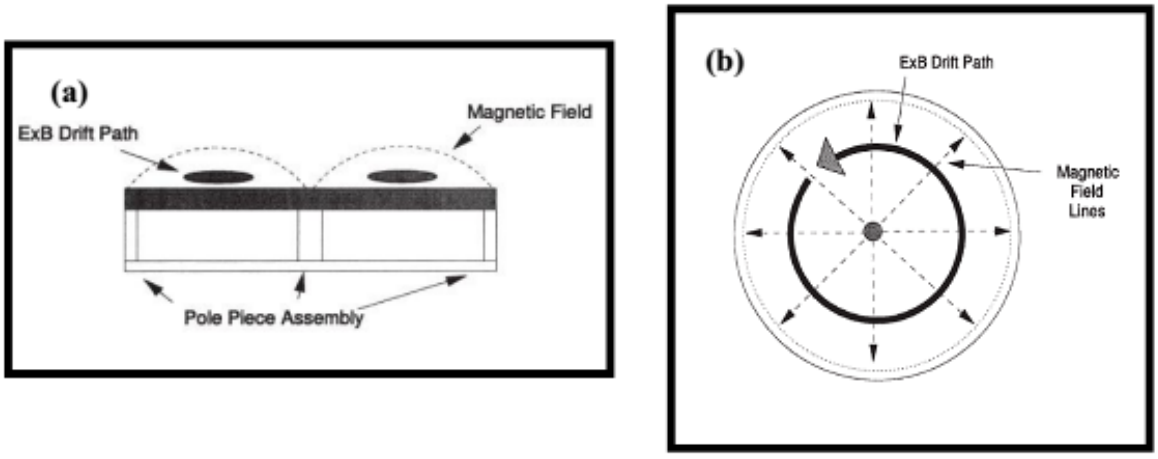

Fig. 2.3 (a) Side and **(b)** top view of magnetic field configuration for a circular planar magnetron cathode.

In this arrangement, secondary electrons are essentially trapped in a region close to the cathode. They lose their kinetic energy due to collisions with gas atoms (ionization) or with other electrons (electron heating). This is quite easily visible in a magnetron sputtering system. The location of this ring is also known as the etch track because the erosion of the cathode is highest here and deep groves can be eroded onto the cathode (target). Dense plasma near the target increases the deposition rate as it enhances the ionization of sputtering gas. However, this plasma does not affect the ejected atoms, as they have no charge and remain unaffected by the magnetic field. The magnetron requires cooling because of the heat generated by the energetic collisions around the target. So the sputtering target generally is actively cooled as the cold surface minimizes the amount of radiant heat in a sputtering system and is an advantage over thermal evaporation in vacuum where the radiant heat load can be appreciable. The low level of radiant heat is one factor that allows thermally-sensitive surfaces to be placed near the target. Cooling also prevents diffusion in the target which could lead to changes in the elemental composition in the surface region when alloy targets are used.

The simplest and least expensive way to operate the magnetron is using a DC power supply that was discussed earlier. Nowadays, a special power supply for sputter deposition is used, which include an arc suppression unit. Arcs often occur during reactive sputter deposition if oxygen/nitrogen as reactive gases is used that may build up oxide/nitirde on the edges of the erosion groove where the sputter rate is low. Arcs can be characterized as a low voltage and high current discharge. When the electric circuit ‘detects’ a strong decrease in the discharge voltage and/or a strong increase in the discharge current, it switches the power off for a small period (typically a few microseconds) to draw electrons, decrease charging, and prevent the arc from fully developing. Arcing can seriously damage a target by local melting, but it also degrades quality of the deposited film owing to the presence of particulates and/or pinholes while eventually destroying the power supply.

2.3.3 Reactive Magnetron Sputtering

Reactive sputtering is the sputtering of an elemental target in the presence of a gas that will react with the target material to form a compound. In one sense, all sputtering is reactive because there are always residual gases in the chamber that will react with the sputtered species. However in reality, reactive sputtering occurs when a gas is purposely added to the sputtering chamber to react with the sputtered material. Examples are when oxygen is injected

into the chamber with the sputtering of aluminum to form aluminum oxide or when nitrogen is added with the sputtering of titanium to form titanium nitride. Reactive sputtering was developed in the 1950s to deposit the doped Ti-N films for hybrid circuits (Sproul et al. 2005) **[203]**.

Reactive sputter deposition (Westwood et al. 1990) **[204]** relies on: (a) the reaction of the depositing species with a gaseous species, such as oxygen or nitrogen, (b) reaction with an adsorbed species, or (c) reaction with a co-depositing species such as carbon to form a compound. The reactive gas may be in the molecular state (e.g., N_2, O_2) or may be "activated" to form a more chemically reactive or more easily adsorbed species. Typically, the reactive gases have a low atomic masses (N=14, O=16) and are thus not effective in sputtering. It is therefore desirable to have a heavier inert gas such as argon to aid in sputtering. Mixing argon with the reactive gas also aids in activating the reactive gas by the excitation processes. The nature of the sputtering gas influences the rate of sputtering from the target. The use of inert and reactive gas mixtures probably results in a metallic mode of sputtering, while the use of only reactive gas for example (N_2) is likely to result in a nitride mode of sputtering with a significantly lower sputtering rate.

The basic issue faced during reactive puttering is that the reactive gas combines with target material to form a compound. Ideally this reaction takes place on the surface of the substrate, but in reality it occurs not only at the substrate but also on the fixturing and chamber walls and on the target. It is the reaction on the target surface that leads to the classic reactive sputtering problem known as "poisoning" of the sputtering target. The sputtering rate for the compound material that forms on the target is usually significantly less than the rate for the elemental target material thus reducing the deposition rate and sputtering efficiency. This problem is controlled by having a high sputtering rate (magnetron sputtering) and controlling the availability of the reactive gas by mass flow controller such that there will be enough reactive species to react with the copper cold finger surface to deposit the desired compound but not so much that it will unduly poison the target surface.

In some reactive deposition configurations, the inert gas is injected around the sputtering target and the reactive gas is injected near the substrate surface. This inert "gas blanket" over the target surface is helpful in reducing target poisoning in some cases. In reactive deposition, the depositing material must react rapidly or it will be buried by subsequent depositing material. Therefore, the reaction rate is an important consideration. The reaction rate is

determined by the reactivity of the reactive species, their availability, and the temperature of the surface. The reactive species can be activated by a number of processes including:

- Dissociation of molecular species to more chemically reactive radicals

  (e.g., $N_2 + e^- \rightarrow 2N^o$ and $NH_3 + e^- \rightarrow N^o + 3H^o$)

- Production of new molecular species that are more chemically reactive and/or more easily absorbed on surfaces

  (e.g., $O_2 + e^- \rightarrow 2O^o$ then $O^o + O_2 \rightarrow O_3$)

- Production of ions−recombination at surfaces releases energy
- Adding internal energy to atoms and molecules by creating metastable excited states-deexcitation at surfaces releases energy
- Increasing the temperature of the gas
- Generating short wavelength photons (UV) that can stimulate chemical reactions
- Generating energetic electrons that stimulate chemical reactions.
- Ions accelerated from the plasma to the surface promote chemical reactions on the surface (bombardment enhanced chemical reactions).

The use of reactive sputtering has proliferated, particularly over the past decade. It is used to produce oxide such as ZrO_2, CuO, WO_3 and MnO_2 in the nanorange which are used to in the kinetics of degradation of chemical warfare agent and removal of heavy metal ions from aqueous solution. Reactive sputtering is also used extensively by manufacturers of coated architectural glass, roll or web coatings, coated cutting tools, optical coatings, decorative and functional coatings for plumbing and hardware items, microelectronic devices (barrier layers, high k dielectrics, and resistive films), automotive windshields and mirrors, micro-electro-mechanical systems (MEMS) devices, surface acoustic wave devices and transparent conductive oxides.

2.3.4 Description of Sputter Deposition Technique

The actual magnetron sputtering system that was custom designed by Excel Instruments, India and installed in Nano Science laboratory is shown in **Fig. 2.4 (a)**. The pumps and gauges fitted in to the chamber are from Pfeiffer Vacuum. For DC sputtering, 'Aplab' high voltage DC power supply (50–1000 V, 0–1 A) was used. Also, The chamber consist of different ports to hold sputtering gun, gas connecting line, glass window etc. The copper cold finger was used as

a substrate which was put from the above side into the chamber and continuously filled up by liquid N_2 to cool it. The reason for keeping low temperature of the coper cold finger substrate is to inhibit the grain growth in the plane of the film leading to production of nanoparticles. Also, contamination due to the possible diffusion of atoms from the substrate with the deposited material is minimized at lower temperature. Firstly, a base pressure of 4×10^{-6} Torr or more could be achieved by pumping the chamber. After evacuation, one of the inert gas such as argon/helium (99.999% purity) along with reactive gases oxygen (99.999%) required for preparation of metal oxides nanostructures materials are supplied into the chamber via gas inlet valve. Simultaneously, the gate valve is brought into almost closed state (throttling) so as to match the gas influx and pumping-out rate. With proper throttling, the inert gas pressure and flow rate inside the chamber can be made very stable. The sputtering pressure measurement inside the chamber was done by Baratron capacitance manometers (MKS Instruments USA). The copper cold finger substrate, sputtering gun and unused and eroded targets used for mounting the target are also shown in **Fig. 2.4**.

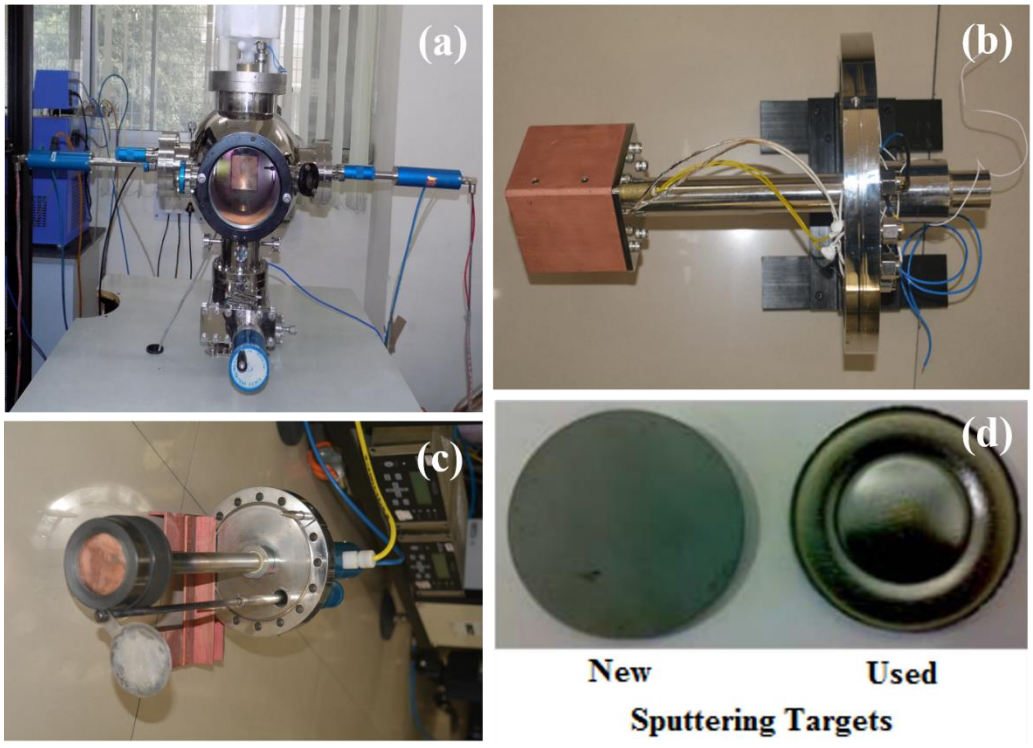

Fig. 2.4 (a) Custom designed DC/RF magnetron sputtering unit set-up in Nano Science Lab for producing nanoparticles, **(b)** copper cold finger, **(c)** Sputtering Gun, **(d)** New & used sputtering target.

2.4 Characterization techniques

After the prepration of metal oxides nanostructures, the structure and properties of the synthesized compounds during the course of the present investigation have been characterized by various techniques. The description and the principle of operation of these techniques are discussed briefly in this chapter.

2.4.1 X−ray diffraction (XRD)

X–ray diffraction (Cullity et al. 2001) **[205]** is the most powerful tool for determining the structure of solid matter and it finds wide range of applications in material characterization, especially for

- identification of unknown substances,
- trace analysis,
- determination of crystal structure,
- phase analysis,
- detection of crystal imperfection,
- layer thickness determination,
- determination of preferred orientation and crystallite size

X−ray diffraction is a non-destructive technique. The basic principle of the XRD is Bragg's law which describes the condition for constructive interference for X–rays scattered from atomic planes of a crystal. The angle between the diffracted beam and the incident beam is always 2θ, and it is this angle, rather than θ, which is usually measured experimentally

$$2dsin\theta = n\lambda \qquad (2.1)$$

where n is integer (1, 2, 3, ….,) that indicates the order of the reflection, θ is the angle between the incident ray and scattering plane called as Bragg angle, λ is the wavelength of the X–ray beam and d is the interplanar distance between the lattice planes (**Fig. 2.5**).

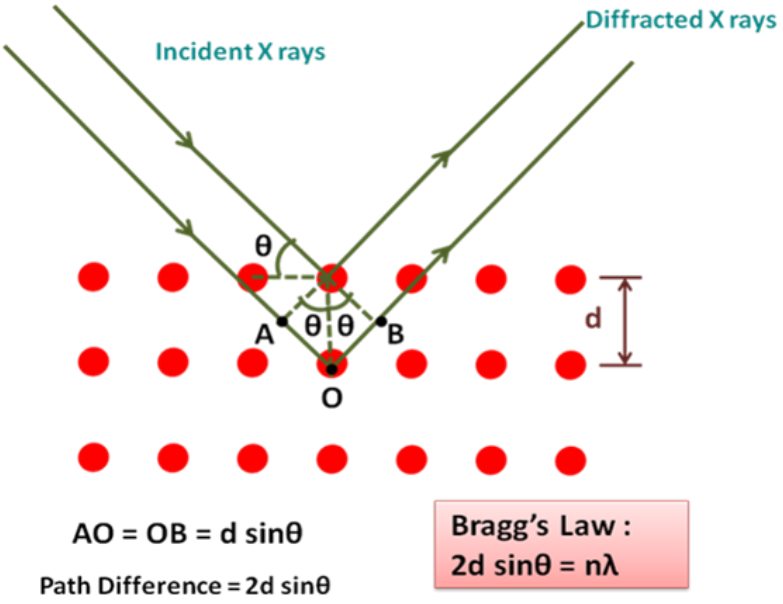

Fig. 2.5 Diffraction of X–rays from parallel planes in a solid.

The interplanar distance between the lattice planes which is given by **eq. 2.2**

$$d = \left[\frac{h^2}{a^2} + \frac{k^2}{b^2} + \frac{l^2}{c^2} \right]^{-1/2} \qquad (2.2)$$

The crystallographic information is obtained by evaluating 'd' values and indexing of reflections. The characteristics diffraction pattern of a given substance can always be obtained whether the substance is present in pure state or as one constituent in a mixture of several substances. This fact is the basis of the diffraction method of chemical analysis. X–ray diffraction pattern is characterized by a set of line positions (2θ) and a set of relative intensities (I). The angular position of lines depends on the wavelength of the incident ray and spacing (*d*) of the lattice planes.

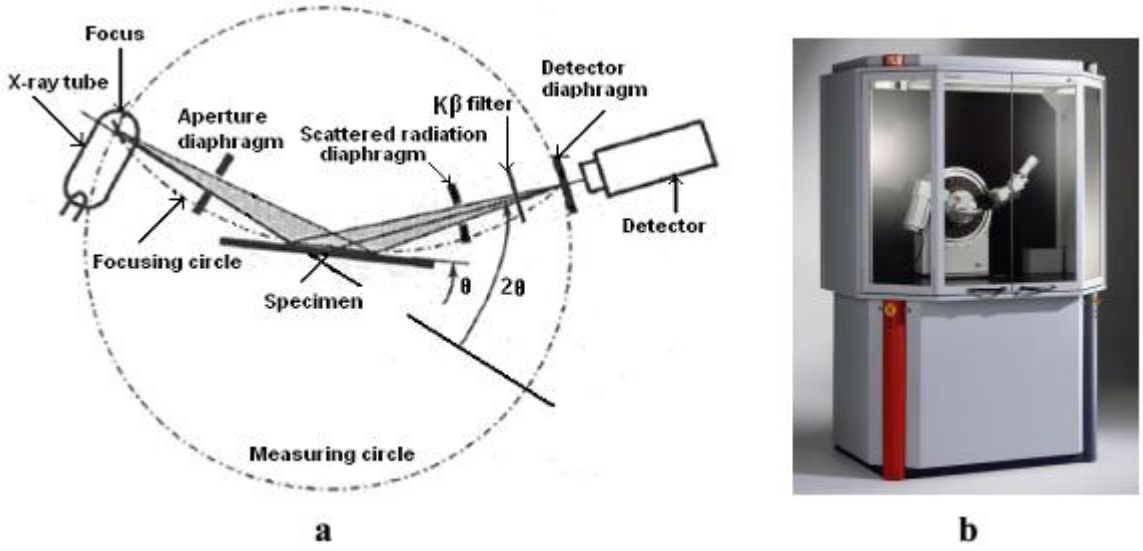

Fig. 2.6 (a) Schematic diagram of beam path, **(b)** Photograph of Bruker D8 advance X–ray diffractometer.

The schematic diagram of X–ray diffractometer and its experimental set up (Bruker D8 Advance) are shown in in **Fig. 2.6 (a) Fig. 2.6 (b)**. The Cu Kα (λ =1.54 Å) radiation at applied voltage of 40 kV and filament current of 30 mA in Bragg-Brentano (θ–2θ) scan mode was employed. Whenever the Bragg condition ($2d \sin\theta = n\lambda$) is satisfied, the incident X–ρay beam is diffracted at the specimen and reaches the detector. The detector converts the X–ray quanta into electron pulses, which are recorded by recorder. Bruker D8 Advance diffractometer uses NaI scintillation counter as a detector which can detect the diffracted radiations in the wavelength ranging from 0.5 to 3 Å. Monochromators are used to suppress the undesired portions of radiation. To restrict the irradiated specimen area, aperture diaphragm is arranged between the tube and the specimen. The second aperture diaphragm shields the strong scattered radiation of the first aperture diaphragm. The resolution depends upon the detector diaphragm. The scattered radiation diaphragm is used to suppress undesired scattered radiation. The phase identification for all samples reported here was performed by matching the peak positions and intensities in the experimental diffraction patterns to those in the JCPDS (Joint Committee on Powder Diffraction Standards) database.

One of the frequent applications of XRD analysis is to determine the average crystallite size and lattice strain in nanocrystalline materials. The peak broadening in XRD patterns for nanomaterials is the result of the finite size effect. For a finite size nanocrystal, the number of

X–ray radiation reflected from successive lattice planes that add up to produce constructive or destructive interference becomes finite and therefore they cannot reinforce or cancel out completely. So, for nanocrystalline materials, the average crystallite size which is an important parameter can be determined from the width of the Bragg reflection and is given by the Scherrer formula

$$D_{avg} = \frac{0.9\lambda}{\beta\cos\theta} \qquad (2.3)$$

where is the average crystallite dimension perpendicular to the reflecting planes, λ is the X–ray wavelength, β is the finite size broadening i.e. full width at half maximum (FWHM) of the Bragg reflection in the radians on the 2θ scale and is the Bragg reflection angle. The average crystallite size for all deposited thin films was calculated by using the **Eq. (2.3)**.

2.4.2 Raman spectroscopy

Raman spectroscopy **[206]** is a non–destructive technique, used to determine the local site symmetry of the polyhedra in the structures. It is one of the most elegant analytical tool which gives the structural information required for both basic and applied research. A very small amount of sample is required for recording the spectrum. For qualitative analysis, Raman lines in Raman spectrum are narrow and well resolved, representing the fingerprints of a chemical compound, so identification of an unknown compound is fast and accurate. For structural studies, high resolution Raman spectrum with the possibility of polarization helps to investigate the vibrational states of solids, liquids and gaseous systems either alone or complementary to IR technique. For industrial purpose, Raman spectroscopy has made an important breakthrough since there is no sampling; and the technique is simple, robust, fast, precise and user-friendly.

Raman effect occurs when light impinges upon a molecule and interacts with the electron cloud of the molecule. The interaction between ultraviolet, visible or near-infrared photons with matter gives rise to a Raman spectrum characterizing its different vibrational transitions. These vibrational transitions may be IR active or Raman active or both depending on the selection rules. When the molecule emits a photon and returns to the ground state, it returns to a different rotational or vibrational state. The difference in energy between the original state and this new state leads to a shift in the emitted photon's frequency away from the excitation wavelength (**Fig. 2.7**). If the final state of the sample is more energetic than the initial state,

then the emitted photon will be shifted to a lower frequency in order for the total energy of the system to remain balanced. This shift in frequency is designated as a Stokes shift. If the final state is less energetic than the initial state, then the emitted photon will be shifted to a higher frequency, and this is designated as an Anti-Stokes shift **[206]**.

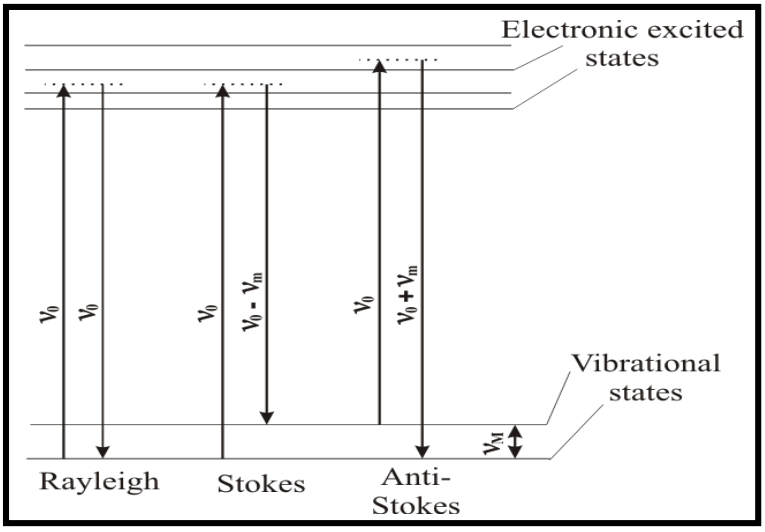

Fig. 2.7 Energy level diagram showing the states involved in Raman signal.

In the present study, the Raman spectra were recorded using a Renishaw inVia Raman microscope equipped with a CCD system consisting of an Ar^+ laser (λ = 514.5 nm, 785 nm) (**Fig. 2.8**).

Fig. 2.8 Digital photograph of the Renishaw inVia Raman spectrophotometer.

It is based on an incoherent inelastic scattering process of light by matter in the solid state. In the Raman spectrophotometer, the laser beam from the Argon–ion laser is filtered for monochromaticity and directed by a system of mirrors to a focussing/collecting lens (**Fig. 2.9**). Physically, it is separated into two stages. The first stage is called a monochromator, but is really used as a filter. Its structure consists of basically two diffraction gratings, separated by a slit, with input and output focussing mirrors. The incoming signal from the collecting lenses is focussed on the first grating, which separates the different wavelengths. This spread–out light is then passed through a slit. Because light of different wavelengths is now travelling in different directions, the slit width can be tuned to reject wavelengths outside of a user–defined range. This rejection is often used to eliminate the light at the laser frequency. The light which makes it through the slit is then refocussed on the second grating, whose purpose is only to compensate for any wavelength–dependence in the dispersion of the first grating. This grating is oriented such that its dispersion pattern is the mirror image of that from the first grating. Finally the light is refocussed and sent out to the second stage. The second stage focuses the filtered light on the final grating. The dispersed light is now analyzed as a function of position, which corresponds to wavelength. The signal as a function of position is read by the system detector. The detector is a multichannel charge–coupled device array (CCD) in which the different positions are read simultaneously. The wavelength/intensity information is then read by a computer and converted in software to frequency/intensity.

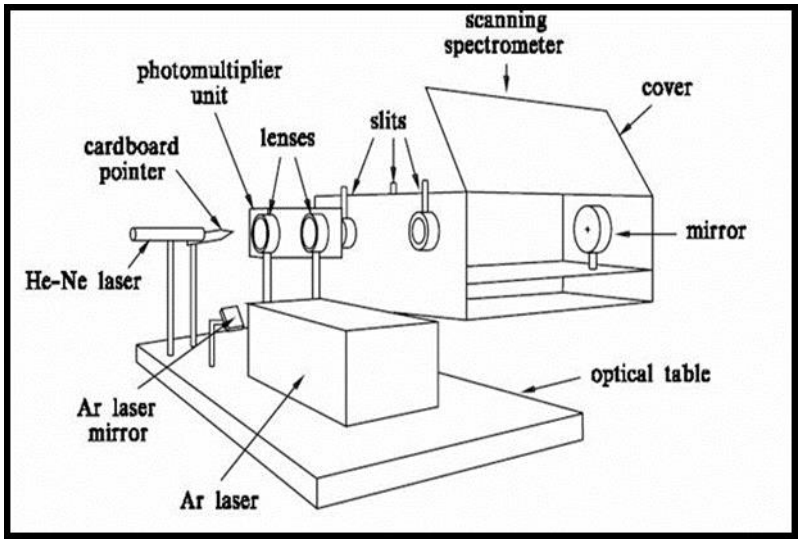

Fig. 2.9 Schematic diagram of Raman spectrometer.

2.4.3 Fourier transform-infra red (FT–IR) spectroscopy

FT-IR spectroscopy has become an efficient technique in the hands of materials scientists for the determination of the internal structure and the nature of chemical bonds in the crystals **[207]**. It is a non-destructive analysis and minimum amount of the sample is required for the structure analysis. It also has great importance in resolving the order-disorder of various ions or groups present in the samples. The compounds synthesized were characterized by FT–IR spectra in the region 400–4000 cm^{-1} using Perkin Elmer FT–IR Spectrometer model Spectrum 2000 (**Fig. 2.10**) and Thermo Scientific FT–IR spectrophotometer, in which KBr was used as the dispersal medium. A typical FT–IR instrument is based on the principle of Michelson Interferometer. It consists of three active components: a moving mirror, a fixed mirror, and a beam splitter. The two mirrors are perpendicular to each other. The beam splitter is a semi reflecting device and is often made by depositing a thin film of germanium onto a flat KBr substrate. Radiation from the broadband IR source is collimated and directed into the interferometer, and impinges on the beam splitter. At the beam splitter, half the IR beam is transmitted to the fixed mirror and the remaining half is reflected to the moving mirror. A schematic representation of FT–IR Instrument with Michelson Interferometer is shown in **Fig. 2.11**.

Fig 2.10 Digital photograph of Perkin Elmer FT–IR Spectrometer.

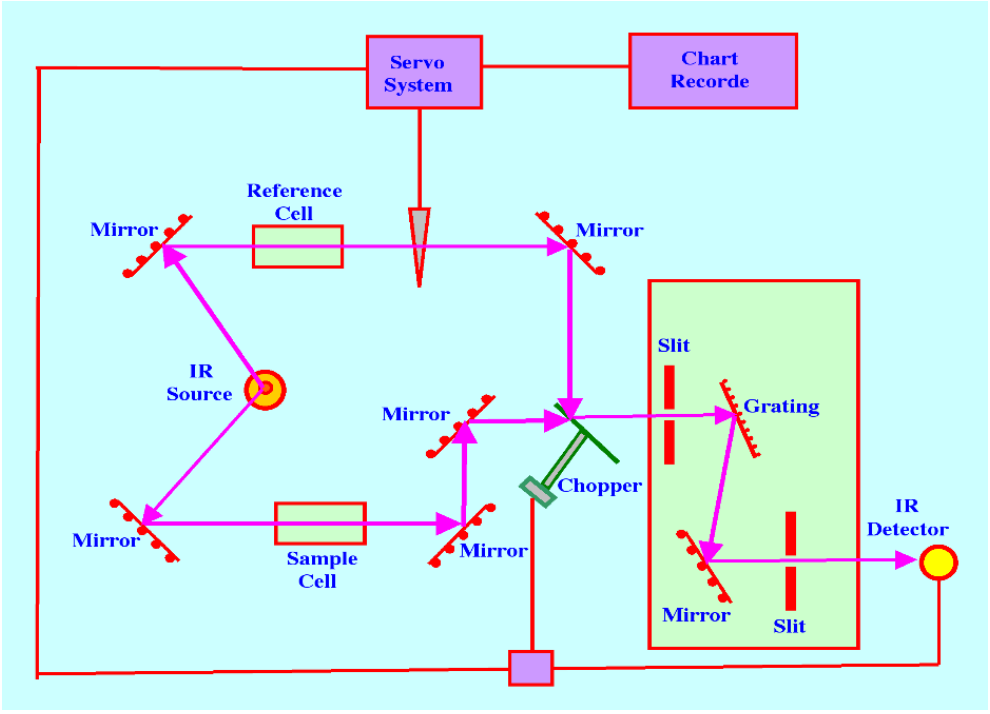

Fig. 2.11 Schematic representation of FT–IR Instrument with Michelson Interferometer **[207].**

2.4.4 Field emission scanning electron microscopy (FE–SEM)

The scanning electron microscope (SEM) is one of the most versatile instruments available for the examination and analysis of the microstructure morphology and chemical composition characterizations, Fleger et al. (1993) **[208].** To understand the working principle of FE–SEM, first we need to know the kind of interaction an energetic electron beam has with samples and the phenomena which take place after this interaction.

When an incident electron beam strikes the specimen composed of a crystalline and/or amorphous structure, it undergoes a series of complex interactions with the nuclei and electrons of the atoms of the sample. These interactions can be divided into two major categories: elastic interactions and inelastic interactions.

Elastic interactions: Elastic scattering results from the deflection of the incident electron by the specimen atomic nucleus or by outer shell electrons of similar energy. This kind of interaction is characterized by negligible energy loss during the collision. Incident electrons that are elastically scattered through an angle of more than 90° are called backscattered electrons (BSE), and yield a useful signal for imaging the sample.

Inelastic interactions: Inelastic scattering occurs through a variety of interactions between the incident electrons and atoms of the sample, and results in the primary beam electron

transferring substantial energy to that atom. The amount of energy loss depends on whether the specimen electrons are excited singly or collectively and on the binding energy of the electron to the atom. As a result, the excitation of the specimen electrons during the ionization of specimen atoms leads to the generation of secondary electrons (SE), which are conventionally defined as possessing energies of less than 50 eV and can be used to image or analyze the sample. In addition to those signals that are utilized to form an image, a number of other signals are produced when an electron beam strikes a sample, including the emission of characteristic X–rays, Auger electrons, and cathodoluminescence. **Fig. 2.12** schematically shows the interaction of electron beam with the specimen and shows the regions from which different signals are detected. **Fig. 2.13** shows the tear drop model for electron beam interaction with solids and explains the interaction volume in the specimen and shows different kind of signals coming from the sample from various depths.

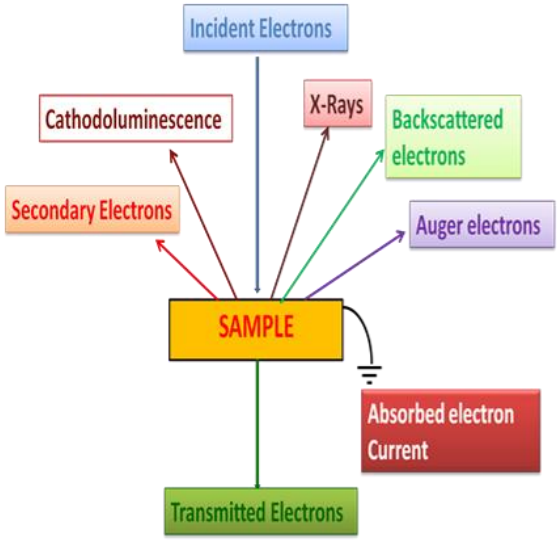

Fig. 2.12 Schematic view of electron beam interaction with specimen.

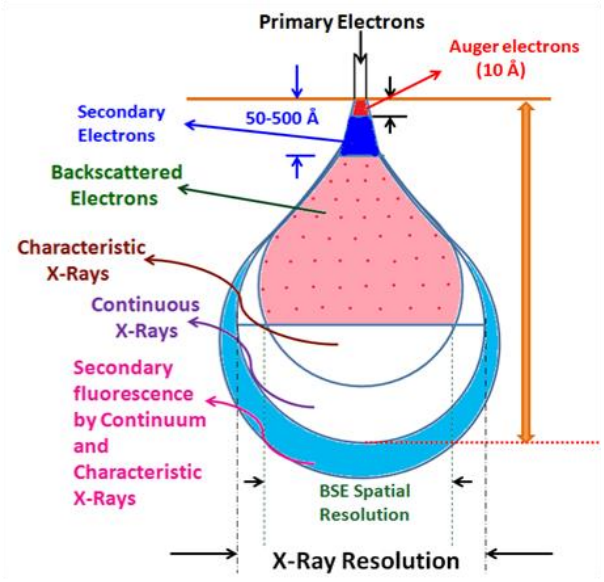

Fig. 2.13 Tear drop model for electron beam interaction with solids.

Secondary electrons: When the primary beam strikes the sample surface causing the ionization of specimen atoms, loosely bound electrons may be emitted and these are referred to as secondary electrons. As they have low energy, typically an average of around 3–5 eV, they can only escape from a region within a few nanometers of the material surface. So, secondary

electrons accurately mark the position of the beam and give topographic information with good resolution.

Backscattered electrons: A backscattered electron (BSE) is defined as one which undergoes a single or multiple scattering events and which escapes from the surface with energy greater than 50 eV. The elastic collision between an electron and the atomic nucleus of specimen causes the electron to bounce back with wide–angle directional change. Approximately 10–50% of the beam electrons are backscattered toward their source with on an average 60–80% of their initial energy retained. Elements with higher atomic numbers have more positive charges on the nucleus, and as a result, more electrons are backscattered, causing the resulting backscattered signal to be higher. Thus, the backscattered yield, defined as the percentage of incident electrons that are reemitted by the sample, is dependent upon the atomic number of the sample. Since BSEs have a large energy (that prevents them from being absorbed by the sample) the region of the specimen from which BSEs are produced is considerably larger than it is for secondary electrons.

Characteristic X–rays: Another class of signals produced by the interaction of the primary electron beam with the specimen is characteristic X–rays. When an inner shell electron is displaced by collision with a primary electron, an outer shell electron may fall into the inner shell to reestablish the proper charge balance in its orbital following an ionization event. Thus, by the emission of an X–ray photon, the ionized atom returns to ground state. The X–ray obtained is known as characteristic X–ray. The analysis of these characteristic X–rays is very helpful in providing chemical composition the material used as specimen.

Auger Electrons: Auger electrons are produced following the ionization of an atom by the incident electron beam and the falling back of an outer shell electron to fill an inner shell vacancy. The excess energy released by this process may be carried away by an Auger electron. This electron has a characteristic energy and can therefore be used to provide chemical information. Because of their low energies, Auger electrons are emitted only from near the surface. They have escape depths of only a few nanometers and are principally used in surface analysis.

Having understood the electron beam interaction with solids, it is easy to understand the working of FE–SEM. Scanning electron microscope has a large depth of field, which allows a large amount of the sample to be in focus at one time. The SEM also produces images of high

resolution, which means that closely spaced features can be examined at a high magnification. FE−SEM uses field emission electron gun which provides improved spatial resolution down to 1.5 nm that is 3 to 6 times better than conventional SEM and minimized sample charging and damage. The basic mechanism of field emission is that a high voltage applied between a pointed cathode and a plate anode caused a current to flow. The tip of diameter 100 to 1000 Å is used, which is generally made of a single crystal tungsten wire sharpened by electrolytic etching. The field emission process itself depends on the work function of the metal, which can be affected by adsorbed gases. This is the reason a very high vacuum is required. A schematic diagram of the optical column of the FE–SEM is shown in **Fig. 2.14 (a)**. The electron beam is energized by the accelerating potential of few hundred eV to 20 keV and the divergent beam is focused by two condenser lenses into a beam with a very fine focal spot size. The first condenser lens that works in conjunction with the condenser aperture helps to narrow the beam and also limit its current. The second condenser lens then makes the electron beam more thin and coherent. The objective lens does the final focusing of the beam onto the sample. During scanning, electron beam is thus made to deflect over the specimen in the raster form. At each point the secondary and back–scattered electrons reaching the detector are counted to be used for determining the relative intensity of the pixel representing that point in the final image. The higher the atomic number of the specimen material, the greater is the number of secondary electrons that reach the detector, giving rise to a higher intensity in the image. Limitation associated with the SEM is that the specimen that has to be analyzed should be conducting. In case of non-metals, it is required to make them conducting by covering the sample with a thin layer of conductive material like gold or platinum in order to enhance the signals.

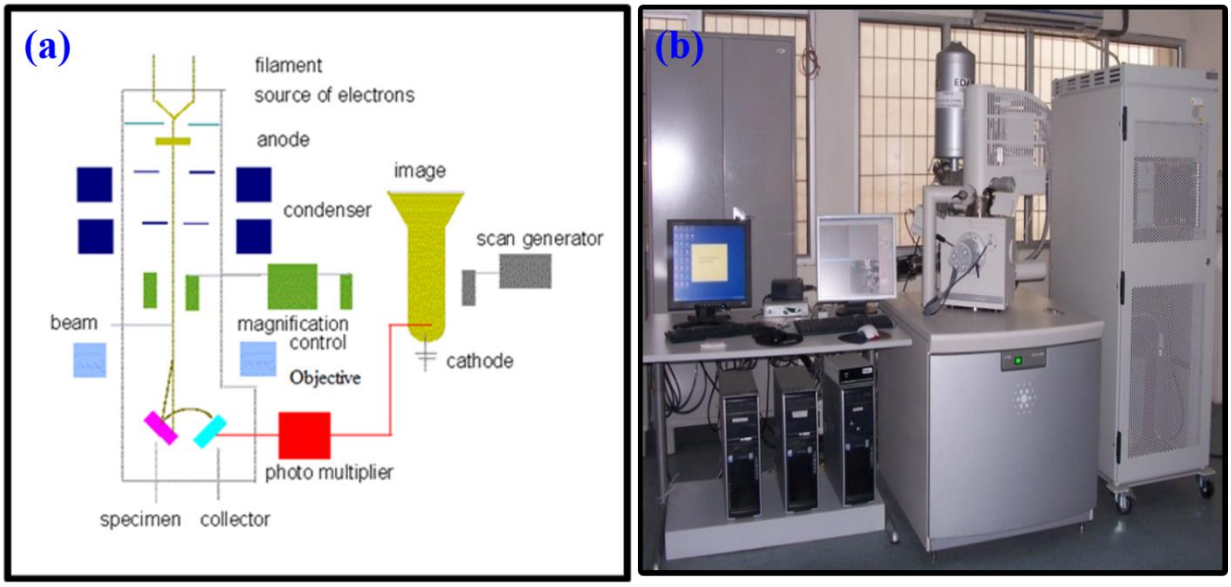

Fig. 2.14 (a) A Schematic diagram of the Scanning electron microscope **(b)** Photograph of FE–SEM available at IIT Roorkee.

In the present study, field emission scanning electron microscope (Zeiss Ultra Plus55) with resolution of 2 nm and upto 4,00,000X magnification were used to study the surface morphology of the synthesized nanostructures (**Fig. 2.14 (b)**). Elemental composition analysis can also be performed by using the energy dispersive X–ray analysis (EDAX) attached with the FE–SEM system. An EDAX spectrum normally displays peaks corresponding to the energy levels for which the most X–rays had been received. Each of these peaks is unique to an atom, and therefore corresponds to a single element. The higher a peak in a spectrum, the more concentrated the element is in the specimen. The working principle of EDAX is explained below.

2.4.5 Energy Dispersive X–ray Spectrometry (EDS)

EDS makes use of the X–ray spectrum emitted by a solid sample bombarded with a focused beam of electrons to obtain a localized chemical analysis. All elements from atomic number (Z) 4 (Be) to 92 (U) can be detected in principle, though not all instruments are equipped for 'light' elements (Z < 10). An EDS system comprises three basic components that must be designed to work together to achieve optimum results: the X–ray detector or spectrometer, the pulse processor, and the analyzer. The EDS converts the energy of each individual X–ray into a voltage signal of proportional size. This is achieved through a three stage process. Firstly the

X–ray is converted into a charge by the ionization of atoms in a semiconductor crystal. Secondly this charge is converted into the voltage signal by the FET (Field Effect Transistor) preamplifier. Finally the voltage signal is input into the pulse processor for measurement. The output from the preamplifier is a voltage 'ramp' where each X–ray appears as a voltage step on the ramp. EDS detectors are designed to convert the X–ray energy into the voltage signal as accurately as possible. At the same time electronic noise must be minimized to allow detection of the lowest X–ray energies. An EDS detector has several components like Collimator assembly, 'Be' window, a semiconductor crystal, Field-effect transistor, Cryostat etc. The functioning of each component is described below.

Collimator assembly: The collimator provides a limiting aperture through which X–rays must pass to reach the detector. This ensures that only X–rays from the area being excited by the electron beam are detected and stray X–rays from other parts of the microscope chamber are not included in the analysis.

Beryllium (Be) window: The window provides a barrier to maintain vacuum within the detector whilst being as transparent as possible to low energy X–rays. 'Be' is highly robust, but strongly absorbs low energy X–rays meaning that only elements from sodium (Na) can be detected accurately. Polymer-based thin windows can be also be used as they can be made much thinner than 'Be' windows and therefore are transparent to much lower energy X–rays, allowing detection of X–rays down to 100 eV. Although these window materials are far less robust in comparison to 'Be' windows.

Semiconductor Crystal: The crystal is a semiconductor device that, through the process of ionization converts an X–ray of particular energy into electric charge of proportional size. To achieve this, a charge-free region within the device is created. Two main materials are used for the detecting crystal. The most common is silicon (Si), into which is drifted lithium (Li) to compensate for small levels of impurity. High purity germanium crystals (HPGe) are also used. HPGe offers performance advantages when measuring higher energy X–rays. Si (Li) was the first material used in EDS detectors and remains the most common choice today. When an incident X–ray strikes the detector crystal, its energy is absorbed by a series of ionizations within the semiconductor to create a number of electron-hole pairs. The electrons are raised into the conduction band of the semiconductor and are free to move within the crystal lattice. When an electron is raised into the conduction band, it leaves behind a 'hole', which behaves

like a free positive charge within the crystal (**Fig. 2.15 (a)**). A high bias voltage, applied between electrical contacts on the front face and back of the crystal, then sweeps the electrons and holes to these opposite electrodes, producing a charge signal, the size of which is directly proportional to the energy of the incident X–ray. EDS detectors are available with different sizes of crystals. The crystal size is often measured in area: 5 mm^2, 10 mm^2, 30 mm^2, 50 mm^2 etc. Normally the larger the crystal, the worse will be its resolution, particularly at low energy.

Field–effect transistor: The field–effect transistor (FET) (**Fig. 2.15 (b)**) is positioned just behind the detecting crystal. It is the first stage of the amplification process that measures the charge liberated in the crystal by an incident X–ray and converts it to a voltage output. The charge is converted to a voltage signal by the FET preamplifier (**Fig. 2.15 (b)**).

Cryostat: The charge signals generated by the detector are small and can only be separated from the electronic noise of the detector if the noise is reduced by cooling the crystal and FET. Most EDS detectors work at close to liquid nitrogen temperatures, and are cooled using a reservoir of liquid nitrogen held in a Dewar. The vacuum is maintained at a low enough level to prevent the condensation of molecules on the crystal.

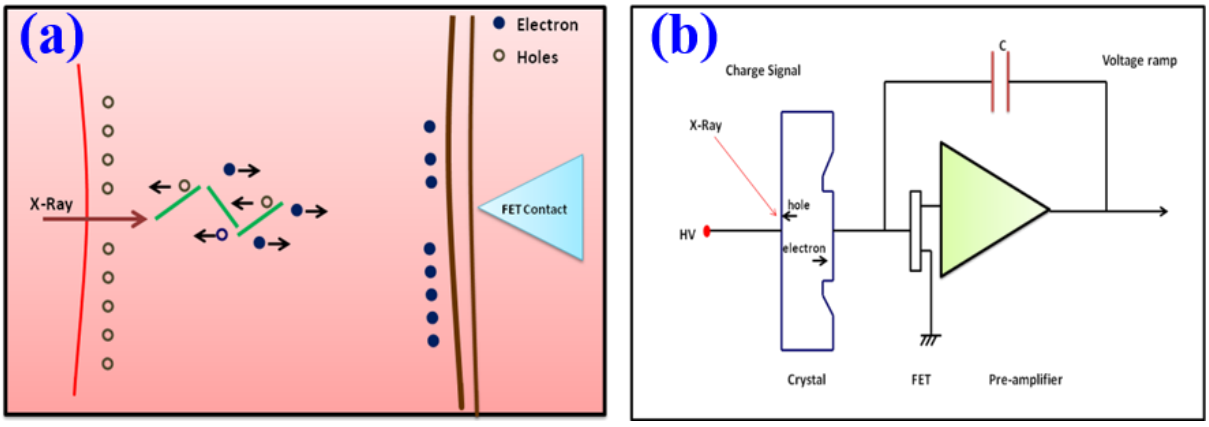

Fig. 2.15 Conversion of X–ray signals into a voltage 'ramp' by the EDS detector **(a)** Generation and measurement of electron-hole pairs in the crystal. **(b)** Circuit diagram of the EDS detector.

In the present study EDS attached to FE–SEM (Zeiss Ultra Plus55) procured from FEI Company Netherland was used to study the chemical composition of synthesized nanostructures materials.

2.4.6 Transmission electron microscopy (TEM)

TEM is an imaging technique, (Williams et al. **[209]**), whereby, a beam of electrons is focused onto a specimen causing an enlarged version to appear on a fluorescent screen or to be detected by a CCD camera. It produces a transmitted electron image of a thin specimen magnified from 100 to1000000 times with a high resolution of 0.2 Å.

The schematic diagram and photograph of High Resolution TEM (FEI Tecnai–20 G^2) are shown in **Fig. 2.16 (a) and (b)**. At the top of the TEM column was the filament assembly, which was connected to the high voltage supply. TEM may use accelerating voltage of 200 kV with wavelength of 0.025 Å. The accelerating voltage increased the theoretical resolution. Below the filament tip and above the anode was a beam volume called cross over. In this area of the filament chamber, the electron beam was condensed to its highest density. In a TEM, the diameter of the electron beam at cross over was approximately 50 μm. The electron beam traveled to condenser lens system. Modern TEM have two condenser lenses. The condenser-lens system was used to control electro illumination on the specimen and on the viewing screen. The first condenser lens could condense the 50 μm electron beam to as small as 1 μm. The second condenser lens was weaker, variable lenses that control the size of the beam from 1 μm to 10 μm and was used to change the beam brightness for image viewing. The condenser lenses were fitted with apertures, which are usually small platinum disks with holes of various sizes. Condenser-lens apertures protect specimen from too many stray electrons, which could contribute to excessive heat and limit X–ray production farther down the column. The most important function of a condenser lens and its aperture is to define the angular aperture of illumination. The maximum angular aperture occurred when the beam was at crossover. In this condition the beam was round and was at maximum intensity. The objective lens is the most important and complex lens in the TEM. Because it is the first magnifying lens, any imperfections in the objective lens will be magnifying further by the other lenses. The specimen was inserted into the objective lens, which must be designed so that the specimen could be moved in both x, y and z directions with tilting and rotating capabilities. The objective apertures in TEM are also referred to as contrast apertures. They absorb most of the elastically scattered electrons and few of the in-elastically scattered electrons from the image. Final image magnification in a TEM is the product of the magnifications of each magnifying lens: the objective lens, the diffraction lens, the intermediate lens and the projector lens. The objective lens, the first magnifying lens in the TEM, is a high power lens. The diffraction lens, below the

objective lens, is a very low power lens. The intermediate lens was a weak lens but with variable power. It is the current in this lens that was adjusted to control the final magnification of the image. The last lens is the projector lens, which was a high power lens that projects the final magnified image on to the viewing screen.

Most often TEM is operated in one of the following modes:

1. Image Mode: Imaging mode allows the imaging of the crystallographic structure of a specimen at an atomic scale. Because of its high resolution, it is an invaluable tool to study nanoscale properties of crystalline material. In image mode, image contrast comes from the scattering of the incident electron beam by the specimen. By using electrons accelerated to high voltages, atomic planes of the crystal can be resolved. In this mode, intermediate aperture is removed and only objective aperture is used. Intermediate lens is used to focus on the image plane of the objective lens. In image mode, two imaging systems are used:

(a) Bright field image mode: When an incident electron beam strikes a sample, some of the electrons pass directly through, while others may undergo slight inelastic scattering from the transmitted beam. Contrast in an image appears by differences in scattering. By inserting an aperture in the back focal plane, an image can be produced with these transmitted electrons. The resulting image is known as a bright field image. Bright field images are commonly used to examine micro-structural related features.

(b) Dark field image mode: If a sample is crystalline, many of the electrons will undergo elastic scattering from the various planes. This scattering produces many diffracted beams. If any one of these diffracted beams is allowed to pass through the objective aperture, an image can be obtained. This image is known as a dark field image. Dark field images are particularly useful in examining microstructural detail in a single crystalline phase.

2. Diffraction mode: The diffraction pattern that is always present in the back focal plane of the objective is brought into focus by the objective lens. Individual spots are seen when the specimen is a single crystal, while for polycrystalline material concentric rings are observed. In diffraction mode, objective aperture is removed and only intermediate aperture is used which passes the diffraction pattern of a selected region. For a single crystal, the diffraction spots from planes which are equivalent by symmetry are placed symmetrically around the central spot. Interplanar distance, *d* can be calculated from the expression:

$$R.d = L.\lambda \qquad (2.5)$$

where, λ is the wavelength of the electron beam (0.025 Å for 200 kV), *R* is the distance of a particular spot form the central bright spot and *L* is the distance between the specimen and the diffraction plane, known as the lens constant or camera length.

3. High resolution mode: High resolution mode is an imaging mode of the TEM that allows the imaging of the crystallographic structure of a specimen at an atomic scale. Because of its high resolution, it is an invaluable tool to study nanoscale properties of crystalline material such as semiconductors and metals. TEM image contrast comes from the scattering of the incident electron beam by the specimen. Phase contrast is very sensitive to many factors such as small change in thickness, orientation and variations in the focus of the objective lens. This sensitivity is also the reason that phase contrast can be used to image the atomic structure of thin specimens. By using electrons accelerated to high voltages, atomic planes of the crystal can be resolved, **[209].**

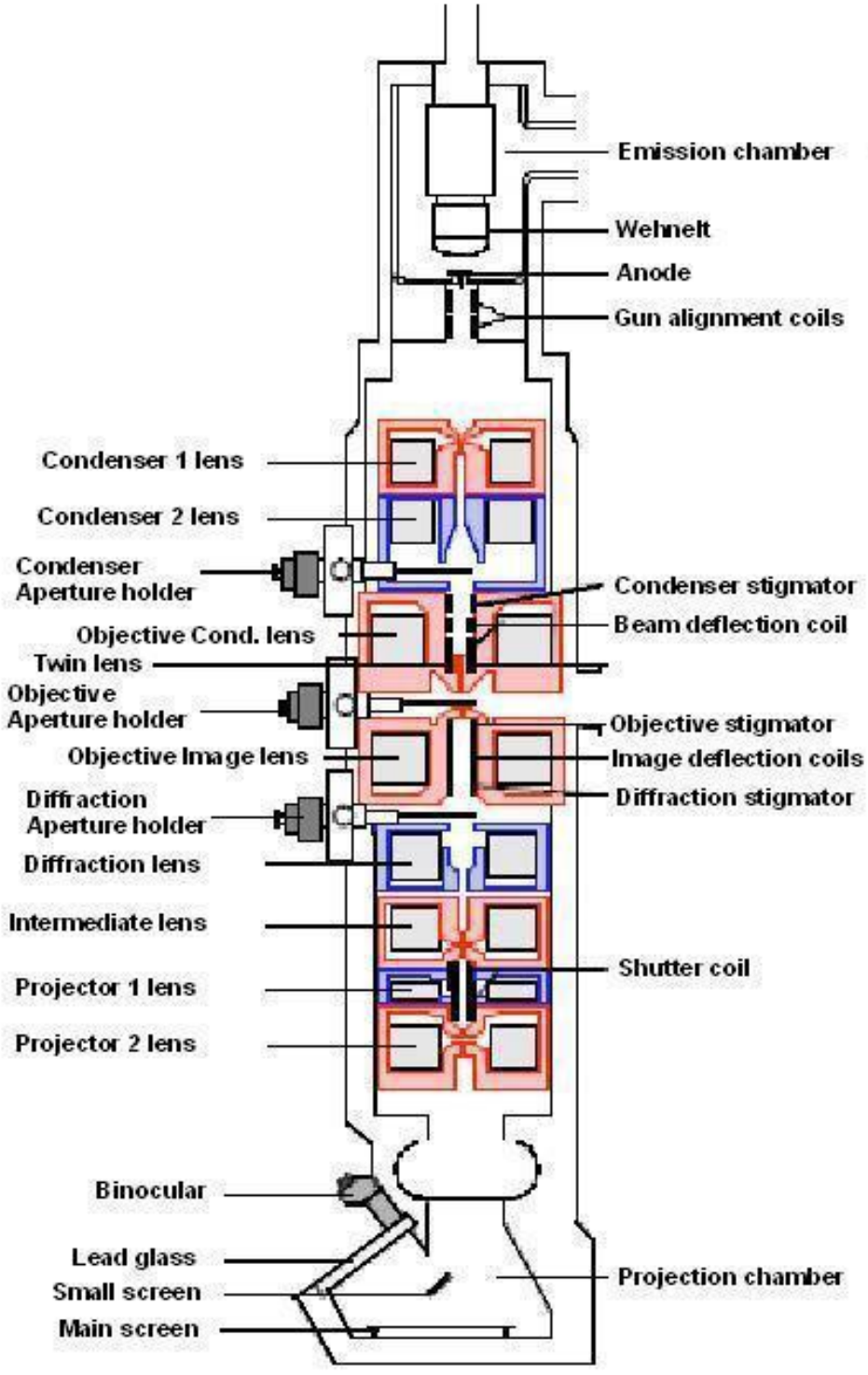

Fig. 2.16 (a) Schematic diagram of HR–TEM.

Fig. 2.16 (b) Photograph of HR–TEM (FEI Tecnai–20 G^2).

2.4.7 Thermogravimetric analysis (TGA)

Thermal analysis techniques have been employed to study the thermal behaviour of the compounds **[210]**. It was performed using EXSTAR 6300 TG/DTA (**Fig. 2.17**) from ambient temperature at a heating rate of 10°C/min with the sample mass ~25 mg using alumina pan. It is a technique wherein the change in the sample mass (mass loss/gain) is determined as a function of temperature or time, while the sample is subjected to a controlled temperature program, in an

atmosphere of nitrogen, argon, oxygen. Usually sample masses were recorded by having them in suitable environment by varying the temperature at a linear rate. The equipment consists of a precision balance, a furnace with a programming facility, a reaction chamber and a suitable recording system (**Fig. 2.18**). The sensitivity of the technique depends on the balance employed. The chromel-constantan thermocouple is usually placed in close proximity of the sample.

Fig. 2.17 Digital photograph of Perkin Elmer TG/DTA system.

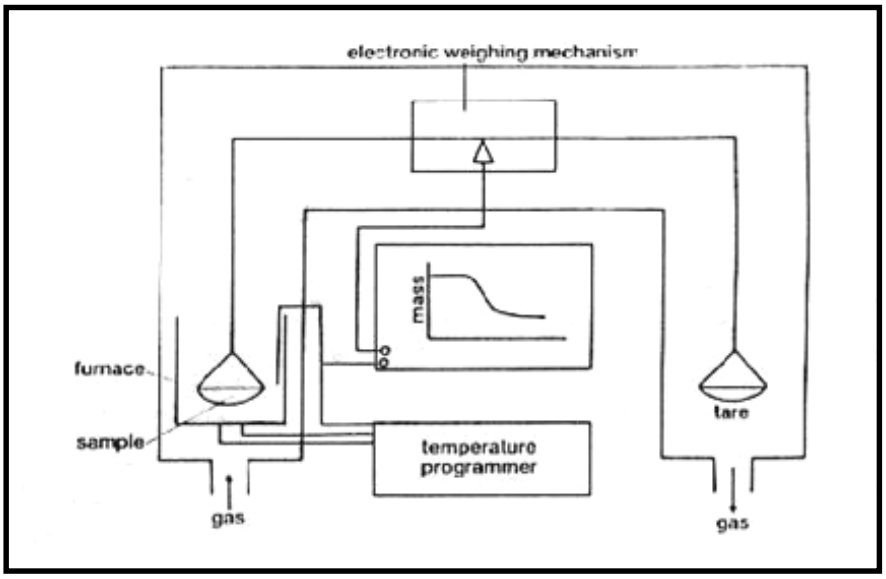

Fig. 2.18 Schematic diagram of a thermal analyzer.

2.4.8 Gas chrometograph equiped with flame ionoization deteactor (GC–FID)

A gas chromatograph (GC) is an analytical instrument that measures the content of various components in a sample. The measurment was carried out from the solution that was injected into the instrument in the form of stream. This instrument transports the sample into the separation tube known as column. Helium or nitrogen is used as the carrier gas. The various components are separated inside the column. The flame ionization detector (FID) measures the quantity of the components that exit the column. To measure a sample with an unknown concentration, a standard sample with known concentration is injected into the instrument. The standard sample peak retention time (appearance time) and area are compared to the test sample to calculate the concentration.

FID is one of the most used detectors for GC to measure the concentrations of organic species in a gas stream. when the sample was injected, it undergoes a combustion in a hydrogen/synthetic air flame. Ions and free electrons are formed in the flame.

The charged particles produce a measurable current flow in the gap between two electrodes in the detector. The resulting current flow is of greater strength than the signal produced by the pure carrier gas and the fuel gas flame alone. This signal differential provides information about the sample. The current is proportional to the information which depends on the composition of the separated sample. The schematic presentation of FID is shown in **Fig. 2.19 (a)** and the GC–FID photograph is shown in **Fig. 2.19 (b).**

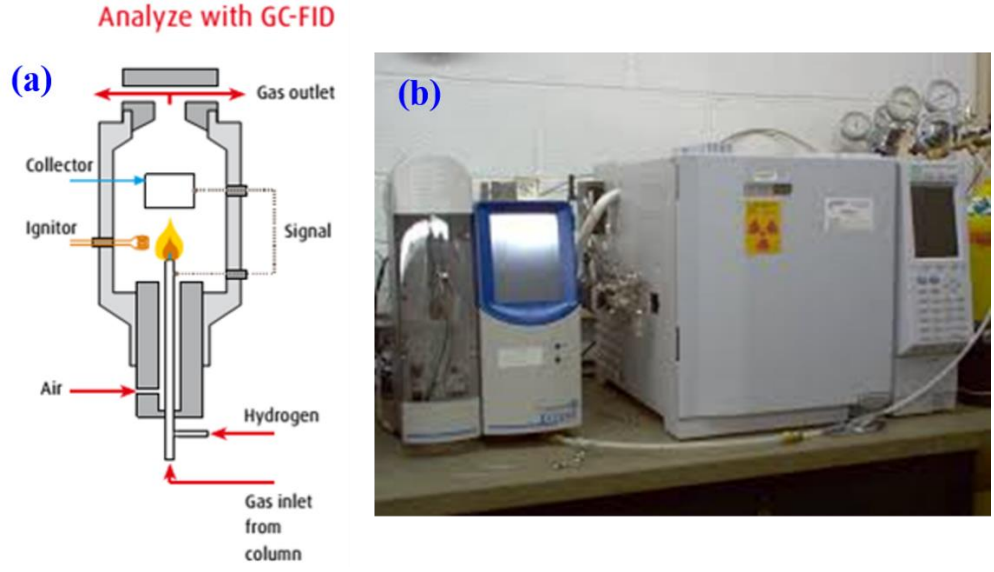

Fig. 2.19 (a) Schematic diagram of flame ionization detector and **(b)** photograph of GC–FID model Chemito 8610.

2.4.9 Gas chrometograph equiped with mass spectroscopy (GC–MS)

Mass spectrometry is a powerful analytical technique used to quantify known materials, to identify unknown compounds within a sample, and to elucidate the structure and chemical properties of different molecules. The complete process involves the conversion of the sample into gaseous ions, with or without fragmentation, which are then characterized by their mass to charge ratios (m/z) and relative abundances. This technique basically studies the effect of ionizing energy on molecules. It depends upon chemical reactions in the gas phase in which sample molecules are consumed during the formation of ionic and neutral species.

A mass spectrometer generates multiple ions from the sample under investigation, it then separates them according to their specific mass-to-charge ratio (m/z), and then records the relative abundance of each ion type.

The first step in the mass spectrometric analysis of compounds is the production of gas phase ions of the compound, basically by electron ionization. This molecular ion undergoes fragmentation. Each primary product ion derived from the molecular ion, in turn, undergoes fragmentation, and so on. The ions are separated in the mass spectrometer according to their mass-to-charge ratio, and are detected in proportion to their abundance. A mass spectrum of the molecule is thus produced. It displays the result in the form of a plot of ion abundance versus mass-to-charge ratio. Ions provide information concerning the nature and the structure of their precursor molecule. In the spectrum of a pure compound, the molecular ion, if present, appears at the highest value of m/z (followed by ions containing heavier isotopes) and gives the molecular mass of the compound. The schematic presentation of MS is shown in **Fig. 2.20.**

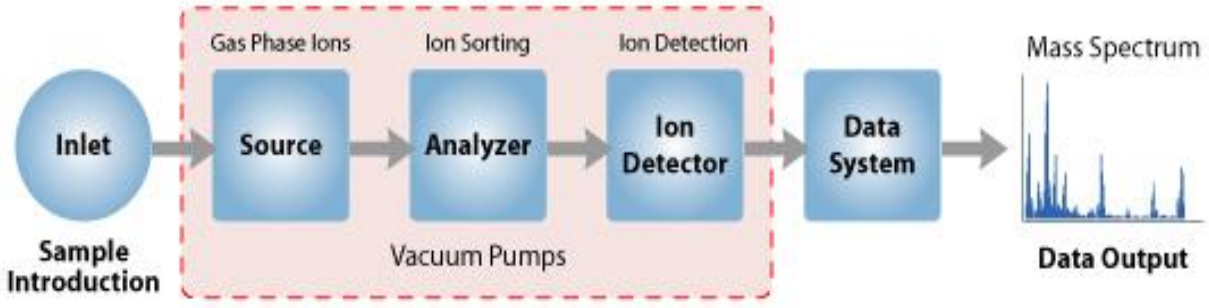

Fig. 2.20 schematic presentation of MS.

The instrument consists of three major components:

1. **Ion Source:** For producing gaseous ions from the substance being studied.
2. **Analyzer:** For resolving the ions into their characteristics mass components according to their mass-to-charge ratio.
3. **Detector System:** For detecting the ions and recording the relative abundance of each of the resolved ionic species.

In addition, a sample introduction system is necessary to admit the samples to be studied to the ion source while maintaining the high vacuum requirements (~10^{-6} to 10^{-8} mm of mercury) of the technique; and a computer is required to control the instrument, acquire and manipulate data, and compare spectra to reference libraries. The GC–MS photograph of 5973 model is shown in **Fig. 2.21**.

Fig. 2.21 GC–MS photograph of 5973 model.

2.4.10 Atomic Adsorption Spectroscopy (AAS)

AAS is used for the quantitative determination of metal elements in aqueous and solid sample by the absorption of optical radiation (light) by free atoms in the gaseous state. This techniques makes use of adsorption spectroscopy in which the electrons of the atoms in the

atomizer promoted to higher orbitals (excited state) for a short period of time (nanoseconds) by absorbing a selective quantity of energy (radiation of a given wavelength). This amount of energy, i.e., wavelength, is specific to a particular electron transition in a particular element. Generally, each wavelength is corresponding to only one element, and the width of an absorption line is only of the order of a few picometers (pm), which gives the technique its elemental selectivity. The radiation flux without a sample and with a sample in the atomizer is measured using a detector, and the ratio between the two values (the absorbance) is converted to analyte concentration or mass using the Beer-Lambert Law. The most commanly used atomizers are flame whose temperature with acetylene and oxygen becomes nearly 2300 ºC and with nitrous oxide (N_2O) and acetylene becomes 2700 ºC. The schematic presentation of AAS is shown in **Fig. 2.22** and the AAS instrument of Perkin Elmer Company of model AAnalyst 800 is shown in **Fig. 2.23**.

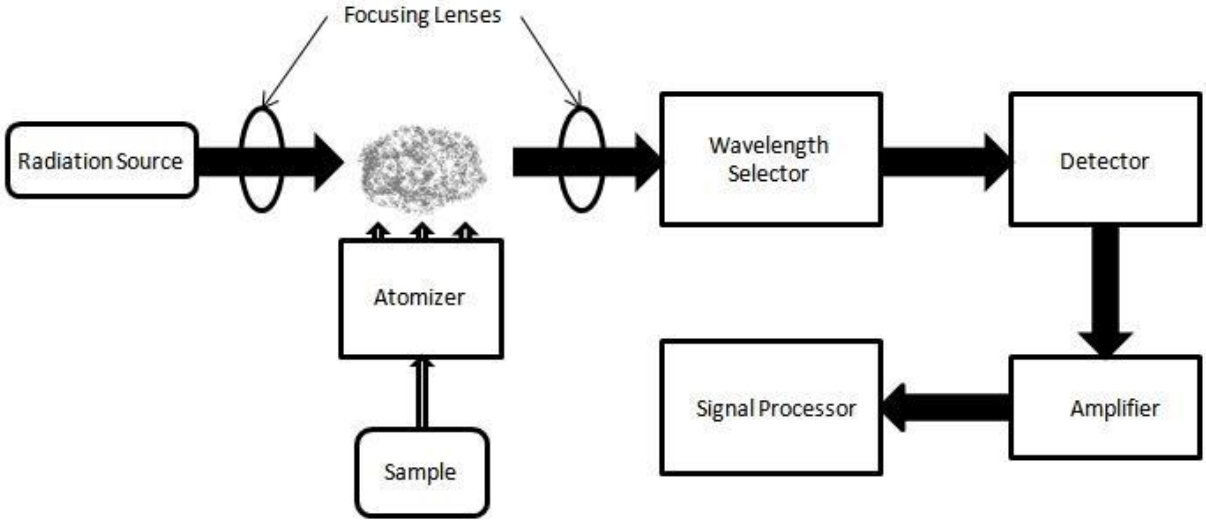

Fig. 2.21 schematic presentation of AAS.

Fig. 2.23 AAS instrument of Perkin Elmer Company of model AAnalyst 800.

CHAPTER 3

SYNTHESIS AND CHARACTERIZATION OF CuO NANOPARTICLES

3.1 Introduction

From the last few decades, the scientific community has demonstrated great concern about the use of toxic chemical warfare agents (CWA) by terrorists and highly ambitious nation **[132, 211].** Hence, research is focused to find out safe and effective measures to detoxify the CWAs without endangering the human life or the environment **[212, 213].** An important way to solve the current problem and achieve protection against these CWAs is to utilize inorganic oxide material that not only possesses high surface area but have numerous edge and corners for the adsorption and decontamination applications. The reactivity of these metal oxides enhances when the size of material changes from bulk to nanometer range associated with increasing surface area (surface area to volume ratio), corner defects sites, large number of highly reactive edges, and unusual lattice planes **[214, 215].** They remove the CWAs rapidly from the contaminated surfaces and react by various processes like hydrolysis, elimination, oxidation and surface complexation reactions **[130, 155].** The nanosized metal oxides such as MgO, CaO, Al_2O_3, MnO_2, and ZnO have emerged as a potential adsorbent material for the catalytic decontamination of CWAs **[97, 111, 130, 168, 216].** CuO also seems to be a promising adsorbent material for the degradation of environmental pollutants and widely used as an environmental catalyst **[137].** The synthesis of CuO nanoparticles at different calcined temperature for the degradation of HD found that the rate of degradation decreases as the calcination temperature increases. At lower calcinations temperature, hydrolysis products are formed while at higher calcinations temperature, the elimination products predominate. Inspired by these advantages, we have synthesized copper oxide nanoparticles for detoxification of CEES **[137].**

CuO nanoparticles have been synthesized by different methods such as thermal decomposition **[115]**, precipitation **[217]**, sol-gel **[218]** and alcothermal method **[219].** In this chapter, CuO nanoparticles have been synthesized using dc magnetron sputtering technique which provides high surface area, reproducibility, narrow size distribution, uniformity and high purity to the nanoparticles **[220].** Thereafter, annealed at different temperatures and used for the

decontamination of 2–chloro ethyl ethyl sulphide (CEES), well known simulants of sulfur mustard, king of CWA. Also, studied the structural, morphological and thermal properties of CuO nanoparticles synthesized at different sputtering power and pressure.

3.2 Synthesis of sputter deposited CuO nanoparticles and their use for Decontamination of 2–Chloro Ethyl Ethyl Sulphide (CEES)

3.2.1 Synthesis of CuO nanoparticles

Copper oxide nanoparticles have been synthesized in a 12″ diameter custom designed vacuum chamber (Excel Instrument, Mumbai). Copper target of 2″ diameter and 5 mm thickness was used to prepare sputtering. The chamber was initially evacuated up to 10^{-7} Torr with a turbo molecular pump backed by rotary pump. **Table 3.1** lists the values of other sputtering parameters used for the nanoparticles synthesis. An optimum working pressure was maintained in the sputtering chamber, with argon and oxygen gas in a specific ratio. Before acquiring the working pressure, the hollow copper cold finger was continuously filled up with liquid nitrogen (Liq–N_2) to cool the substrate to ≤ –194 ºC. Also, during sputtering Liq–N_2 was continuously filled up to maintain the desired substrate temperature. The reason for keeping low substrate temperature is to inhibit the grain growth in the plane of the film leading to production of nanoparticles. Also, contamination due to the possible diffusion of atoms from the substrate with the deposited material is minimized at lower temperature. After deposition of nanoparticles on the substrate, when room temperature occur then these nanoparticles were scratched carefully and crushed in a pestle mortar to homogenize and then annealed in the temperature range of 200–900 ºC in air.

Table 3.1 Sputtering parameters for the synthesis of CuO nanoparticles.

Target	Base Pressure	Working Pressure	Gas Used	Deposition Time	(d)	Power (Watt)	Substrate Temp.	Annealing Temperatures
Cu	8.6×10^{-7}Torr	10 mTorr	Ar:O_2 ::40:10	12 hrs	4.5 Cm	80 W	-194 ºC	As-deposited, 200, 400, 600, 750, 900 ºC

d=distance between substrate and target

3.2.2 Reaction procedure

The reaction of CEES was done with CuO nanoparticles to understand the decontamination capacity of the synthesized material. For this purpose, 100 µl solution of dichloromethane

having 5 µl of CEES was added to 100 mg CuO nanoparticles in seven separate test tubes of equal size and then stirred for two minutes to ensure uniform mixing. After decontamination reaction, the remaining CEES from the mixture was extracted with the help of 5.0 ml acetonitrile for 5 times (each time 1 ml) within a time interval of 1h, 2h, 4h, 6h, 8h, 16 h and 24 h. Extracted solutions were quantitatively analyzed by gas chromatograph equipped with flame ionization detector in the programming mode from 120 to 250 ºC at a rate of 10 ºC/min to determine the amount (in %) of remaining CEES. During this analysis, the injection port was kept at 240 ºC while the detector port was kept at 250 ºC. The experiments were repeated seven times in order to ensure the reproducibility of the kinetics results.

3.2.3 Results and discussion

3.2.3.1 Characterization of CuO nanoparticles

Fig. 3.1 represents the X-ray diffraction (XRD) patterns of as-deposited and annealed CuO nanoparticles. The annealing was carried out at different temperatures i.e. 200 ºC, 400 ºC, 600 ºC, 750 ºC and 900 ºC. The XRD patterns show that the crystallinity of the CuO nanoparticles increases with increasing annealing temperature. The dominant peaks obtained are (–111) and (111) at 2θ values of 35.5 and 38.35, respectively. However, for CuO nanoparticles annealed at higher temperatures (≥ 600 ºC), weak peaks orientations (110) (–202), (020) (202) (–113) (022) and (113) were also formed at 2θ: 32.52, 48.76, 53.41, 58.31, 61.57, 66.22, 68.14. The average particle size of the CuO nanoparticles was determined from XRD pattern using the Scherer formula after subtracting the CuK_{α} contribution and making allowance for instrumental broadening. **Table 3.2** lists the particle size of CuO nanoparticles and clearly reveal that as the annealing temperature was increased from 200 to 900 ºC, the particle size also increases from 7 nm to 86 nm. The reason for the increase in particle size with annealing temperature is that, at lower temperature, grain boundaries merge into neighboring grains while, at higher temperature smaller nanoparticles merge into larger ones (agglomeration) **[221]**. The values of 2θ clearly reveal that all the CuO nanoparticles exhibit monoclinic structure (JCPDF 00–005–0661). No other XRD peaks belonging to any impurity such as Cu_2O, $Cu(OH)_2$ was present in the XRD pattern which clearly indicates the formation of high purity CuO nanoparticles.

Table 3.2 Particle size of CuO nanoparticles at different annealing temperatures.

	Annealing temperature of CuO (°C)					
	As–deposited	**200**	**400**	**600**	**750**	**900**
Particle size (nm) from XRD	7	21	34	48	67	86
Particle size (nm) from TEM	9	23	37	53	73	90

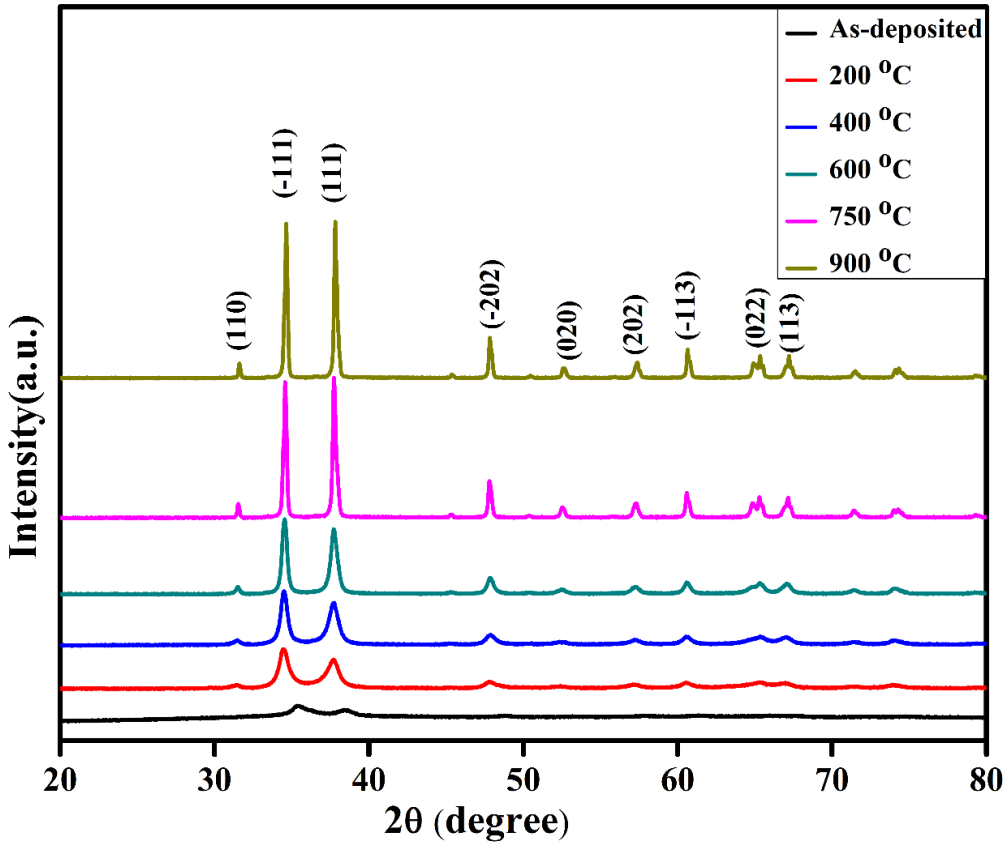

Fig. 3.1 XRD patterns of CuO nanoparticles.

Fig. 3.2 (a)–(f) represent the FE–SEM images of the CuO nanoparticles. Spherical type morphology was observed for all type of CuO nanoparticles. It is also observed that with increase in annealing temperature the grain growth of larger particles takes place at the cost of smaller ones. Thus, verifying the XRD results.

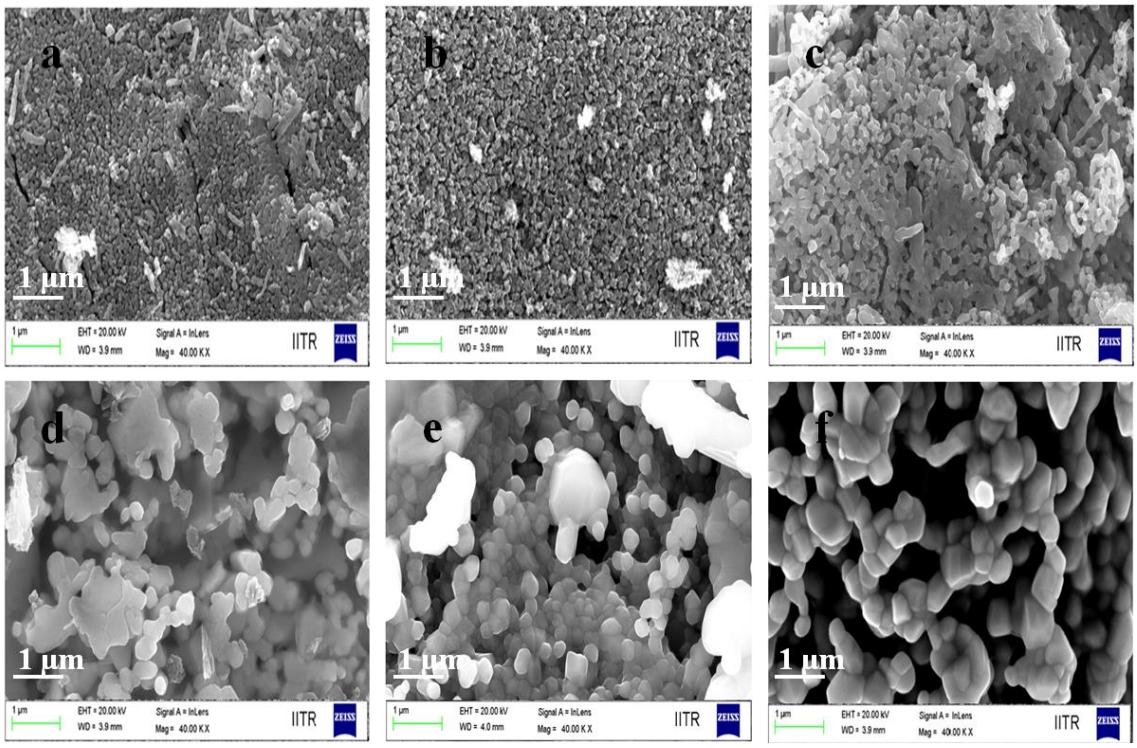

Fig. 3.2 FE–SEM images of Copper oxide nanoparticles **(a)** as-deposited and annealed at **(b)** 200 ºC **(c)** 400 ºC **(d)** 600 ºC **(e)** 750 ºC and **(f)** 900 ºC.

The EDS spectrum of the as-deposited CuO nanoparticles was shown in **Fig. 3.3**. The spectrum clearly reveals the high purity of the synthesized material because only Cu and O are present in proper stoichiometric ratio in the nanoparticles.

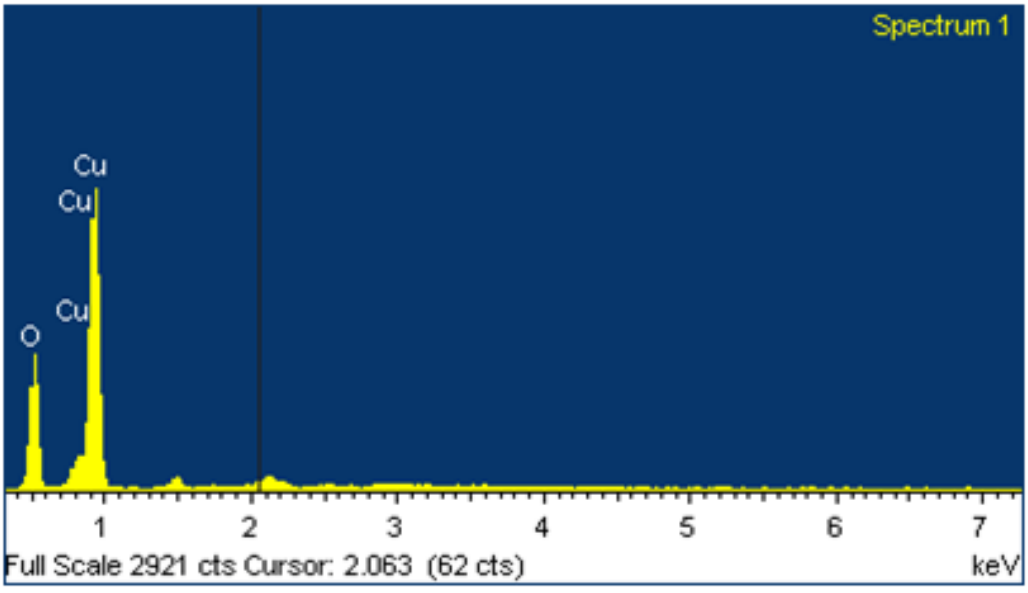

Fig. 3.3 EDS spectra of as-deposited CuO nanoparticles.

Fig. 3.4 (a)–(f) represent the TEM images of all the CuO nanoparticles. **Table 3.2** lists the particle size of CuO as measured from TEM images. It was observed that TEM analysis give enhanced particle size compare to Debye–Scherrer formula. This is due to the fact that XRD measures crystallite size while TEM measures grain size. Grain size is normally larger than crystallite size as it contains several crystallite sizes of the particles. It is clear that the particle size increases as the annealing temperature is raised from 200 to 900 ºC.

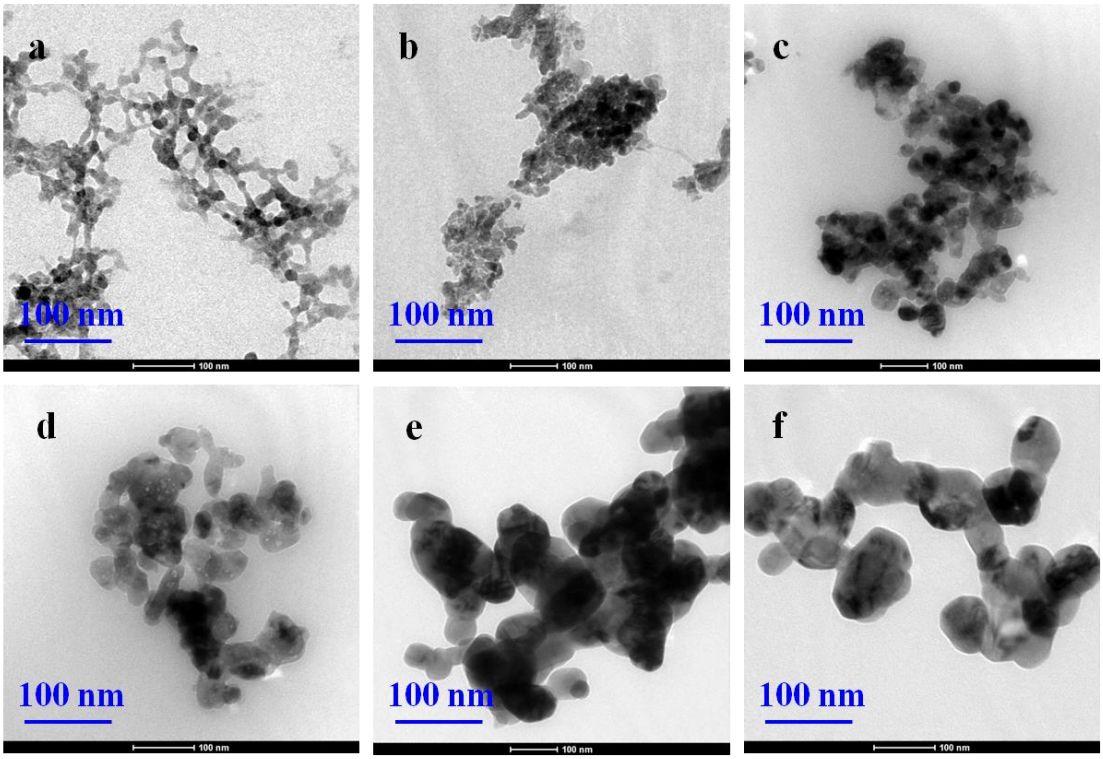

Fig. 3.4 TEM images of CuO nanoparticles **(a)** as-deposited and annealed at **(b)** 200 ºC **(c)** 400 ºC **(d)** 600 ºC **(e)** 750 ºC and **(f)** 900 ºC.

The selected area diffraction pattern (SAED) of as–deposited CuO nanoparticles is shown in **Fig. 3.5**. The ring patterns are assigned the (–111), (111), (–202), (020), (–113) and (022) orientation of the polycrystalline monoclinic structure of CuO nanoparticles. The high resolution TEM image shown in **Fig. 3.6** represents the crystalline structure with d–spacing of 0.187 nm. This matches with the (–202) planes of CuO nanoparticles. Thus, data obtained by XRD, SEM, EDS and TEM clearly indicates the formation of CuO nanoparticles and is also consistent with the reported results **[104]**.

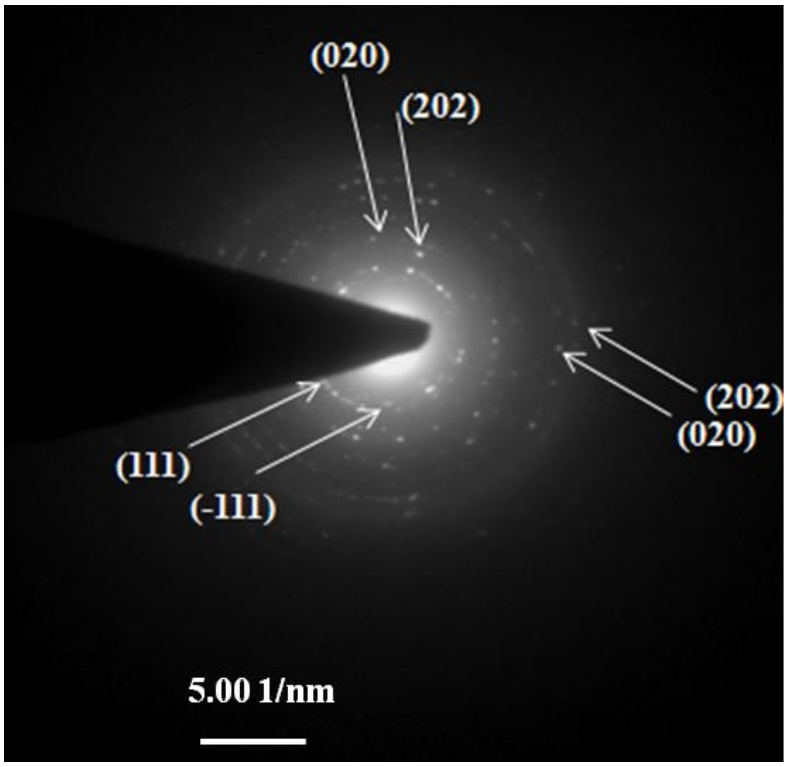

Fig. 3.5 SAED of the as–deposited CuO nanoparticles showing polycrystalline rings.

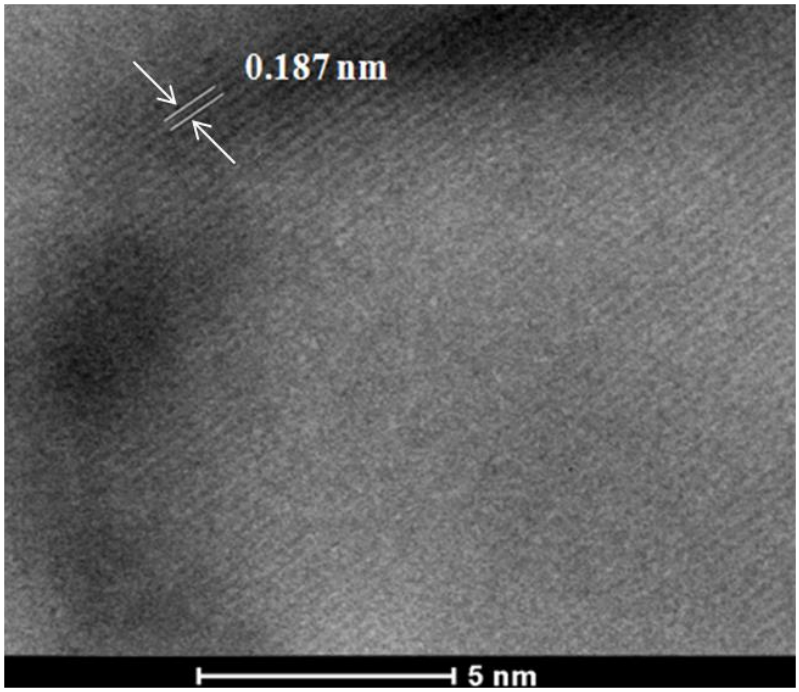

Fig. 3.6 HR–TEM image of as-deposited CuO nanopartticle showing d-spacing for the (–202).

The surface area and the pore size distribution of the CuO nanoparticles were determined using Brunauner–Emmet–Teller (BET) and Barrett–Joyner–Halenda (BJH) methods respectively. **Fig. 3.7** represents the N_2 adsorption–desorption isotherm of type III and **Fig. 3.8** represents the pore size distribution of as–deposited CuO nanoparticles. The obtained values of surface area and the pore volume are given in **Table 3.3**. The samples exhibit high surface area values ranging from 110.27 m^2/g–36.42 m^2/g. The literature has reveals a lesser value of surface area (30 m^2/g) for the CuO nanoparticles **[137]**. The calculated values of pore volume lie in the range 0.214–0.047 cm^3/g. It is clear from the data that as the annealing temperature was increased from 200 to 900 ºC, both surface area and pore volume decreases. It may be attributed due to increase in the particle size as revealed by XRD and TEM data.

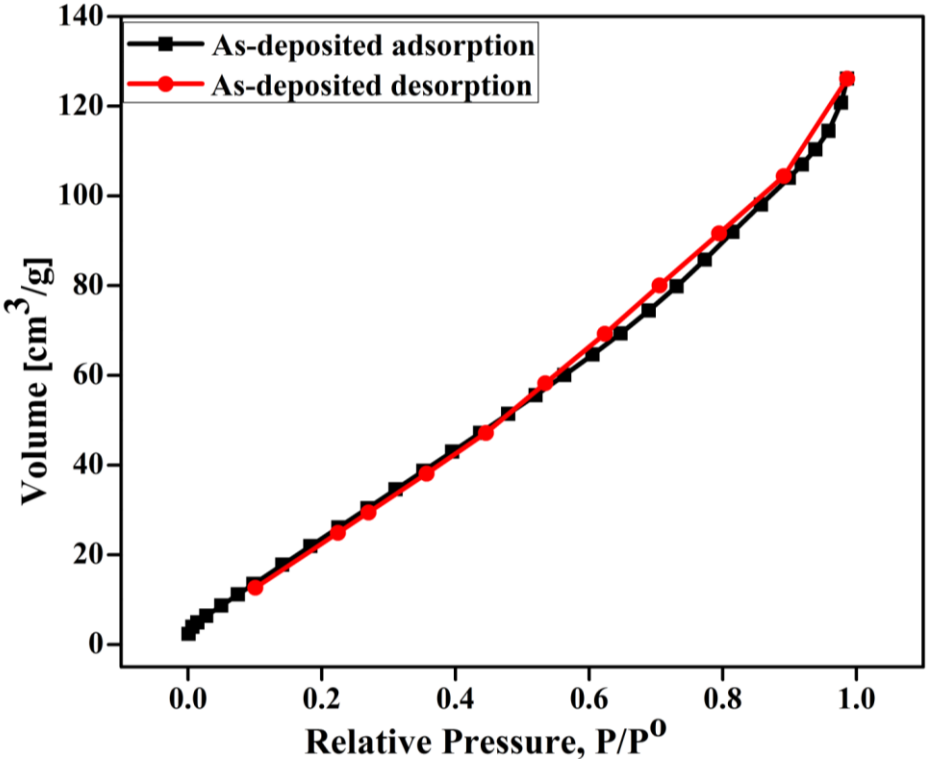

Fig. 3.7 Adsorption-desorption isotherm of as-deposited CuO nanoparticles.

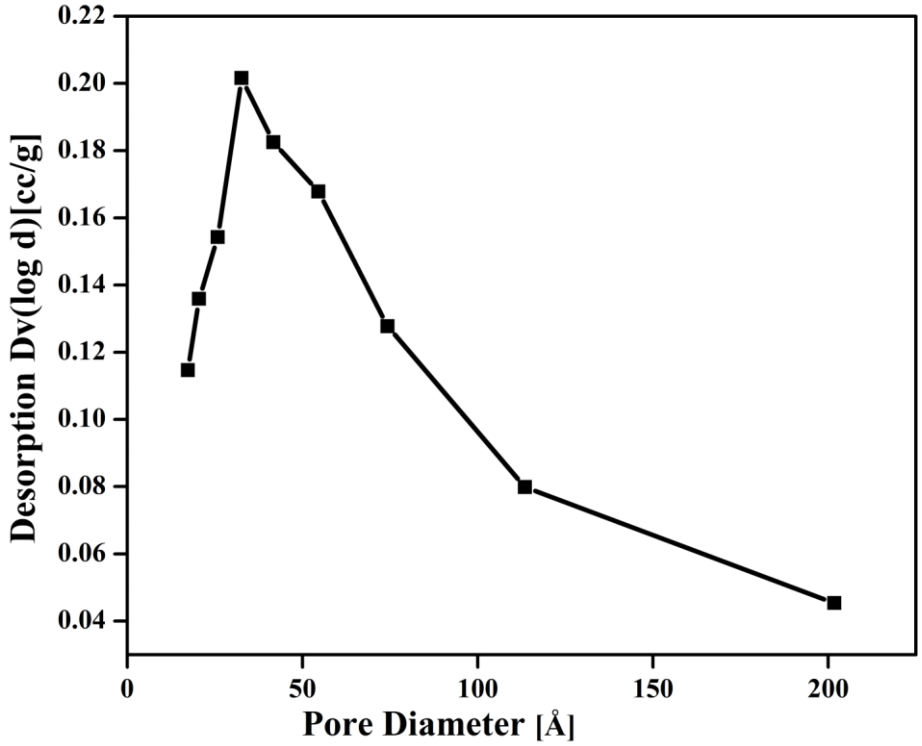

Fig. 3.8 BJH pore size distribution of as-deposited CuO nanoparticles.

Table 3.3 Surface area and pore volume values of CuO nanoparticles of different sizes.

	Particle size of CuO nanoparticles (nm)					
	9	**23**	**37**	**53**	**73**	**90**
Surface area (m^2/g)	110.27	93.30	78.82	64.45	52.45	36.42
Pore volume (ml/g)	0.214	0.158	0.139	0.092	0.079	0.047

3.2.3.2 Kinetics of CEES decontamination

The kinetics of CEES decontamination simply means the change in decontamination rate of CEES with the change in available hydroxyl group/water. To study the kinetics of CEES degradation, the CuO nanoparticles of different sizes were exposed to CEES for a period of 24 h. The unreacted CEES was removed from the reaction mixture by using acetonitrile at regular kinetic interval of time. The concentration of unreacted CEES was determined by GC–FID. Subsequently, the obtained kinetics data were plotted by taking log of the unreacted CEES (mg/ml) on Y–axis and time (h) on X–axis as shown in **Fig. 3.9**. The kinetics plots indicate that

the concentration of CEES for all the CuO nanoparticles decreases with time indicating first order kinetics **[155]**. It is clear from the figure that more than 96.2% of CEES was degraded within 24 hours. Also, the kinetics plot indicates that the linear curve occur with fast initial reactions and a steady state at later stages of the reactions. The probable reason is the rapid adsorption and distribution of the liquid within the pores and its interaction with the accessible reactive sites and hydroxyl group. When the sites are exhausted, the limited surface reaction occurs obviously, replacing the initial fast reaction by the steady state reaction. The values of the rate constant (k) and half life time ($t_{1/2}$) of the degradation of the CEES on the CuO nanoparticles of different sizes were calculated by using the first order rate equation i.e. k = 2.303×slope and 0.6932/(2.303×slope) respectively and are given in **Table 3.4**.

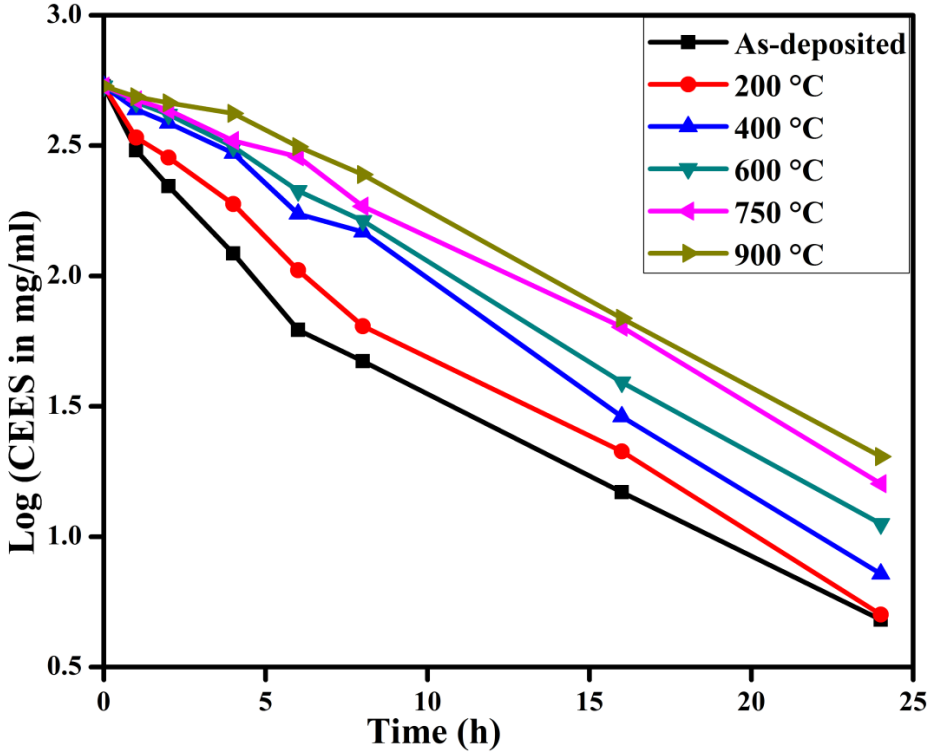

Fig. 3.9 Kinetics of degradation of CEES on the CuO nanoparticles.

Table 3.4 Results of degradation of CEES on the surface of different sizes CuO nanoparticles.

	Particle size of CuO nanoparticles (nm)					
	9	**23**	**37**	**53**	**73**	**90**
K (h^{-1})	0.434	0.405	0.250	0.222	0.169	0.134
$t_{1/2}$ (h)	1.59	1.71	2.77	3.12	4.10	5.17

It is clear from the experimental results that the rate of degradation of CEES decreases as the particle size increases i.e. smaller particles have high degradation properties compare to bigger particles. The probable reason for the decrease in degradation rate with increase in particle size is the surface area. The higher surface area seemed to have imparted more adsorption capacity towards CEES. Due to large adsorption capacity of CuO nanoparticles, CEES was found to be rapid adsorption followed by its distribution within their pores and react with the reactive sites of synthesized nanoparticles and convert them into non-toxic form. Also, decrement in the surface area reduces the adsorption capacity which in turn lessens the degradation properties. Gu et al. reported that the variation in annealing temperature modifies surface structure of metal oxides and hence change its acidic and redox properties **[222]**. Also with the increase in annealing temperature, the amount of OH group/hydrated water decreases, which in turn reduces the rate of reaction. Tang and co-workers reported that the reactivity of the metal oxides towards CWAs not only depends on surface structure but also on the amount of water content **[157]**. The rate of degradation was found to increase with increase in water content. With increasing annealing temperature, the particle size increases (as observed in FE−SEM and TEM studies) due to which surface area of the synthesized nanoparticles decreases **[158]**. Due to decrease in surface area, the available active sites for the adsorption and the activation of the reactant towards CEES decreases which in turn reduces the rate of degradation reaction.

No excess water was added to the CuO nanoparticles, whatever moisture adsorbed from the atmosphere while transferring the samples along with other reactive functionalities seems to have facilitated the decontamination. CuO nanoparticles were characterized using TGA in order to investigate the amount of water present on their surface. Initially, the synthesized samples were dried and then subjected to TGA. **Fig. 3.10** shows the TGA pattern of as−deposited CuO nanoparticles. It is clear that the weight loss up to 240ºC is due to desorption of physisorbed water and the small amount of weight loss observed above 240 ºC was due to dehydroxylation. TGA data also reveals that CuO nanoparticles of 7, 21, 34, 48, 67 and 86 nm sizes have a weight loss of 9.13, 5.54, 4.00, 3.36, 1.98 and 0.8 percent, respectively. So, it is clear that with increase in particle size through annealing temperature, the amount of physisorbed water/ hydroxyl group on the surface of CuO nanoparticles decreases due to which weight loss decreases.

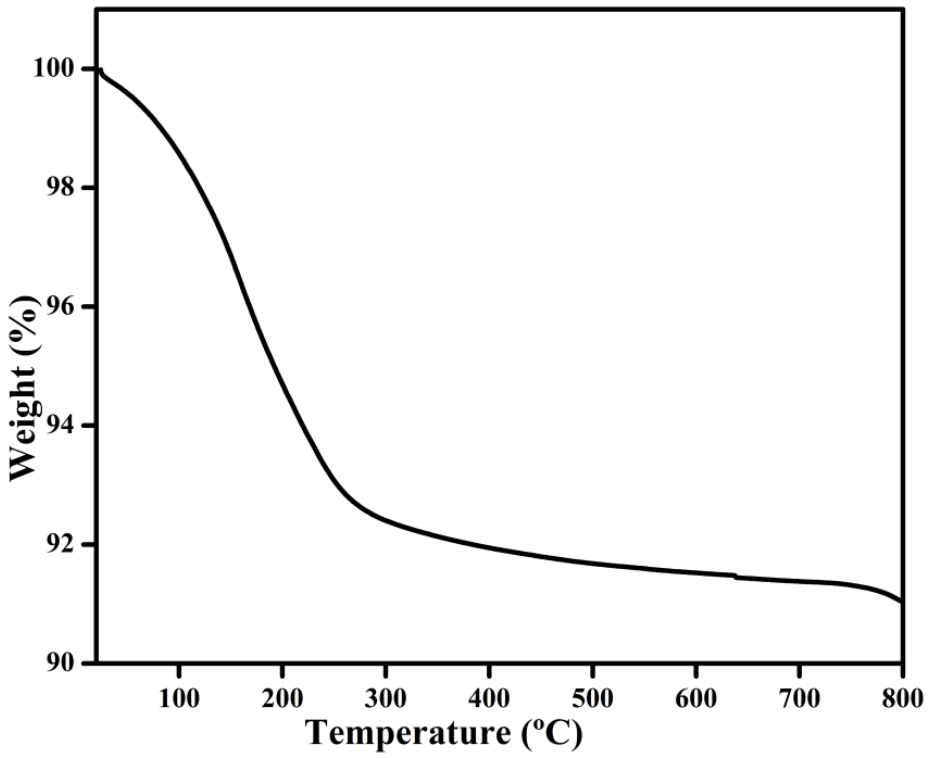

Fig. 3.10 TGA patterns of as-deposited CuO nanoparticles.

3.2.3.3 GC–MS analysis

The extracted reaction mixtures were analyzed by GC–MS and FT–IR to understand the reaction mechanism and products formed. Since hydrolysis product of CEES has polar and non-volatile nature due to which they were derivatised before GC–MS analysis. GC–MS data was obtained after silylating the extracted reaction mixture using BSTFA [bis(trimethylsilyl) btriflouro acetamide. For all the samples, GC–MS data indicates the m/z values at 106, 75, 61 and 47 for the extracted reaction mixture from CEES treated with CuO nanoparticles. This clearly indicates the formation of hydroxyl ethyl ethyl sulphide (HEES) with further emphasizing the role of hydrolysis reaction in the decontamination of CEES to HEES thereby rendering them to non-toxic form. In addition to the hydrolysis product, the residual CEES was also identified with the m/z values at 124, 75, 61, 47 and 27. Furthermore, the FT–IR investigations on the exposed samples reveals the extinction of band intensity at 700 cm^{-1} (C–Cl), change of peak at around 1440 and 1295 cm^{-1} (CH_2–Cl) and small change in peak intensity at 3430 cm^{-1} (–O–H) which further confirms the hydrolysis of CEES to convert into HEES.

Based on the above observations, the reaction scheme for the decontamination of CEES on the CuO nanoparticles is proposed in **Fig. 3.11**. According to the above scheme, CEES molecules react with the CuO nanoparticles in two different ways. In one way, they reacted with the physisorbed or intercalated water molecules which were present on the surface of the CuO nanoparticles to form HEES in which cyclic sulphonium ion seems to be formed as shown in the scheme. The sulphonium ion is formed due to the attack of sulphide on the β carbon atom of CEES and is considered as SN1 reaction. Sulphonium ion being highly unstable, it could not be extracted out and detected by GC **[33]**. Subsequently, the sulphonium ion undergoes hydrolysis reaction with water molecules adsorbed by CuO nanoparticles (no more water is added to the reaction) giving rise to the formation of HEES. In the second way, CEES molecules react with isolated hydroxyl group (Cu–OH) and Lewis acid (Cu^{2+}) sites to form surface bound alkoxy species **[130, 155, 157]**. No other elimination and oxidation products were observed, indicating the presence of large amount of water or hydroxyl groups on the CuO nanoparticles. Collectively, the CuO nanoparticles which offer large surface area facilitates faster adsorption and encapsulation of CEES, physisorbed water, isolated hydroxyl groups and Lewis acid sites to make toxic agents as non-toxic. Results of decontamination reaction of CEES on the CuO nanoparticles which have been presently synthesized were compared with those prepared and studied earlier with HD at different calcinations temperatures. The CuO nanoparticles that were prepared and studied presently exhibited better reactivity than the earlier CuO nanoparticles for HD degradation and other decontaminating agents **[97, 111, 113, 130, 137, 147, 154, 155]**. These results show that dc sputtered CuO nanoparticles exhibit much better results as compared to existing solid decontamination systems such as CuO nanoparticles prepared by other methods.

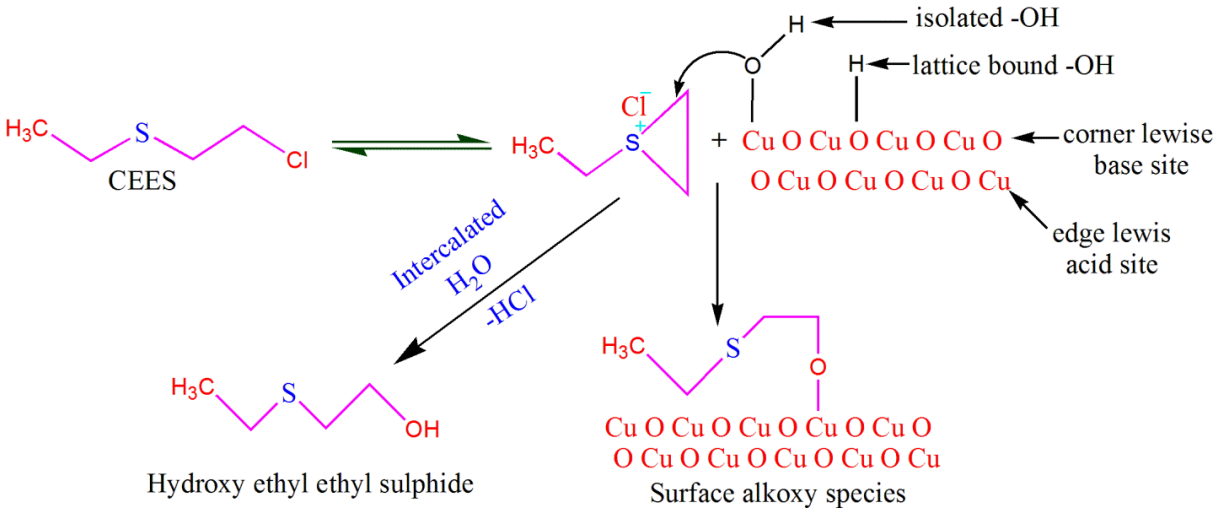

Fig. 3.11 Reaction scheme of CEES occurring on the surface of CuO nanoparticles.

3.2.4 Conclusion

The decontamination of CEES over various sizes CuO nanoparticles have been studied in the present work. The CuO nanoparticles have been synthesized by dc magnetron sputtering technique. Thereafter, they were annealed at different temperatures to vary the particle size. This novel PVD technique provides nanoparticles of high purity with a narrow size distribution and high surface area. Due to these advantages, dc sputtered CuO nanoparticles show enhanced decontamination of CEES over earlier studied CuO prepared by different techniques such as hydrothermal process. Decontamination reactions exhibited first order steady state (predominantly hydrolysis) behavior. The rate constant (0.434 h^{-1}) and half life (1.59 h) value of decontamination of CEES over CuO nanoparticles was found to be minimum for nanoparticles having size of ~7 nm. The future work will focus on the decontamination of other CWAs' simulants and sensing application of these nanoparticles synthesized using dc magnetron sputtering process.

3.3 CuO nanoparticles: sputtering based synthesis and it's structural, morphological and studies

3.3.1 Synthesis of CuO nanoparticles

CuO nanoparticles have been synthesized in a 12″ diameter custom designed vacuum chamber (Excel Instrument, Mumbai). The chamber consists of different ports to hold sputtering gun, copper cold finger arrangement to cool the substrate with liquid nitrogen (Liq–N_2), gas line and glass window. The CuO nanoparticles were deposited by dc magnetron sputtering onto copper cold figure using copper target of 99.99% purity (2″ diameter and 5 mm thickness). Prior to fixing in the sputtering chamber, the cold finger was cleaned by acetone and methanol to ensure the removal of any unwanted impurity. The chamber was initially evacuated to 10^{-8} Torr with the help of turbo molecular pump backed by rotary pump. Thereafter, an optimum working pressure was maintained in the sputtering chamber with argon and oxygen gas in a specific ratio (40:10). The sputtering parameters used for the synthesis of nanoparticles are listed in **Table 3.5**. Before acquiring the working pressure, the hollow copper cold finger was continuously filled up with liq–N_2 to cool it to a temperature ≤ −194 ºC (or 79 K). During sputtering, liq–N_2 was continuously filled up in the copper cold finger to maintain the desired temperature. The probable reason for keeping low temperature of copper cold finger is to inhibit the grain growth in the plane of the film. The low temperature leads to condensation of the deposited material in the form of nanoparticles and minimizes the contamination due to the possible diffusion of atoms from the substrate with the deposited material. During sputtering, the Cu atoms were sputtered from the target and react with the oxygen atoms in chamber or on the copper cold finger substrate during deposition and form CuO nanoparticles. After sputtering, when the copper cold finger reaches room temperature, the particles were scratched carefully and crushed in a pestle mortar to homogenize them.

Table 3.5 Sputtering parameters for the synthesis of CuO nanoparticles.

Target	Base Pressure	Working Pressure	Gas Used	Deposition Time	Distance (d)	Power (Watt)	Substrate Temperature
Cu	8.8×10^{-8} Torr	10, 20, 30, 40, 50 mTorr	Ar:O_2 :: 40:10	10 hrs	4.5 Cm	80 W	−194 ºC

d = Distance between target and substrate

3.3.2 Results and discussions

The XRD patterns of CuO nanoparticles synthesized at various sputtering pressure are represented in **Fig. 3.12**. For all the samples, the peaks are well resolved at 2θ values of 32.29º, 35.34º, 38.48º, 48.91º, 58.01º, 61.44º, 66.21º, 67.70º and 74.77º corresponding to (110), (–111), (111), (202), (–113), (–311), (113) and (221) planes of the monoclinic phase (space group C2/c; a = 4.685 Å, b = 3.423 Å, c = 5.132, β = 99.47º ; JCPDS file no. 01–072–0629), respectively. No other characteristic peaks of any impurity such as $Cu_2O/Cu(OH)_2$ were observed, indicating high purity monoclinic phase of CuO nanoparticles. The broadening of peaks indicates that the particle size is very small. XRD patterns show that the intensity of the dominants peaks (–111) and (111) increases with increasing sputtering pressure from 10 mTorr to 50 mTorr, which indicate an increase in the average crystallite size (δ) and hence crystallinity of the nanoparticles. The average crystallite size of the CuO nanoparticles was calculated using the Scherer formula.

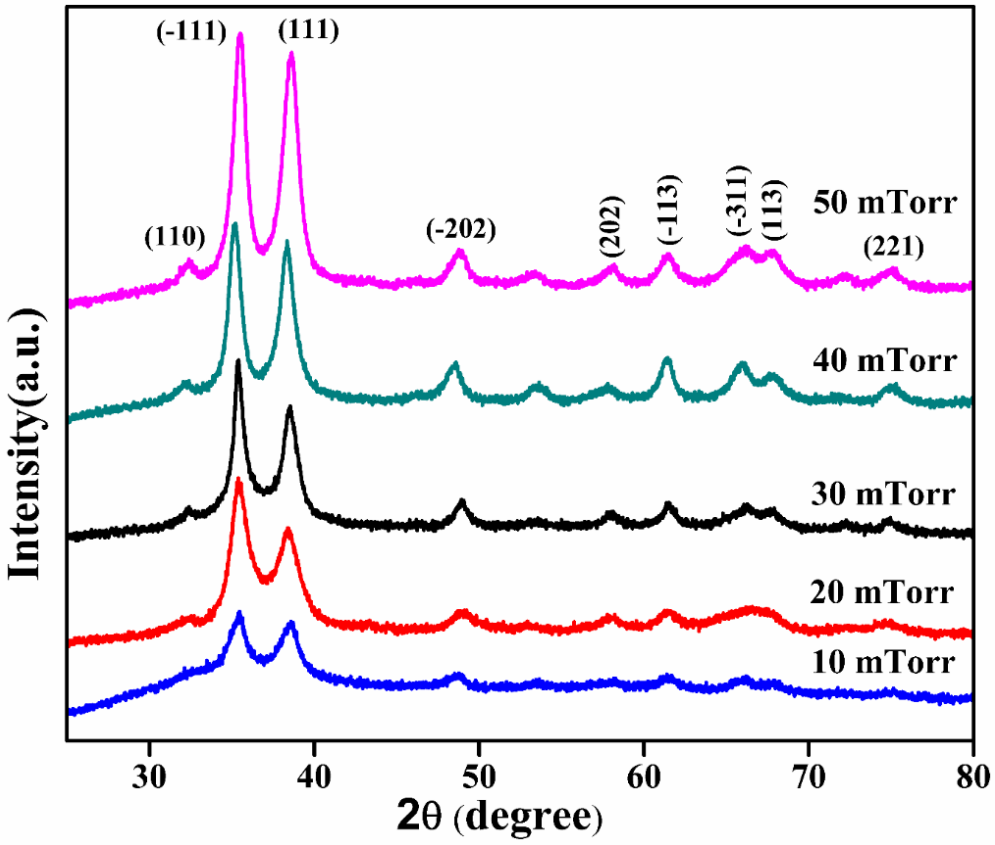

Fig. 3.12 XRD patterns of CuO nanoparticles synthesized at different sputtering pressures.

Eq. 3.1 represents the variation of average crystallite size of nanoparticles as a function of sputtering pressure. The increase in the average crystallite size with increasing sputtering pressure can be explained by using the relationship between the mean free path (d_m) and molecular diameter of the sputtering gas as examined by:

$$d_m = 2.330 \times 10^{-20} \frac{T}{(P\lambda^2)} \qquad (3.1)$$

Where, T (K) is the temperature, P (Pa) is the sputtering pressure and λ (cm) is the molecular diameter. **Eq. 3.1** indicates that sputtering pressure is inversely proportional to the mean free path, therefore, as the sputtering pressure is increased, the mean free path decreases so that the sputtered atoms undergo a large number of collisions leading to agglomeration and growth of the particles before reaching at the copper cold finger substrate **[220, 223]**. Also, we observed a slow growth of the particles with increasing sputtering pressure in comparison to thin film growth. The reason behind the slow growth is the low substrate temperature (−194 ºC) which affect the thermal gradient between the target and substrate. The low temperature of the substrate increases the convective velocity of the sputtered particles and decreases the collision frequency. However, at low gas pressure, when the mean free path of the sputtered atoms becomes of the order of target−substrate distance, the average crystallite size becomes independent of the substrate temperature. These observations clearly disclose that the growth for maximum number of particles occurs between the substrate and target environment and not on the substrate. It appears that the important effect of the low substrate temperature is to provide an accelerating potential to the sputtered particles towards substrate. FT−IR spectroscopy is a powerful tool to provide additional information about metal−oxygen bonding in the CuO nanoparticles. FT−IR spectrum of the CuO nanoparticles synthesized at 10 mTorr is shown in **Fig. 3.13**. There are three adsorption peaks observed at 437 cm^{-1}, 532 cm^{-1} and 584 cm^{-1} assigned to the $2B_u$ and A_u mode, respectively. These frequency modes are due to Cu (II)–O of CuO nanoparticles, which are in good agreement with the previous reports **[224, 225].**

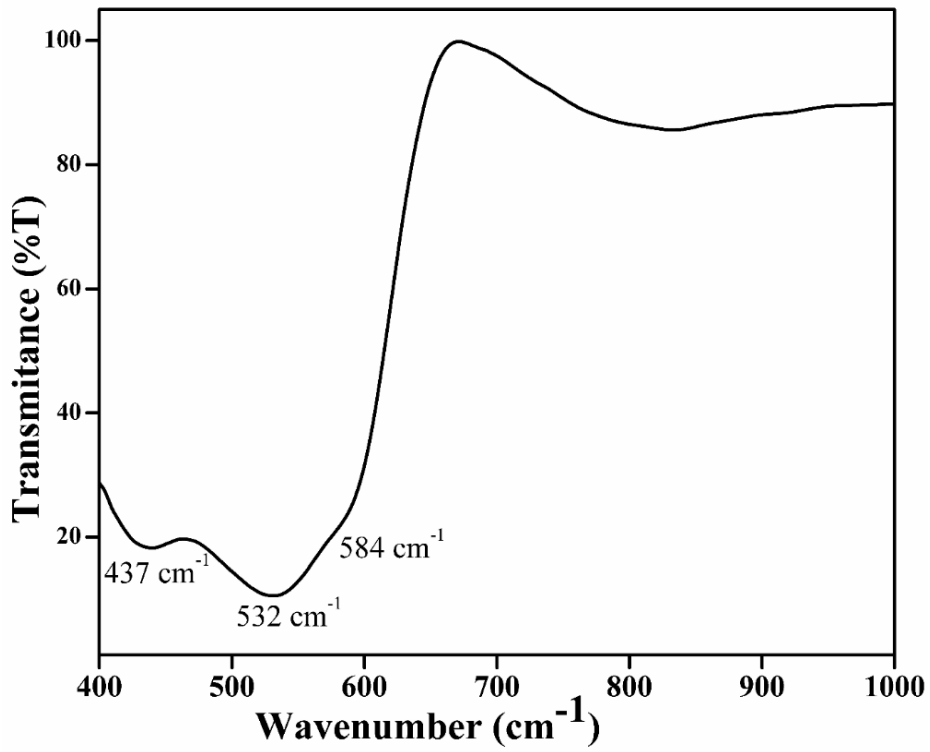

Fig. 3.13 FT–IR spectrum of the CuO nanoparticles.

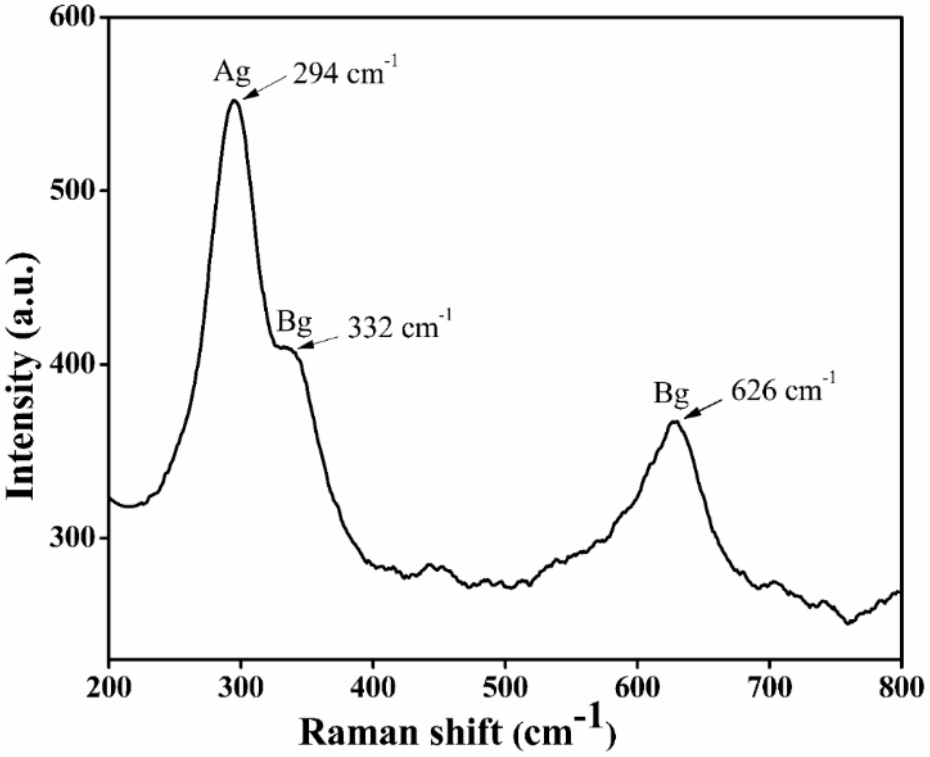

Fig. 3.14 Raman Spectrum of CuO nanoparticles.

To further confirm the phase of CuO nanoparticles, Raman spectrum of the CuO nanoparticles was carried out and is shown in **Fig. 3.14**. CuO nanoparticles belong to C^{6}_{2h} space group with twelve vibration modes at zero centre including three acoustic modes (A_u+$2B_u$), six infrared active modes ($3A_u$+$3B_g$) and three Raman active modes (A_g+$2B_g$). The Raman spectrum shows three peaks, the peak observed at 294 cm^{-1} belongs to A_g mode and the peaks at 332 cm^{-1} and 623 cm^{-1} belongs to B_g mode which are correlated to the monoclinic phase of CuO nanoparticles **[226, 227]**.

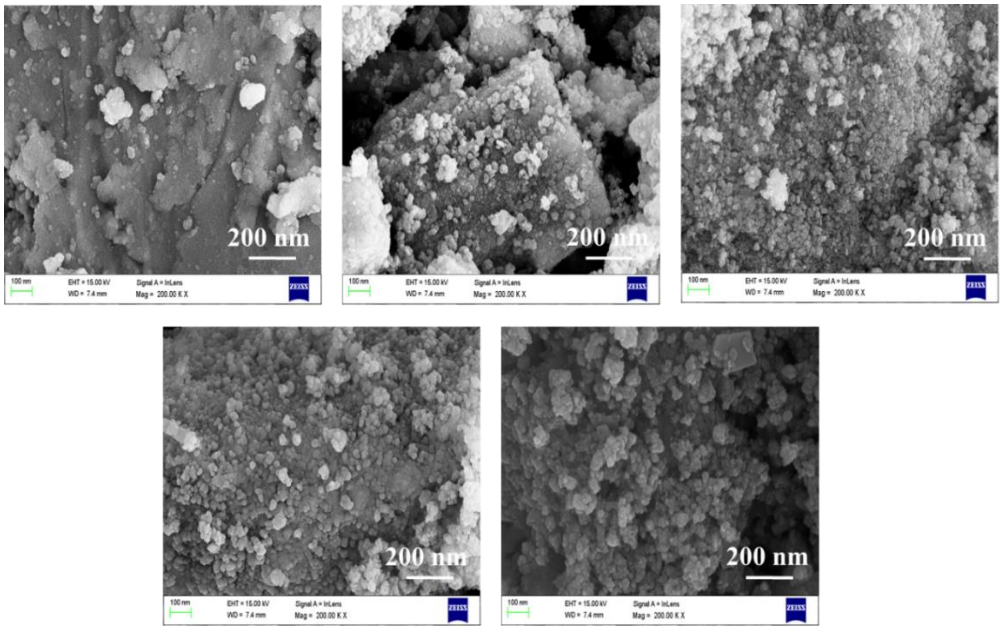

Fig. 3.15 FE–SEM images of CuO nanoparticles synthesized at **(a)** 10 mTorr **(b)** 20 mTorr **(c)** 30 mTorr **(d)** 40 mTorr and **(e)** 50 mTorr sputtering pressure.

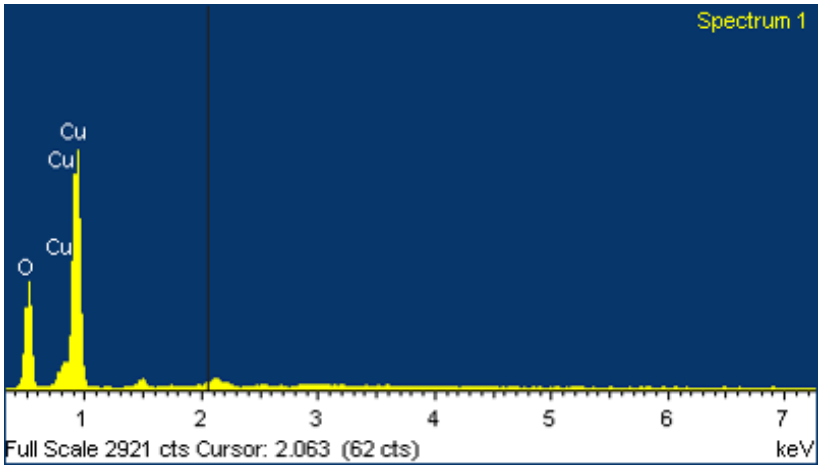

Fig. 3.16 EDS spectra of CuO nanoparticles.

The particle size and crystalline nature of CuO nanoparticles were again confirmed by TEM images and selected area electron diffraction (SAED), respectively. The TEM images (**Fig. 3.17**) clearly show well defined uniform spherical shape in partially aggregated form having narrow size distribution. The particle size increases from 6 nm to 13 nm with increasing sputtering pressure from 10 mTorr to 50 mTorr, which is in good agreement with the average crystallite size calculated from XRD. The SAED of the CuO nanoparticles synthesized at 10 mTorr sputtering pressure (**Fig. 3.18**) exhibits some concentric diffraction rings indicating the polycrystalline nature of the nanoparticles. These diffraction rings correspond to the (–111), (111), (–202), (202), (–113), (–311) and (113) planes, respectively, as observed in the powder XRD patterns and confirm the monoclinic phase of CuO nanoparticles. The HR–TEM image of CuO nanoparticles (**Fig. 3.19**) exhibits visible lattice fringes which reflect the crystalline nature of the nanoparticles. The interplanar spacing is nearly 0.252 nm which correspond to the (–111) planes of monoclinic CuO nanoparticles. The TEM results illustrate that the growth direction of synthesized CuO nanoparticles is along (–111) plane. The data obtained from XRD, FE–SEM, EDS, FT–IR, Raman and TEM analysis clearly indicate the formation of high purity CuO nanoparticles.

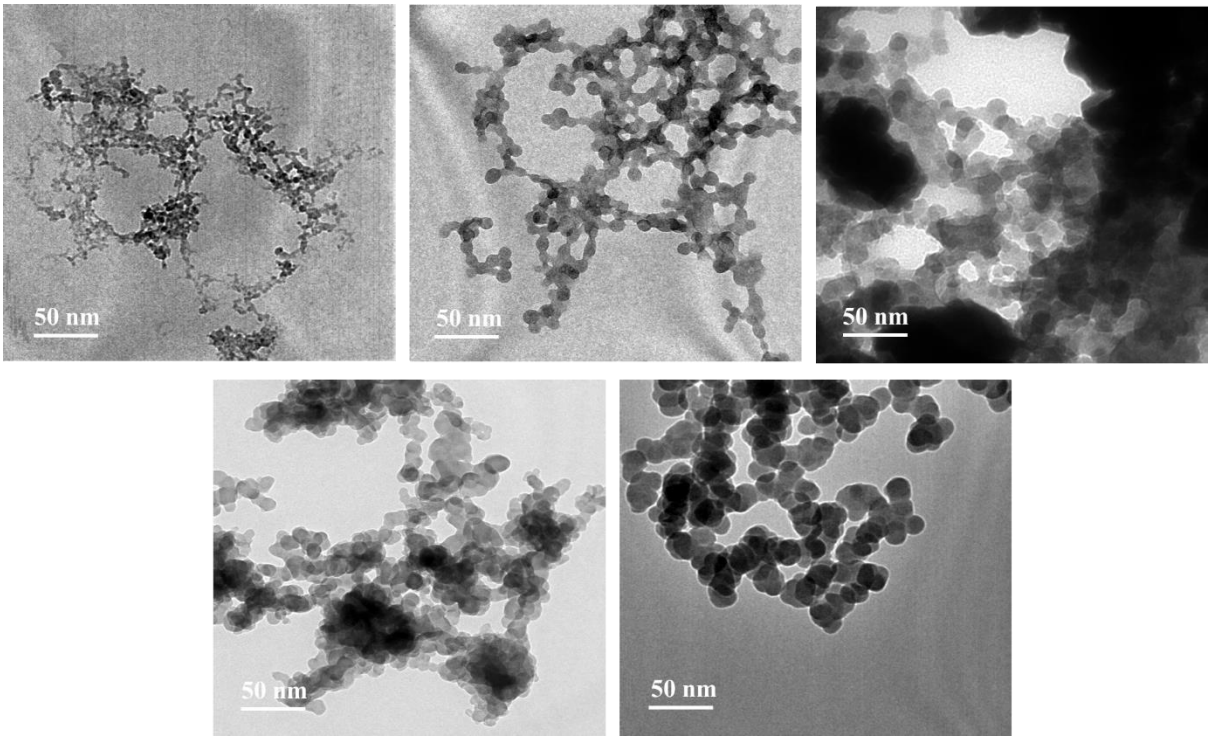

Fig. 3.17 TEM images of CuO nanoparticles synthesized at **(a)** 10 mTorr **(b)** 20 mTorr **(c)** 30 mTorr **(d)** 40 mTorr and **(e)** 50 mTorr sputtering pressure.

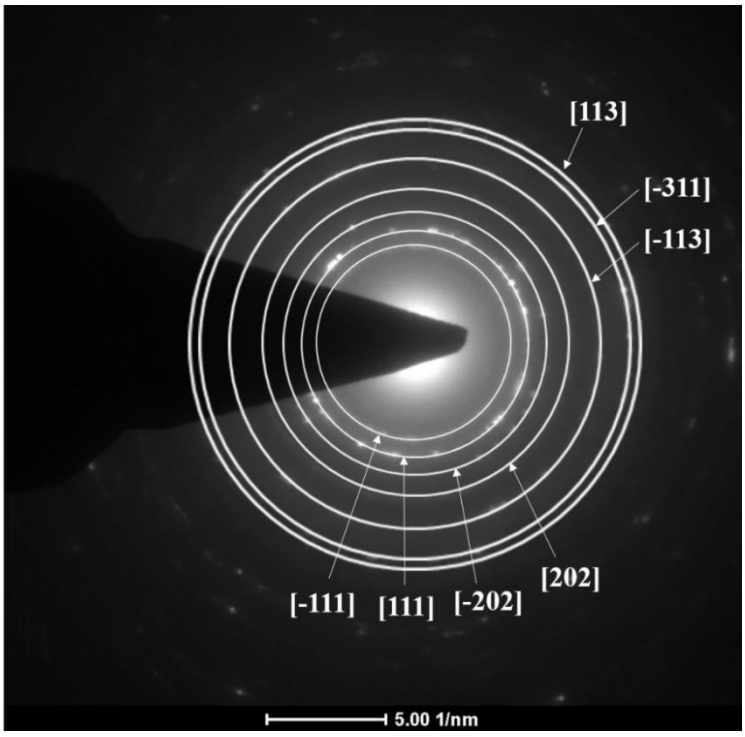

Fig. 3. 18 SAED pattern of CuO nanoparticles showing polycrystalline rings.

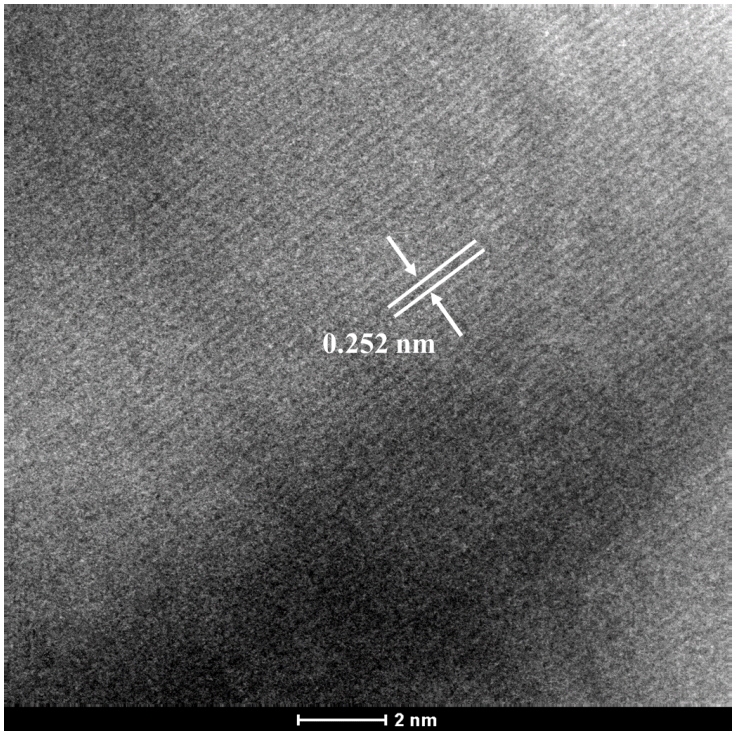

Fig. 3.19 HR–TEM image of CuO nanoparticle showing d–spacing corresponding to (–111) plane.

The nitrogen adsorption–desorption isotherm and the pore size distribution of CuO nanoparticles is shown in **Fig. 3.20**. Nitrogen adsorption–desorption isotherms show hysteresis loop which resembles to type III IUPAC (International Union of Pure and Applied Chemistry) and the pore size distribution (inset in **Fig. 3.20**) shows the Mesoporous nature, centred at 3.42 nm. The BET surface area and total pore volume calculated by BJH method are 84.32 m^2/g and 0.209 cm^3/g, respectively.

The TG pattern of CuO nanoparticles (**Fig. 3.21**) shows that the weight loss up to 200 ºC is due to loss of physisorbed water (0.87%), while, above this temperature (up to 750 ºC) a very small amount of weight loss (0.65%) was observed due to dehydroxylation. The TG pattern shows that the weight loss was only due to physisorbed water/hydroxyl group present over the surface of nanoparticles.

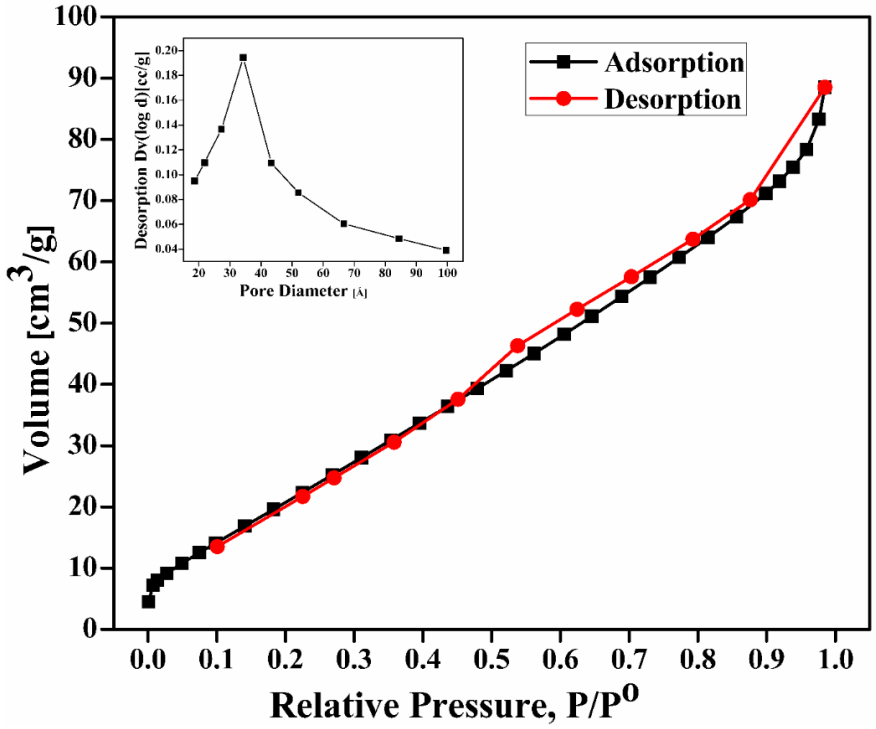

Fig. 3.20 Adsorption–desorption isotherm of CuO nanoparticles and insets show pore size distribution of nanoparticles.

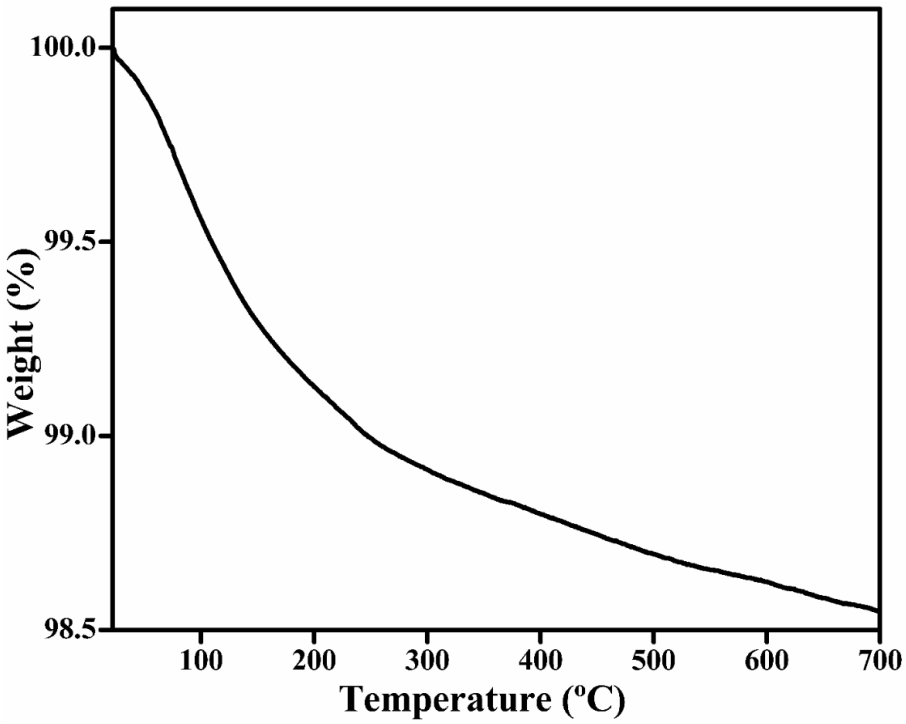

Fig. 3.21 TG pattern of CuO nanoparticles.

3.3.3 Conclusion

The CuO nanoparticles have been successfully synthesized using reactive magnetron sputtering technique at various sputtering pressure and then characterized through XRD, Raman spectroscopy, FE–SEM, TEM etc. This synthesis technique provides nanoparticles with high purity, narrow size distribution and having high surface area (84.32 m^2/g). The XRD results show that the nanoparticles are purely crystalline having monoclinic phase and the average crystallite size was found to increase from 6 nm to 13 nm with increasing sputtering pressure from 10 mTorr to 50 mTorr. FE–SEM and TEM results suggest the formation of aggregated small particles with a mean diameter of 6 nm to ~13 nm which are in good agreement with the XRD data. Raman spectra confirmed the monoclinic phase of synthesized nanoparticles. The observation of higher surface area of synthesized CuO nanoparticles make it potential candidate for water purification application.

CHAPTER 4

SYNTHESIS AND CHARACTERIZATION OF WO_3 NANOPARTICLES

4.1 Introduction

In this chapter we are discussing about the decontamination ability of WO_3 nanoparticles. Inorganic metal oxide nanomaterials indicate intriguing adsorption and chemical reactivity towards chemical warfare agents (CWA) **[215, 228]**. They possess high surface area, high adsorption capacity, large number of reactive functional groups and reactive morphology which facilitate superior decontamination capacity towards CWAs and environment pollutants **[229], [230]**. The higher surface area possess great interest to decontaminate the CWA by adsorption and decomposition (chemical degradation) approach.

Sulphur mustard (HD) and sarin (GB) are the well known CWA which have been detoxify time to time using different decontaminant such as bleaching powder, DS2 solution, other chemicals such as o-iodo benzoic acid, peroxides, oximes, chloramines, beta cyclodextrin and stopped on metal oxides materials. A number of various nanosized metal oxides such as MgO, CaO, Al_2O_3, ZnO, MnO_2 nanobelts, $V_{1.02}O_{2.98}$ nanotubes possess enhanced chemical reactivity towards CWAs including HD and GB and their simulants **[111, 113, 155, 231, 232]**. These metal oxides play an active role to decontaminate CWAs through hydrolysis, elimination and oxidation reactions on the surface of nanomaterials. Inspired by these results, we have chosen newer material having high adsorption capacity to degrade CWAs with in few hours of duration.

In the present work we have chosen tungsten oxide (WO_3) nanomaterials. WO_3 nanoparticles have been synthesized using different methods such as sol–gel, precipitation, thermal decomposition, and hydrothermal process **[233–236]**. Over the chemical synthesis route, physical vapor deposition (PVD) such as magnetron sputtering holds distinguishes advantages such as high purity, reproducibility, uniformity and narrow size distribution **[237]**. Hence, WO_3 nanoparticles was synthesized using DC magnetron sputtering technique under optimized conditions for the removal and detoxification of CWA. Also, studied the power effect on structural and thermal properties of WO_3 Nanoparticles synthesized through sputtering.

4.2 Synthesis of magnetron sputtered WO_3 nanoparticles–degradation of 2-chloro ethyl ethyl sulphide and dimethyl methyl phosphonate

4.2.1 Synthesis of WO_3 nanoparticles

Tungsten oxide nanoparticles have been synthesized in a 12″ diameter custom designed vacuum chamber (Excel Instrument, Mumbai). The chamber consists of various ports to accommodate sputtering gun, copper cold finger arrangement to cool the substrate with liquid nitrogen (Liq–N_2), gas line, glass window and a scraper for collecting the particles from the substrate. Sputtering was carried out using tungsten target of 2″ diameter and 5 mm thickness. The chamber was initially evacuated to 10^{-7} torr using a turbo molecular pump backed by rotary pump. Thereafter, an optimum working pressure was maintained in the sputtering chamber with argon and oxygen gas in a specific ratio. Before acquiring the working pressure, the hollow copper cold finger was continuously filled up with liquid nitrogen (liq–N_2) to cool the substrate to ≤ –194 ºC (79 K). During sputtering, liq–N_2 was also continuously filled up in the copper cold finger to maintain the desired substrate temperature. The reason for keeping low substrate temperature is to inhibit the grain growth in the plane of the film leading to production of nanoparticles. Also, contamination due to the possible diffusion of atoms from the substrate with the deposited material is minimized at lower temperature. During sputtering the W atoms were sputtered from the target and react with the oxygen atoms in chamber or on the copper cold finger substrate during deposition and form WO_3 nanoparticles. The nanoparticles were scratched carefully at room temperature (25 ºC) and then crushed in a pestle mortar to homogenize. The nanoparticles were annealed in air at temperature range of 200–500 ºC for 3 h. **Table 4.1** lists the sputtering parameters used for the synthesis of WO_3 nanoparticles.

Table 4.1 Sputtering parameters for the synthesis of WO_3 nanoparticles.

Target	Base Pressure	Working Pressure	Gas Used	Deposition Time	Distance (d)	Power (Watt)	Substrate Temp.	Annealing Temperatures
W	4.7×10^{-7}Torr	30 mTorr	Ar:O_2 ::40:10	16 h	5 Cm	80 W	-194 ºC	As-deposited, 200, 300, 400, 500 ºC

d = Distance between target and substrate.

4.2.2 Reaction procedure of decontamination

The reaction of CEES or DMMP was carried out on the surface of WO_3 nanoparticles to understand the decontamination capacity of the synthesized material. For this purpose, 100 µl solution of dichloromethane (DCM) having 5 µl of CEES was added to 100 mg WO_3 nanoparticles in seven separate test tubes of equal size and then stirred for two minutes to ensure uniform mixing. The DCM was used to facilitate the uniform distribution of agent molecules (CEES or DMMP) within the bulk powder. The remaining agents were extracted with the help of acetonitrile within a time interval of 1 h, 2 h, 4 h, 6 h, 8 h, 16 h and 24 h to study the kinetics of degradation. The remaining agents were extracted by using 5.0 ml of acetonitrile for five times (each time 1 ml) in order to complete extraction. Extracted solutions were quantitatively analyzed by gas chromatograph equipped with flame ionization detector in the programming mode from 120 to 250 ºC at a rate of 10 ºC/min by calibrating the concentrations. The injection port and detector port were kept at 240º and 250 ºC, respectively. The concentration of extracted solutions was calibrated with standard solutions for accurate quantification. The experiments were repeated more than six times in order to ensure the accuracy of the kinetics results.

4.2.3 Results and Discussion

4.2.3.1 Characterization of WO_3 nanoparticles

Fig. 4.1 shows the XRD patterns of as-deposited and annealed WO_3 nanoparticles. The XRD patterns show that crystallinity of the WO_3 nanoparticles increased with increasing the annealing temperature. The XRD peaks of as-deposited and annealed (at 200 ºC) nanoparticles have large full width at half maxima (FWHM) resulting overlap of peaks and hence nanoparticles exhibited XRD amorphous nature. On the other hand as the annealing temperature increased to 300 ºC and above, the peaks are clearly separated due to increased crystalline nature of WO_3 nanoparticles. The higher crystallinity indicates the smaller FWHM and increment in particle size. It was observed that the nanoparticles show monoclinic phase (JCPDF file no. 01–072–0677) with (002), (020) and (200) preferred crystallographic orientation of the peaks at 23.08, 23.58 and 24.32º of 2θ values, respectively. However, at 400 ºC, one additional peak was found at 24.08º and assigned to (303) plane of $W_{20}O_{58}$ (JCPDF file no. 00–005–0386). The average crystallite size of the annealed nanoparticles was calculated

using Debye-Scherer formula. It has been observed that the particle size of WO_3 nanoparticles increased (9 to 47 nm) with annealing temperature. Maximum size (~47 nm) nanoparticles were obtained after annealing at 500 ºC in open atmosphere. No other XRD peak due to any impurity was observed from the XRD pattern and which clearly indicates the formation of high purity WO_3 nanoparticles.

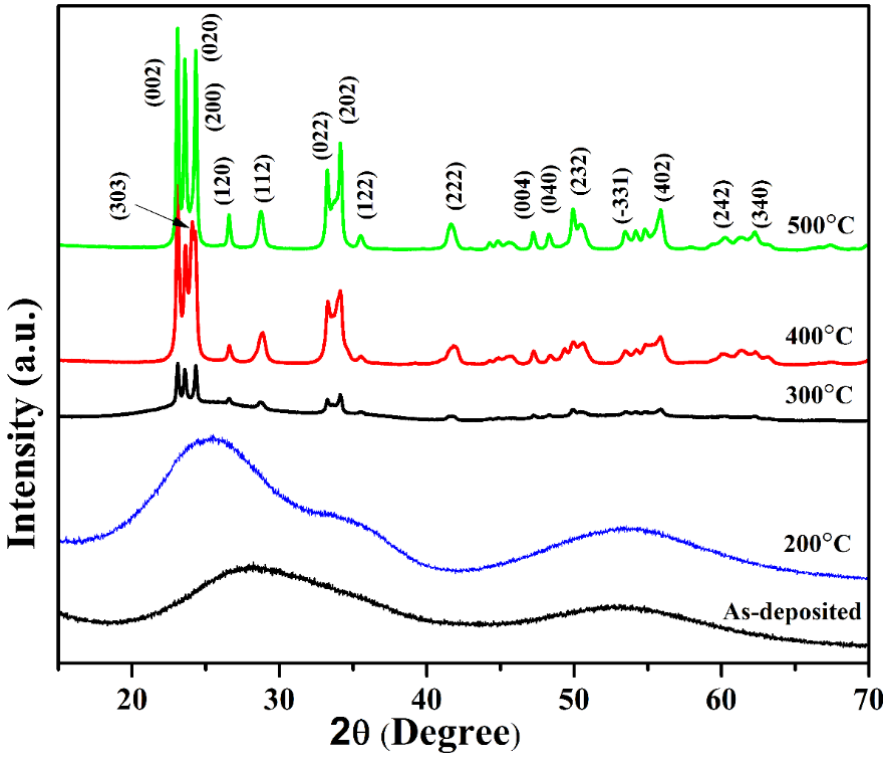

Fig. 4.1 XRD patterns of WO_3 nanoparticles.

To confirm the structure phase of as–deposited nanoparticles Raman spectrum was carried out as shown in **Fig. 4.2**, clearly indicate that WO_3 nanoparticles have two regions at 200–400 and 600–900 cm^{-1}. The Raman peaks observed at lower wave numbers 260 and 325 cm^{-1} indicating the bending modes of O–W–O. The higher wave number peaks at 707 cm^{-1} is due to O–W–O vibration and 804 cm^{-1} is corresponding to crystalline WO_3 stretching vibration mode of bridging oxygen of W–O–W. These two peaks clearly attributes to the formation of monoclinic phase of WO_3 nanoparticles **[238, 239].**

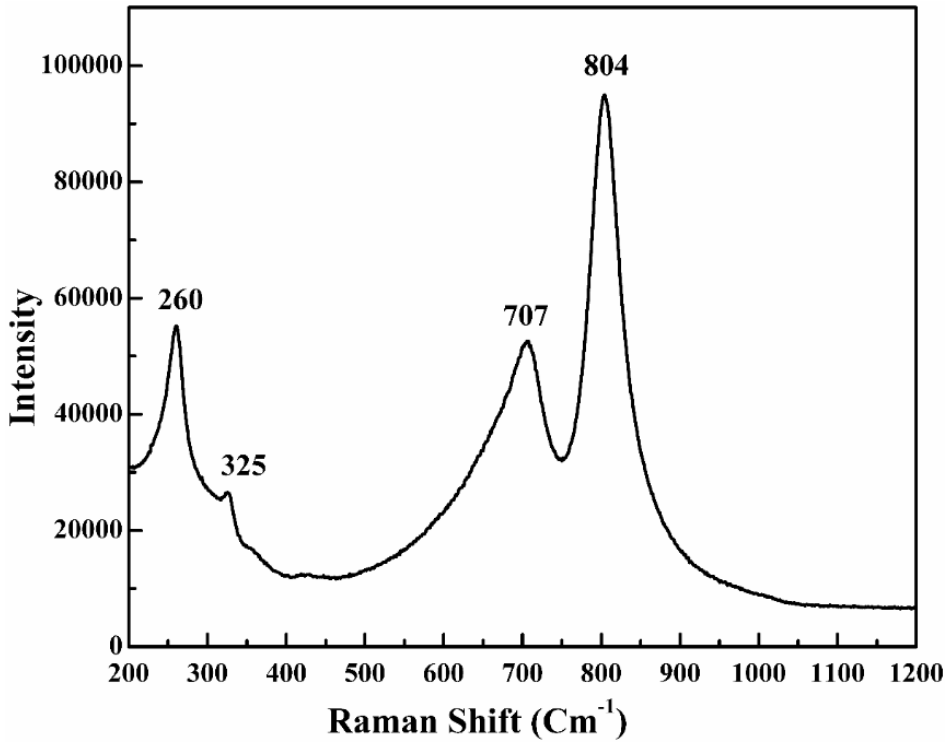

Fig. 4.2 Raman Spectra of as−deposited WO_3 nanoparticles.

Fig. 4.3 represents the FE−SEM images of as−deposited and annealed WO_3 nanoparticles. It has been observed from FE−SEM images that the annealed nanoparticles are less agglomerated as compare to as−deposited WO_3 nanoparticles. Moreover, the particle size and size distribution of WO_3 nanoparticles increases continuously with increasing annealing temperature from 200 to 500 ºC. The increase in particle size with annealing temperature is attributed to the merging of grains and smaller nanoparticles into neighbouring bigger particles **[240, 241].**

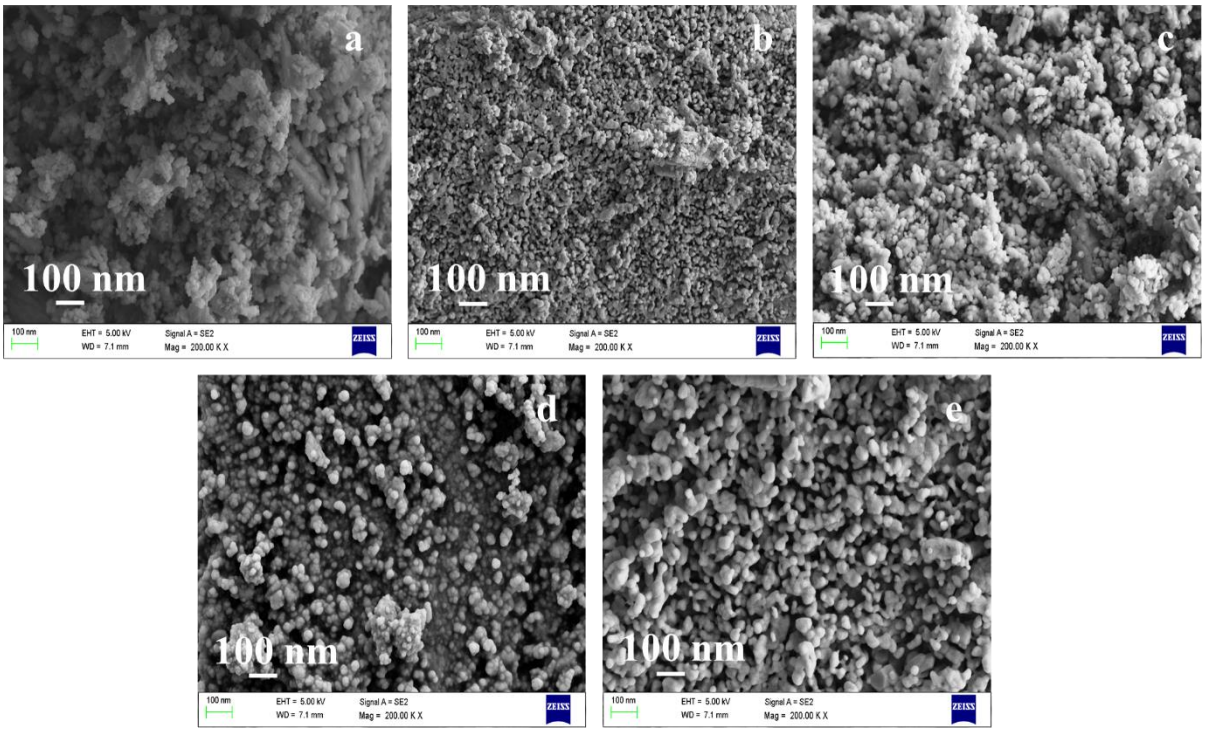

Fig. 4.3 FE–SEM images of tungsten oxide nanoparticles **(a)** as–deposited and annealed at **(b)** 200 ºC **(c)** 300 ºC **(d)** 400 ºC and **(e)** 500 ºC.

The EDS spectra of as–deposited WO_3 nanoparticles is shown in **Fig. 4.4**. Spectra clearly reveal that WO_3 nanoparticles are in the proper stoichiometric ratio of W and O towards 1 : 3. The Au and C signals are coming due to gold coating and double sided tape used during the EDS analysis. No other elements can be detected which indicate the synthesis of high purity WO_3 nanoparticles.

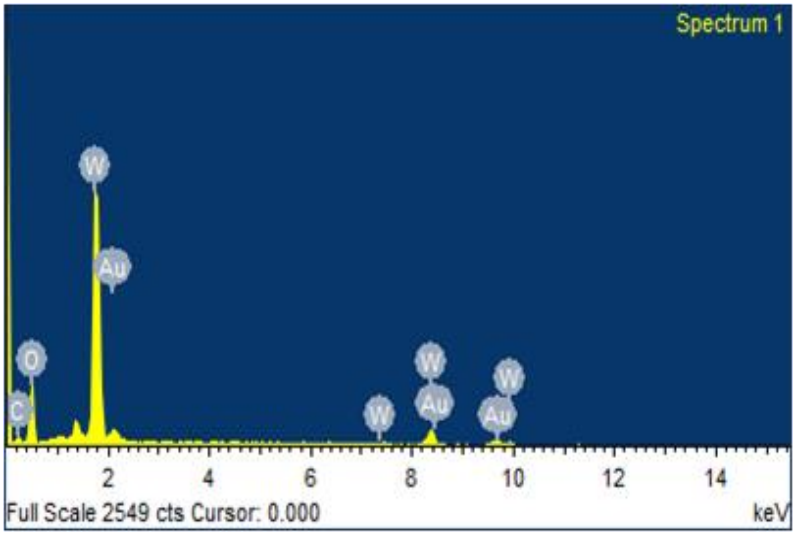

Fig. 4.4 EDS spectra of as–deposited WO_3 nanoparticles.

Fig. 4.5 shows the TEM images of the as-deposited and annealed WO_3 nanoparticles. The TEM images indicate the spherical type morphology of WO_3 nanoparticles. **Table 4.2** lists the size of nanoparticles as calculated from TEM images. It is clear that the particle size increases as the annealing temperature raised from 200 to 500 ºC.

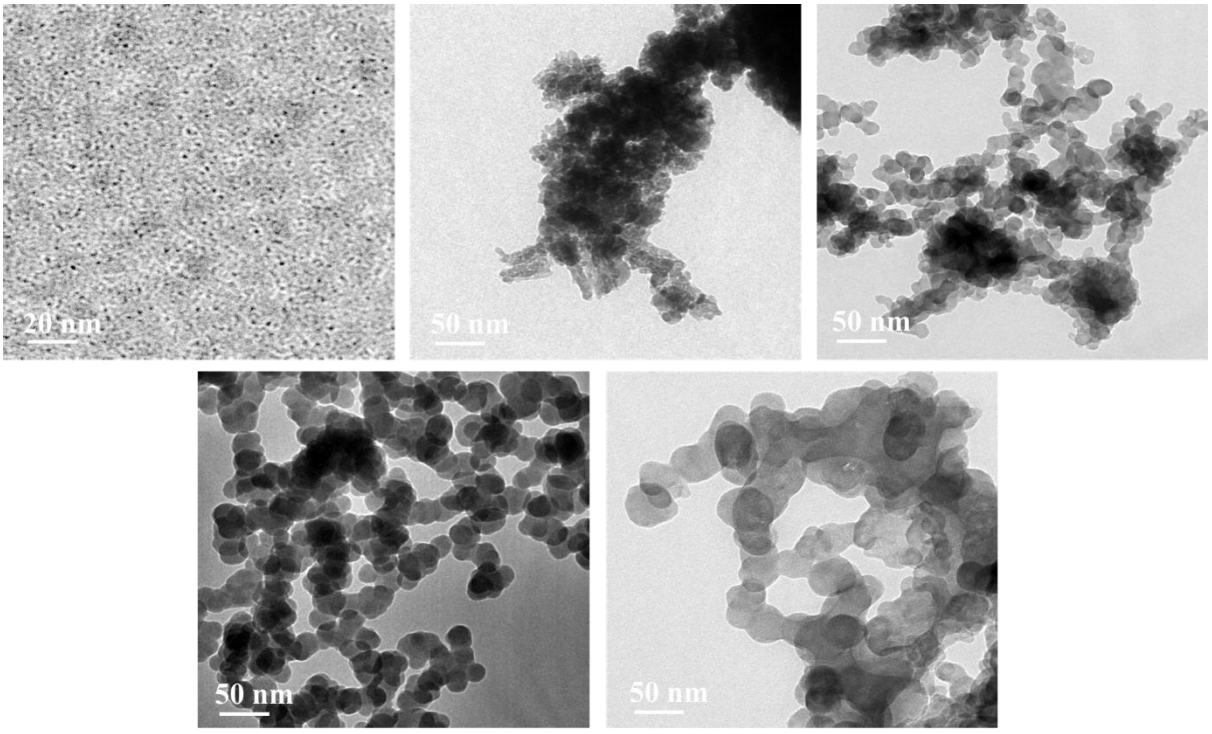

Fig. 4.5 TEM images of WO_3 nanoparticles **(a)** as–deposited and annealed at **(b)** 200 ºC **(c)** 300 ºC **(d)** 400 ºC and **(e)** 500 ºC.

Table 4.2 Particle size, surface area, and pore volume of WO_3 nanoparticles of as–deposited and annealed at different temperatures.

	Annealing temperature of WO_3 (ºC)				
	As–deposited	**200**	**300**	**400**	**500**
Particle size	2	9	21	36	47
Surface area (m^2/g)	63.22	54.90	50.89	40.28	33.28
Pore volume (ml/g)	0.128	0.118	0.111	0.101	0.082

The selected area electron diffraction (SAED) of the as-deposited WO_3 nanoparticles is shown in **Fig. 4.6**. The ring patterns appeared for as–deposited nanoparticles clearly indicate

that the nanoparticles are highly polycrystalline with principally rings of (002), (120), (122) and (222) which match very well with the XRD results of WO_3 nanoparticles. Thus XRD, Raman, FE–SEM, EDS and TEM analyses clearly indicate the formation of monoclinic phase WO_3 nanoparticles with high purity and narrow size distribution.

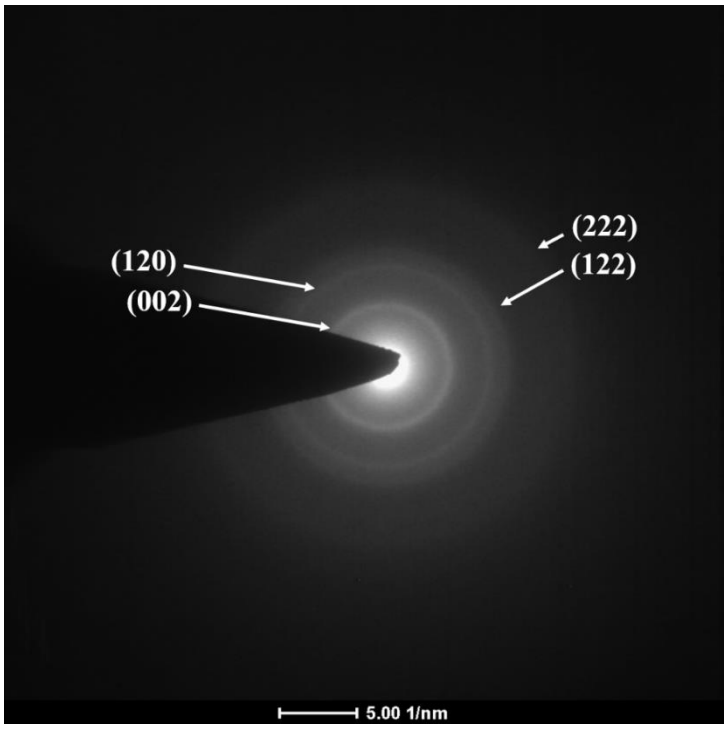

Fig. 4.6 SAED pattern of as–deposited WO_3 nanoparticles showing polycrystalline rings.

The surface area and pore size distribution of WO_3 nanoparticles were carried out by using Brunauner–Emmet–Teller (BET) and Barrett–Joyner–Halenda (BJH) methods, respectively. **Fig. 4.7** represents the N_2 adsorption–desorption isotherm of type IV and **Fig. 4.8** shows the pore size distribution of as–deposited WO_3 nanoparticles. The obtained values of surface area and the pore volume of all the samples are given in **Table 4.2**. The obtained surface area (63.22–33.28 m^2/g) of the magnetron sputtered WO_3 nanoparticles was found to be significantly higher compare to the reported surface area (1.93–16.45 m^2/g) of WO_3 nanoparticles synthesized using different methods **[242–244]**. WO_3 nanoparticles consist of pores in the range of mesopores as depicted by pore size distribution values (**Fig. 4.8**). The calculated values of pore volume lie in the range of 0.1285–0.0821 cm^3/g. The data clearly indicate that as the annealing temperature increases from 200 to 500 ^oC, both surface area and pore volume are decreases. These results are consistent with the reported data **[243]**.

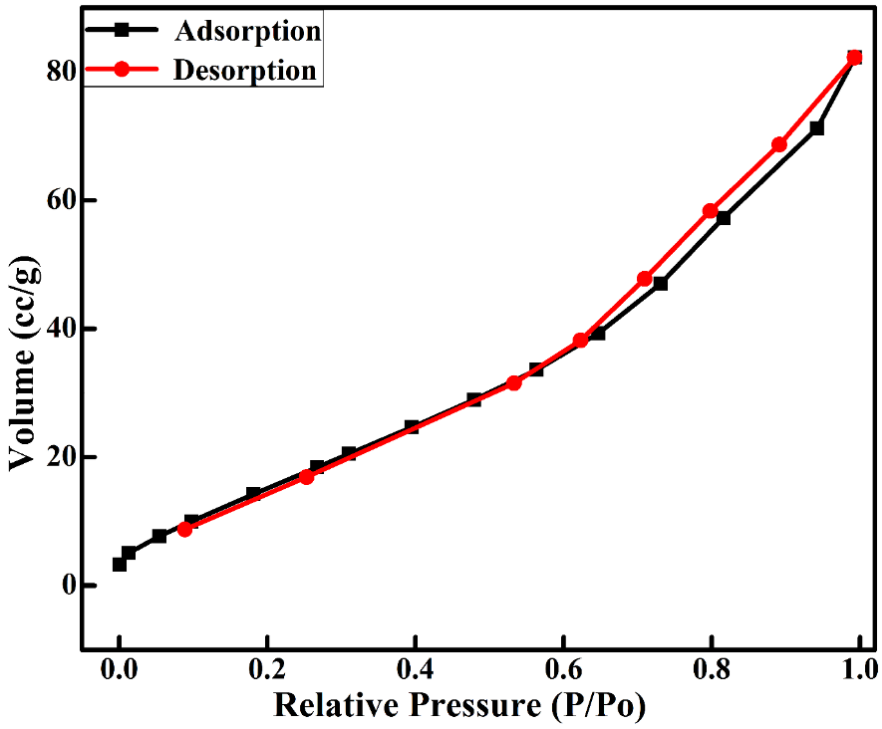

Fig. 4.7 Adsorption–desorption isotherm of as-deposited WO_3 nanoparticles.

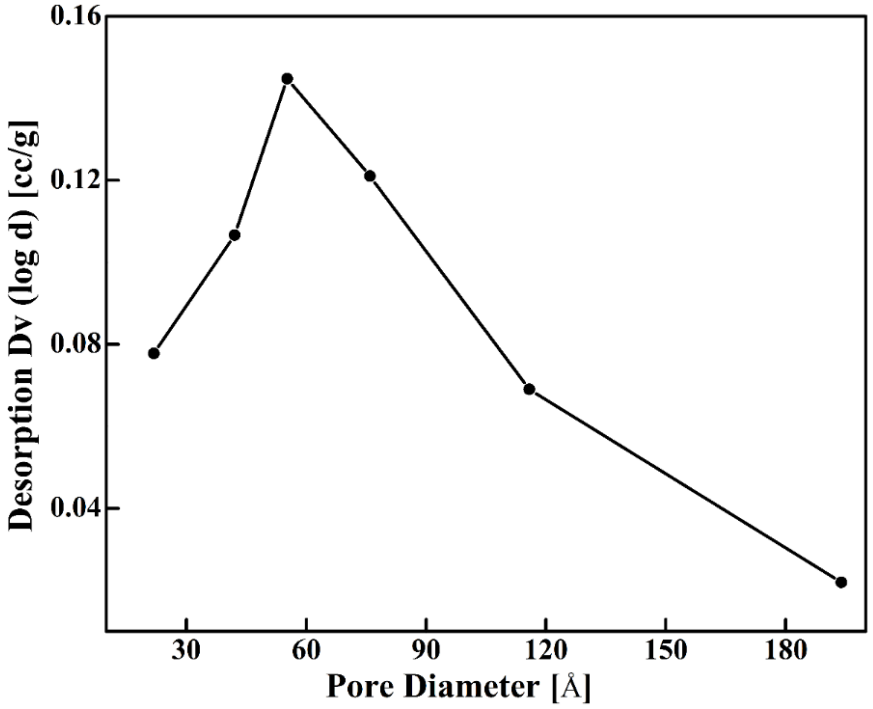

Fig. 4.8 BJH pore size distribution of as–deposited WO_3 nanoparticles.

4.2.3.2 Kinetics of CEES and DMMP decontamination

In order to understand the kinetics of CEES degradation, the WO_3 nanoparticles of different sizes were exposed CEES for a period of 24 h. The concentration of the unreacted CEES was extracted from the reaction mixture by using acetonitrile at a specific interval of time. The concentration of unreacted CEES was find out by GC–FID. Subsequently the obtained kinetics data were plotted by taking the concentration on Y−axis and time on X−axis. Smooth curves occur in the exponential decreasing order of CEES with time for all reaction (not shown here). Whereas linear plots observed by taking the log of unreacted CEES on Y−axis and time on X−axis, depicting the pseudo first order kinetics as shown in **Fig. 4.9** and results are consistent with the reported data **[142, 245]**. The kinetic plots indicate that the concentration of CEES for all the samples decreases with time. Also, kinetic reaction seems to be fast in the initial stage and a study state occur at the later stage of the reaction. The values of rate constant and half life were lie in the range of 0.143–0.109 h^{-1} and 4.82–6.49 h, respectively shown in **Table 4.3**. DMMP also reacted in a similar way indicating the exponential decrease of concentration with time (not shown here) and linear curves as shown in **Fig. 4.10**. The values of rate constant (k) and half life ($t_{1/2}$) were found to be in the range of 0.018–0.010 h^{-1} and 36.87–66.65 h, respectively for all samples as shown in **Table 4.3**. The above data clearly indicate that the reactivity of WO_3 nanoparticles towards DMMP exhibited pseudo first order kinetics behaviour **[113]**. From the GC data it is clearly revel that CEES and DMMP degrade 98 and 53.4% on the surface of as−deposited and it decreases up to 91.8% and 40.7% as the particle size increases after annealing. The fast initial reaction is probably due to rapid adsorption and distribution of the liquid within the pores and its interaction with the accessible reactive sites and hydroxyl groups. When the sites are exhausted, the limited surface reaction occurs obviously, replacing the initial fast reaction by the steady state reaction **[138, 150]**. The values of the rate constant (k) and half life ($t_{1/2}$) of the degradation of CEES and DMMP on the surface of WO_3 nanoparticles of different sizes were calculated by using the first order rate equation i.e. k = 2.303×slope and 0.693/(2.303×slope) respectively and are given in **Table 4.3**.

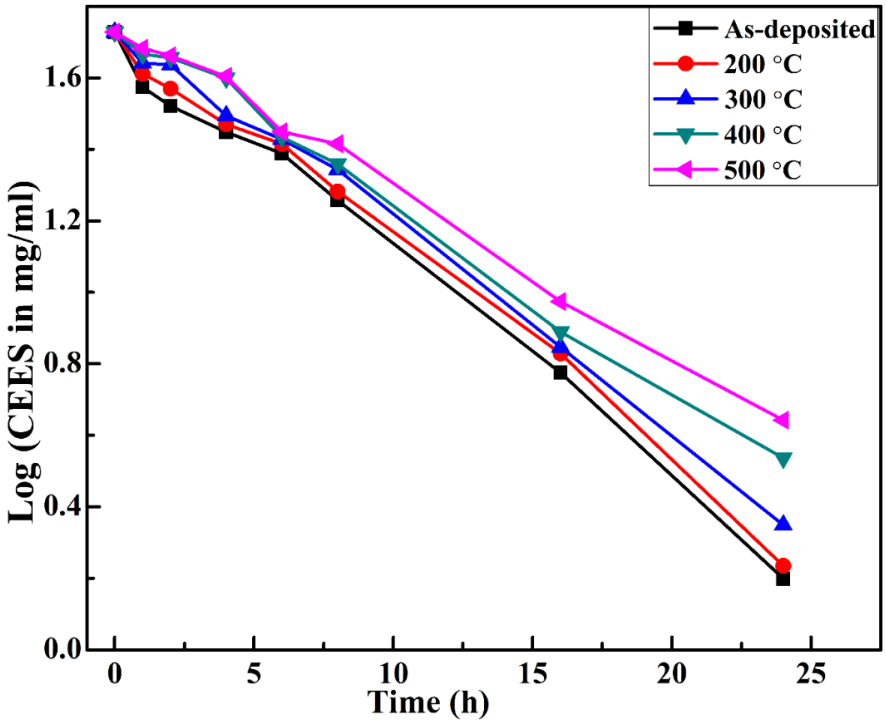

Fig. 4.9 Kinetics of degradation of CEES on the surface of WO_3 nanoparticles.

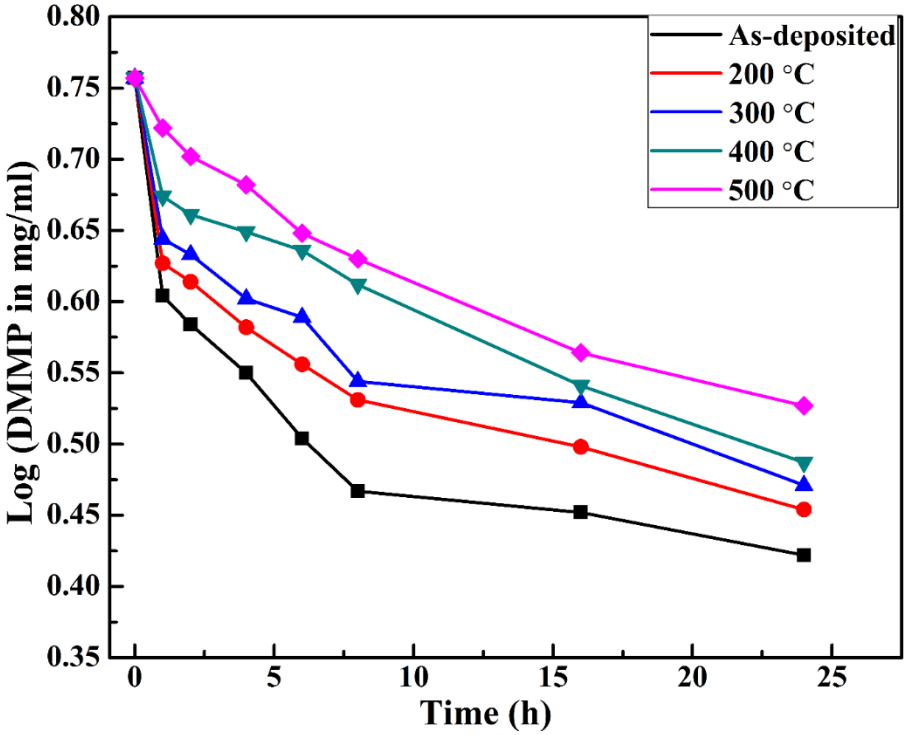

Fig. 4.10 Kinetics of degradation of DMMP on the surface of WO_3 nanoparticles.

Table 4.3 Results of degradation of CEES and DMMP on the surface of different sizes WO_3 nanoparticles.

	Particle size of WO_3 nanoparticles (nm)				
	2	**9**	**21**	**36**	**47**
Kinetic rate constant, (K) h^{-1} of CEES	0.143	0.133	0.126	0.113	0.109
Half life ($t_{1/2}$) h of CEES	4.82	5.18	5.46	6.11	6.49
Kinetic rate constant, (K) h^{-1} of DMMP	0.018	0.015	0.013	0.011	0.010
Half life ($t_{1/2}$) h of DMMP	36.87	45.01	50.23	58.25	66.65

It is clear from the experimental results that the rate of degradation of CEES and DMMP decreases as the particle size increases i.e. smaller particles give high degradation efficiency compare to larger particles. The probable reason for the decrease in degradation rate is due to increase in the particle size is the surface area. The sputtered WO_3 nanoparticles possess higher surface area (~ 63–33 m^2/g) compared to previously reported WO_3 nanoparticles synthesized by others methods which lie in the range of ~1–16 m^2/g as given above. These higher surface areas seemed to have imparted more adsorption capacity towards CEES and DMMP. Due to large adsorption capacity of WO_3 nanoparticles, CEES and DMMP were found to be rapid adsorption followed by its distribution within their pores and react with the reactive sites of synthesized nanoparticles and convert them into non-toxic form. Also, decrement in the surface area with increasing particle size leads to reduction in the adsorption capacity. Gu et al. reported that variation in annealing temperature bought about change in surface structure and hence the surface acidic and redox properties **[222]**. Tang and co workers reported that degradation of CWAs was not only depends on the surface acidic and basic properties of metal oxides but also amount of adsorbed water **[157]**. The rate of degradation of CWA profited through hydrolysis reaction with increasing of water content i.e. positive effect of water found for degradation of CWAs. With increasing the annealing temperature, the particle size increases (agglomeration) as observed in FE-SEM and TEM studies due to which surface area of the synthesized material decreases. Literature also indicate that surface area decreases with

increasing annealing temperature due to further growth of particles **[137]**. Due to decrease in surface area with increasing particle size, the available active sites for the adsorption and the activation of the reactant decreases which in turn reduces the rate of degradation reaction.

No excess of water was added to the WO_3 nanoparticles, whatever moisture adsorbed from the atmosphere while transferring the samples along with other reactive functionalities seems to have facilitated the decontamination. The WO_3 samples were subjected to TGA in order to check the amount of water present on the surface of them. The TGA pattern of as–deposited WO_3 nanoparticles is shown in **Fig. 4.11**. It was observed that the moisture get entrapped into the WO_3 nanoparticles during expose to the atmosphere. From TGA graph, it is clear that WO_3 nanoparticles show weight loss 9.37% up to 250 ºC and no further weight loss was observed up to 800 ºC. This weight loss is only due to desorption of physisorbed water. Data also reveal that WO_3 nanoparticles of 2, 9, 21, 36, 47 nm sizes have a weight loss of 9.96, 7.09, 4.45, 1.73, and 1.63, percent respectively. So, it is clear that with increase in particle size through annealing temperature, the amount of physisorbed water/hydroxyl group on the surface of WO_3 nanoparticles decreases due to which weight loss decreases. The results are consistent with the reported results **[137]**.

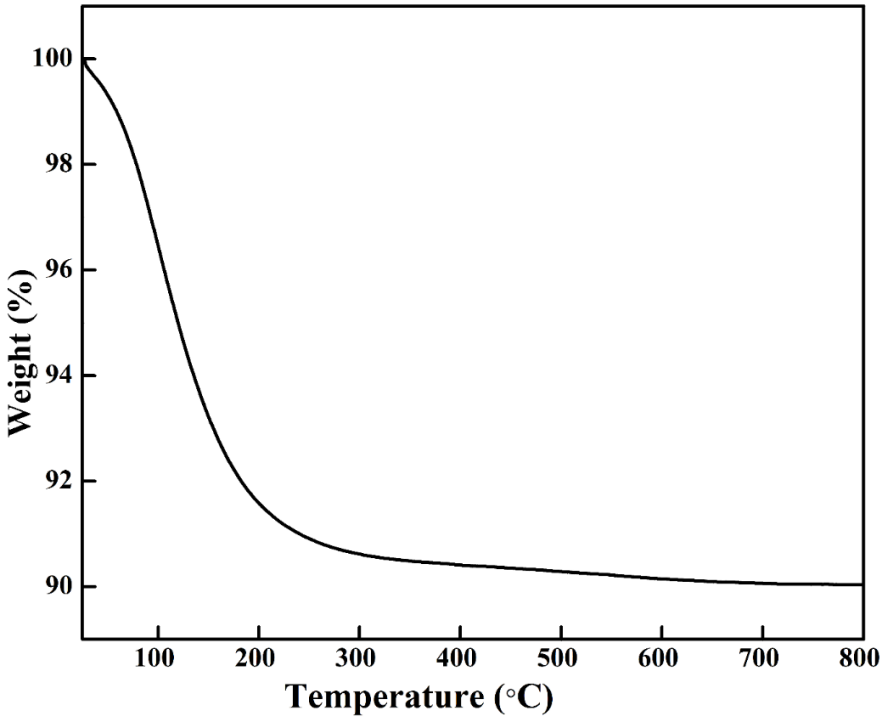

Fig. 4.11 TGA patterns of as-deposited WO_3 nanoparticles.

4.2.3.3 GC–MS analysis

The extracted reaction mixtures were analyzed using GC–MS and FT–IR in order to understand the reaction mechanism and the products formed during the degradation. Since hydrolysis products of CEES and DMMP have polar and non-volatile nature due to which they were derivatised before GC–MS analysis. For all the samples, GC–MS data indicates the m/z values at 178, 163, 103, 89, and 73. These m/z values clearly reveal the formation of hydrolysis product of CEES i.e. hydroxyl ethyl ethyl sulphide (HEES), emphasizing the role of WO_3 nanoparticles in hydrolysis reaction for decontamination CEES to HEES thereby rendering them to non-toxic form. Moreover, FT–IR data for all the samples that were exposed to CEES reveal that the band intensity at 700cm^{-1} of C–Cl disappeared and, change of peak pattern at around 1440 and 1295 cm^{-1} of (CH_2–Cl) occur. Another one peak occur of small increase in intensity at 3411 cm^{-1} of (–O–H). These observations confirm the hydrolysis of CEES on the surface of WO_3 nanoparticles and formation of HEES.

Based on the above GC–MS and FT–IR data, the reaction mechanism for the decontamination of CEES on the surface of WO_3 nanoparticles is proposed in **Fig. 4.12**. According to the above scheme, CEES molecules reacted with WO_3 nanoparticles in two ways. In one way, they reacted with physisorbed or intercalated waters molecules which were present on the surface of WO_3 nanoparticles to form HEES in which cyclic sulphonium ion seemed to be formed as shown in **Fig. 4.12** This cyclic sulphonium ion is formed due to attack of sulphide on the β carbon atom of CEES and is considered as SN1 reaction. Since sulphonium ion is highly unstable due to which it could not be extracted out and detected by GC **[33]**. Subsequently sulphonium ion undergoes hydrolysis reaction with water molecules adsorbed by WO3 nanoparticles (no more water was added to the reaction) giving rise to the formation of HEES. In second way, CEES molecules reacted with isolated hydroxyl group (W–OH) and Lewis acid (W^{6+}) sites to form surface bound alkoxy species. The mechanism and results are consistent with the previously reported results **[113, 155]**.

Subsequently, formation of silylated hydrolysis product of DMMP i.e. methyl phosphonic acid (MPA) (m/z = 240, 225, 194, 147, 133, and 73), emphasized the role of hydrolysis reaction in the decontamination of DMMP to form non–toxic product. In addition to this, in FT–IR data, the bands present at 1275 cm^{-1} (P=O) and 1020 cm^{-1} (P–O–C) of DMMP disappeared. One band at 1234 cm^{-1} indicates the interaction of P=O with the surface

functional group of WO_3 nanoparticles. Another peak occurs at 3411 cm^{-1} indicating the presence of –OH group. These observations confirm the formation of MPA on the surface of WO3 nanoparticles surface through hydrolysis reaction.

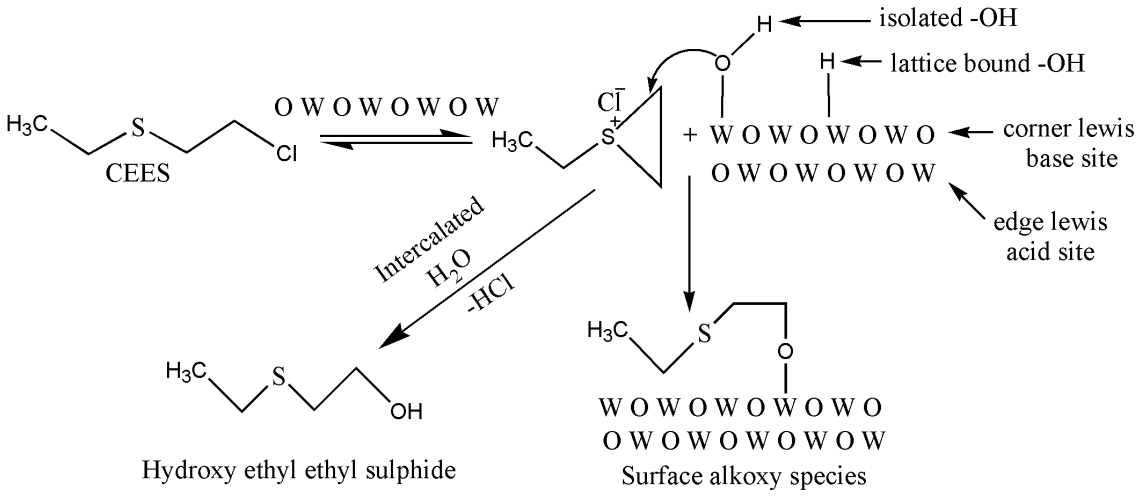

Fig. 4.12 Reaction scheme of CEES occurring on the surface of WO_3 nanoparticles.

Based on the GC–MS and FT–IR data, the reaction mechanism for the degradation of DMMP on the surface of WO_3 nanoparticles is proposed in **Fig. 4.12**. As per this, DMMP molecules reacted with similar way as in case of CEES. In one way they reacted with physisorbed or water molecules to form MPA (non-toxic products) and in another way, they reacted with isolated hydroxyl group (W–OH) and Lewis acid (W^{6+}) sites to form surface bound phosphonates. The mechanism and results are consistent with the previous reported data **[111, 113, 246]**. Overall hydrolysis reactions occur on the surface of WO_3 nanoparticles with formation of surface bound alkoxy or surface bound phosphonates which facilitated the decontamination of CEES and DMMP and rendering them non-toxic. Collectively, the WO_3 nanoparticles synthesized by magnetron sputtering offer large values of surface area which facilities faster adsorption and encapsulation of CEES and DMMP, physisorbed waters, isolated hydroxyl group, Lewis acid (W^{6+}) sites to make toxic agents as non–toxic. The currently synthesized sputtered WO_3 nanoparticles give better reaction rate constant values than earlier reported sorbent decontaminants such as Fullers earth, mesoporous MnO_2, V_2O_3 nanotubes etc. **[113, 138]**. These materials exhibited relatively lower reactivity towards CEES and decontaminate it less than 90% with rate constant (k) values ~0.02–0.026 h^{-1} in comparison to the presently synthesized WO_3 nanoparticles which degraded CEES up to 98% with rate constant (k) values 0.143–0.109 h^{-1}. Also, in case of DMMP, WO_3 nanoparticles

presently synthesized give effective rate constant (0.188–0.0104 h^{-1}) than reported earlier using activated carbon (0.008–0.020 h^{-1}) **[246]**. These results clearly showed that, sputtered WO_3 nanoparticles give superior results compare to existing solid decontaminants.

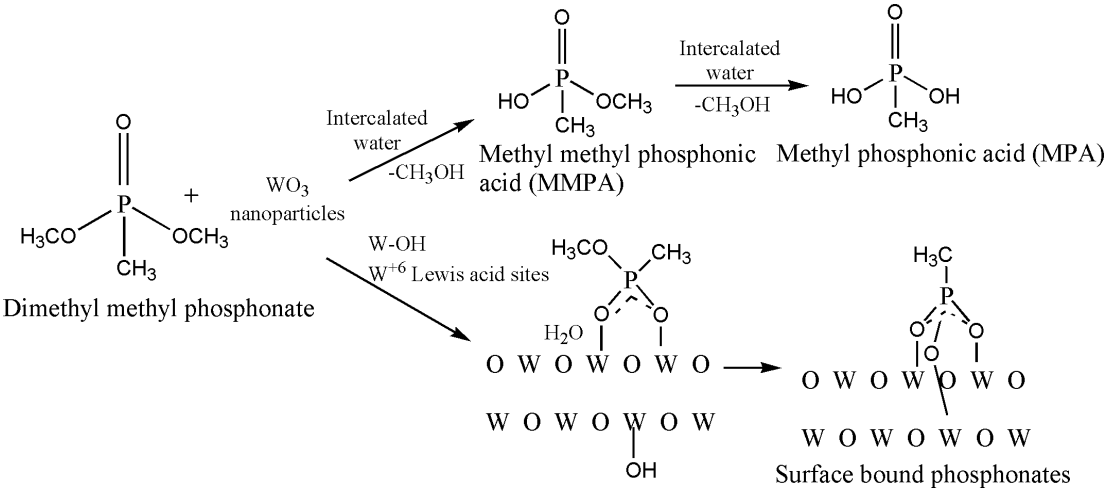

Fig. 4.13 Reaction scheme of DMMP occurring on the surface of WO_3 nanoparticles.

4.2.4 Conclusion

The decontamination of CEES and DMMP over various sizes WO_3 nanoparticles have been studied in the present work. The WO_3 nanoparticles have been synthesized using magnetron sputtering technique. Thereafter, they were annealed at different temperatures to vary the particle size. This novel PVD technique provides WO_3 nanoparticles of high purity with a narrow size distribution and high surface area. Due to these advantages, DC sputtered WO_3 nanoparticles show enhanced decontamination of CEES and DMMP over earlier studied existing solid decontaminants such as Fullers earth, mesoporous MnO_2, V_2O_3 nanotubes and activated carbon etc. The decontamination reactions exhibited pseudo first order steady state (predominantly hydrolysis) with rate constant (k) and half life ($t_{1/2}$) values 0.143–0.109 h^{-1} and 4.82–6.49 h for CEES and 0.018–0.010 h^{-1} and 36.87–66.65 h for DMMP with increase in particle size, respectively. The magnetron sputtered WO_3 nanoparticles (as–deposited and annealed) give superior decontamination results compare to reported literature. Among various WO_3 nanoparticles, as–deposited show better decontaminating results over the annealed nanoparticles. The future work will focus on the decontamination of other CWA simulants and

photocatalytic application of these nanoparticles synthesized using DC magnetron sputtering process.

4.3 Power effect on structural and thermal properties of magnetron sputtered WO_3 Nanoparticles

4.3.1 Synthesis of WO_3 nanoparticles

Copper oxide nanoparticles have been synthesized in a 12″ diameter custom designed vacuum chamber (Excel Instrument, Mumbai). The chamber was initially evacuated to 10^{-7} torr using a turbo molecular pump backed by rotary pump. Thereafter, an optimum working pressure was maintained in the sputtering chamber, with argon and oxygen gas in a specific ratio. Before acquiring the working pressure, the hollow copper cold finger was continuously filled up with liquid nitrogen (Liq–N_2) to cool the substrate to ≤ −194 ºC (or 79 K). During sputtering the W atoms were sputtered from the target and react with the oxygen atoms in chamber or on the copper cold finger substrate during deposition and form WO_3 nanoparticles. When the temperature of the cold finger come to room level, particles were scratched carefully and crushed in a pestle mortar to homogenize them. **Table 4.4** lists the value of sputtering parameters used during the synthesis of WO_3 nanoparticles.

Table. 4.4 Sputtering parameters for the synthesizing of WO_3 nanoparticles at various sputtering powers.

Target	Base Pressure	Working Pressure	Gas Used	Deposition Time	Distance (d)	Power (Watt)	Substrate Temperature
W	7.7×10^{-7} Torr	30 mTorr	Ar:O_2 ::40:10	8 hrs	5 Cm	40 W, 60 W, 80 W, 100 W	–194 ºC

4.3.2 Results and Discussion

The XRD patterns of the WO_3 nanoparticles synthesized at different sputtering powers 40 W, 60 W, 80 W, and 100 W are representing in **Fig. 4.14**. From the XRD results, WO_3 nanoparticles show no distinct peaks, revealing the amorphous type nature but these are crystalline. The probable reason for looking amorphous nature may be smaller particle size due to higher the full width half maxima (FWHM) of the peaks so that these peaks do overlap to each other and looks amorphous type nature. In XRD patterns two humps are shown, first hump occur from 18–42 º and another hump occur from 46–66 º values of 2θ. Overall, from XRD patterns, it is difficult to explain crystallinity of WO_3 nanoparticles.

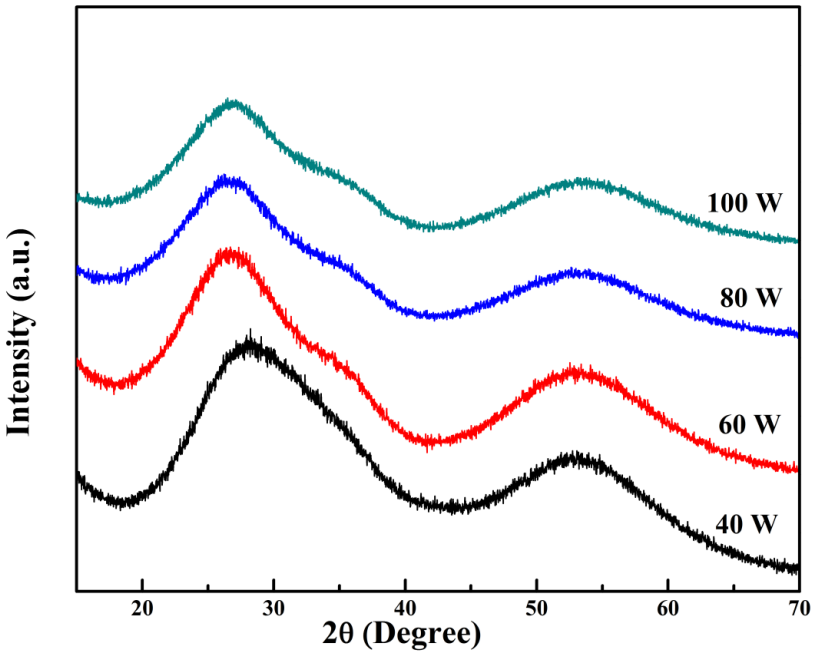

Fig. 4.14 XRD patterns of WO_3 nanoparticles synthesized at various sputtering powers.

To check the crystalline nature of synthesized WO_3 nanoparticles, the selected area electron diffraction (SAED) pattern of WO_3 nanoaprticles was observed and shown in **Fig. 4.15**, clearly representing the different crystallites rings. These crystallite rings indicate the polycrystalline nature of WO_3 nanoparticles.

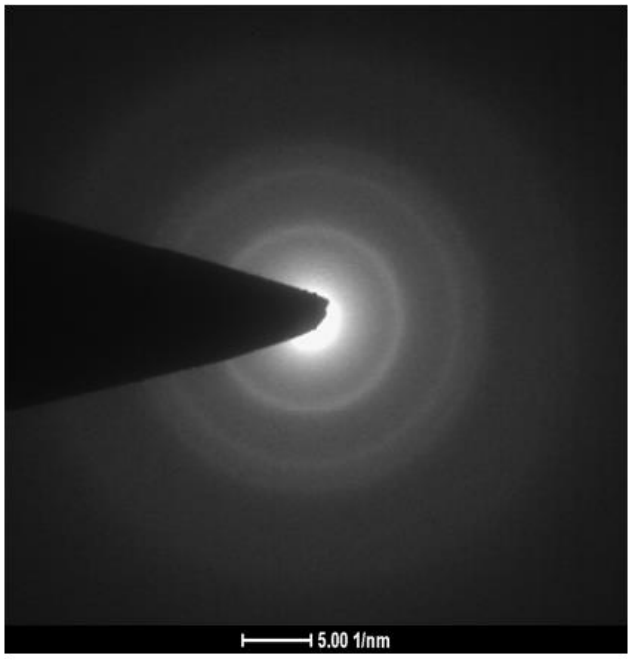

Fig. 4.15 SAED pattern of WO_3 nanoparticles of 40 W sputtering power.

In order to confirm the crystalline nature of synthesized WO_3 nanoparticles, Raman spectroscopy was used which supports the formation of well defined crystalline nature of WO_3 nanoparticles. **Fig. 4.16** represents the Raman spectrum of the WO_3 nanoparticles synthesized at 40 W sputtering power. It can be seen that WO_3 nanoparticles have two regions at 200–400 and 600–900 cm^{-1}. In first region, Raman peaks observed at lower wave numbers 260 and 325 cm^{-1} indicating the bending modes of W–O–W. The higher wave number peaks at 707 cm^{-1} is due to O–W–O vibration and 804 cm^{-1} is corresponding to crystalline WO_3 stretching vibration mode of bridging oxygen of W–O–W. These last two peaks clearly attributes to the formation of monoclinic phase of WO_3 as reported in available literature **[238, 239].**

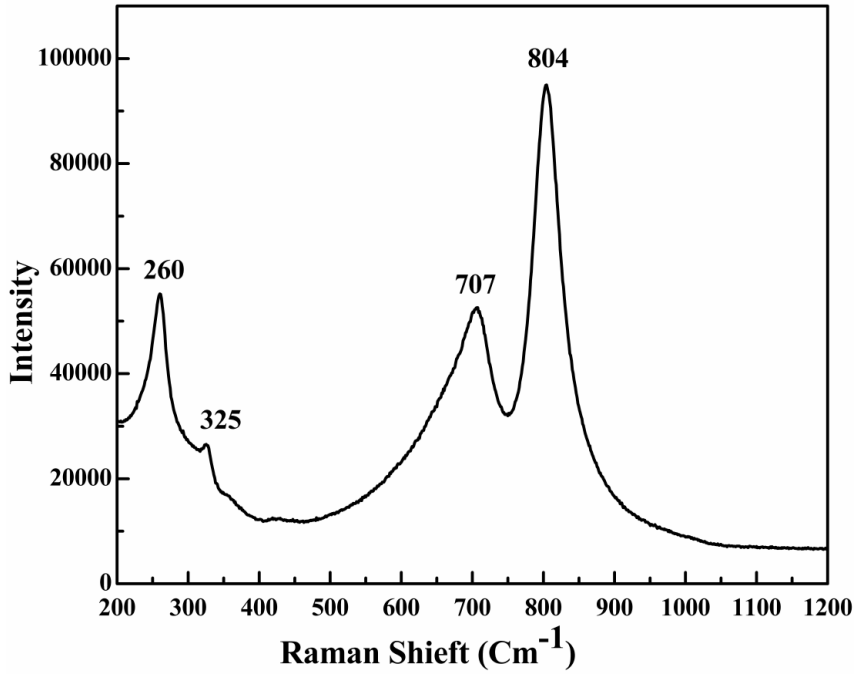

Fig. 4.16. Raman spectra of WO_3 nanoparticles synthesized at 40 W sputtering power.

The surface morphology of the WO_3 nanoparticles at different sputtering power is depicted in **Fig. 4.17**. It is clear from the images that the nanoparticles synthesized at different sputtering power are very small in size and have narrow size distribution. Also, at all sputtering powers, narrow size distribution occur. Also, at lower power (40 W), the particles have large aggregation and as the sputtering power increases up to 100 W, the aggregation of nanoparticles decreases and appear in some individual form. The particles appear in spherical form.

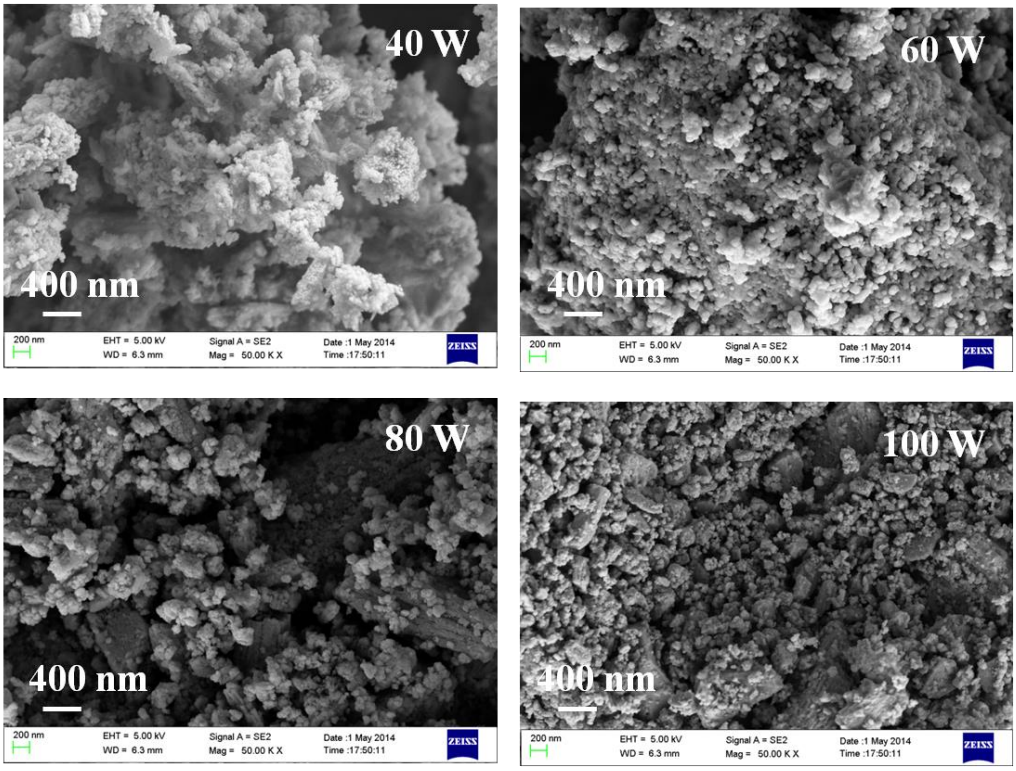

Fig. 4.17 FE–SEM images of WO_3 nanoparticles at various sputtering power.

The elemental composition of the dc sputtered WO_3 nanoparticles determined by using EDS analysis (**Fig. 4.18**), which clearly reveal that only oxygen and tungsten elements are exist in the product with the specific molar ratio of about 1:3 (W:O). The presence of Au and C signals are due to the gold coating and carbon film supporting the specimen in SEM observation. Therefore the prepared WO_3 nanoparticles were highly free of impurities compare to under the current synthetic route.

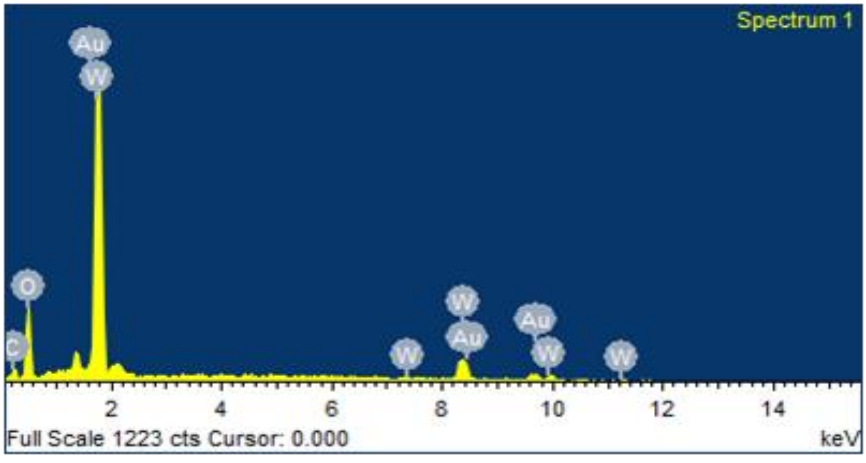

Fig. 4.18 EDS spectra of WO_3 nanoparticles.

The spherical particles were further analyzed by using TEM for morphology and to calculate the particle size. The TEM images at different sputtering power are shown in **Fig. 4.19 (a)–(d).** It is clear that the particles show spherical type structure with perfect uniform size distribution. The particle size calculated from form TEM is ~2, 4, 5 and 6 nm at sputtering powers 40 W, 60 W, 80 W, and 100 W respectively. It is clearly revealed that as the sputtering power increases from 40 W to 100 W, the particle size increases continuously.

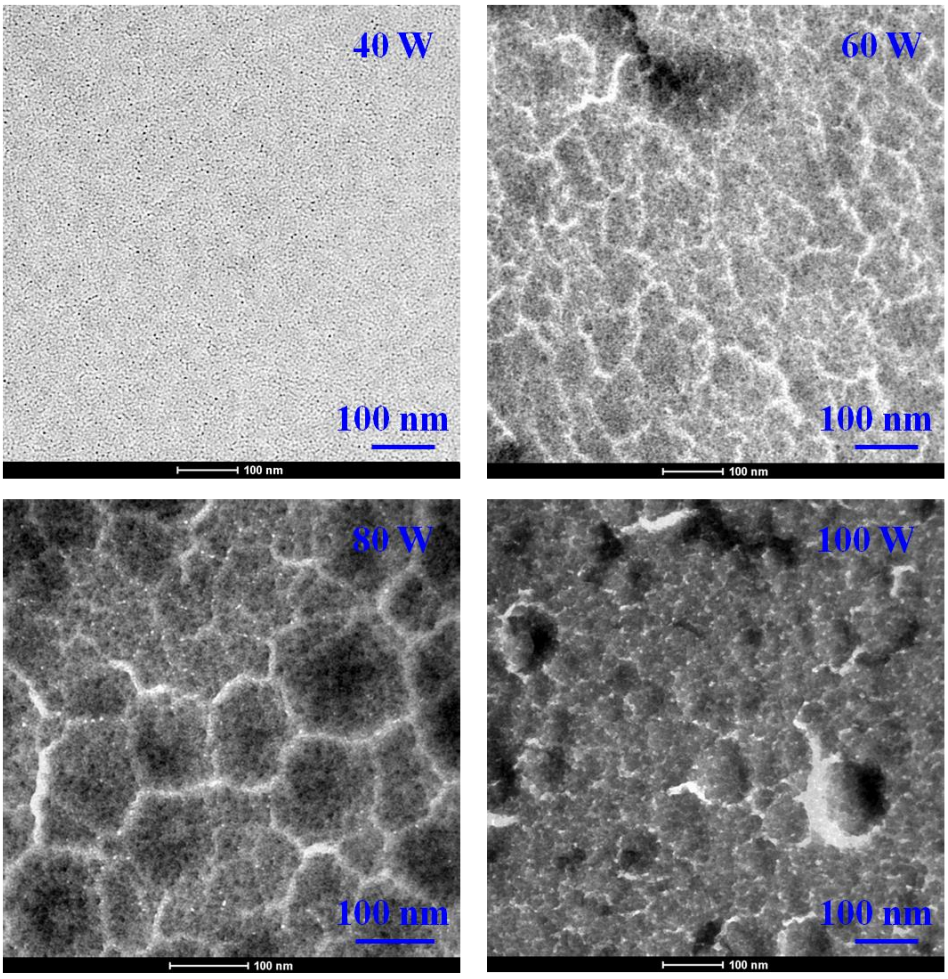

Fig. 4.19 TEM images of WO_3 nanoparticles at various sputtering power.

Also, in XRD patterns, intensity of hump slightly enhanced and sharper with increase in sputtering power. This means that the crystallinity of the WO_3 nanoparticles improved and the grain size become larger with the increase of sputtering power up to 100W. The results can be explained by the following reason. As the sputtering power increases, the number or the energy of the electrons and ions in glow discharge plasma increases in case of metal oxide targets. That is the energy of the sputtered tungsten atoms which is obtained by collision of the positive

ions to the target will increase with increase sputtering power. Thus the energy of the tungsten atoms arriving at the copper cold finger substrate increases with increasing sputtering power up to 100 W and facilitate further small increase in crystallization, resulting increase in particle size with sharpness of hump. It is also possible that with increasing sputtering power, the electrons with high energy will attack on the surface of copper cold finger for growing the particles, providing in the form of thermal energy. This energy might act as additional energy to promote the growth of crystalline. Therefore from the above discussion, it is finalized that as the sputtering power increases, the number and momentum of the sputtering particles will also increase. Thus the atoms on the substrate surface become more energetic, as a result of crystallinity increases.

In order to investigate the amount of water content in synthesized WO_3 nanoparticles, the samples were first dried and then subjected to TGA analysis. The TGA curve of WO_3 nanoparticles synthesized at 40 W sputtering power is shown in **Fig. 4.20**. The curve clearly reveal that a continuous weight loss occur up to 300 ºC which clearly indicate that the samples are purely hydrous since weight loss is sufficient (~10.9%) up to 300 ºC. No further weight loss occur up to 600 ºC indicating the high purity of WO_3 nanoparticles. The reason of sufficient amount of water content in samples is that when the synthesized samples exposed to atmosphere after deposition, the moisture get entrapped in samples.

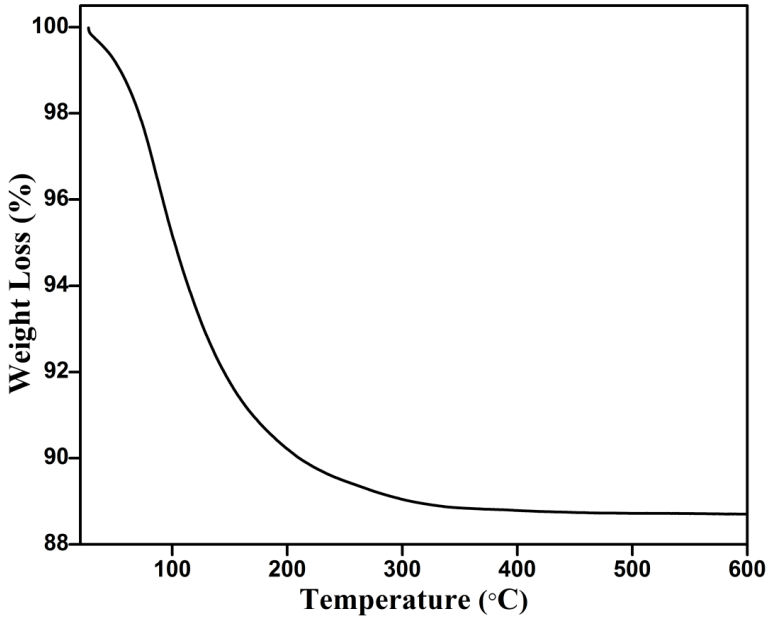

Fig. 4.20 TG curve of WO_3 nanoparticles synthesized at 40 W sputtering power.

4.3.3 Conclusion

The WO_3 nanoparticles were synthesized using magnetron sputtering method at different sputtering power and then investigated the structural, morphological and thermal properties. The XRD gives amorphous nature of the WO_3 nanoparticles but SAED shows the crystalline nature. This crystallinity was confirmed using Raman spectrum which give monoclinic phase of WO_3 nanoparticles. The particle size was found to be in the increasing form (2-6 nm) with increasing sputtering power. TG analysis show that the weight loss was only due to loss of physisorption water.

CHAPTER 5

SYNTHESIS AND CHARACTERIZATION OF ZrO_2 NANOPARTICLES

5.1 Introduction

Reactive sorbents composed of inorganic metal oxides nanomaterials demonstrate promising approach for the decontamination of chemical warfare agents (CWA) **[247, 248].** They possess high adorability and enhanced reactivity in the application of CWA decontamination as well as environmental remediation **[249, 250]**. These interesting applications are ascribed to their higher surface area and the reactive acid/base sites that exist in the form of edges and corner defects and unusual lattice planes **[230, 251]**.

Sulphur mustard (HD) and sarin (GB), well known CWA, were effectively employed in the World Wars (WW I and WW II) followed by their usage in several other incidents (e.g. in Gulf War and in Japan by terrorists). HD and GB acts on DNA and nervous system, respectively, thereby causing adverse health effects. Therefore, removal and detoxification of these CWA in the battle field environment is a challenging task for the scientific community for the sake of national security. For this purpose, several decontaminants including metal oxides have been reported for better decontamination properties towards CWA through adsorption and decontamination reactions which show lower adsorption capacity to degrade CWA **[111]**, **[113]**. In addition, the rate constant values and contamination free area were found to be very low for the above sorbent decontaminants as compared to the liquid decontaminant. To overcome these issues, search for the newer liquid free solid sorbent decontaminants is desirable, which exhibit high adsorbent capacity to adsorb the CWA strongly into their pores and convert them into non-toxic form.

ZrO_2 nanoparticles serve as good sorbent with high adsorption property **[252]** and have been synthesized using various methods such as sol-gel process, hydrothermal route, precipitation process, thermal decomposition, and microwave irradiation **[253–259]**. In the present chapter, we have prepared ZrO_2 nanoparticles using reactive magnetron sputtering technique at very low temperature (–194 ºC) for the removal and degradation of 2–chloro ethyl ethyl sulphide (CEES) and dimethyl methyl phosphonate (DMMP). The structural and thermal characterization was carried out using powder XRD, FE–SEM, TGA, TEM, and N_2–BET. The

decontamination reactions were examined by GC and the reaction products were analysed by GC–MS and FT–IR analysis.

5.2 ZrO_2 nanoparticles: A good decontaminating agent for 2–chloro ethyl ethyl sulphide and dimethyl methyl phosphonate

5.2.1 Synthesis of ZrO_2 Nanoparticles

ZrO_2 Nanoparticles were synthesized using reactive magnetron sputtering technique in a custom designed vacuum chamber (Excel Instruments, Mumbai). The copper cold finger was used as a substrate. The chamber consist of different ports to hold sputtering gun, gas connecting line, glass window and copper cold finger which was continuously filled up by liquid N_2 to cool the substrate. Sputtering was carried out using high purity (99.99%) Zr target of 2 inch diameter and 5 mm thickness. The copper cold finger was firstly cleaned up with acetone and then mounted on the chamber to create vacuum up to 10^{-7} Torr using a turbomolecular pump backed by rotary pump. The Ar and O_2 gases were introduced into the chamber separately during sputtering. The standard mass flow controller (MFC) and manometers were used to control and measure the flow of the gases, respectively. Thereafter, an optimum working pressure was set into the chamber using Ar and O_2 gases in specific ratio and then pre sputtering was carried out for ten minutes to remove the contamination from the target surface. During sputtering, the liquid nitrogen (Liq. N_2) was filled into hollow copper cold finger to maintain the low temperature (~ –194 ºC). At low temperature, the grain growth was stopped in the plane of the film on the substrate to produce nanoparticles. Furthermore, contamination due to diffusion of atoms from the substrate to sputtered material becomes minimized at low temperature. During sputtering, Zr atoms react with O_2 atoms in the chamber during transit or on the substrate surface to form ZrO_2 nanoparticles. After deposition, the particles were scratched at room temperature and crushed in a pestle mortar to homogenize them. Thereafter, the nanoparticles were annealed ex-situ in a tubular furnace in the temperature range of 200 ºC to 600 ºC in open atmosphere (air). The sputtering parameters are given in **Table 5.1**.

Table 5.1 Sputtering parameters for the synthesis of ZrO_2 nanoparticles.

Target	Base Pressure	Working Pressure	Gas Used	Deposition Time	Distance (d)	Power (Watt)	Substrate Temperature	Annealing Temperatures
Zr	$8.3*10^{-7}$ Torr	30 mTorr	Ar:O_2 ::40:5	72 h	4.5 Cm	90 W	–194 ºC	As–deposited, 300, 450, 600 ºC

d = Distance between target and substrate

5.2.2 Reaction Procedure

Reactions of CEES with ZrO_2 nanoparticles were studied by treating 100 µl of dichloromethane (DCM) having 5 µl CEES with 100 mg ZrO_2 nanoparticles in seven different test tubes of equal size and then stirred for 2-3 minutes to confirm uniform mixing. DCM play important role in the uniform distribution of CEES within ZrO2 nanoparticles. The remaining agent was extracted using 5 mL acetonitrile with periodic intervals of time until 24 h to study the kinetics of degradation. Thereafter, extracted solutions were quantitatively analyzed using GC–FID under a temperature programming mode from 110 to 260 ºC at a rate of 8 ºC/min to find the amount of remaining CEES. During this time, the injection port was kept at 240 ºC while the detector port was kept at 250 ºC. The concentration of CEES in extracted solution was calibrated with the standard prepared solution for exact quantification. In case of DMMP, same procedure was applied except that DMMP in extract solution were quantitatively analyzed by GC–FID under the temperature of 120 ºC. The experiments were repeated five times to confirm the reproducibility and accuracy in the kinetics data.

5.2.3 Results and discussion

5.2.3.1 Characterization of ZrO_2 nanoparticles

Powder X–ray diffraction patterns of as-deposited and annealed nanoparticles at various temperatures is shown in **Fig. 5.1**. XRD patterns show reflection planes of monoclinic and tetragonal structure of ZrO_2 nanoparticles, which is in agreement with the standard JCPDS File No 00–036–0420 and 00–017–0923, respectively. As-deposited nanoparticles show amorphous type patterns due to broadening of peaks with very small particle size (~2 nm). After annealing at 300 ºC and above, XRD patterns indicate the mixture of tetragonal and monoclinic phase. At 300 ºC, tetragonal phase leads with preferred orientation (111) (marked by *) and remains up to

450 ºC. The further increase in annealing temperature up to 600 ºC, monoclinic phase start to lead with preferred orientation (–111) over the tetragonal phase. ZrO_2 mainly exists in three important phases namely monoclinic, tetragonal and cubic. The monoclinic phase is thermodynamically stable from room temperature to 1170 ºC, while tetragonal and cubic phase becomes dominant at higher temperature (≥ 1170 ºC and 2380 ºC). The presence of tetragonal phase in XRD patterns of ZrO_2 may be attributed to small specific surface free energy (0.77 J/m^2) **[260]** in comparison to the monoclinic phase (1.13 J/m^2) **[261]**. The large surface area of as-deposited and annealed at lower temperature in comparison to annealed at higher temperature create a thermodynamic barrier for the transformation of tetragonal to monoclinic phase. Consequently, tetragonal phase is remained after dominating monoclinic phase in the XRD patterns **[258]**. Also, it is clearly observed that as the annealing temperature increases, the crystallinity of the ZrO_2 nanoparticles increases continuously. The crystallite size of annealed ZrO_2 nanoparticles calculated using Scherrer analysis lying in the range of 8–36 nm.

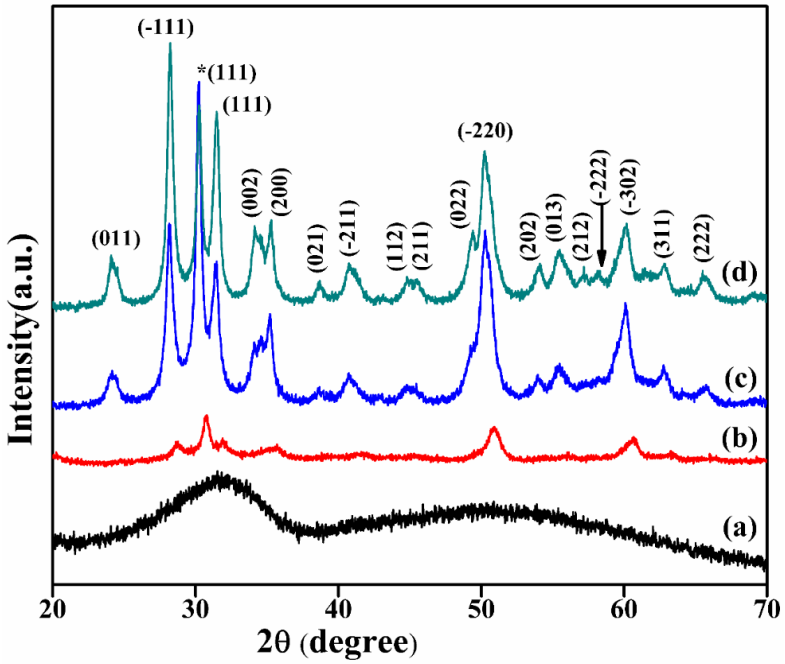

Fig. 5.1 XRD patterns of ZrO_2 nanoparticles **(a)** as-deposited and annealed at **(b)** 300 ºC **(c)** 450 ºC **(d)** and 600 ºC.

Fig. 5.2 displays the Raman spectra of ZrO_2 nanoparticles of as-deposited and annealed at 300 ºC and 600 ºC in the range of 50–750 cm^{-1}. As predicted by the group theory analysis, tetragonal phase of ZrO_2 belongs to P4m2 (D^{15}_{4h}) space group with six Raman active

vibrational modes ($A1_g+2B1_g+3E_g$) and monoclinic ZrO_2 belongs to P21/c (C^5_{2h}) space group with 18 Raman active vibrational modes ($9A_g+9B_g$) **[258]**. The as–deposited ZrO_2 nanoparticles have no characteristic peak indicating amorphous type structure. Raman spectra of annealed ZrO_2 nanoparticles indicate the mixture of tetragonal and monoclinic phase. Among various Raman active modes of monoclinic ZrO_2, fourteen are observed and assigned as 98, 178, 190, 308, 347,477, 559, 637 cm^{-1} to the A_g modes and 222, 333, 381, 505, 538, 619 cm^{-1} to B_g modes. These observed values of Raman active modes match very well with the previously reported Raman spectra of monoclinic ZrO_2 **[257, 259]**. The bands at 147 and 266 cm^{-1} (marked by *) are the Raman active modes of tetragonal phase of ZrO_2 **[262, 263]**. These bands are assigned as 147 cm^{-1} to B_g and 266, 476 and 637 cm^{-1} to E_g modes. Besides, the Raman active modes observed at 477 and 637 cm^{-1} indicate both monoclinic and tetragonal phase of ZrO_2, however, intensity ratio is different. For monoclinic phase the band 477 cm^{-1} is more prominent than the band at 637 cm^{-1} and vice versa. It is clear from the Raman data that at low temperature (300 ºC) tetragonal phase is more prominent with peak intensity of 637 cm^{-1} compared to monoclinic phase of peak 477 cm^{-1} intensity. While at higher temperature (600 ºC) monoclinic phase become prominent with peak intensity of 477 cm^{-1} than tetragonal phase of 637 cm^{-1} intensity. These results match very well with the XRD results.

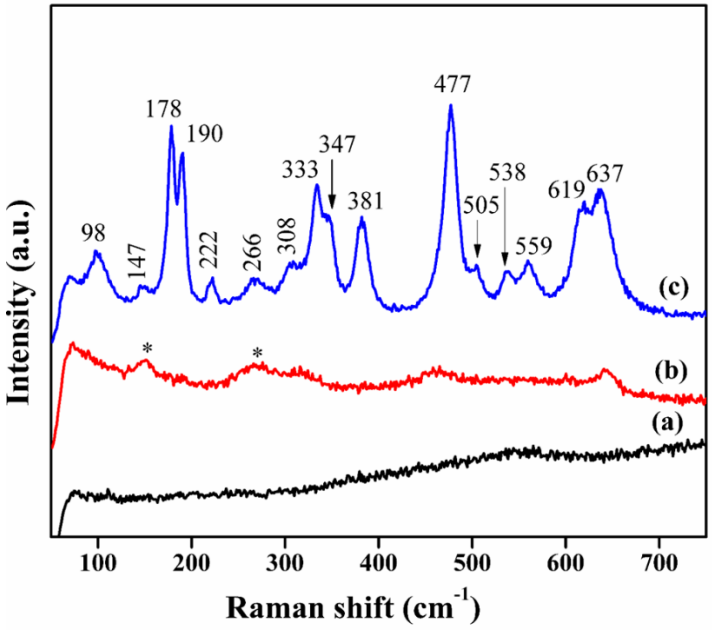

Fig. 5.2 Raman Spectra of ZrO_2 nanoparticles **(a)** as-deposited and annealed at **(b)** 300 ºC and **(c)** 600 ºC.

The FE–SEM images of as-deposited and annealed nanoparticles are represented in **Fig. 5.3**. All the samples exhibit nearly spherical morphology. Also, as the annealing temperature increases, particle size increases continuously with narrow size distribution to wide size distribution.

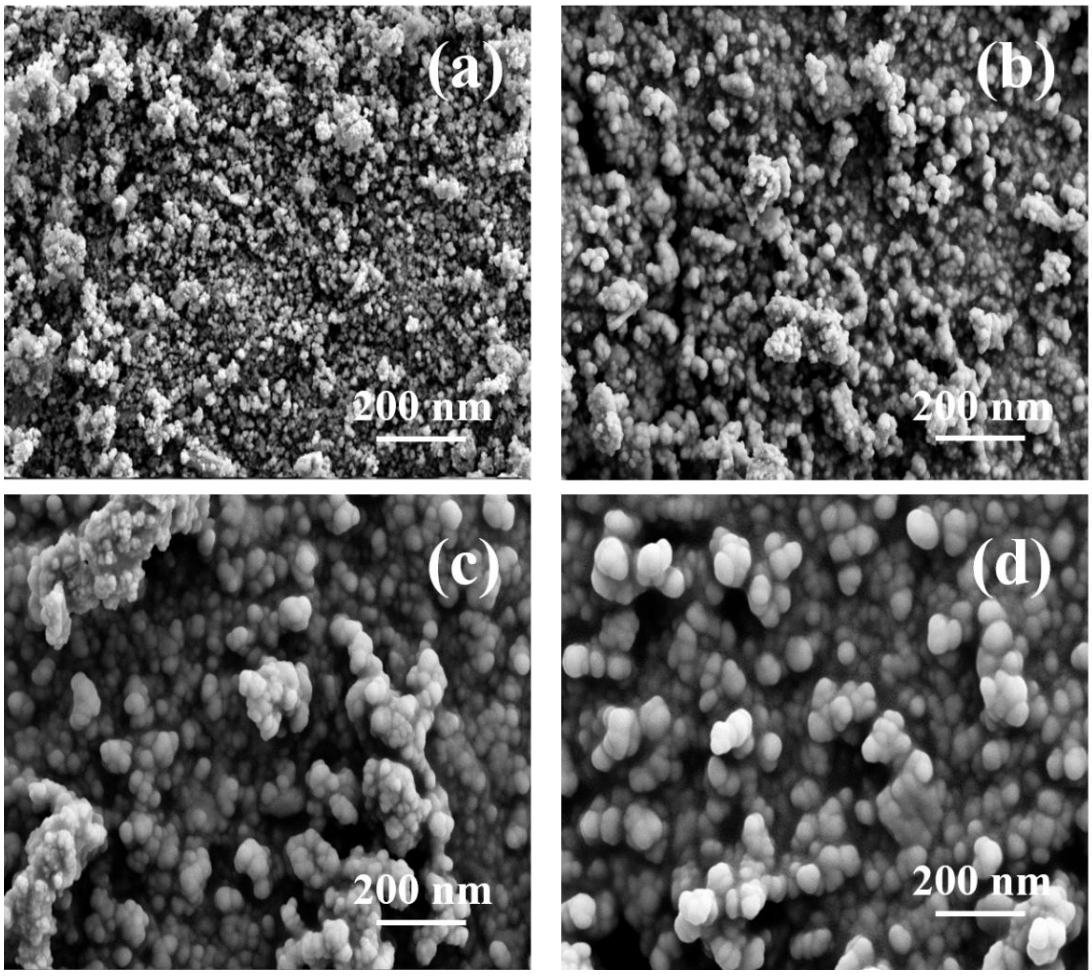

Fig. 5.3 FE–SEM images of ZrO_2 nanoparticles **(a)** as-deposited and annealed at **(b)** 300 ºC **(c)** 450 ºC **(d)** and 600 ºC.

The EDS spectrum (**Fig. 5.4**) of synthesized nanoparticles yields a proper stoichiometric ratio of Zr and O as 1:2. The signals of Au and C in the EDS spectra are due to gold coating and double side carbon tape used for FE–SEM analysis.

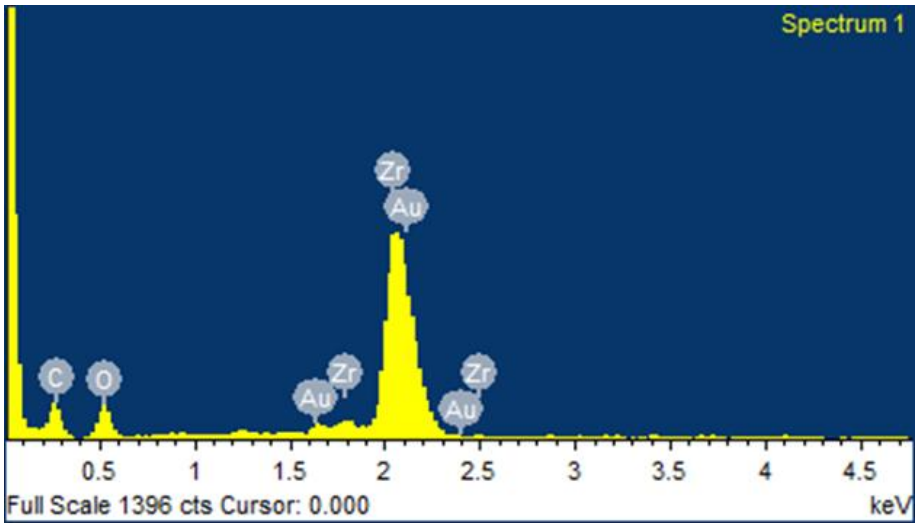

Fig. 5.4 EDS spectrum of the as-deposited ZrO_2 nanoparticles.

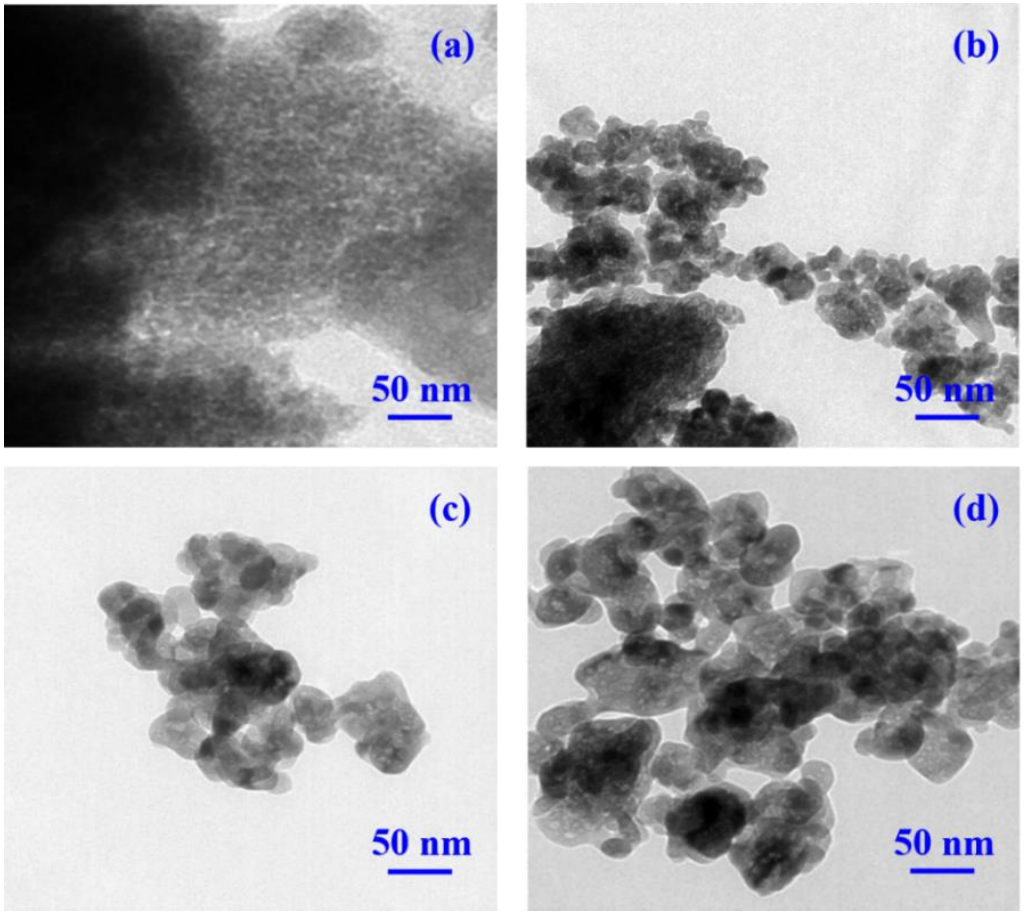

Fig. 5.5 TEM images of ZrO_2 nanoparticles **(a)** as–deposited and annealed at **(b)** 300 ºC **(c)** 450 ºC **(d)** and 600 ºC.

TEM images of all type ZrO_2 nanoparticles represented in **Fig. 5.5**. The images also clearly indicate spherical type morphology and increment in particle size with rising in annealing temperatures. The particle size distributions of the as-deposited and annealed nanoparticles is shown in **Fig. 5.6** which clearly indicate that as the annealing temperature increases, the arrow size distribution moves towards wide size distribution. And, the nanoparticle size calculated observed from particle size distribution is shown in **Table. 5.2**, which are very much correlate with the XRD patterns for annealed nanoparticles.

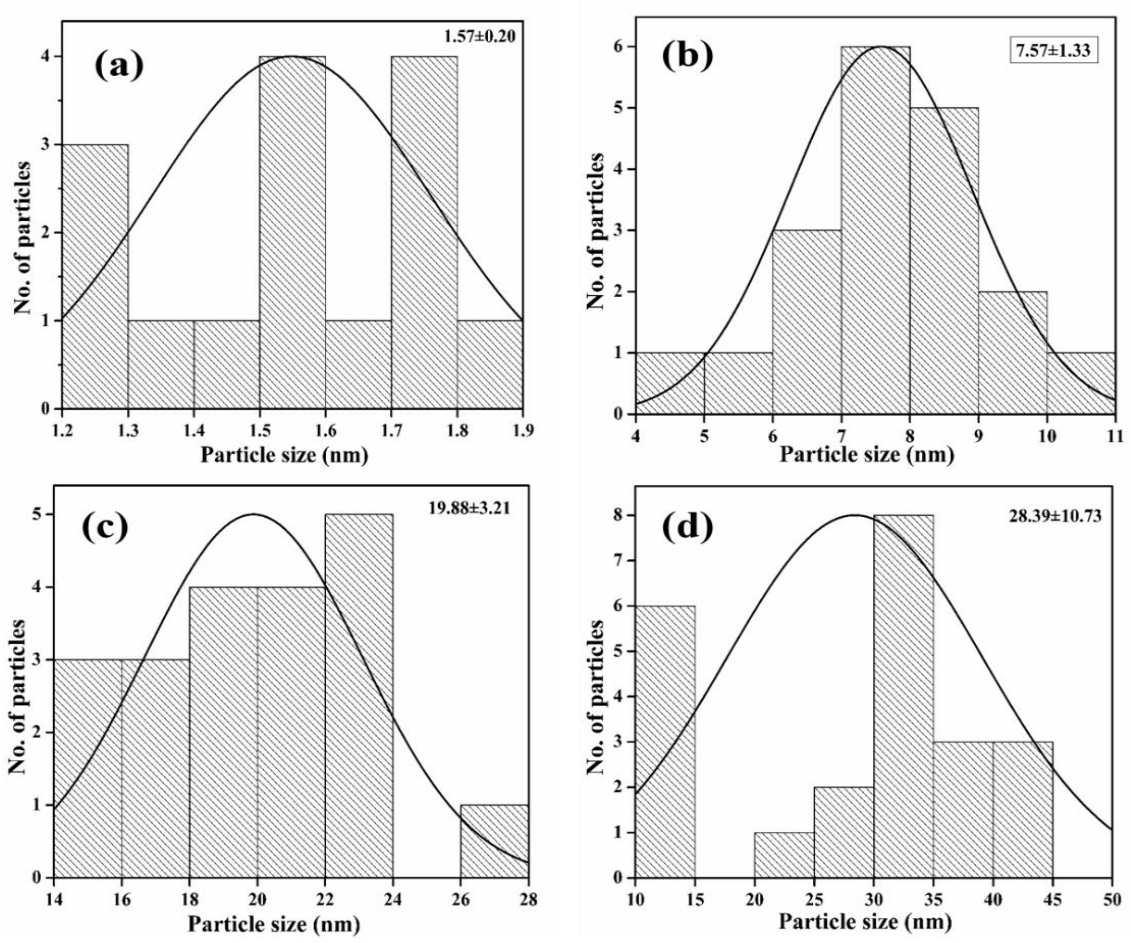

Fig. 5.6 Particle size distribution of **(a)** as–deposited and annealed at **(b)** 300 ºC **(c)** 450 ºC **(d)** and 600 ºC ZrO_2 nanoparticles.

Table 5.2 Particle size, surface area and pore volume of as-deposited and annealed ZrO_2 nanoparticles.

	Annealing temperature of ZrO_2 nanoparticles (ºC)			
	As-deposited	**300**	**450**	**600**
Particle size (nm)	1.57±.20	7.57±1.33	19.88±3.21	28.39±10.73
Surface area (m^2/g)	119.81	98.51	71.06	48.89
Pore volume (ml/g)	0.193	0.182	0.169	0.154

Selected area electron diffraction (SAED) of as-deposited ZrO_2 nanoparticles (**Fig. 5.7**) shows amorphous type nature while those annealed at 300 ºC exhibits crystalline nature (**Fig. 5.8**). The ring patterns corresponding to the (111)*, (–220) and (311) planes in the SAED patterns matches very well with the observed XRD patterns.

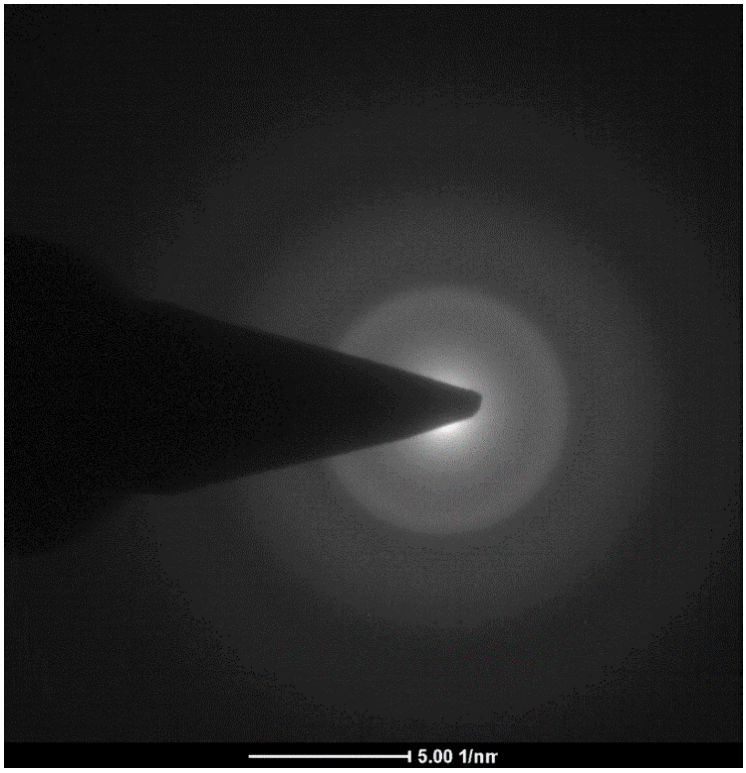

Fig. 5.7 Amorphous nature of as–deposited ZrO_2 nanoparticles.

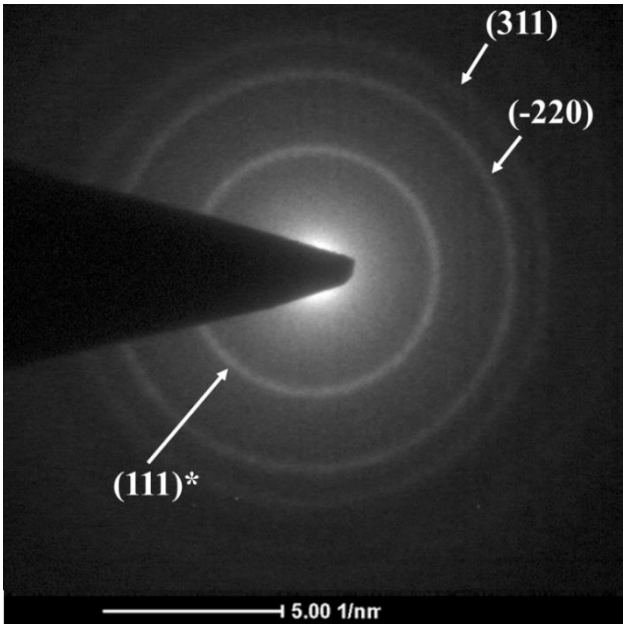

Fig. 5.8 SAED pattern of 300 ºC annealed ZrO_2 nanoparticles showing polycrystalline rings.

Fig. 5.9 shows the high resolution transmission electron microscope (HR–TEM) image of ZrO_2 nanoparticles annealed at 300 ºC, with values of d-spacing ~0.303 nm, 0.221 nm, 0.164 nm and 0.147 nm that clearly matches with the (111)*,(–211), (–113) and (311) planes, respectively, of tetragonal and monoclinic phase of ZrO_2 nanoparticles.

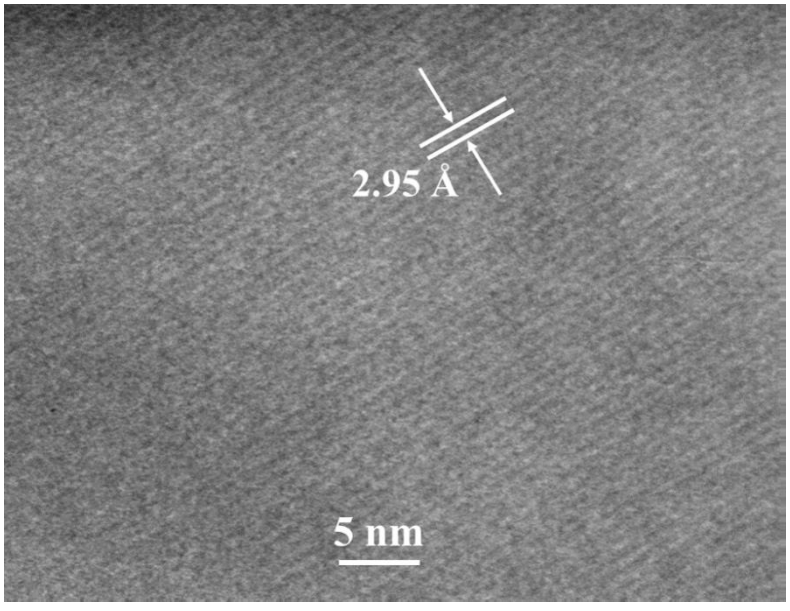

Fig. 5.9 HR–TEM image of ZrO_2 nanoparticle annealed at 300 ºC showing d–spacing for the (111)* plane of tetragonal phase.

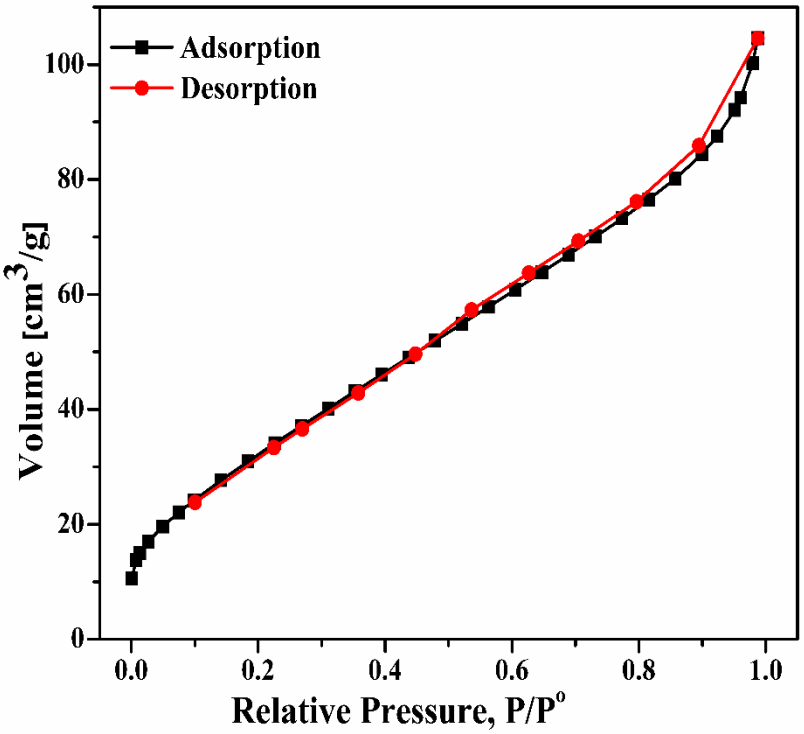

Fig. 5.10 Adsorption–desorption isotherm of as-deposited ZrO_2 nanoparticles.

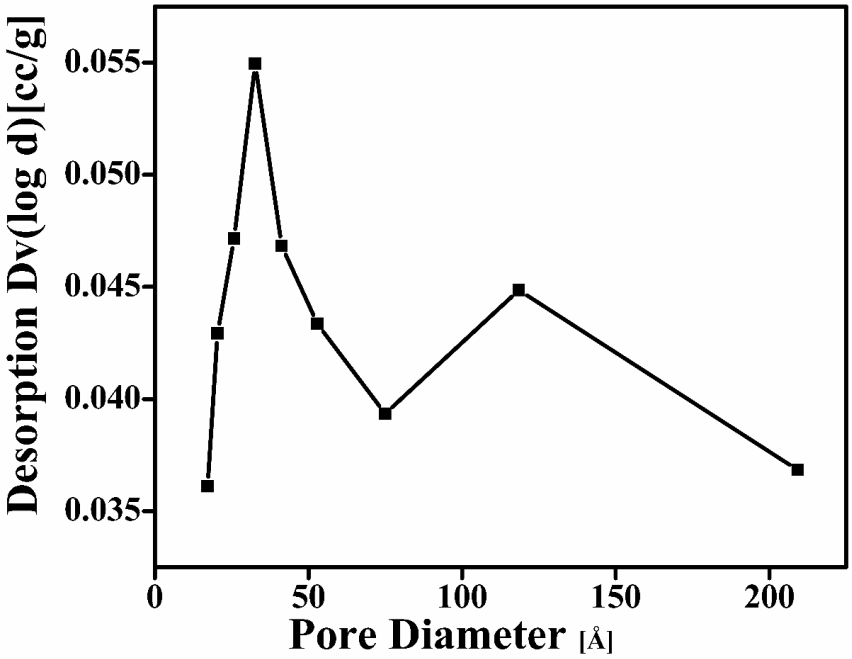

Fig. 5.11 BJH pore size distribution of as-deposited ZrO_2 nanoparticles.

Fig. 5.10 displays the N_2−adsorption-desorption isotherm and **Fig. 5.11** shows the pore size distribution of as-deposited ZrO_2 nanoparticles which clearly indicate high surface area (119.92 m^2/g) with pore volume 0.193 ml/g. **Table 5.2** summarizes the values of surface area and pore volume of ZrO_2 nanoparticles with different particle size. It is clear that both surface area and pore volume decreases with increasing particle size. Thus XRD, Raman, FE−SEM, EDS, TEM and SAED analysis confirm the formation of mixed monoclinic and tetragonal phases with high purity and narrow size distribution.

5.2.3.2 Kinetics of CEES and DMMP decontamination

After characterization, magnetron sputtered ZrO_2 nanoparticles were exposed to CEES and DMMP to study the degradation kinetics of CWA at room temperature. The reactions were monitored using GC. The unreacted CEES was determined at different kinetic time intervals show linear plots depicting pseudo first order kinetics of reaction as shown in **Fig. 5.12 [113**, **142**, **150].** Kinetics plots indicate that the concentration of CEES as well as DMMP for all the samples decreases with increasing reaction time. Rate constant and half life values of CEES degradation with different size ZrO_2 nanoparticles was found to be in the range of 0.178–0.107 h^{-1} and 3.18–6.43 h, respectively as shown in **Table 5.3**. DMMP also reacted in a similar manner and is shown in **Fig. 5.13**. The above data clearly indicate pseudo first order kinetic behaviour of ZrO_2 reactivity towards DMMP as similar to CEES. The values of rate constant and half life values of DMMP degradation lie in the range of 0.034–0.015 h^{-1} and 20.02–45.12 h, respectively as shown in **Table 5.3**. Data also indicate that with the as–deposited ZrO_2 nanoparticles CEES degrade completely (~100%) while DMMP degrade up to 60% within 24 hours. While as the particle size increases up to 36 nm degradation leads to ~92% and ~30%, respectively. CEES and DMMP degradation, reaction takes place faster in the initial stage and reaches to a steady state at later stage of the reaction. The probable reason behind the faster reaction in initial stage is the rapid adsorption and distribution of liquid within the pores and its interaction with the highly existing reactive sites and hydroxyl groups into ZrO_2 nanoparticles. When the all the sites get exhausted, the limited surface reaction occurs, leading to a steady state in later part of the reaction **[38, 150]**. Rate constant (k) and half life ($t_{1/2}$) values of CEES and DMMP degradation with ZrO_2 nanoparticles of different sizes were calculated using first order kinetic equation i.e. k = 2.303×slope and 0.693/(2.303×slope) respectively and are listed in **Table 5.3**.

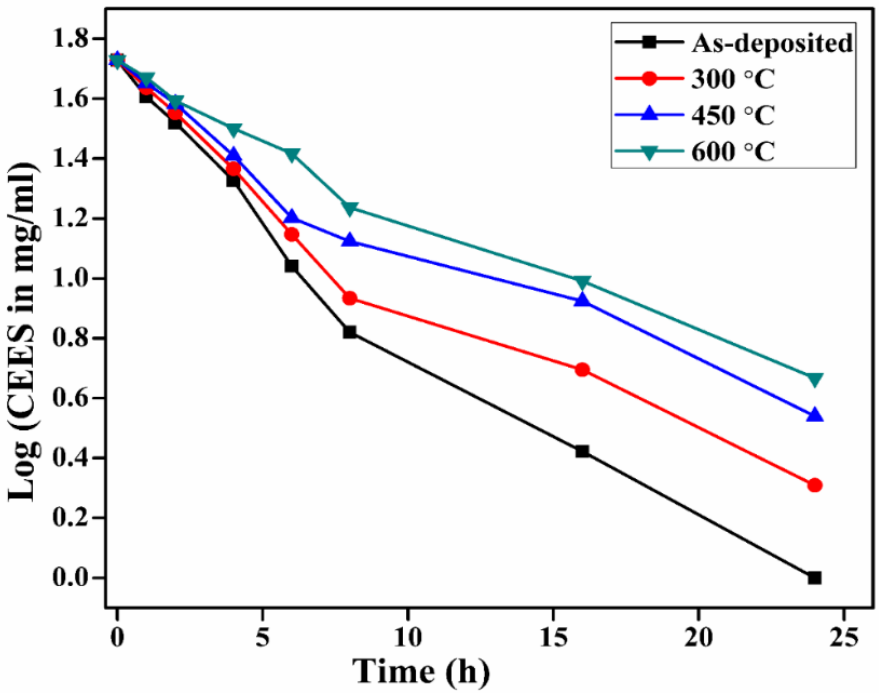

Fig. 5.12 Kinetics of degradation of CEES on the surface of ZrO_2 nanoparticles.

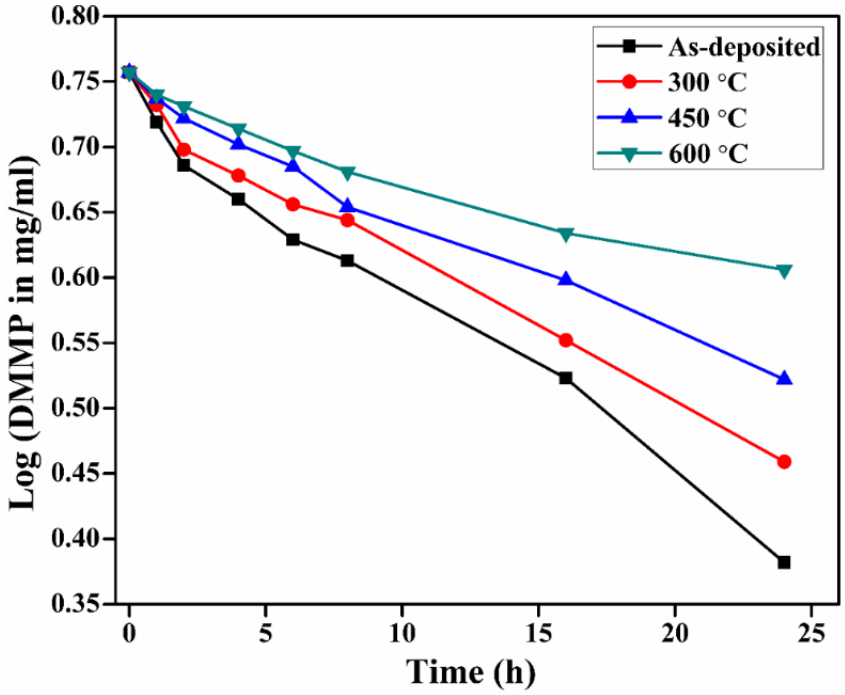

Fig. 5.13 Kinetics of degradation of DMMP on the surface of ZrO_2 nanoparticles.

Table 5.3 Results of degradation of CEES and DMMP on the surface of different sizes ZrO_2 nanoparticles.

	Particle size of ZrO_2 nanoparticles (nm)			
	1.57±.20	7.57±1.33	19.88±3.21	28.39±10.73
Kinetic rate constant, (k) h^{-1} of CEES	0.178	0.146	0.119	0.107
Half life ($t_{1/2}$) h of CEES	3.18	4.073	5.80	6.43
Kinetic rate constant, (k) h^{-1} of DMMP	0.034	0.028	0.022	0.015
Half life ($t_{1/2}$) h of DMMP	20.02	24.59	30.83	45.12

From the experimental results it is clear that the degradation of CEES and DMMP decrease with increase in particle size i.e. smaller particles exhibits better degradation capacity in comparison to the bigger particles. The probable reason for decrease in degradation rate with increase in particle size is the surface area as well as reactive sites. The magnetron sputtered ZrO_2 nanoparticles contains higher surface area (~119 m^2/g) which leads to higher adsorption capacity towards CEES as well as DMMP. Due to large adsorption capacity of ZrO_2 nanoparticles, CEES and DMMP were found to be adsorped promptly and its distribution within their pores and react with the reactive sites, thereby converting them into non-toxic form. Also, increase in particle size provides reduced surface area which leads to decrement in the adsorption capacity. Gu et al. studied the effect of annealing temperature on the structure, acid-base properties and found that variation in annealing temperature brought a change in surface structure, acidic and redox properties **[222]**. With increasing annealing temperature acidic sites decreases i.e. basic sites increases. Also with the increase in annealing temperature, the amount of OH group/hydrated water decreases, which in turn reduce the rate of reaction. Tang and co-workers found that the activity of oxides towards CWA not only depends on surface acidic/basic properties but also amount of adsorb H_2O **[157]**. The rate of CWA degradation increases with the increase of H_2O content i.e. water gives positive effect in the degradation of CWA. The increase in the particle size (agglomeration) with increasing annealing temperature, as observed in FE-SEM and TEM analysis which leads to reduction in surface area of the synthesized ZrO_2 nanoparticles. Recently, Verma et al. reported that with the increase in annealing temperature the particle size increases as well as surface area

decreases **[264, 265].** Due to decrease in surface area the available active sites for the adsorption and degradation of CEES decreases, decreasing the rate of reaction.

GC–MS and FT–IR analysis were used to understand the reaction mechanism and product formed. The data were verified for the product fragmentation patterns based on National Institute of Health (NIH) data bases. For all the samples, GC–MS data (**Fig. 5.14**) indicated the formation of hydroxyl ethyl ethyl sulphide (HEES) with m/z values at 27, 47, 61, 75 and 106 and also vinyl ethyl sulphide with m/z values at 45, 60, 76 and 88. These m/z values emphasize the role of hydrolysis and elimination reactions of ZrO_2 nanoparticles for the decontamination of CEES to convert them into non-toxic form. Moreover, FT–IR investigations of all the samples that were exposed to CEES exhibits the extinction of band at 700 cm^{-1} (C–Cl), variation of peak pattern at around 1440 and 1295 cm^{-1} (CH_2–Cl), observance of peak intensity at 3432 cm^{-1} (–O–H) and 1642 cm^{-1} (C=C) further confirms the hydrolysis and elimination products of CEES i.e. HEES and vinyl ethyl sulphide on the ZrO_2 nanoparticles.

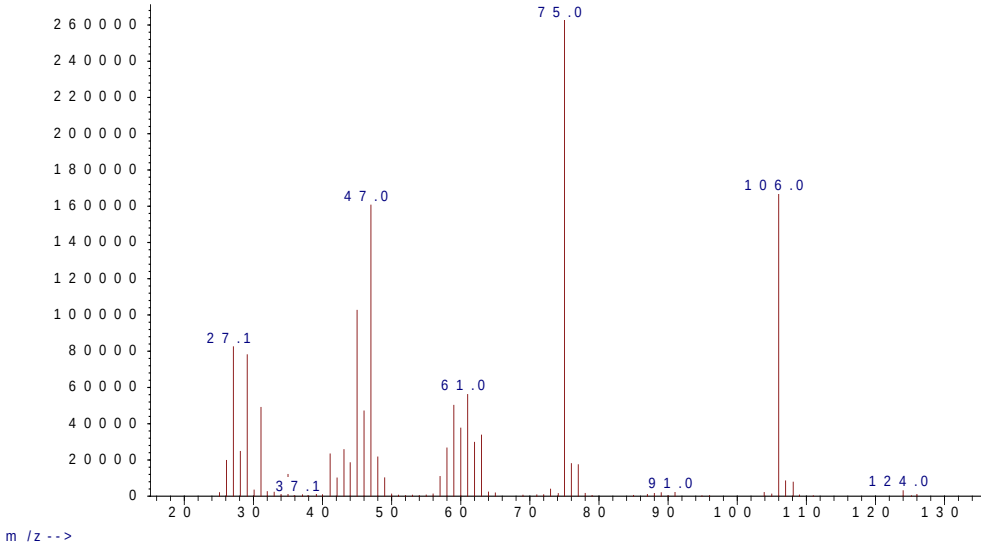

Fig. 5.14 GC–MS data of CEES products after degradation.

According to the GC–MS and FT–IR data the reaction scheme for the CEES decontamination on the ZrO_2 nanoparticles surface is proposed in **Fig. 5.15**. According to this scheme CEES molecules react with ZrO_2 nanoparticles in three ways. In one way, CEES molecules react with physisorbed/intercalated water molecules to form HEES in which cyclic sulphonium ion is formed as intermediate, being in the form of (non-volatile) salt, could not be extracted out and detected by GC **[33]**. Mawhinney et al. also reported the decontamination of

CEES on the surface of Al_2O_3 **[266]**. The adsorption of CEES molecules occur onto the Al_2O_3 through the strong interaction with the surface. This interaction occurs through the sulphur atom which acts as a Lewis base, donating a lone pair of electrons to the Al^{3+} Lewis acid sites. Once adsorbed onto the surface of the alumina, the chlorine atom, rich in electron density, associates with the isolated hydroxyl groups and undergoes hydrogen bond formation followed by the hydrolysis reaction to produce HCl and surface-bound $C_2H_5SC_2H_4$–O–Al species [38]. In second way, they give elimination product by the removal of HCl molecule over the solid acids and bases sites. And in third way, they reacted with surface hydroxyl groups (Zr–OH) and Lewis acid (Zr^{4+}) sites to form surface bound alkoxy species. These observations are strongly consistent with the previously reported data **[111, 113, 155, 267]**.

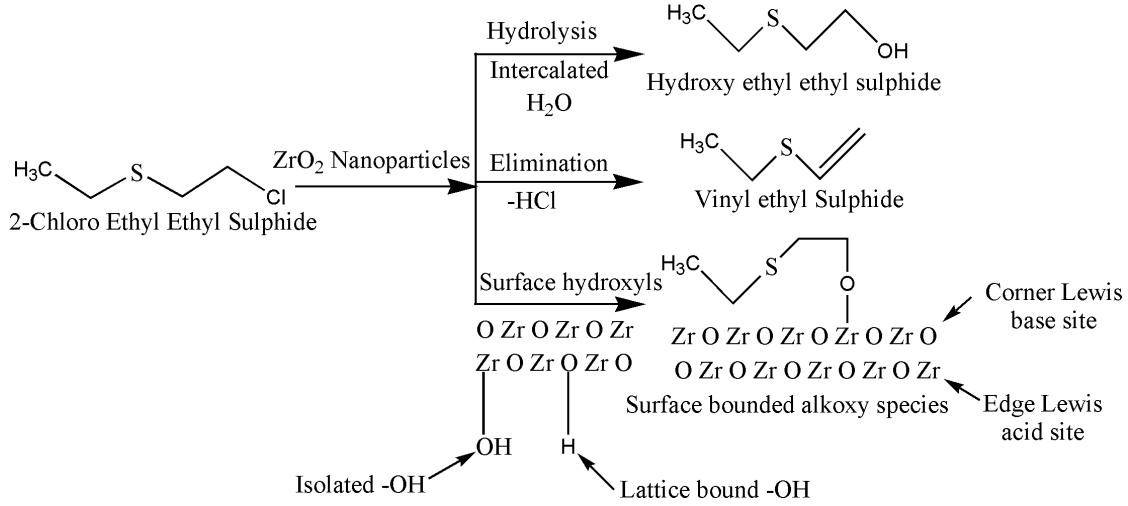

Fig. 5. 15 Reaction scheme of **(a)** CEES and **(b)** DMMP occurring on the surface of ZrO_2 nanoparticles.

Subsequently, due to polar and non–volatile nature of hydrolysis products of DMMP they were derivatised before GC–MS analysis. Data obtained after silylating the extracted reaction mixture using BSTFA [bis(trimethylsilyl) triflouro acetamide. Resulting the formation of hydrolysis product of DMMP i.e. methyl phosphonic acid (MPA) with m/z values at 240, 225, 147, 133 and 73 (**Fig. 5.16**). These m/z values exhibited the role of hydrolysis reaction in the decontamination of DMMP to MPA thereby rendering them to non–toxic product. In addition to this, FT–IR data for the all samples that were exposed to DMMP reveal that the band intensity located at 1275 cm^{-1} (P=O) and 1025 cm^{-1} (P–O–C) of DMMP changed/disappeared. One band at 1234 cm^{-1} indicates the interaction of P=O group with surface functional groups of

ZrO_2 nanoparticles. Also, one peak observed at 3425 cm^{-1} indicating the formation of –O–H group i.e. hydrolysis product. These observations confirm the formation of MPA on the surface ZrO_2 nanoparticles and are consistent with the reported data **[41, 139]**.

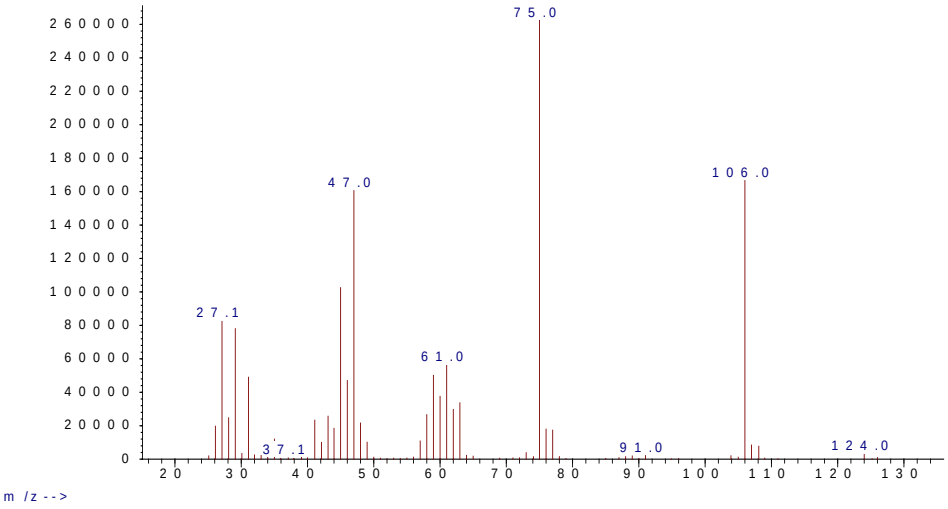

Fig. 5.16 GC–MS data of DMMP products after degradation.

Based on the above GC–MS and FT–IR data, the reaction pathway of DMMP degradation on the ZrO_2 nanoparticles is proposed in **Fig. 5.17**. According to this, DMMP molecules also reacted similar to CEES. They reacted with physisorbed or intercalated water molecules to form non-toxic product i.e. methyl phosphonic acid (MPA). In other way they reacted with isolated hydroxyl group (Zr–OH) and Lewis acid (Zr^{4+}) sites to form surface bound phosphonate. The observations are reflected with the previously observed data **[268, 269]**.

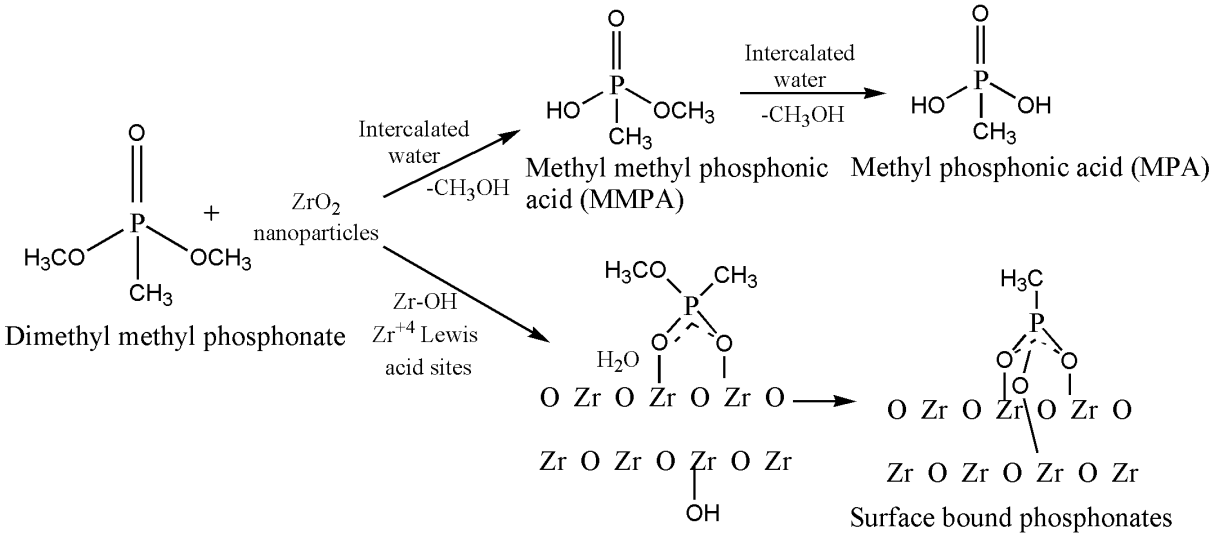

Fig. 5. 17 Reaction scheme of DMMP occurring on the surface of ZrO_2 nanoparticles.

Overall occurrence of hydrolysis reactions on the ZrO_2 nanoparticles surface and formation of surface bound alkoxy species and surface bound phosphonates facilitated the decontamination of CEES and DMMP and rendering them non-toxic. No excess water was added to ZrO_2 nanoparticles, whatever moisture adsorbed from the atmosphere while transferring the samples with reaction functionalities seemed to have facilitated the decontamination. To investigate the amount of water content, ZrO_2 nanoparticles were subjected to TG analysis. **Fig. 5.18** represents the TG pattern of as–deposited ZrO_2 nanoparticles. It indicates that the as-deposited nanoparticles shows a weight loss of 20.28% after heating up to 900 ºC and it decreases up to 4.06% as the particle size increases to 28.39±10.73 nm. ZrO_2 nanoparticles of 1.57±.02 nm, 7.57±1.33 nm, 19.88±3.21 nm, and 28.39±10.73 nm show a weight loss of 20.28, 14.10, 10.47 and 4.06%, respectively. It is clear that with increase in particle size through annealing temperature the amount of water/hydroxyl group decreases, due to which weight loss decreases. Finally, sputtered ZrO_2 nanoparticles provide large surface area and facilitate faster adsorption and encapsulation of CEES and DMMP. And then, physisorbed water/surface hydroxyl groups and Lewis acid sites etc. interacted with the agents thereby converting them into non-toxic products. The decontamination results of CEES and DMMP on ZrO_2 nanoparticles which have been synthesized in the present work were compared with those prepared and reported earlier with CEES and DMMP. In the present case, magnetron sputtered ZrO_2 nanoparticles exhibited better decontamination reactivity compared to existing solid decontaminants such as Fullers earth, MnO_2 nanobelts, and TiO_2 nanotubes etc. They decontaminated CEES less than 80% with rate constant value less than 0.02 h^{-1} whereas, ZrO_2 nanoparticles exhibits effective rate constant values i.e. 0.178–0.107 h^{-1}. Also in case of DMMP degradation, ZrO_2 exhibited better rate constant values (0.034–0.015 h^{-1}) compared to earlier reported rate constant values (0.008–0.020 h^{-1}) of activated carbon. These results show that ZrO_2 nanoparticles provides promising decontamination results on per with the existing solid decontamination sorbents.

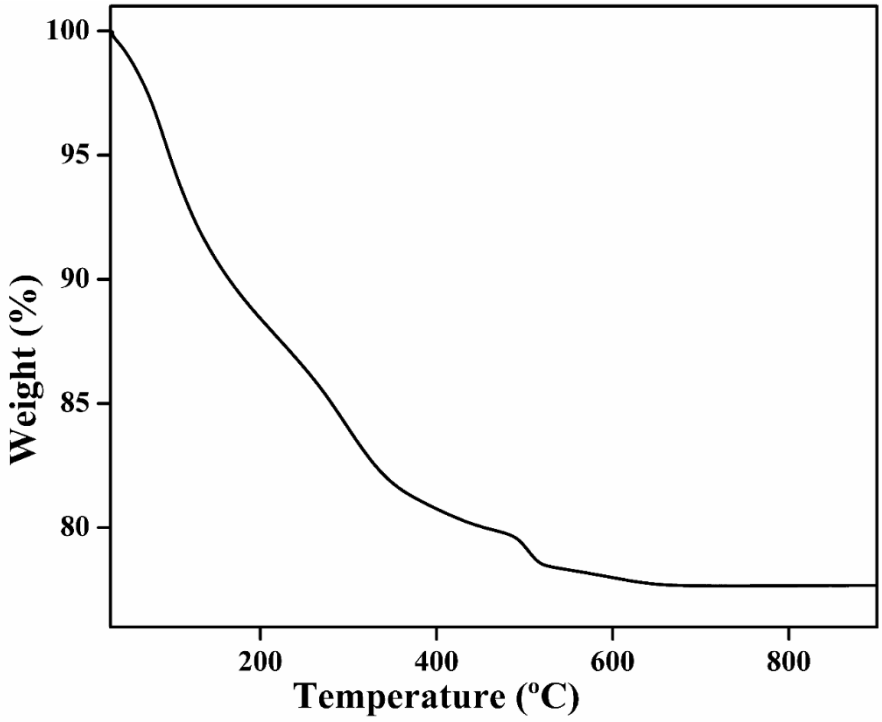

Fig. 5.18 TGA patterns of as-deposited magnetron sputtered ZrO_2 nanoparticles.

5.2.4 Conclusion

ZrO_2 nanoparticles were successfully synthesized using reactive magnetron sputtering process and then annealed at different temperature. The characterization was carried out using XRD, Raman spectroscopy, FE–SEM, EDS TEM etc. of the synthesized ZrO_2 nanoparticles. Thereafter, studied the effect of particle size on the decontamination of CEES and DMMP. The decontaminations results show that magnetron sputtered ZrO_2 nanoparticles have high decontamination ability to decontaminate them in comparison to existing solid decontaminants such as MnO_2 nanobelts, TiO_2 nanotubes and activated carbon etc. They destroy the agents by forming non–toxic hydrolysis and elimination products. The reactions show pseudo first order kinetic behaviour with rate constant values 0.178–0.107 h^{-1} and 0.034–0.015 h^{-1} for CEES and DMMP, respectively with increase in particle size. Also, as–deposited nanoparticles exhibited best decontamination results over annealed nanoparticles.

CHAPTER 6

SYNTHESIS AND CHARACTERIZATION OF MnO_2 NANOSTRUCTURES

6.1 Introduction

Reactive sorbent systems composed of inorganic oxide nanoparticles are currently under consideration as potential adsorbent materials for the detoxification of world wide chemical warfare agents (CWA) and their well known simulants. These materials posses interesting physisorption and chemisorption properties which encourage their use as reactive sorbents for the actual time decontamination of CWA **[157, 247, 248].** Some reactive adsorbents composed of nanocrystalline oxides such as CaO, ZnO, Al_2O_3 and WO_3 etc. were established as favourable materials for the decontamination of CWA **[157, 250].** They have greater reactivity towards CWA due to their higher surface area to volume ratio, large amount of highly reactive edges and corner defects sites, and unexpected lattice planes in comparison to bulk materials **[215, 270].** Also, the metal oxides play as a catalytic role in the autocatalytic reaction in CWA degradation **[132, 215].** Besides that, nanoparticles have a proclivity to get aggregation, due to which some of the existing reactive sites on the surface are not available to the adsorbate molecules. However, another variants of these materials such as nanosheets, nanotubes or nanobelts combined to each others without losing their surface area and due to which encouraging accessibility occur for sorbate molecules towards the surface active sites. This characteristic interaction in the aggregated nanotubes or nanobelts materials occur to minimize the electrostatic and steric repulsion of remaining charges exist on their surface.

The detoxification of the above agents within the MnO_2 nanotubes and nanobelts surface occur through hydrolysis reactions. Inspired by these results, we have synthesized MnO_2 in the form of aggregates composed of nanoparticles and nanorods using reactive magnetron sputtering technique under highly controlled conditions and investigated their decontamination properties against 2−chloro ethyl ethyl sulphide (CEES) and dimethyl methyl phosphonate (DMMP). To the best of our knowledge nobody has reported the synthesis of aggregates composed of MnO_2 nanoparticles and nanorods using magnetron sputtering technique and their use for the degradation of CWA or their simulants. Thereafter, characterization was done using

XRD, FE−SEM, TGA, TEM, and N_2−BET, then the progress of reactions were examined by gas chromatograph and the degradation products were confirmed by GC equipped with MS and FT−IR analysis.

6.2 Synthesis and characterization of new magnetron sputtered manganese oxide nanostructures– application for Decontamination of 2–chloro ethyl ethyl sulphide and dimethyl methyl phosphonate

6.2.1 Synthesis of nanoparticles and nanorods of MnO_2 sorbent

The aggregates of MnO_2 nanoparticles and rods (nanostructures) were synthesized using reactive magnetron sputtering technique in custom designed vacuum chamber (Excel Instrument, Mumbai). A turbo molecular pump and rotatory pump were attached with chamber to create required high vacuum. Sputtering was carried out using high purity (99.98%) manganese target of 2 in. diameter and 5 mm thickness. Initially, the vacuum (lower than 10^{-7} torr) was created in the chamber. The high purity argon and oxygen gases were introduced into the chamber during sputtering. The standard mass flow controller (MFC) and manometers were used to control and measure the flow of the gases respectively. During sputtering, the copper cold finger becomes cooled up to –194 ºC using Liq–N_2. Also, liq–N_2 was continuously filled up to make constant temperature. Lower temperature stopped the grain growth in the plane of the film on the substrate to produce nanostructure materials. Also, low temperature minimized the impurity due to diffusion of atoms from the substrate to synthesized materials. During sputtering, Mn atoms reacted with O_2 atoms in the chamber during transit or on the substrate surface to form aggregates of MnO_2 nanoparticles and nanorods. After deposition, the samples were collected carefully at room temperature. The sputtering parameters for the preparation of MnO_2 nanostructures are listed in **Table 6.1**.

Table. 6.1 Sputtering parameters for the synthesis of aggregates of MnO_2 nanoparticles and nanorods.

Target	Base Pressure	Working Pressure	Gas Used	Deposition Time	Distance (d)	Power (Watt)	Substrate Temperature
Mn	$6.4*10^{-7}$ Torr	30 mTorr	Ar:O_2 ::40:10	18 h	5 Cm	60 W	–194 ºC

d = Distance between target and substrate

6.2.2 Reaction procedure

The reactions of CEES and DMMP with aggregates MnO_2 nanoparticles and nanorods were studied by treating 100 µl of dichloromethane (DCM) solution containing 5 µl of CEES or DMMP with 100 mg of MnO_2 synthesized powder. DCM play important role in the uniform distribution of CEES/DMMP agent molecules. The remaining agent was extracted using 5 mL acetonitrile within a different intervals of time until 24 h in order to study the kinetics of degradation. Acetonitrile was used to extract the remaining agent from the solutions to analysed by GC–FID under isothermal conditions at 110 ºC for CEES and under a temperature programme from 60 to 210 ºC at a rate of 8 ºC/min for DMMP. The calibration of the extracted CEES and DMMP was carried out with the standard solution for perfect quantification. The injection and detector port was kept at 240 and 250 ºC, respectively.

6.2.3 Results and discussion

Generally, metal oxides that have basic surface interact with the toxic agents and covert them into non-toxic products through hydrolysis reactions. Also with basic surface sites, metal oxides hold Lewis and Bronsted acid sites, which degrade the toxic agents into non-toxic by forming surface bound alkoxy species and surface complexation products.

The basic nature was found of the MnO_2 nanostructures surface as reported in literature **[135]**. This material easily decontaminate to the CWA and their simulants through hydrolysis reactions. The mechanism of these reactions is similar to the solution chemistry of the contaminated molecules as earlier reported **[33]**. In order to study the decontamination of CEES and DMMP, aggregates MnO_2 nanoparticles and nanorods was synthesized using reactive magnetron sputtering technique and then studied against CEES and DMMP. After synthesis, the material was characterised using powder XRD as is given in **Fig. 6.1**. XRD pattern shows the high crystalline nature with peaks situated at 28.77º, 37.36º, 42.53º, 56.69º, 64.87º and 72.61º which can be indexed as (110), (101), (111), (211), (002) and (112) reflection planes of tetragonal phase of MnO_2 materials. The XRD pattern shows the high purity MnO_2 which matches very well with the standard XRD pattern phase (JCPDS file No: 00–024–0735; a = 4.3999, b = 4.3999, c = 2.8740 with space group = P42/mnm).

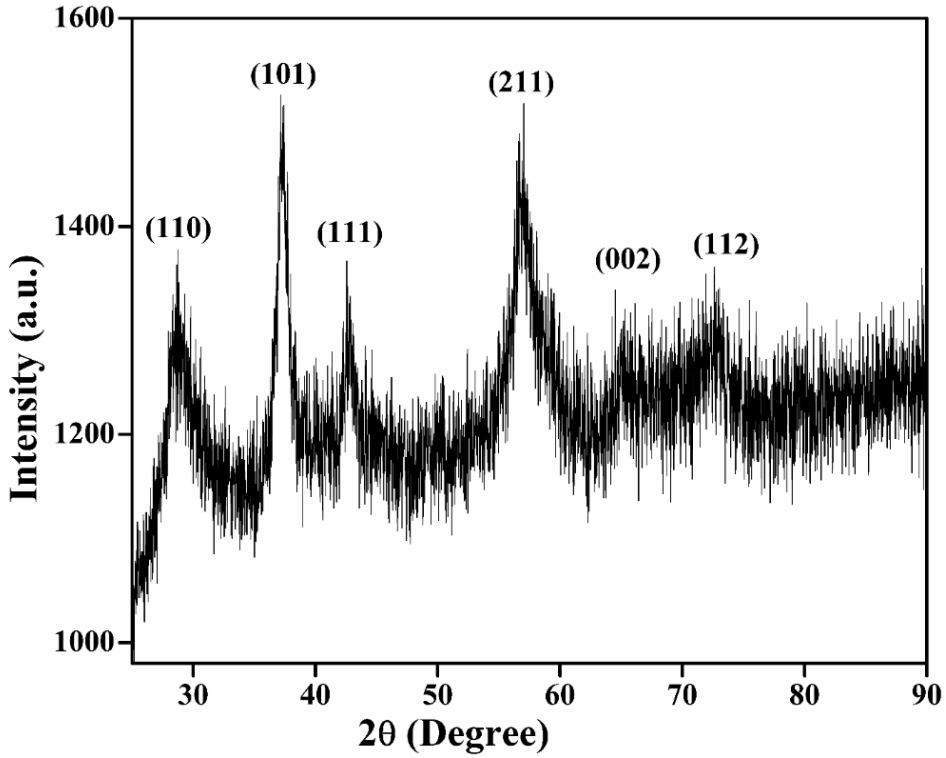

Fig. 6.1 Powder XRD pattern of reactive sorbent based on MnO_2 nanoparticles and nanorods.

To further investigate the structure features of the synthesized nanostructure material, Raman spectrum were carried out as shown in **Fig. 6.2**. The Raman spectrum of synthesized MnO_2 displays two peaks, one peak at 352 cm^{-1} due to Mn–O bending vibrations, and another peak of high intensity at 640 cm^{-1} at the high–frequency region due to Mn–O stretching vibrations, belongs to M_g spectroscopic species that originate from breathing vibrations of octahedral MnO_6 within a tetragonal hollandite-type framework **[271, 272].** The relative intensity of these two modes are correlated to the nature of the tunnel species. Hence, Raman spectrum exhibits the good crystallinity of the MnO_2, which is in agreement with the tetragonal structural studies reported above in XRD.

The FE–SEM image of synthesized MnO_2 material is shown in **Fig. 6.3** shows the aggregates of nanoparticles and nanorods like structure. The nanorods are randomly oriented and the nanoparticles are situated in the space of these randomly oriented nanorods. The nanoparticles are in aggregated form which are in the range of 10–20 nm. The rods are nearly greater than 100 nm in length.

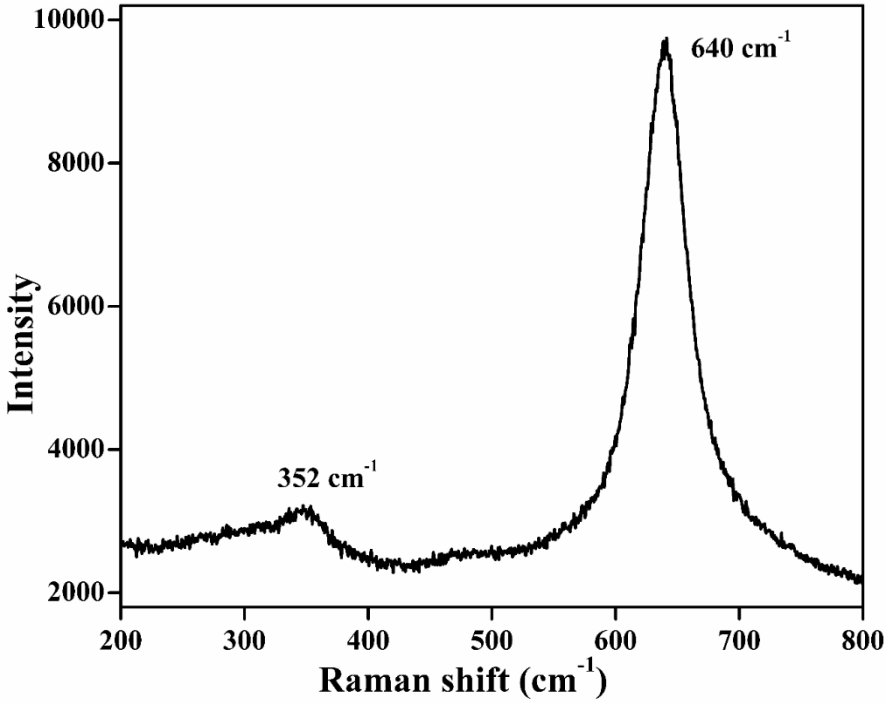

Fig. 6.2 Room temperature Raman spectrum of synthesized sorbent composed of MnO_2 nanoparticles and nanorods.

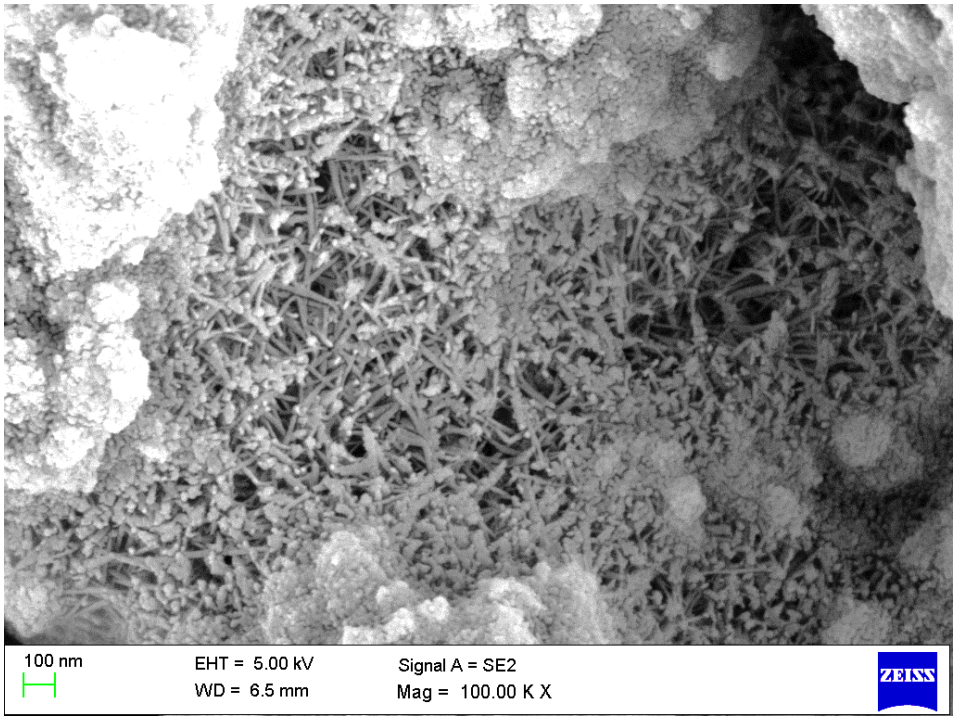

Fig. 6.3 Field emission scanning electron micrograph of the reactive sorbent composed of aggregated MnO_2 nanoparticles and nanorods.

The X–ray energy dispersive spectroscopy (EDS) result (**Fig. 6.4**) demonstrates that the synthesized materials contains mainly Mn and O elements which are in proper stoichiometric ratio (33.6 : 66.4). The others signals obtained for Au and C elements due to gold coating and double side carbon tape used for FE–SEM analysis.

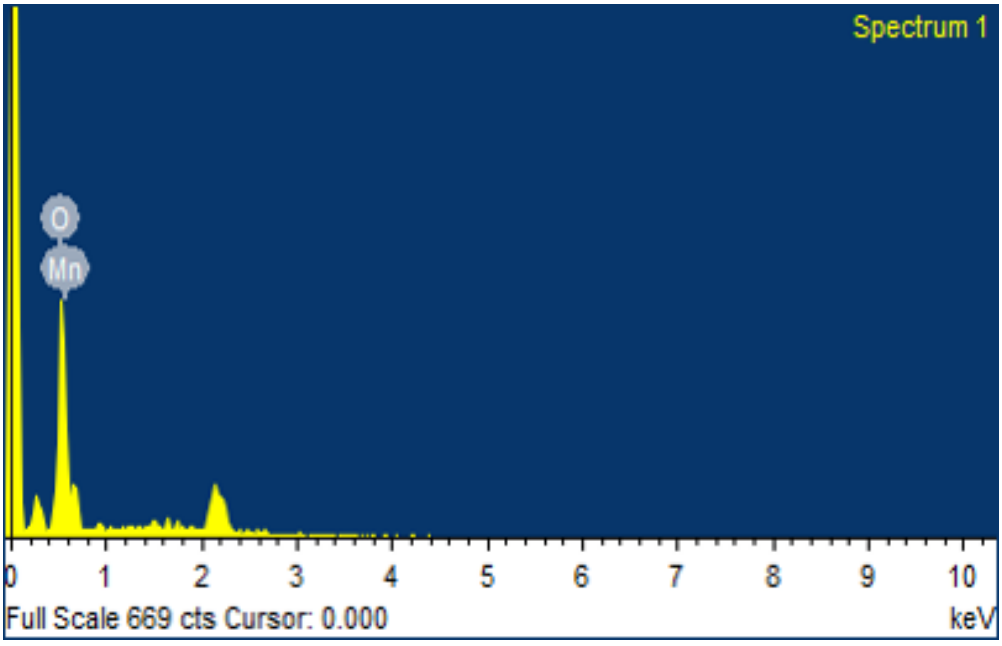

Fig. 6.4 EDS spectra of synthesized reactive sorbent MnO_2 nanoparticles and nanorods.

The morphology and size of the MnO_2 nanostructures was further confirmed by the TEM image in **Fig. 6.5**. At low magnification (**Fig. 6.5 (a)**) it was clearly observed the aggregation of nanoparticles and nanorods. The TEM image at higher magnification (**Fig. 6.5 (b)** and **(c)**) depicts clearly spherical type nanoparticles and rod like nanorods, respectively. These rods are found to be stacking at their tips. Thus show typical structure where nanoparticles are situated in the randomly distributed nanorods. The particle size distribution (**Fig. 6.5 (d)**) gives the nanoparticles in the range of 11.1±4.3 nm diameter while the rods are 9–10 nm in the diameter and the length lies in the range of 190–220 nm.

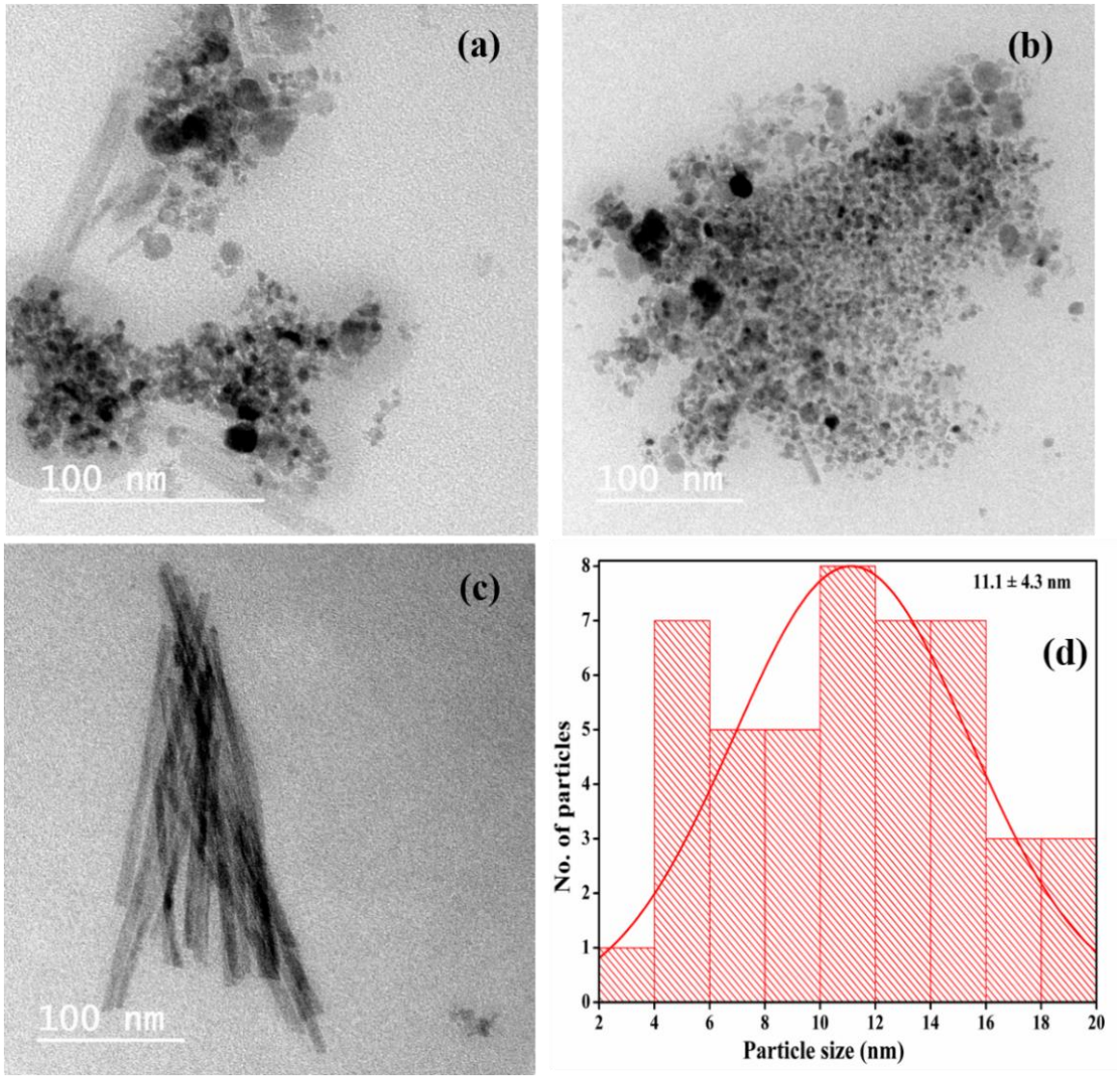

Fig. 6.5 Transmission electron microscope images of reactive sorbent based on MnO_2 nanoparticles and nanorods **(a)** mixture of nanoparticles and nanorods **(b)** nanoparticles **(c)** nanorods and **(d)** particle size distribution.

The high resolution transmission electron microscope (HR–TEM) image of the nanorod is shown in **Fig. 6.6**, clearly shows that the synthesized MnO_2 nanostructures were crystallized with the interplanar spacing 0.168 nm, corresponding to the (211) plane of the tetragonal MnO_2 nanostructure.

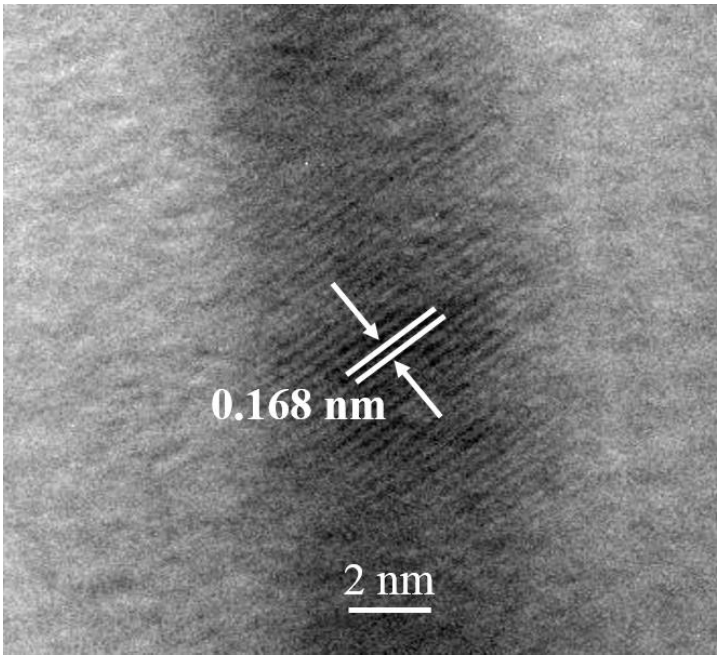

Fig. 6.6 High resolution TEM image of synthesized reactive sorbent based on MnO_2 nanoparticles and nanorods.

The corresponding selected area electron diffraction (SAED) pattern exhibits polycrystalline nature of synthesized of aggregates MnO_2 nanostructure is shown in **Fig. 6.7.** The lattice fringes attributing to the (110), (101) and (211) planes were clearly visible which are in well agreement with the XRD results.

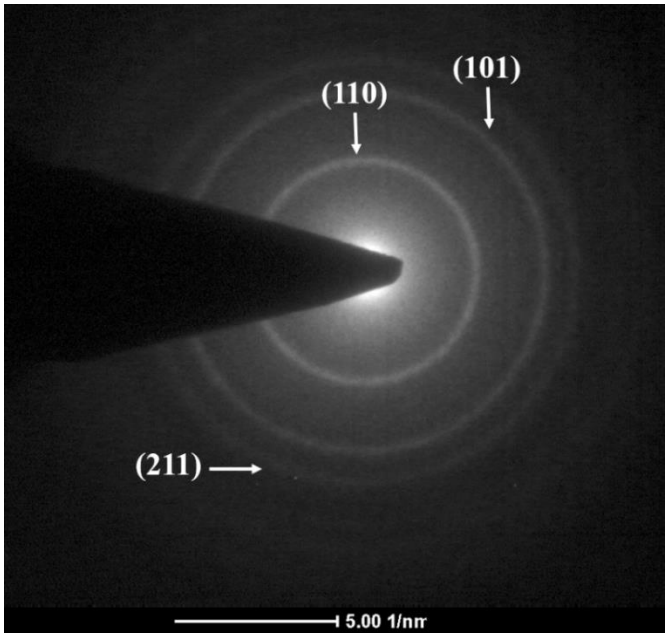

Fig. 6.7 Selected area electron diffraction pattern of synthesized reactive sorbent based on MnO_2 nanoparticles and nanorods.

In order to investigate the value of surface area and pore size distribution of the synthesized material, N_2–BET adsorption and desorption isotherm was carried out as shown in **Fig. 6.8**. The adsorption-desorption isotherm is type IV adsorption isotherm with a hysteresis (H3 type) typical of slit shaped pores as per IUPAC nomenclature. The slit shaped pores were expected to be formed from the synthesized materials. The formation of hysteresis confirm the mesoporosity of the obtained adsorbent composed of MnO_2 nanoparticles and nanorods **[113, [135, 273].** The BJH pore size distribution of the synthesized aggregates MnO_2 nanoparticles and nanorods indicates the pore maxima at 4.49 nm as shown in **Fig. 6.9**.

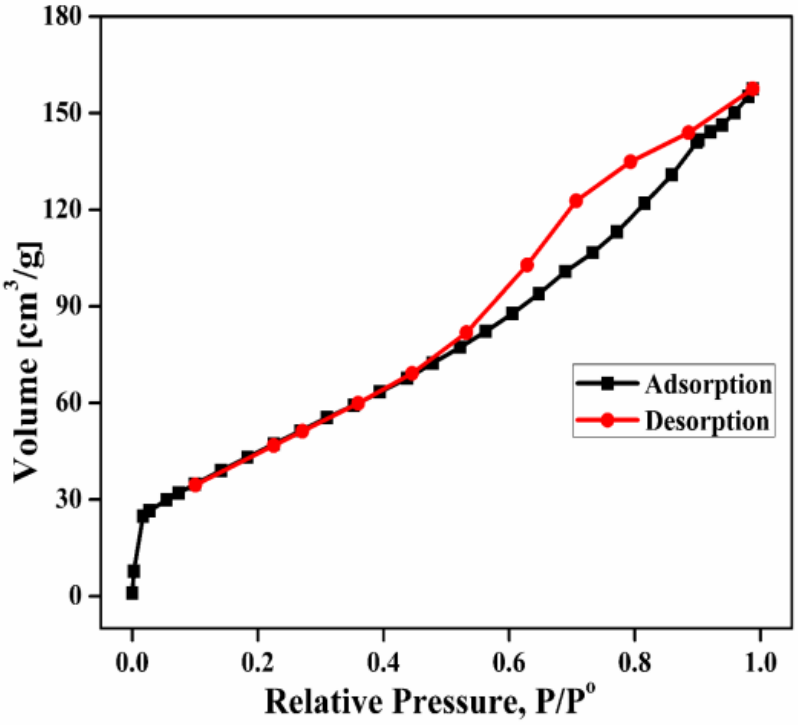

Fig. 6.8 N_2 adsorption–isotherm of the reactive sorbent composed of MnO_2 nanoparticles and nanorods.

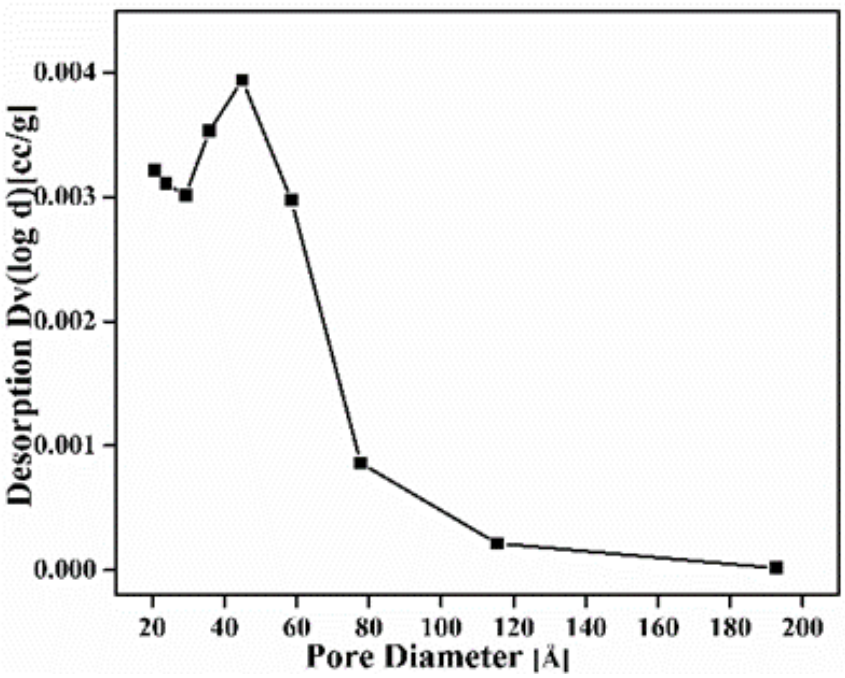

Fig. 6.9 Pore size distribution of the reactive sorbent composed of MnO_2 nanoparticles and nanorods

The surface area and pore volume was 164.28 m^2/g and 0.304 ml/g, respectively. This unexpected large value of surface area can be describe due to random orientation of synthesized aggregates composed of MnO_2 nanoparticles and nanorods as shown in FE−SEM and TEM images. Thus XRD, Raman, FE−SEM, EDS and TEM analyses clearly exhibits the formation of tetragonal phase with high purity and narrow size distribution in the magnetron sputtered MnO_2 nanostructure material.

After characterization, the obtained aggregates MnO_2 nanoparticles and nanorods was used to study the kinetics of reactions with CEES and DMMP at room temperature (25 ºC). The reactions were analysed using GC equipped with flame ionization detector. As per GC data, the remaining CEES was extracted from their reaction mixture with MnO_2 nanostructure at different interval of time and then quantitatively analysed by calibration. Subsequently, the kinetics data were plotted by taking the log of remaining CEES on Y axis and time on X axis. Linear plots occur illustrating the pseudo first order kinetics of reaction towards CEES and the graph is shown in **Fig. 6.10**. Figure indicates the fast initial stage of the reaction and the steady state at the later stages of the reaction which depicts pseudo first order kinetic behaviour of CEES towards aggregates MnO_2 nanostructures. The constant (k) and half life ($t_{1/2}$) was found

to be 0.267 h^{-1} and 2.58 h, respectively. In case of DMMP degradation, same behaviour occur during the decontamination reaction on aggregates MnO_2 nanostructures which indicates the pseudo first order kinetic behaviour (**Fig. 6.11**). The constant (k) and half life ($t_{1/2}$) values of rate was found to be 0.068 h^{-1} and 10.10 h, respectively. The kinetics experiments were repeated more than six times to confirm the reproducibility and accuracy in kinetics data. The experimental results show that CEES molecules degrade completely (100%) while DMMP molecules degrade up to ~64% within 24 h over the surface of aggregates MnO_2 nanostructures. The data exhibits that the CEES/DMMP molecules get interaction immediately with the nano aggregates MnO_2 due to higher surface area value (164.28 m^2/g) and large number of reactive sites i.e. MnO_2 nanostructures have high reachability of CEES as well as DMMP molecules towards the unreactive surface from bulk liquid. Moreover, manganese oxide was mixed with incipient amount of DCM (di chloro methane) solution of CEES/DMMP which promotes these molecules to spread over the maximum surface through pore structure. This spreading of liquid molecules help in the searching of unreactive surface sites, which leads to fast initial reaction. when the solution was spread and the CEES/DMMP molecules reach on the fresh aggregates MnO_2 nanostructures surface and reacted quickly to consume the surface active sites which creates poisoning of the surface and due to which spreading of agents molecules stopped and the steady state reaction occur on the surface of aggregates MnO_2 nanostructures. Also, the CEES/DMMP molecules can come into the contact of fresh surface through diffusion of evaporated molecules, thereby steady state occur within 8 hours. Overall, spreading of liquid, evaporation and diffusion of agent molecules could have influenced pseudo first order kinetics reaction and results matches well with the earlier reported results **[113, 150, 274, 275]**.

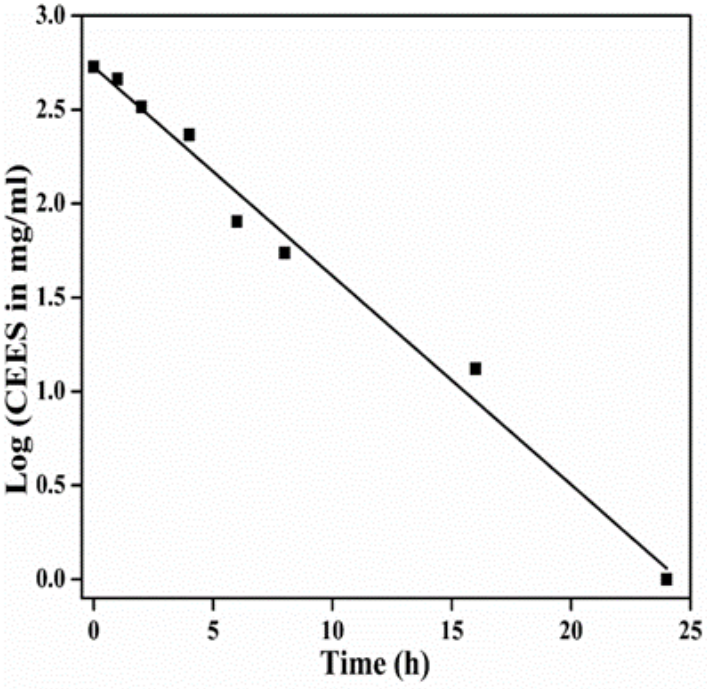

Fig. 6.10 Kinetics of degradation reactions of CEES on the surface of adsorbent composed of MnO_2 nanoparticles and nanorods.

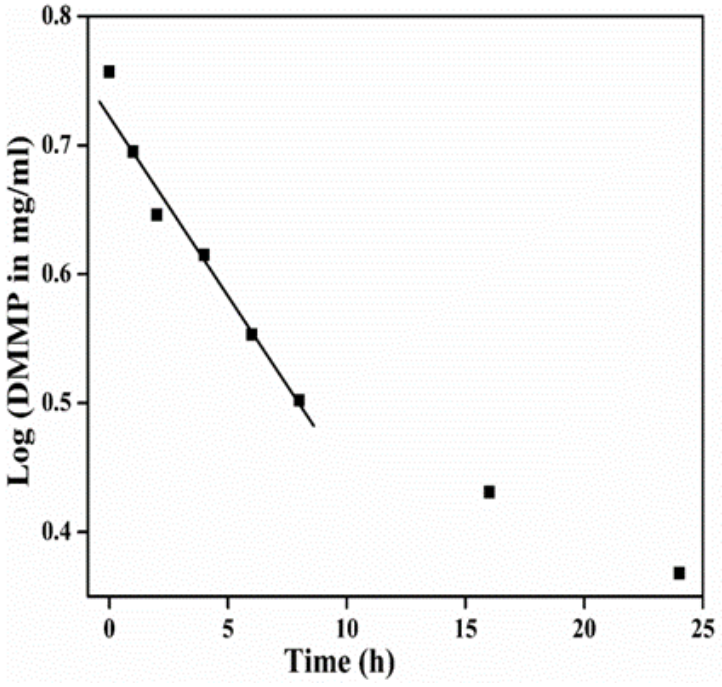

Fig. 6.11 Kinetics of degradation reactions of DMMP on the surface of adsorbent composed of MnO_2 nanoparticles and nanorods.

Thereafter, GC–MS and FT–IR techniques were applied on the reaction mixtures obtained from aggregates MnO_2 nanostructures to characterize the reaction products. The data were confirmed for the product fragmentation patterns based on NIH (National Institute of Health) data bases. In case of CEES decontamination reaction, data exhibits the m/z values at 29, 47, 61, 75, 91 and 106 which displays the formation of HEES (hydroxyl ethyl ethyl sulphide) product. This formation of hydrolysis product confirm the emphasising the role of hydrolysis reaction to convert it into non-toxic form. In addition to this, FT–IR data of aggregates MnO_2 nanostructures that were exposed to CEES displays the disappearance of band at 700 cm^{-1} (C–Cl) and change of peaks pattern at 1440 cm^{-1} and 1295 cm^{-1} (CH_2–Cl) occur. Another one peak occur of small intensity at 3425 cm^{-1} (–O–H) indicating the formation of hydrolysis product i.e. HEES. The results obtained from GC–MS and FT–IR data confirm the formation hydrolysis product of CEES on the surface of aggregates MnO_2 nanostructures material. According to the above GC–MS and FT–IR data, the proposed reaction mechanism of CEES decontamination on aggregates MnO_2 nanostructures is shown in **Fig. 6.12**. As per this, CEES molecules reacted with aggregated MnO_2 in two ways. In first way, CEES molecules reacted with physisorbed or encapsulated water molecules which were present on the MnO_2 surface to form non-toxic hydrolysis product i.e. HEES. The removal of Cl^- ion from CEES molecule on the surface of aggregates composed of MnO_2 nanostructures can be attributed due to their basic nature. During reaction, cyclic sulphonium ion is formed in the initial stage as shown in figure. This sulphonium ion is highly unstable in nature, that's why, it could not be detected by GC **[30]**. Subsequently, sulphonium ion reacts with water molecules exist in the aggregates MnO_2 nanoparticles and nanorods (no extra water was added during reaction) to form hydrolysis product i.e. HEES **[113, 135, 276]**. In another way, CEES molecules give surface bound alkoxy species after the reaction with isolated hydroxyl group (Mn-OH) and Lewis acid (Mn^{4+}) sites **[277, 278]**. Also, being a potential oxidising agent, aggregates MnO_2 nanostructures could not oxidise the CEES into its oxidation product. The observation can be attributed due to the predominant formation of highly unstable cyclic sulphonium ion intermediate which further reacted with the water molecules to form HEES. Another reason is the poisoning of the essential existing sites or functional groups on the aggregates MnO_2 nanostructures surface which are responsible for the oxidation reaction.

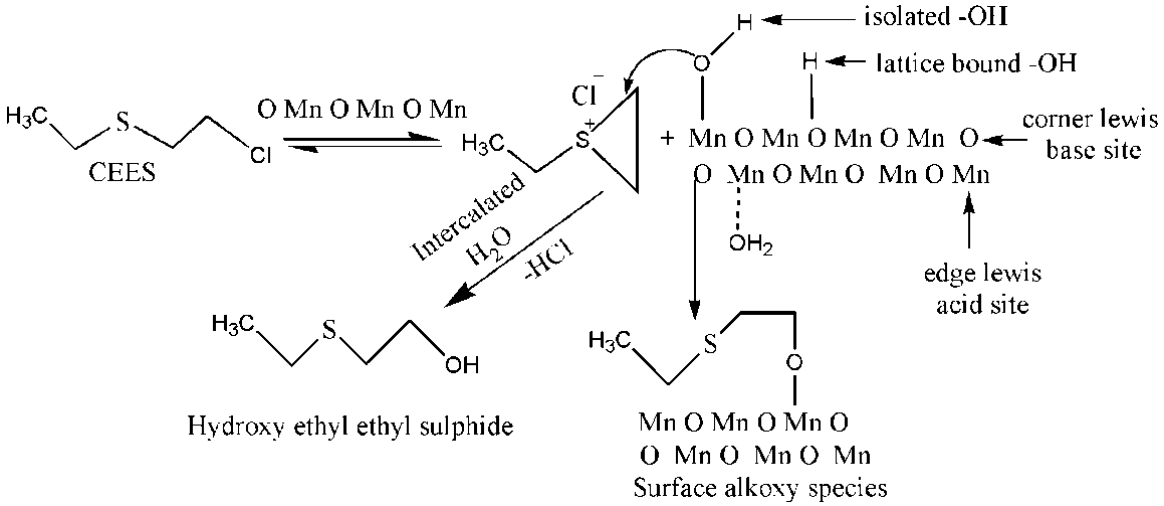

Fig. 6.12 Reactions scheme of CEES occurring on the surface of sorbent composed of MnO_2 nanoparticles and nanorods.

In case of DMMP degradation, GC–MS analysis of the expected degradation product of DMMP i.e. Methyl phosphonic acid (MPA) is difficult due to its polar and non–volatile nature. Hence, they were silylated by Bis (trimethylsilyl) trifluoro acetamide then analysed. Data obtained after silylation illustrates the m/z values at 73, 133, 147, 225 and 240 illustrates the formation of hydrolysis product of DMMP i.e. MPA further emphasizing the role of hydrolysis reaction thereby converting it to non–toxic. Moreover, FT–IR investigations of nanoaggregates MnO_2 that was exposed to DMMP reveals that the band intensity situated at 1275 cm^{-1} due to P=O and 1025 cm^{-1} due to P–O–C of DMMP changed and another band occur at 1336 cm^{-1} which indicates the interaction of P=O group with surface function group of aggregates MnO_2 nanostructures. Also, one peak occur at 3440 cm^{-1} indicates the formation of non–toxic hydrolysis product. These observation obtained from GC–MS and FT–IR results confirm the formation of MPA on the surface aggregates MnO_2 nanostructures and matches well with the previous reported data **[111]**.

Based on the GC–MS and FT–IR data, the proposed reaction scheme of DMMP decontamination to form MPA and surface bound phosphonate is given in **Fig. 6.13**. DMMP molecules also reacted with nanoaggregates MnO_2 in two ways. In one way, DMMP molecules interacted with physisorbed/intercalated H_2O to form methyl phosphonic acid (MPA), a non–toxic product and in another way they form surface bound phosphonates after the reaction

with isolated hydroxyl groups (Mn–OH) and Lewis acid (Mn^{+4}) sites. These observations matches very well with the previously reported results **[155, 264]**.

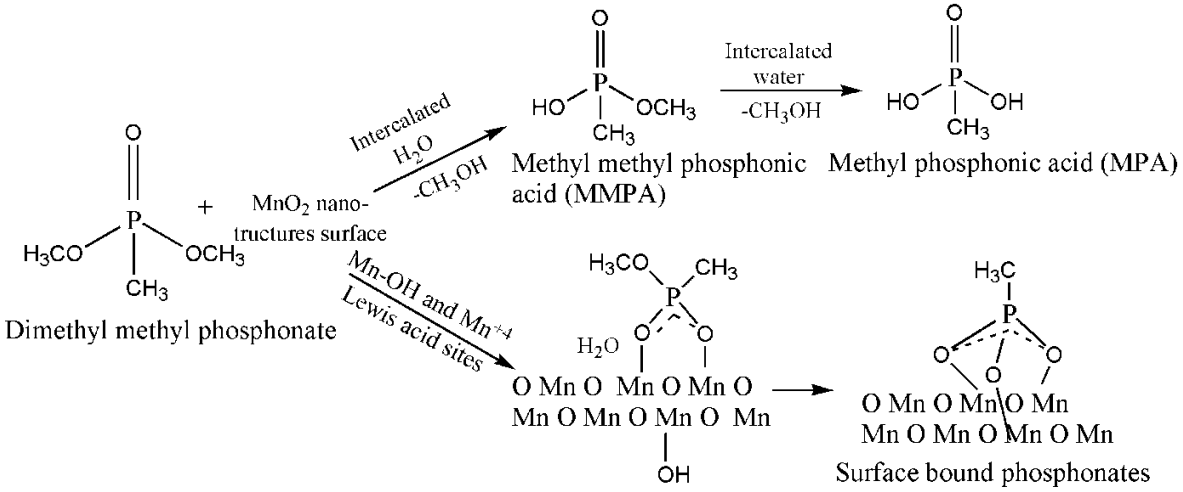

Fig. 6.13 DMMP reaction scheme occurring on the surface of sorbent composed of MnO_2 nanoparticles and nanorods.

Overall, occurrence of reactions within the sorbent composed aggregates MnO_2 nanostructures and formation of hydrolysis and surface bound species confirmed the degradation of CEES and DMMP and converting them into non–toxic form. In order to check the water content in the nanoaggregates MnO_2, TG analysis was carried out as depicted in **Fig. 6.14**. Figure shows 16.5% weight loss up to 220 ºC and it can be due to loss of water content present within the intercalated spaces of aggregates MnO_2 nanoparticles and nanorods.

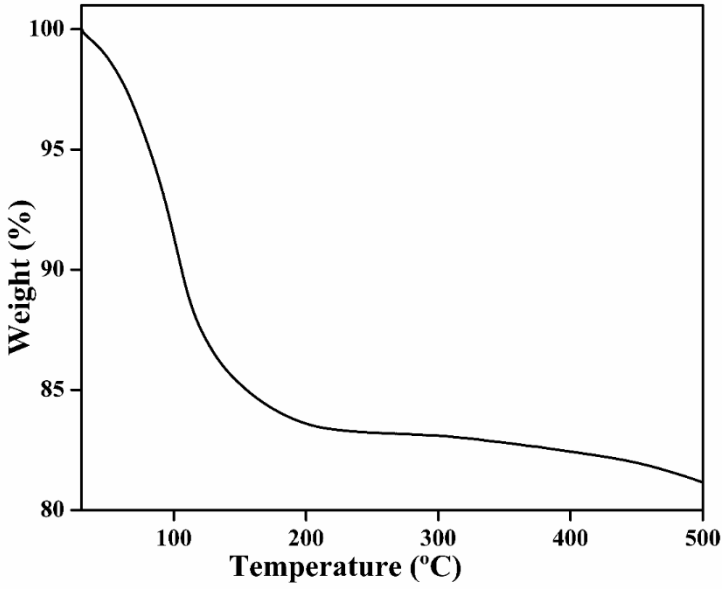

Fig. 6.14 TGA pattern of synthesized sorbent composed MnO_2 nanoparticles and nanorods.

Precisely, aggregates of MnO_2 nanoparticles and nanorods synthesized using reactive magnetron sputtering technique offer sufficient surface area and facilitate the sorption and encapsulation of the CEES as well as DMMP molecules. And then, water content in the intercalated sites, surface hydroxyl groups, Lewis sites etc. will react with the CEES/DMMP molecules thereby converting them into non−toxic products. The decontamination results of CEES and DMMP on the reactive sorbent composed of aggregates MnO_2 nanoparticles and nanorods synthesized in the current study were compared with earlier prepared and reported metal oxides nanostructures. In the case of CEES decontamination, magnetron sputtered nanoaggregates MnO_2 displays better decontamination reactivity compared to on per with existing solid decontaminants such as nanosized MgO, Al_2O_3, TiO_2 nanotubes, MnO_2 nanobelts, nanosheets and nanotubes etc. They exhibited relatively lower decontamination (>80%) with less rate constant values (>0.02 h^{-1}) than the currently synthesized aggregates MnO_2 nanoparticles and nanorods which decontaminate the CEES completely (100%) with better rate constant value (0.267 h^{-1}). Also, in case of DMMP decontamination, currently synthesized aggregates MnO_2 nanostructures exhibited better rate constant value (0.068 h^{-1}) than earlier reported rate constant values (>0.02 h^{-1}) of WO_3 nanoparticles and activated carbon . These results show that sputtered aggregates of MnO_2 nanoparticles and nanorods provides encouraging decontamination results on per with the existing solid decontamination sorbents.

6.2.4 Conclusion

Novel reactive adsorbent composed of aggregates MnO_2 nanoparticles and nanorods was synthesized using novel reactive magnetron sputtering technique and then characterised using XRD, FE−SEM, TEM, Raman, FT−IR, TGA etc. Thereafter, decontamination reactions of these MnO_2 nanostructures with CEES and DMMP was studied. The results indicate that aggregates MnO_2 nanostructures is promising sorbent for the decontamination of CEES as well as DMMP. It destroy the agents (predominantly through hydrolysis reactions) by pseudo first order kinetic reaction with rate constant and half life value 0.267 h^{-1} and 2.58 h for CEES, also 0.068 h^{-1} and 10.10 h for DMMP, respectively. Moreover, these synthesized aggregates MnO_2 nanostructures offers large surface area and enhanced chemical reactivity for immediate adsorption and detoxification of CWA to converting them into non−toxic form.

CHAPTER 7

CuO NANOPARTICLES APPLICATIONS FOR THE REMOVAL OF Cr (VI) AND Pb (II) IONS FROM AQUEOUS SOLUTION

7.1 Introduction

Recently, water pollution due to existence of heavy metal ions, which are introduced by industries, creates a global environmental issue especially due to their toxic bio-accumulative nature. The presence of the different heavy metals (Pb, Cr, Cd, Hg, As etc.) in water creates an alarming threat to humans, animals, aquatic organisms, plants, organisms of the ecosystem due to their harmful effects. Among them, Chromium (Cr) and lead (Pb) are used on large scale in preparation industries such as dyes, leather, textile, plating, wood preservation and metal cleaning are one of the most dangerous heavy metal pollutants **[279, 280].** Cr (III) and Cr (VI) are two important oxidation states in which, Cr (VI) is highly toxic and creates skin irradiation and carcinogenic, mutagenic and teratogenic effect in human body **[281]** and difficult to be adsorb onto inorganic material surfaces **[282].** The Pb^{2+} ion presence affects the growth, liver, kidneys, central nervous system and gastrointestinal system at low level of exposure while, it creates high blood pressure which causes fertility problems, muscle and joint pain, memory and concentration problem and irritability mentality regardless, coma at high level of exposure. Therefore, there is an urgent need of a newer effective method to remove the heavy metal ions from polluted water.

From the last few years, a number of various techniques such as sedimentation **[283]**, ion exchange **[284]** adsorption **[285]** membrane separation **[286]** and chemical precipitation **[287]** have been applied for the removal of heavy metal ions from polluted water. Among these, adsorption is an effective, feasible and low cost method. A number of adsorbents such as zeolite, activated carbon, metallic oxidant, waste industrial material, nanocomposites etc. have been used time to time for the removal of heavy metal ions from polluted water **[287–292].** However, they have high cost, large access time and low adsorption efficiency. Therefore, it is necessary to search for the newer adsorbent that gives high adsorption capacity within a short time to remove the Cr (VI) ions from water.

Metal oxides in the nano range exhibit considerable research interest related to removal of toxic heavy metal ions from polluted water due to their unique physical and chemical properties

and their exceptional performances due to their large specific surface area and active sites **[194, 293].** However, among different type of heavy metal ion pollutants, the removal efficiency of Cr (VI) and Pb (II) ions by various adsorbents is very limited.

In the present work, we have chosen copper oxide (CuO) nanoparticles as an adsorbent for the removal of Cr (VI) and Pb (II) ions. The CuO nanoparticles were synthesized using reactive magnetron sputtering, a novel physical vapor deposition (PVD) technique. Thereafter, different techniques were used to characterize them and then finally the adsorption properties for the removal of Cr (VI) and Pb (II) ions were studied.

7.2 Removal of hexavalent chromium ions using CuO nanoparticles for water purification applications

7.2.1 Preparation of CuO nanoparticles

CuO nanoparticles were deposited using reactive magnetron sputtering technique. The sputtering was carried out in a vacuum chamber using Cu target (5 mm thickness and 2 inch diameter). The base vacuum was ~10^{-7} Torr using a turbo molecular pump (TMP) backed by rotary pump before starting the sputtering. Thereafter, specific ratio of argon and oxygen gases was filled for sputtering. During sputtering, the temperature of the substrate was kept very low by filling the copper cold finger with liquid nitrogen (Liq. N_2). The low temperature was helpful to prevent the grain growth of the film and to produce nanoparticles. Also, low temperature minimizes the contamination of the deposited material. During sputtering, Cu atoms react with O_2 in the chamber or on the substrate to form CuO nanoparticles. After deposition, when the copper cold finger approaches room temperature, the particles were collected carefully. Sputtering parameters are listed in the **Table 7.1**.

Table. 7.1 Sputtering parameters for the synthesized CuO nanoparticles.

Target	Initial Pressure	Working Pressure	Gas Used	Deposition Time	Distance (d)	Power (Watt)	Substrate Temperature (ºC)
Copper	7.4×10^{-7} Torr	30×10^{-3} Torr	Ar/O_2 = 40/10	24 hours	4.5 cm	90 W	–194

d = Distance between target and substrate

7.2.2 Adsorption experiments

The standard stock solution of Cr (VI) ions (1 g/L) was developed by dissolving 2.8288 g $K_2Cr_2O_7$ in 1 litre distilled water. The desired concentrations were acquired by diluting the

stock solution with distilled water. The contents in the flasks were shaken for 180 min. with 250 rotations per min. (rpm) in a water bath shaker to get equilibrium at room temperature. Thereafter, the mixtures were centrifuged and residual Cr (VI) ions were analyzed using atomic adsorption spectrometer. The experiments were performed to examine the effect of different parameters such as pH, initial concentration, adsorbent dose, kinetic effect, temperature effect etc.

The removal efficiency and specific amount of contaminant at equilibrium was calculated as follows:

$$\% \text{ removal} = (C_o - C_e)/C_o \times 100 \qquad (7.1)$$

$$Q_e = (C_o - C_e) \times V/W \qquad (7.2)$$

Where, Q_e (mg/g) is the adsorption capacity in the solid at equilibrium; C_o and C_e are the initial and equilibrium concentrations of Cr (VI) ions (mg/L), respectively; V (mL) is the volume of the solution and W (g) is the weight of adsorbent used in the experiments. The pH effect on the chromium removal was studied by adjusting the pH values using 0.1 M HCl or 0.1 M NaOH solution. The adsorption kinetics experiment was performed to investigate the effect of contact time and then evaluate the kinetic properties under optimum experimental conditions by taking 1.6 g/L adsorbent dose, pH 3, 250 rpm and contact time 180 minutes.

7.2.3 Results and discussion

7.2.3.1 Characterization

Fig. 7.1 shows the typical XRD pattern of synthesized CuO nanoparticles which is identical with the single phase monoclinic CuO with lattice constants of a = 4.6883 Å, b = 3.4229 Å, c = 5.1319 Å and β = 99.5060º and matches well with the JCPDF card no. 00–048–1548. No other peak of any impurity was found in the XRD pattern thus indicating the high purity phase of the CuO nanoparticles. The broadening of the peaks depicts the small crystallite size of the nanoparticles, which was calculated from the prominent (11–1) and (111) diffraction peaks using Scherer formula and found to be ~8 nm. To further confirm the phase of the synthesized CuO nanoparticles, Raman spectrum was also recorded and is shown in **Fig. 7.2**. CuO belongs to the C_{2h}^6 space group having twelve vibrational modes at zero centre including three normally acoustic modes (A_u+2B_u), six infrared actives modes (3A_u+3B_u) and three Raman active modes

(A_g+2B_g). The Raman spectrum of the CuO nanoparticles shows three Raman active modes at 294, 332 and 626 cm^{-1}. The peak situated at 294 cm^{-1} belongs to the A_g mode and the peaks situated at 332 and 626 cm^{-1} belong to the B_g modes. These results match well with the previously reported data **[226, 227].** The broadening of peaks exhibits the small particle size of the synthesized nanoparticles as observed in XRD.

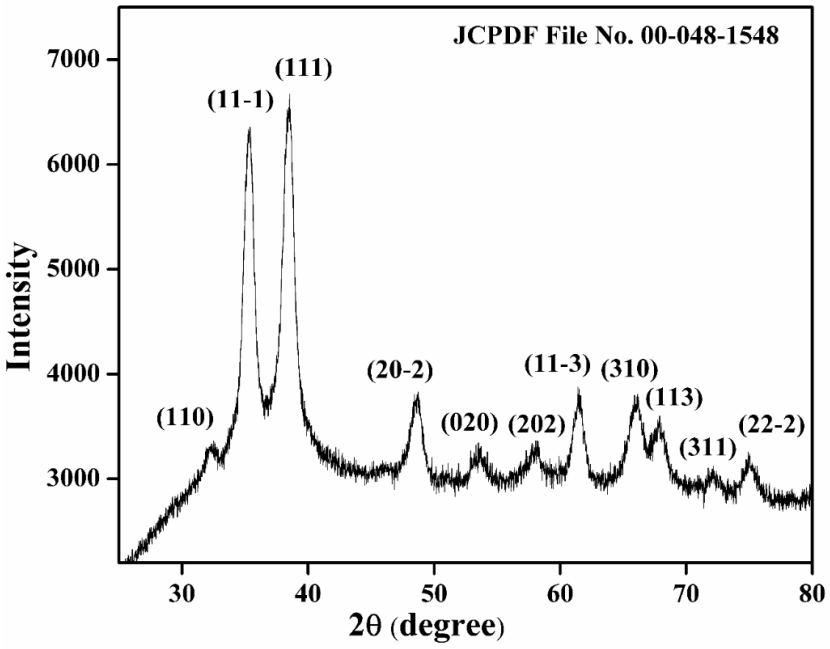

Fig. 7.1 XRD pattern of magnetron sputtered CuO nanoparticles.

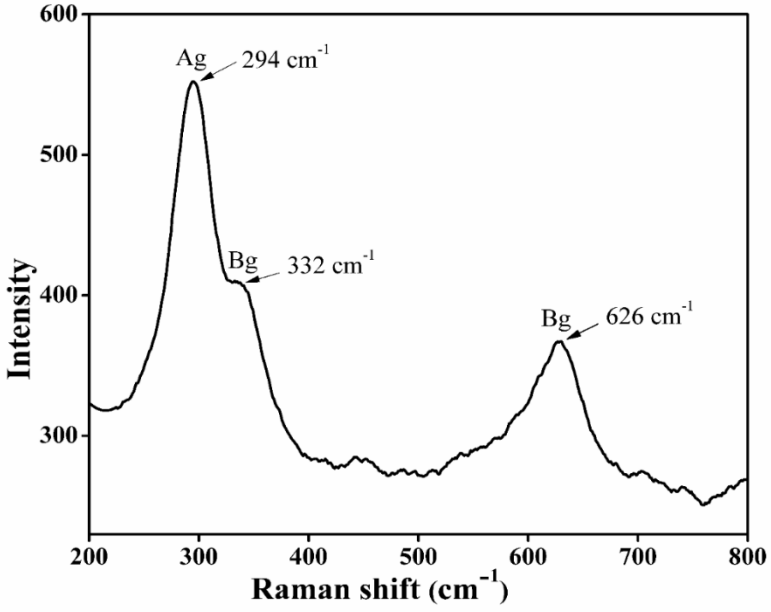

Fig. 7.2 Raman spectra of synthesized CuO nanoparticles.

The FE–SEM image of CuO nanoparticles represented in **Fig. 7.3** clearly reveals that the particles are uniformly distributed in the aggregated form with nearly spherical morphology. **Fig. 7.4** represents the EDS spectrum of the synthesized CuO nanoparticles, giving a proper stoichiometric ratio of Cu and O (1:1), which confirms the formation of pure CuO nanoparticles.

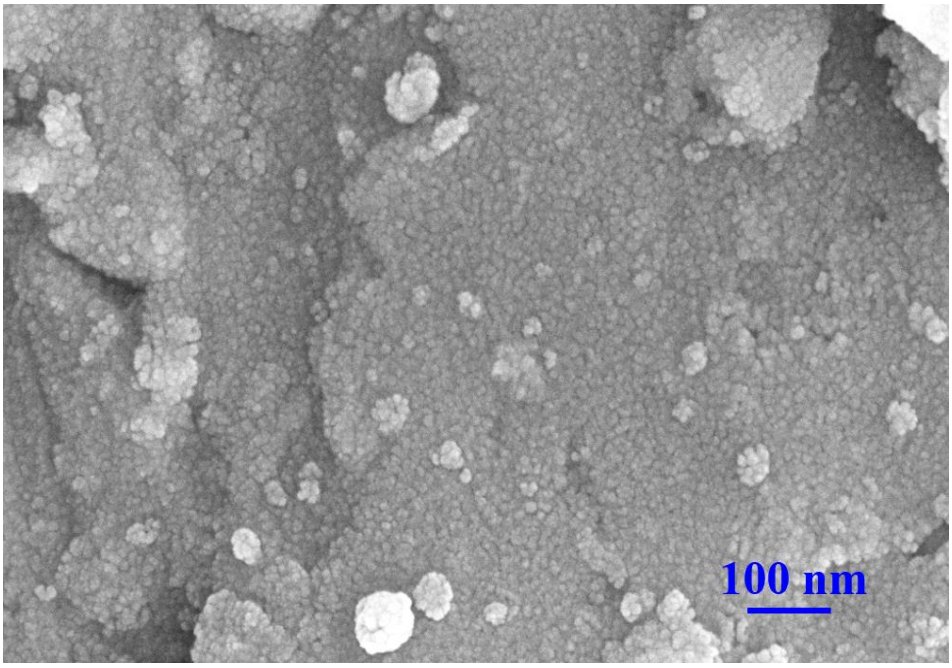

Fig. 7.3 FE–SEM image of synthesized nano-size CuO nanoparticles.

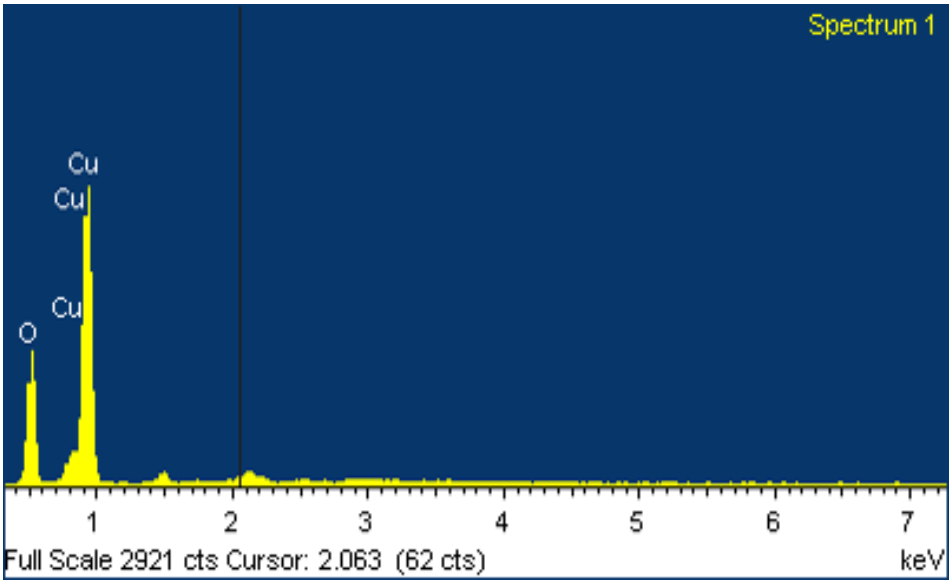

Fig. 7.4 EDS spectra of synthesized CuO nanoparticles.

The morphology and size of the nanoparticles was further evaluated by TEM image as shown in **Fig. 7.5**. The image shows that the nanoparticles are nearly spherical in aggregated form with a diameter ~8 nm which is in good agreement with the FE−SEM and XRD results.

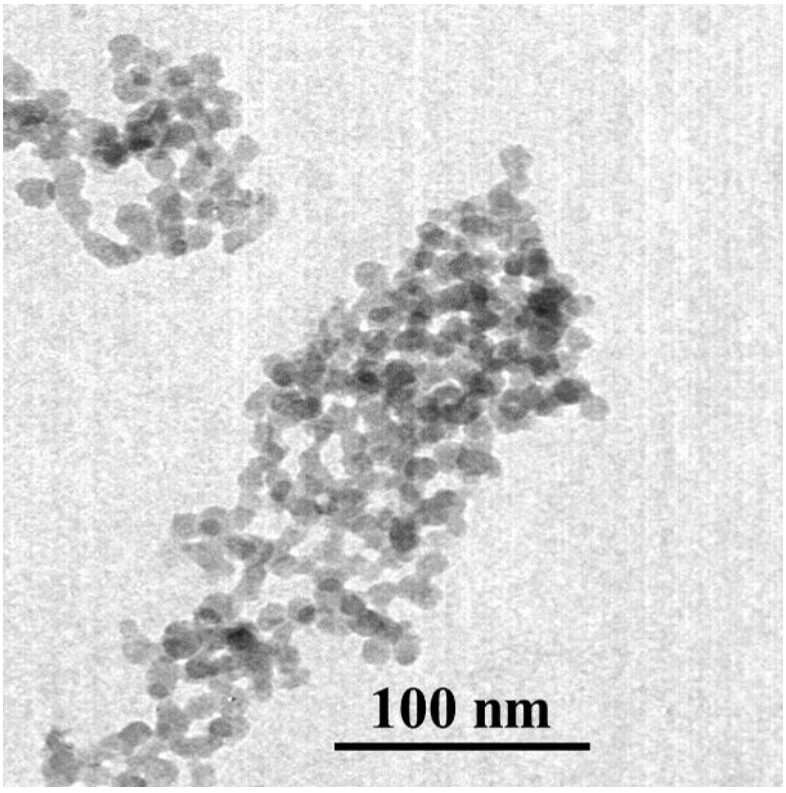

Fig. 7.5 TEM image of nano-size CuO nanoparticles.

The selected area electron diffraction (SAED) pattern of the TEM micrograph is shown in **Fig. 7.6**. This pattern exhibits the formation of concentric rings. The indexed diffraction rings can be ascribed to (11−1), (111), (20−2), (020), (202) and (11−3) planes of the monoclinic CuO, verifying the XRD and Raman results. The HR−TEM image of the CuO nanoparticles (**Fig. 7.7**) exhibits lattice fringes of 0.170 nm spacing which corresponds to the d spacing of the (020) plane, again confirming the crystalline structure of the synthesized CuO nanoparticles. The specific surface area of CuO nanoparticles calculated from BET surface area analyzer was 84.327 m^2/g. The pH_{zpc} of CuO nanoparticles was discussed in the earlier section and value of pH_{zpc} is found to be 6.9 which concluded that the adsorbent surface had a positive charge in aqueous medium.

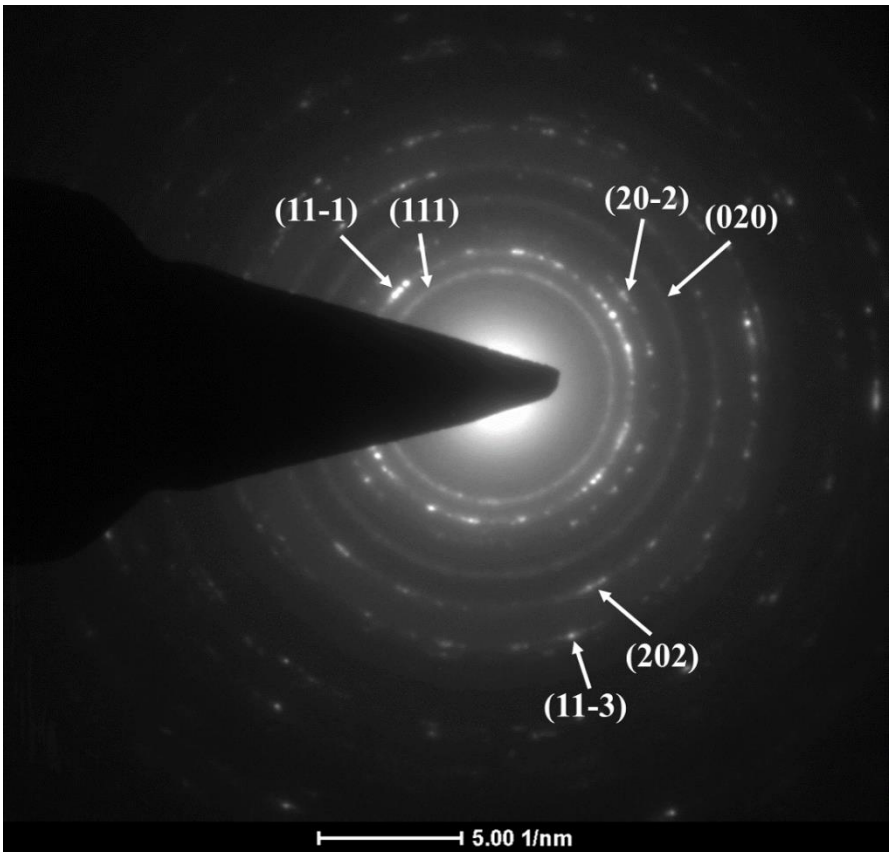

Fig. 7.6 SAED pattern of prepared CuO nanoparticles.

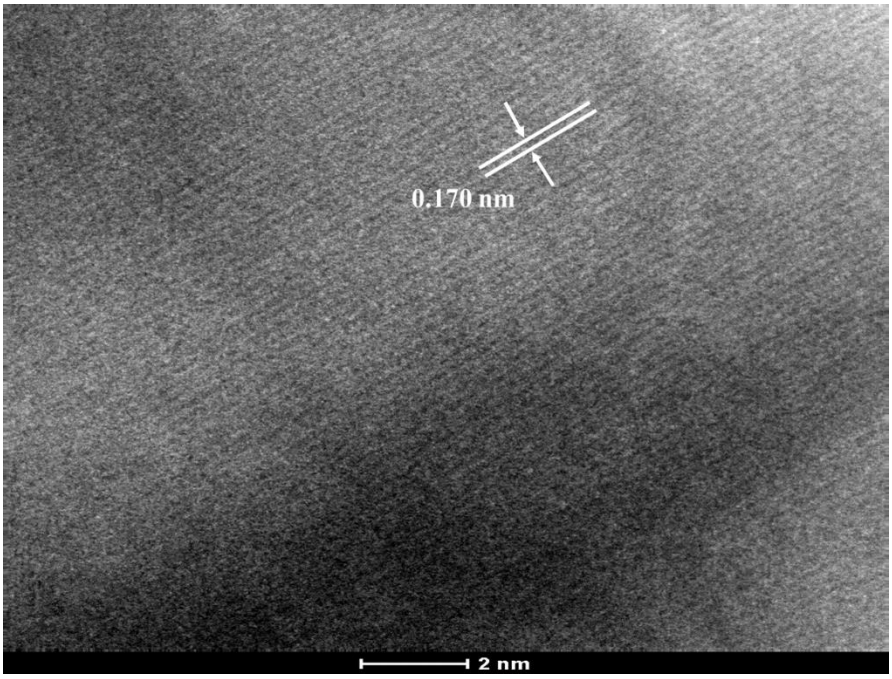

Fig. 7.7 HR–TEM of prepared CuO nanoparticles.

7.2.3.2 Effect of pH

pH is an important parameter in the Cr (VI) ions adsorption experiments in aqueous solution. The predominant Cr (VI) species, monovalent bichromate ($HCrO_4^-$) and dichromate ($Cr_2O_7^{2-}$), were formed in aqueous solution with 1< pH< 6 and dominant species (CrO_4^{2-}) were formed at above pH 6 **[294].** Among these anions, $HCrO_4^-$ is preferentially adsorbed on the positively charged surface of CuO nanoparticles **[295, 296].** So, to find out the best pH value at which maximum removal of Cr (VI) ions occur, the experiments were carried out with 100 mL of 20 mg/L Cr (VI) ions concentration, adsorbent dose 1g/L, contact time 180 min at different pH values from 2–11 at room temperature. **Fig. 7.8** indicates that the percentage of removal increased from 59.5 to 65.5% with increasing pH from 2 to 3 followed by gradual decrease upto 33.05% on further increase in pH value upto 10. The best pH value for Cr (VI) ions adsorption over CuO nanoparticles was 3 at which maximum percentage removal (65.6%) and adsorption capacity (13.1 mg/g) occur. This pH is well consistent with the previous reports in the similar range of Cr (VI) ions concentrations **[297].** The high removal efficiency at low pH can be explained on the basis of aqueous chemistry of Cr (VI) ions and charge distribution over the adsorbent surface in response to various pH. In acidic medium, the adsorbent surface contain high quantities of hydronium ions (H^+) which leads to stronger electrostatic attraction between negatively charged chromium oxy-anions and protonated sorbent, favouring the metal adsorption. At high acidic pH, adsorbent surface becomes frail and less stable due to the surface oxidation which leads to organic leaching and results into lower metal adsorption **[295].** These findings are supported by the point of zero charge (pH_{zpc}) of CuO nanoparticles which is nearly 6.9. Therefore, with the increase in pH from the best pH value (i.e. at pH 3) to the alkaline range, the degree of protonation of CuO nanoparticles surface continuously decreased up to 6.9. Above this value, the surface attends a net negative charge which is not a favourable condition for the adsorption of chromium oxyanions. Moreover, at higher pH, the number of hydroxyl group (OH^-) in the solution increases which creates repulsion between chromium oxyanions and OH^- for the limited adsorption sites. As a result, efficiency of Cr (VI) ions removal decreases in adsorption.

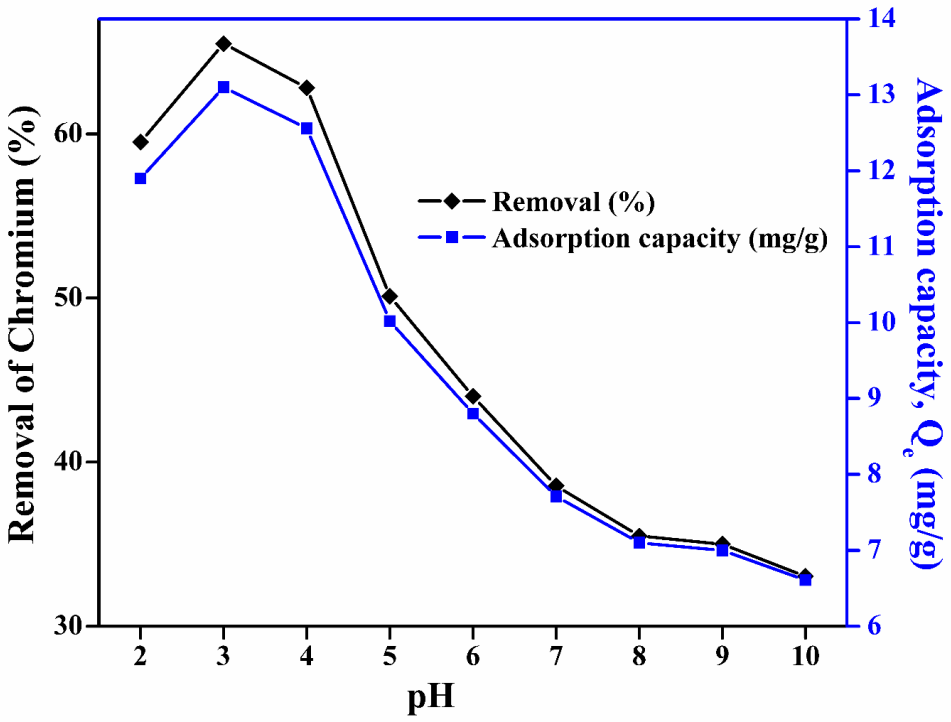

Fig. 7.8 Effect of pH on Cr (VI) ions removal and uptake capacity with CuO nanoparticles.

7.2.3.3 Effect of dose

During adsorbent dose effect, the CuO nanoparticles dose in a range of 0.4–5 mg/L was used for adsorption of Cr (VI) ions, pH 3 and initial Cr (VI) ions concentration of 20 mg/L were used as experimental conditions at room temperature and the results are represented in **Fig. 7.9**. As can be seen from the figure, the Cr (VI) ions removal was increased from 34.5% to 83% as the adsorbent dose increased from 0.4 g/L to 1.6 g/L and after that it reached upto 92.8% as the adsorbent dose was increased to 5 g/L. The results reveal that, with increase in the adsorbent dose from 0.4 g/L to 5 g/L, the adsorption capacity of CuO nanoparticles gradually decreases from 86.25 to 18.56 mg/g. In fact, the adsorption capacity of the adsorbent depends upon the metal to binding sites ratio. At higher dose, the available Cr (VI) ions were insufficient to saturate the entire binding sites existing on CuO nanoparticles surface, thus resulting into lesser adsorbed Cr (VI) ions on per unit weight of CuO adsorbent and leading to lower adsorption capacity. In addition, the percentage removal of Cr (VI) ions increases due to sufficient availability of large surface area and vacant adsorption sites at higher adsorbent dose. After attaining the equilibrium state, further increase in adsorbent dose had not shown any enhanced effect in adsorption. Therefore, to maintain the reasonable values of both i.e. high removal

efficiency and adsorption capacity per unit mass of CuO adsorbent, a dosage of 1.6 g/L was used for further experiments.

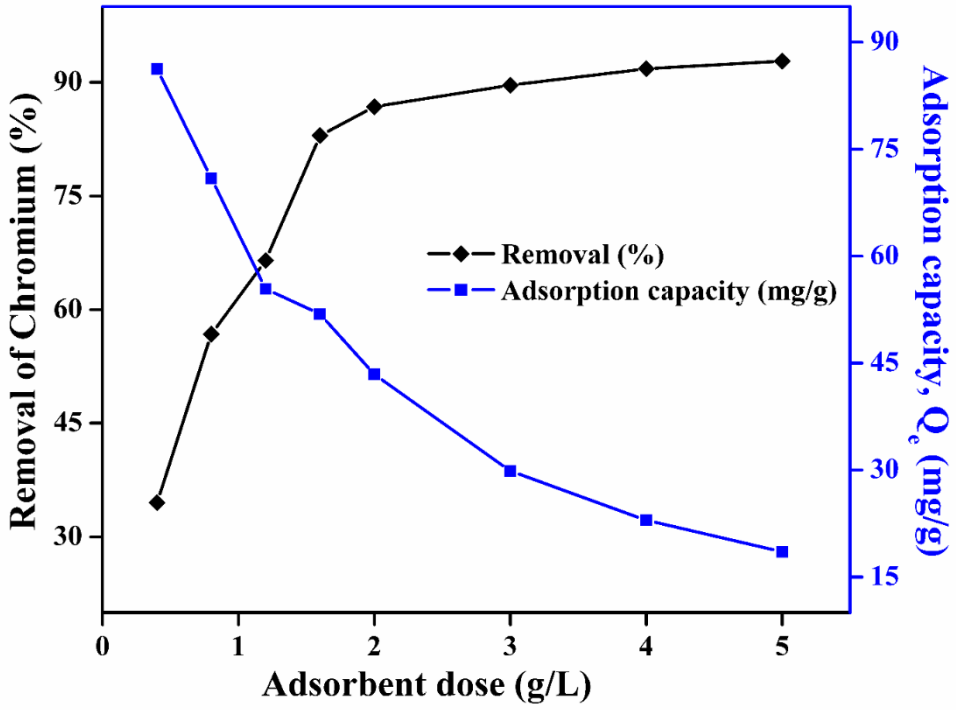

Fig. 7.9 Effect of adsorbent dose on Cr (VI) ions removal and uptake capacity with CuO nanoparticles.

7.2.3.4 Effect of contact time

The contact time experiment was carried out to investigate the time of equilibrium for Cr (VI) ions adsorption on CuO nanoparticles at optimum experimental conditions. In this case, Cr (VI) ions concentration 20 mg/L, pH 3 and dose 1.6 g/L were used at room temperature. The removal of Cr (VI) ions in solution was consistently observed until equilibrium did not occur. The results, as displayed in **Fig. 7.10**, represented that rapid adsorption occurs in the initial phase (first 10 min) and then attend equilibrium state within ~60 min. Initially, rapid adsorption occurs due to present of sufficient vacant sites that are available and a great concentration gradient exists between the adsorbate in the aqueous and solid phases. Thereafter, it became slow due to interparticular competition of ions for the available binding sites and ultimately equilibrium was accomplished.

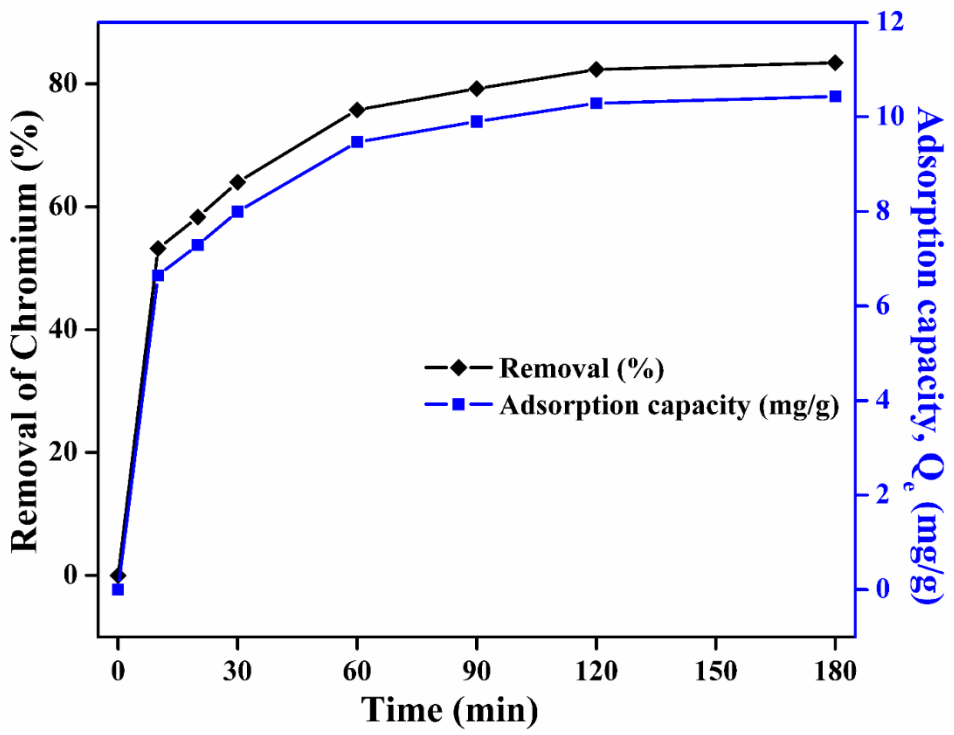

Fig. 7.10 Effect of contact time on Cr (VI) ions removal and uptake capacity with CuO nanoparticles.

7.2.3.5 Effect of Cr (VI) ions concentration

The effect of concentration was investigated by taking 10, 20, 30, 50, 70, 100 and 150 mg/L concentration of Cr (VI) ions, contact time 180 min, pH 3, and dose 1.6 g/L at room temperature. The results shown in **Fig. 7.11** indicate that, at very low initial metal ions concentration (10 mg/L), the maximum removal efficiency (96.3%) was achieved. When the initial concentration of Cr (VI) ions was increased from 10 to 150 mg/L the removal efficiency continuously decreased from 96.3 to 16.33%. Whereas, the adsorption capacity of CuO nanoparticles increased from 6.01 to 13.21 mg/g with increase in the initial Cr (VI) ions concentration from 10 to 50 mg/L and thereafter it became nearly constant on further increase in metal ion concentration. At lower concentration, higher removal efficiency is obtained due to presence of large surface area as well as binding sites of CuO nanoparticles. While, as initial metal ion concentration becomes high, the removal efficiency will be low due to presence of less available sites for Cr (VI) ions.

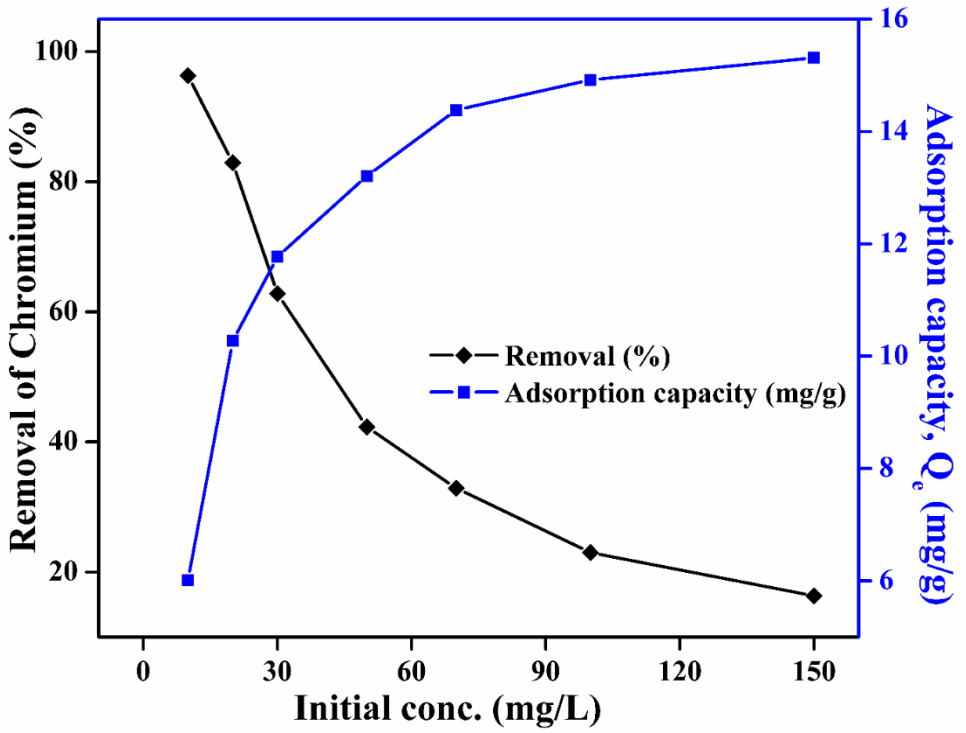

Fig. 7.11 Effect of initial metal ion concentration on Cr (VI) ions removal and uptake capacity with CuO nanoparticles.

7.2.3.6 Effect of stirring speed

Stirring speed is also another parameter in the adsorption experiments since it affects the solute distribution in the bulk solution which forms the external boundary layer. From the experimental results, it was observed that, the percentage removal of chromium ion on CuO nanoparticles adsorbent at three different stirring speeds 200, 250, 300 rpm had no impact on Cr (VI) ions adsorption. This confirms that the solid adsorbent was completely and homogeneously mixed in solution. Hence, stirring speed had no outstanding effect on the rate of adsorption. It was also clear that external diffusion was not the rate limiting step in this adsorption process.

7.2.3.7 Thermodynamic study

The temperature effect was carried out in the range of 25–45 ºC on CuO nanoparticles based adsorbent, while all other optimized parameters such as pH 3, adsorbent dose 1.6 g/L, Cr (VI) ions concentration 20 mg/L and contact time 180 min were fixed. The results show that, as the temperature was increased from 25 to 45 ºC, the adsorptive removal of Cr (VI) ions increased

from 83 to 94%. The thermodynamic parameters such as Gibb's free energy change (ΔG), enthalpy change (ΔH) and entropy change (ΔS) for adsorption process were calculated using the following equations (3), (4) and (5), respectively **[298, 299]**.

$$\Delta G = -RT \ln K_L \qquad (7.3)$$

$$\Delta G = \Delta H - T\Delta S \qquad (7.4)$$

From both the above equations, we get:

$$\ln K_L = -\Delta H / RT + \Delta S/R \qquad (7.5)$$

Where R (8.314 J mol^{-1} K) is the ideal gas constant and T is the temperature in Kelvin. The values of ΔG, ΔH, ΔS and can be find out by plotting the ln K_L versus 1/T. The results are summarized in **Table 7.2**. Positive ΔH value indicates the endothermic behaviour of Cr (VI) ions adsorption and negative values of ΔG concluded the spontaneous nature of adsorption. The low value of ΔS shows that, during the adsorption experiments, no significant changes occur in the entropy. Also, the positive ΔS value reflects the increase in randomness of metal ions in solid-solution interaction and also indicate the occurrence of ion replacement reactions during adsorption **[300].**

Table. 7.2 Thermodynamics parameters for the Cr (VI) ions adsorption onto CuO nanoparticles.

Temperature (K)	ΔH (kJ/mol)	ΔS (kJ/mol/K)	ΔG (kJ/mol)
298	190.216	0.700	–18.568
308			–25.574
318			–32.581

7.2.3.8 Kinetics of Adsorption

The kinetics of chromium adsorption onto CuO nanoparticles was evaluated by three models viz. pseudo first-order **[301]**, pseudo second-order **[302]** and intraparticle diffusion **[303]**

models and the results are given in **Fig. 7.12–7.14**. The pseudo first-order equation (**eq. 7.6**) assumes that the binding is originated from physical adsorption.

$$\ln (Q_e - Q_t) = \ln Q_e - k_1 t \qquad (7.6)$$

The pseudo second-order model (**eq. 7**) gives chemical adsorption (chemisorption).

$$\frac{t}{Q_t} = \frac{1}{k_2 Q_e^2} + \frac{t}{Q_e} \qquad (7.7)$$

In addition to this, the intraparticle diffusion model (**eq. 7.8**) was applied to identify the diffusion mechanism.

$$Q_t = k_i\, t^{1/2} + C \qquad (7.8)$$

Where, Q_e and Q_t are the adsorption capacity (mg/g) of CuO nanoparticles at equilibrium and at time t (min), respectively. k_1 (per min) and k_2 (g/mg×min) are the pseudo first-order and pseudo second-order rate constant values, respectively. The k_i (mg/g×$min^{0.5}$) and C are the intraparticle diffusion rate constant and intercept, respectively. The initial adsorption rate was calculated using the relation: $h = k_2 Q_e^2$. The linearized results are represented in **Table. 7.3**

Table. 7.3 Coefficients studies of kinetic models for the Cr (VI) ions adsorption over CuO nanoparticles.

Kinetics models	**CuO nanoparticles**
Kinetic study and model parameters	
Pseudo first-order model	
R^2	0.982
Q_e (mg/g)	5.566
k_1 (min^{-1})	0.0287
Pseudo second-order model	
R^2	0.998
Q_e (mg/g)	11.111
k_2 (g/mg min)	0.00955
h (mg/g min	1.178

Intraparticle diffusion model	
R^2	0.963
k_i	0.487
C	5.240

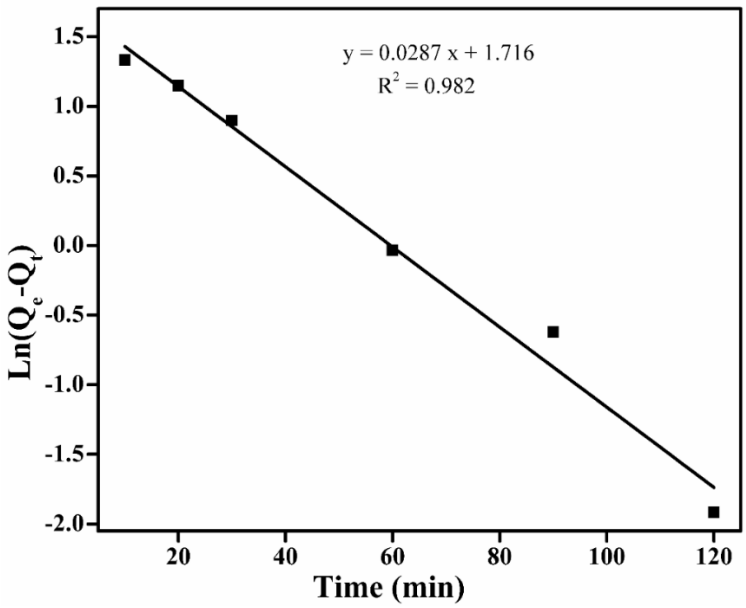

Fig. 7.12 Pseudo first-order kinetic model for Cr (VI) ions adsorption for CuO nanoparticles.

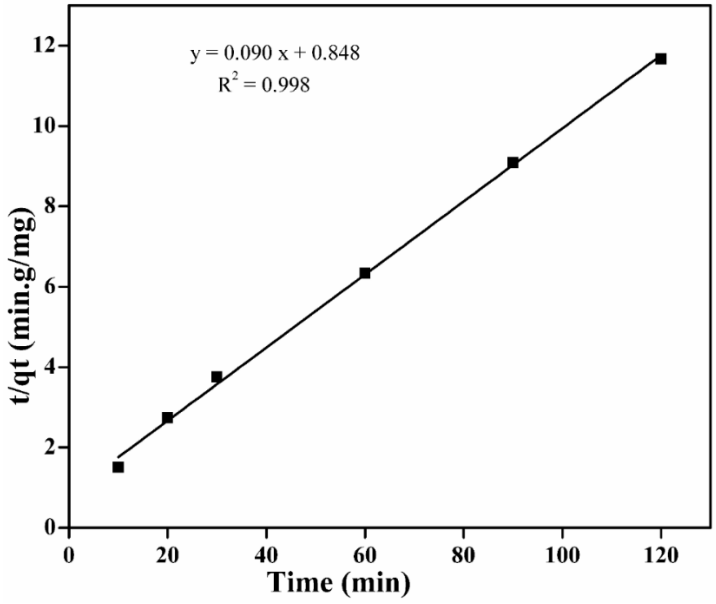

Fig. 7.13 Pseudo second-order kinetic model for Cr (VI) ions adsorption for CuO nanoparticles

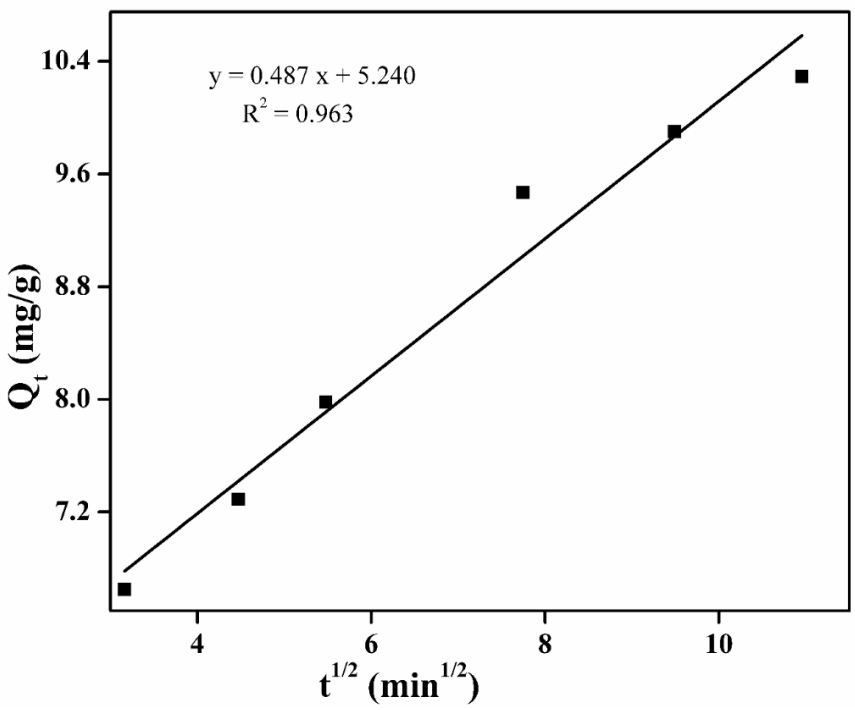

Fig. 7.14 Intra particle diffusion kinetic model for Cr (VI) ions adsorption for CuO nanoparticles.

From the large value of correlation coefficient (R^2), the kinetics results display that the adsorption process of Cr (VI) ions is followed by pseudo second-order model (R^2 = 0.998) rather than pseudo first-order (R = 0.982) and intraparticle diffusion (R^2 = 0.963) model, which indicates that the adsorption process of Cr (VI) ions was due to chemisorption. The hypothesis behind the pseudo second-order model is that the rate-limiting step in the current process may be chemisorption involving valence forces through sharing or exchange of electrons between adsorbent and adsorbate **[304].**

7.2.3.9 Adsorption isotherm

Adsorption isotherms provide a relationship between the amount of adsorbate per unit mass of adsorbent at a specific temperature and its concentration in equilibrium. A number of isotherm models such as Langmuir, Freundlich, Tempkin, Dubinin-Radushkevich, Redlich-Peterso and Ships have been reported to explain the equilibrium between adsorbent and solution **[305].** Here, Langmuir and Freundlich isotherm models were used for the isotherm studies by varying the initial Cr (VI) ions concentration from 10 to 150 mg/L.

The well known linearized equation of Langmuir isotherm model **[306]** is represented as

$$\frac{C_e}{Q_e} = \frac{1}{Q_o K_L} + \left(\frac{1}{Q_o}\right) C_e \qquad (7.9)$$

Where, C_e is the equilibrium concentration in mg/L, Q_e is the amount of adsorbate adsorbed at equilibrium in mg/g and Q_o (mg/g) and K_L (L/mg) are the Langmuir constants related to the adsorption capacity and the rate of adsorption, respectively. When C_e/Q_e vs C_e was plotted, a straight line with slope $1/Q_o$ and intercept $1/(Q_o K_L)$ is obtained as shown in **Fig. 7.15**. From these, Langmuir constants Q_o and K_L were calculated and are listed in **Table 7.4**. To determine the effect of adsorption isotherm, another important parameter R_L, a dimensionless constant which is referred to as separation factor or equilibrium parameter is defined by the following relation **[307]**.

$$R_L = \frac{1}{1 + K_L C_0} \qquad (7.10)$$

Where K_L (L/mg) is the Langmuir constant, C_o (mg/L) is the highest initial Cr (VI) ions concentration. The value of R_L signifies whether the adsorption will be favourable or not. Adsorption will be unfavourable if $R_L > 1$, Linear if $R_L = 0$ and favourable if $0 < R_L < 1$ **[308]**. Here, the obtained value of R_L is 0.0182 for Cr (VI) ions adsorption, which is greater than zero and less than 1, thus indicating favourable adsorption.

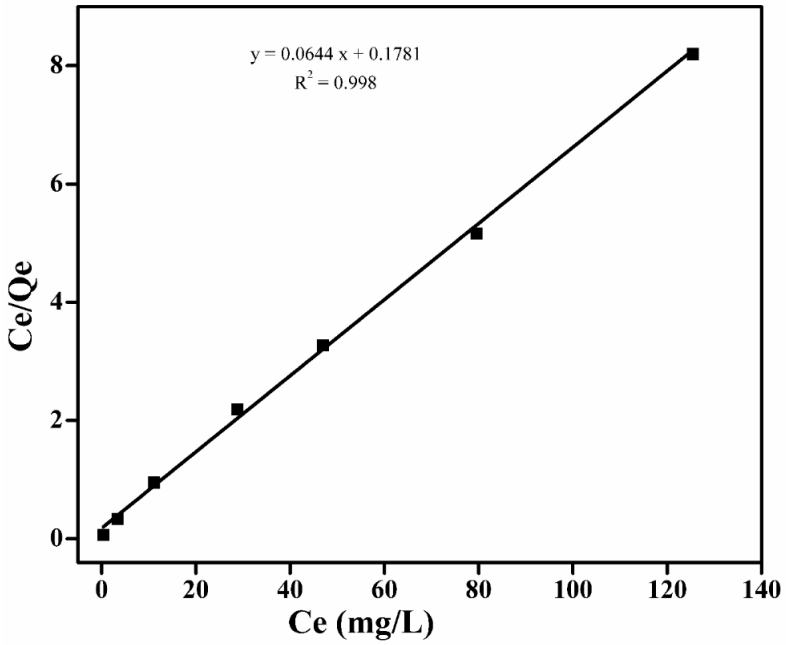

Fig. 7.15 Langmuir isotherm for Cr (VI) ions adsorption onto CuO nanoparticles.

Table 7.4 Coefficients studies of isotherm models for the Cr (VI) ions adsorption over CuO nanoparticles at different temperatures.

Isotherm	Parameters	25 ºC	35 ºC	45 ºC
Langmuir	Q_e (mg/g)	15.625	17.636	18.518
	K_L (L/mg)	0.0359	0.388	4.50
	R^2	0.998	0.994	0.999
	R_L	0.0182	0.0168	0.00147
Freundlich	n	6.451	6.493	7.751
	K_F (mg/g)(L/mg)$^{1/n}$	7.667	8.944	11.279
	R^2	0.946	0.926	0.940

The Freundlich isotherm model exhibits an empirical relationship which describes the heterogeneity of sorbent surface and reflects as multilayer adsorption. The linearized form of Freundlich isotherm is given below **[309]**.

$$\ln Q_e = \ln K_F + \frac{1}{n} \ln C_e \qquad (7.11)$$

Where, Q_e and C_e are the same as in Langmuir isotherm, K_F and n are the Freundlich constants (in **Eq. 7.11**). K_F [(mg/g) (L/g)$^{1/n}$] is related to the binding energy of the adsorbent and n is the heterogeneity factor which measures the deviation from linearity of the adsorption. It exhibits the degree of non-linearity between the adsorption and solution concentration. The adsorption will be favourable if the value will be in the range of 1 to 10. The plot between ln Q_e vs ln C_e gives a straight line with slope 1/n and intercept ln K_F, as represented in **Fig. 7.16**. The values of Freundlich constants are given in **Table 7.4**. Both the isotherm experiments were carried out at room temperature.

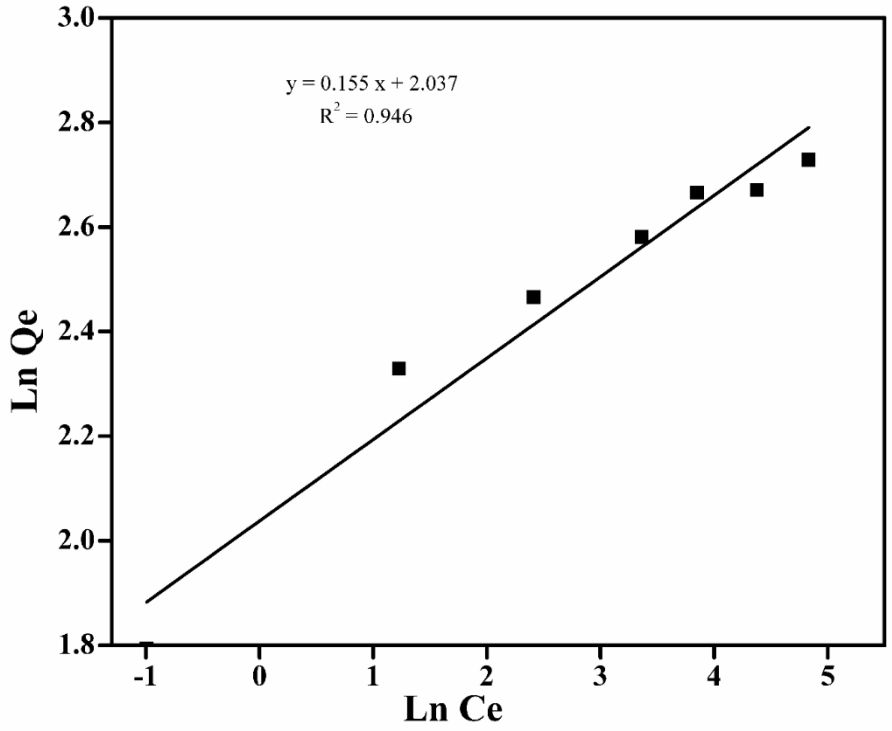

Fig. 7.16 Freundlich isotherm for Cr (VI) ions adsorption onto CuO nanoparticles.

The higher value of correlation coefficients R^2 depicts that the adsorption follows Langmuir isotherm model rather than the Freundlich isotherm model. Fitness of Langmuir isotherm model exhibits that the adsorption of Cr (VI) ions on the surface of CuO nanoparticles was monolayer and adsorption energy was uniformly distributed over the adsorbent surface.

A comparison was carried out of the contact time and adsorption capacity for Cr (VI) ions removal by other adsorbents with currently synthesized CuO nanoparticles in the present work and is shown in **Table 7.5** and **Table 7.6** respectively. The high adsorption capacity within a short contact time in this study reveals that magnetron sputtered CuO nanoparticles could be a promising adsorbent for Cr (VI) ions removal.

Table 7.5. Comparison between different adsorbent for the Cr (VI) ions removal.

Adsorbent	Contact time (min)	References
Fe^0 nanorods modified with chitosan in porous anodic alumina (PAA)	400	**[316]**
Titanium oxide–Ag composite (TOAC)	720	**[317]**
magnetic graphene oxide via ethylenediamine	360	**[318]**
graphene sand composite (GSC)	100	**[319]**
Magnetron sputtered CuO nanoparticles	180	Current study

Table 7.6 A comparative study of various adsorption capacities for Cr (VI) ions.

Adsorbent	Adsorption capacity (mg/g)	References
Single-walled carbon nanotubes	2.35	**[315]**
Multi-walled carbon nanotubes	1.26	**[315]**
CuO nanoparticles synthesized through green route	8.42	**[108]**
Cationic surfactant-modified Activated carbon	1.81	**[320]**
Sawdust activated carbon	3.46	**[321]**
Granular activated carbon	7.20	**[322]**
Polypyrrole/graphene oxide composite	9.56	**[312]**
Almond	10.62	**[323]**
Sulphur acid-modified waste activated carbon	7.49	**[324]**
Magnetron sputtered CuO nanoparticles	15.625	Current study

7.2.4 Conclusion

Copper (II) oxide nanoparticles have been successfully synthesized using reactive magnetron sputtering technique and then characterized by various techniques such as powder XRD, FT–IR, Raman, FE–SEM, TEM and N_2–BET which confirm the formation of

monoclinic phase with high purity and narrow size distribution. CuO nanoparticles were found to be an effective nano-adsorbent for the removal of Cr (VI) ions from waste water. The optimized conditions for the Cr (VI) ions removal were found to be: pH of 3, adsorbent dose of 1.6 g/L and Cr (VI) ions concentration of 20 mg/L. The removal efficiency of CuO nanoparticles was found to decrease with increase in the concentration of Cr (VI) ions. Thermodynamic studies show the feasible, endothermic and spontaneous nature of adsorption process. The Cr (VI) ions adsorption follows pseudo-second order kinetics. The isotherm data shows well fit to Langmuir model with maximum adsorption efficiency of 15.62 mg/g which confirms monolayer adsorption over the CuO nanoparticles surface.

7.3 Adsorptive removal of Pb (II) ions from aqueous solution using CuO nanoparticles synthesized by sputtering method

7.3.1 Synthesis of CuO nanoparticles

CuO nanoparticles were deposited onto a copper cold finger substrate using reactive magnetron sputtering technique. The sputtering was carried out in a vacuum chamber using Cu target (5 mm thickness and 2 inch diameter). The vacuum was created upto 10^{-7} Torr using a turbo molecular pump (TMP) backed by rotary pump before starting the sputtering. Argon and oxygen gases were filled in the specific ratio for sputtering. During sputtering, the temperature of the substrate was putted very low by filling the liquid nitrogen (Liq. N_2), which helps to prevent the grain growth of the film producing nanoparticles. Also, low temperature minimizes the contamination to the deposited material. During sputtering, Cu atoms were reacted with O_2 atoms in the chamber or on the substrate to form CuO nanoparticles. After deposition, when the copper cold finger attends the room temperature, the particles were collected carefully. The sputtering parameters are listed in **Table 7.7**.

Table 7.7 Sputtering parameters for the CuO nanoparticles preparation.

Target	Initial Pressure	Working Pressure	Gas Used	Deposition Time	Distance (d)	Power (Watt)	Substrate Temperature (ºC)
Copper	7.4×10^{-7} Torr	30×10^{-3} Torr	$Ar/O_2 = 40/10$	24 hours	4.5 cm	90 W	–194

d = Distance between target and substrate

7.3.2 Batch adsorption experiments

The standard stock solution of Pb (II) (1g/L) was prepared carefully by dissolving the 1.5984 g $Pb(NO_3)_2$ in 1 L distilled water. The desired concentrations of the solutions were obtained by diluting the standard stock solution with distilled water. The series of batch adsorption experiments studies were conducted by mixing a specific amount of adsorbent with 100 mL of working standard solution in 250 mL Erlenmeyer flasks. The contents in the flasks were shaken for 180 minutes with 300 rotations per minutes (rpm) in a water bath shaker to get equilibrium at room temperature. Thereafter, the mixtures were centrifuged and remaining Pb (II) ions were analyzed using atomic adsorption spectrometer (AAS). The batch adsorption experiments were performed to investigate the effect of different parameters such as pH, initial concentration, adsorbent dose, kinetic effect, temperature effect.

The removal efficiency and specific amount of contaminant at equilibrium was calculated from the **eq. (1)** and **(2)** The adsorption kinetic experiment was performed to investigate the effect of contact time and then evaluate the kinetic properties under optimum experimental conditions by taking adsorbent dose 20 g/L, pH 6, 300 rpm, contact time 180 minutes. All the experiments were performed three times and the average value of the obtained data was accepted for the analysis.

7.3.3 Results and discussion

7.3.3.1 Characterization

The powder XRD pattern of the synthesized CuO nanoparticles is shown in **Fig. 7.17**, identical to the pure monoclinic phase of CuO with of a = 4.6837 Å, b = 3.4226 Å, c = 5.1288 Å and β = 99.5400º α = γ = 90.000° which matches well with the JCPDF card no.01–072–0629. No other peak of any purity such as $Cu(OH)_2$ or Cu_2O was observed in XRD pattern, indicating the high purity phase of CuO nanoparticles. The average crystallite size of the synthesized CuO nanoparticles was found to be ~9 nm calculated using Scherer formula from the dominant peaks (11–1) and (111).

The structural phase was further confirmed by Raman analysis as shown in **Fig. 7.18**. CuO belongs to the C_{2h}^6 space group having twelve vibrational modes at zero centre including three normally acoustic modes (A_u+2B_u), six infrared actives modes (3A_u+3B_u) and three Raman active modes (A_g+2B_g). The spectrum of the CuO nanoparticles shows three Raman active modes at 290, 334 and 626 cm^{-1}. The peak situated at 290 cm^{-1} belongs to the Ag mode and the peaks situated at 334 and 626 cm^{-1} belong to the B_g modes which are in good agreement with the previously reported data **[226, 227].**

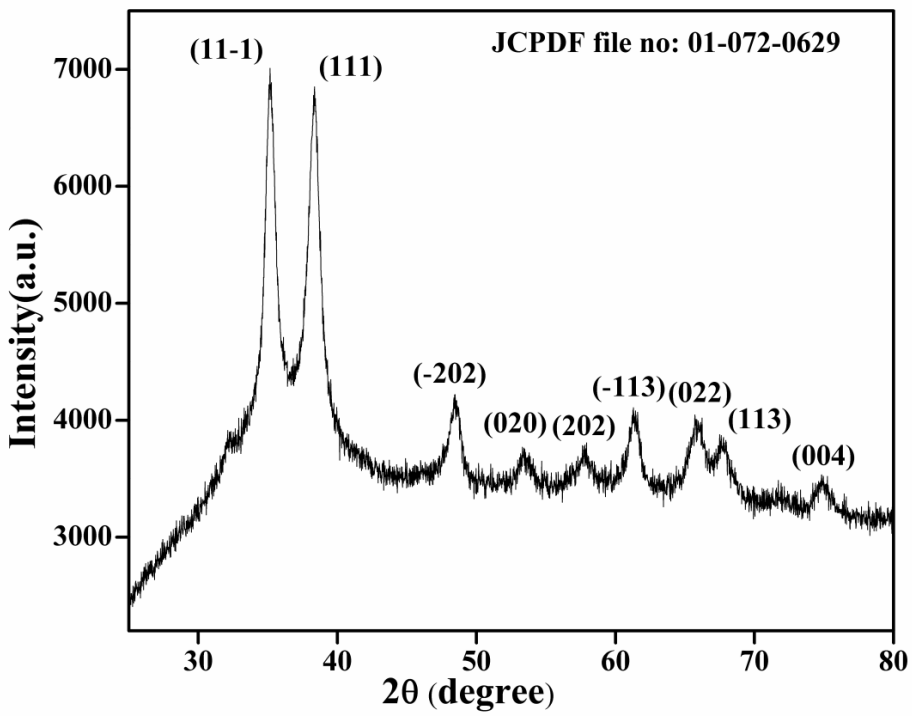

Fig. 7.17 XRD pattern of synthesized CuO nanoparticles.

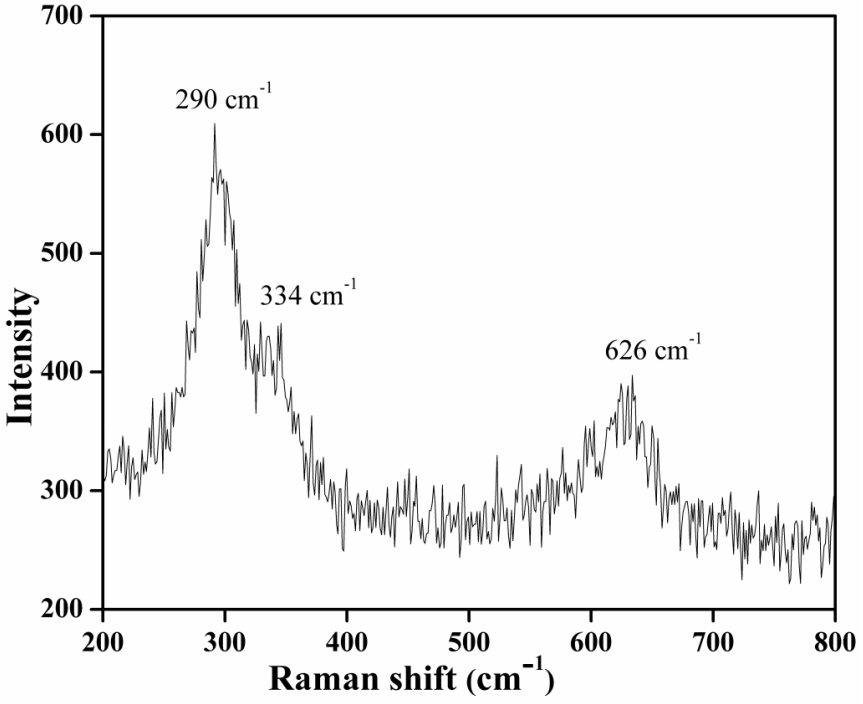

Fig. 7.18 Raman spectrum of synthesized CuO nanoparticles.

Fig. 7.19 representing the FE−SEM image of synthesized CuO nanoparticles clearly reveals the uniform distribution with nearly spherical type morphology. **Fig. 7.20** represents the EDS spectra of the synthesized CuO nanoparticles, indicates the proper stoichiometric ratio of Cu and O (1:1), again confirms the formation of pure CuO nanoparticles.

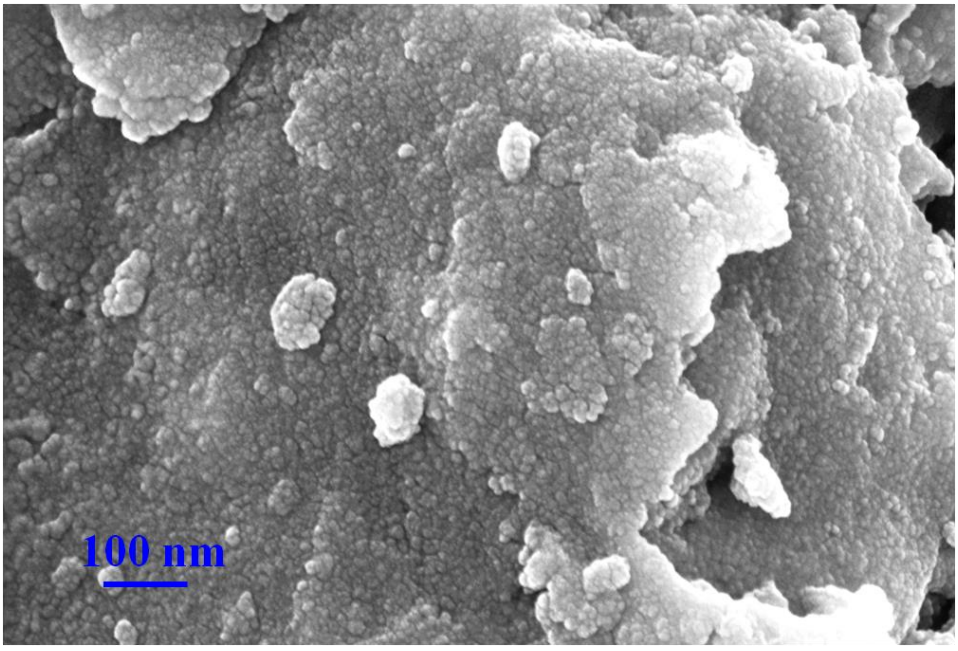

Fig. 7.19 FE-SEM image of CuO nanoparticles.

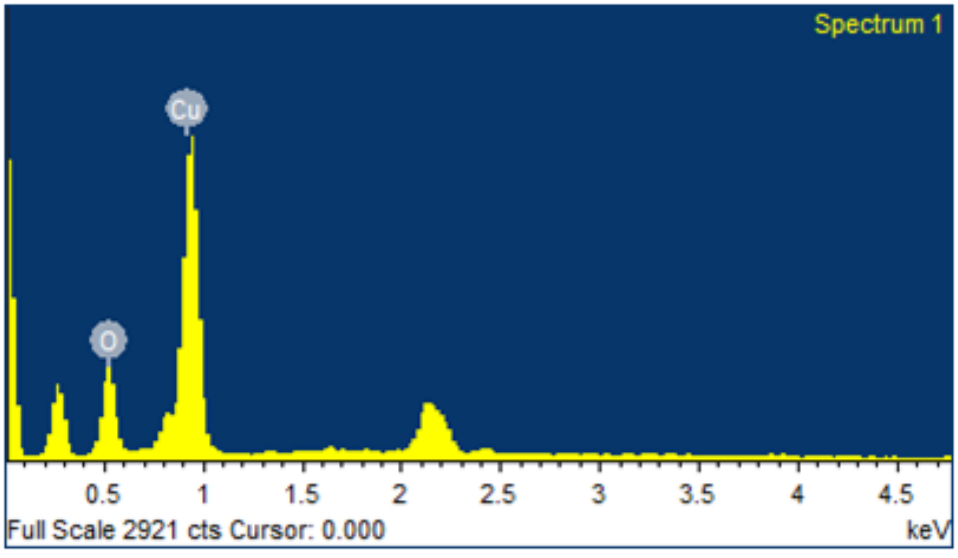

Fig. 7.20 EDS spectrum of CuO nanoparticles.

The size and morphology of the nanoparticles was further evaluated by TEM image as shown in **Fig. 7.21**. The image clearly shows the spherical type morphology with a diameter of 9 nm which is in good agreement with the estimated by the Scherer formula from XRD result.

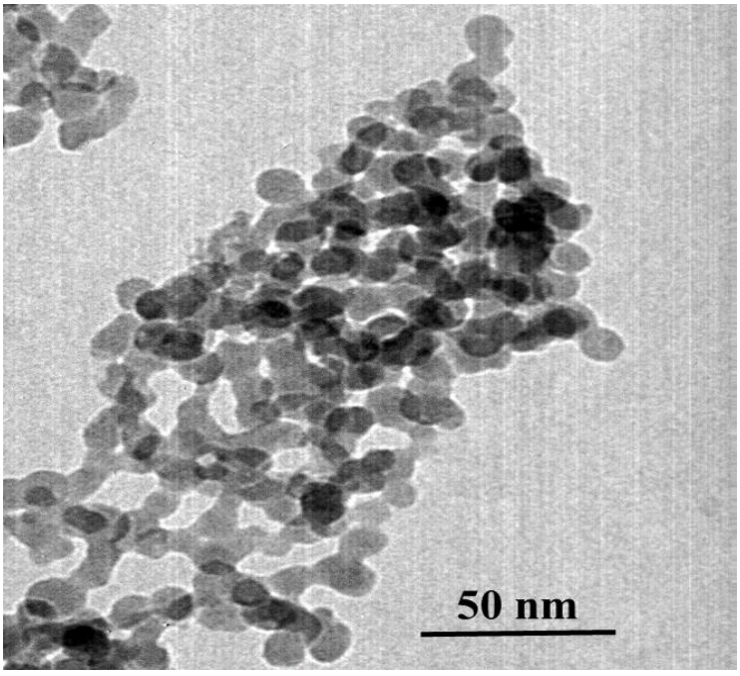

Fig. 7.21 TEM image of CuO nanoparticles.

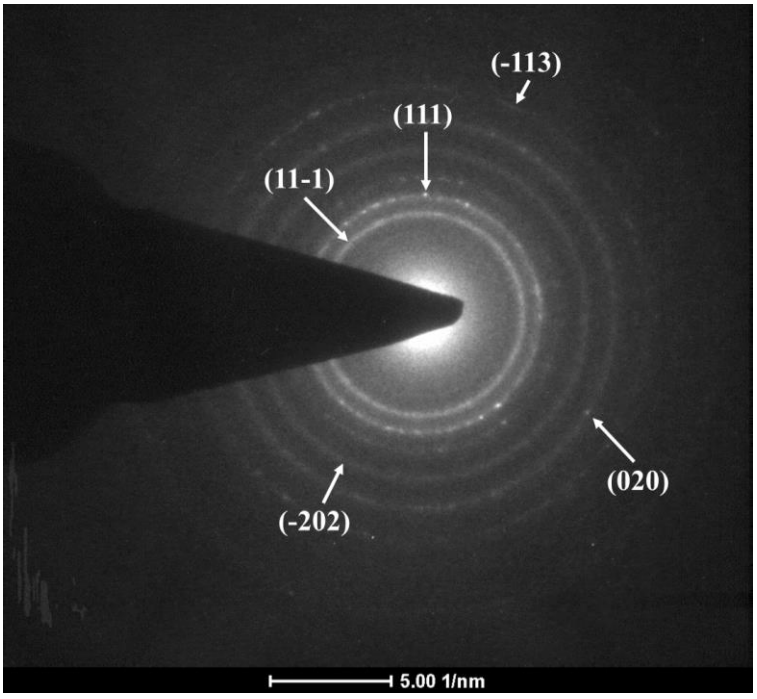

Fig. 7.22 SAED pattern of synthesized CuO nanoparticles.

The selected area electron diffraction (SAED) pattern of the TEM micrograph is shown in **Fig. 7.22**, exhibits the formation of concentric rings. The indexed diffraction rings can be ascribed to (11−1), (111), (−202), (020), and (−113) planes of the monoclinic CuO, verifying the XRD and Raman results. The HR−TEM image of the CuO nanoparticle (**Fig. 7.23**) exhibits lattice fringes of 1.701 Å spacing which is corresponding to the d spacing of the (020) plane, again confirm the crystalline structure of the synthesized CuO nanoparticles. The specific surface area calculated form BET surface area analyzer was 82.82 m^2/g. The pH_{zpc} of copper oxide nanoparticles was plotted and discussed in subsequent section. It was found that pH_{zpc} value of CuO nanoparticles was at pH 6.9 which concluded that the adsorbent surface had a positive charge in aqueous medium.

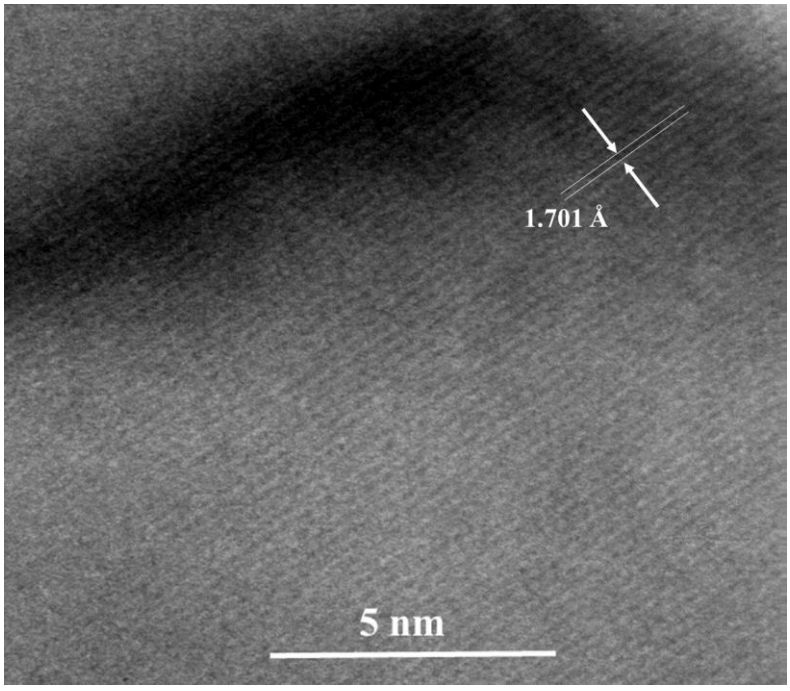

Fig. 7.23 HR−TEM pattern of synthesized CuO nanoparticles.

7.3.3.2 pH effect

pH is identified as an important factor which highly affects the removal of cations from solution. The sorption of metal ions on pH dependence is related to the metal chemistry in solution and ionization state of the functional group of the sorbent which affect the availability of binding sites **[325, 326].** The effect of pH on adsorption was carried out by taking 100 mL of 50 mg/L Pb (II) ion concentration, adsorption dose 2 mg/L and contact time 180 min at room temperature. **Fig. 7.24** shows the pH effect in the range of 2−6 to avoid the precipitation of Pb

$(OH)_2$ on the Pb (II) ions adsorption onto CuO nanoparticles. The removal of Pb (II) ions and adsorption capacity increases from 11.14% to 76.50% and 13.2 to 95.62 mg/g as the pH of the solution increases from 2 to 6, respectively. So, the best pH value was 6 at which maximum percentage removal (76.5%) and adsorption capacity (95.625 mg/g) occur. Same behavior was observed in the previous reported literature for the adsorption capacity on different type adsorbent **[327].** At lower pH, the percentage removal of Pb (II) ion is low, as most of the surface of the adsorbent contains hydronium ion (H_3O^+) and holds many protonated sites which results the electrostatic repulsion between Pb (II) ions and positively charged surface. Consequently, percentage removal of Pb (II) ions decreases at lower pH. The positive charge on the adsorbent surface decreases as the pH of the solvent increases, thus reducing the electrostatic repulsion between sorbent surface and Pb (II) ion, as a result the percentage removal of Pb (II) increase as the pH value increases of the solvent. Also lower H^+ concentration favors the cations adsorption by mass adsorption **[327].** Thus optimum pH for the maximum adsorptive removal of Pb (II) ion was found to be 6.

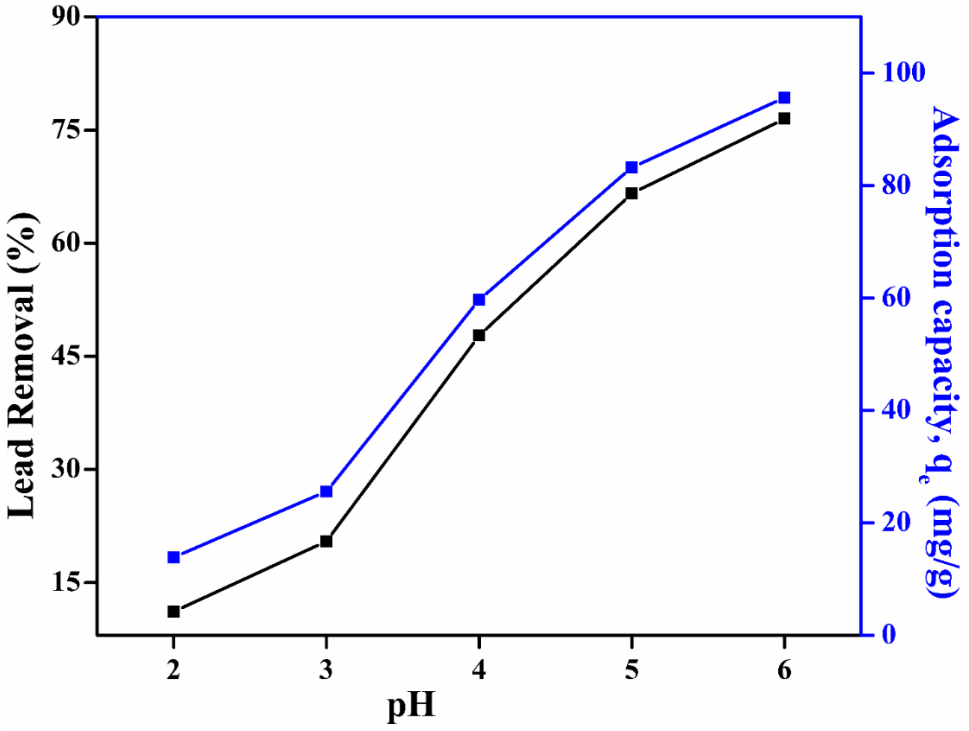

Fig. 7.24 Effect of pH on Pb (II) ions removal and uptake capacity with CuO nanoparticles.

7.3.3.3 Effect of CuO nanoparticles dose

The adsorbent dose is another important parameter for the removal efficiency of lead by adsorption. In the experimental conditions, the CuO nanoparticles dose range 0.1 mg//L to 6 mg/L, while keeping pH (6.0), initial Pb (II) concentration 50 mg/L was used for the adsorption of lead ion at room temperature and the results are representing in **Fig. 7.25**. As can be seen from the figure that the removal of Pb (II) ions was increased from 46.08% to 95.86% as the adsorbent dose increased from 0.1 g/L to 2 g/L and after that it reached upto 98.96% as the adsorbent dose increased to 6 g/L. As from the results, increasing the adsorbent dose from 0.1 g/L to 6 g/L, the adsorption capacity of CuO nanoparticles gradually decreased from 230.4 mg/g to 8.24 mg/g. In fact, the adsorption capacity of the adsorbent depends upon the metal to binding sites ratio. At higher dose, the available Pb (II) ions were not sufficient to saturate the entire binding sites present on CuO nanoparticles surface, resulting into lesser ions adsorbed on per unit mass of CuO adsorbent leading to lower adsorption capacity of CuO nanoparticles. On the other hand, the percentage removal of Pb (II) ions increases due to sufficient availability of large surface area and vacant adsorption sites at higher adsorbent dose. After getting the equilibrium state, further increase in adsorbent dose had not shown enhance effect in adsorption. Therefore, to maintain the both reasonable high removal efficiency and adsorption capacity of per unit mass of CuO adsorbent, a dosage of 2.0 g/L was used for further experiments.

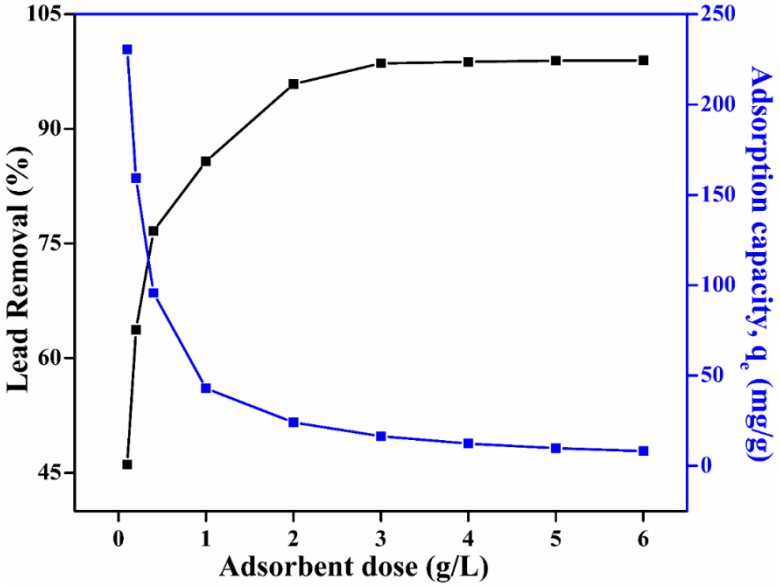

Fig. 7.25 Effect of adsorbent dose on Pb (II) ions removal and uptake capacity with CuO nanoparticles.

7.3.3.4 Effect of contact time

The contact time experiment was carried out to investigate the time of equilibrium for maximum adsorption of Pb (II) ions on CuO nanoparticles at arbitrary experimental conditions. In that case, initial concentration of Pb (II) 50 mg/L, adsorbent dose 2.0 g/L and pH 6 were used at room temperature. The removal of Pb (II) ions in solution was consistently observed until equilibrium was not occur. The results, as displayed in **Fig. 7.26**, exhibited that the removal of Pb (II) ions was increased as the contact time increase and the maximum removal (93.42%) of Pb (II) ions occur at within the staring 60 min of contact time. Thereafter, it reached up to 96.22% as the contact time was increased up to 180 min i.e. no significant change occurs in the Pb (II) ions. Thus 60 min was the equilibrium time at which maximum removal of Pb (II) ions by CuO nanoparticles. Initially, rapid removal of Pb (II) ions occurs due to present of adequate vacant sites that are available and a great concentration gradient exists between the adsorbate in the aqueous and solid phases. Thereafter, it goes slow down due to inter-particular competition of ions for the available binding sites and ultimately equilibrium accomplished.

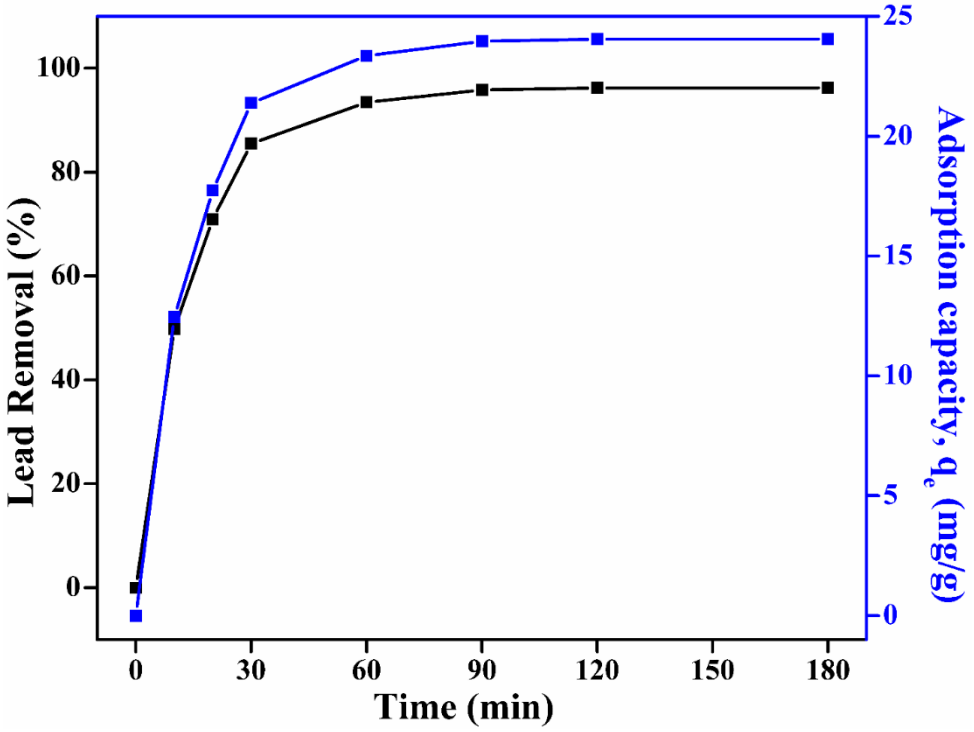

Fig. 7.26 Contact time effect on Pb (II) ions removal and uptake capacity with CuO nanoparticles.

7.3.3.5 Effect of metal ion concentration

The performance of Pb (II) ions removal on CuO nanoparticles was investigated at different concentration of 10, 20, 30, 50, 70, 100 and 150 mg/L at pH 6 with contact time 180 min, adsorbent dose 2.0 g/L at room temperature. The result shown in **Fig. 7.27**, indicates that at low metal ion concentration (10 mg/L), the maximum removal efficiency (99.73%) was occurred. While, as the initial metal ion concentration increased from 10 to 150 mg/L the removal efficiency was continuously decreased from 99.73% to 47.36%, whereas, the adsorption was increased from 4.98 mg/g to 35.52 mg/g with increasing the initial Pb (II) ions concentration from 10 to 150 mg/L. At lower Pb (II) ions concentration, higher removal efficiency occurs due to large surface area and active sites of CuO nanoparticles being available for the adsorption of Pb (II) ions. When the initial metal ion concentration becomes high, the removal efficiency will be low because the available active sites for adsorption will be less with increasing the initial metal ion concentration.

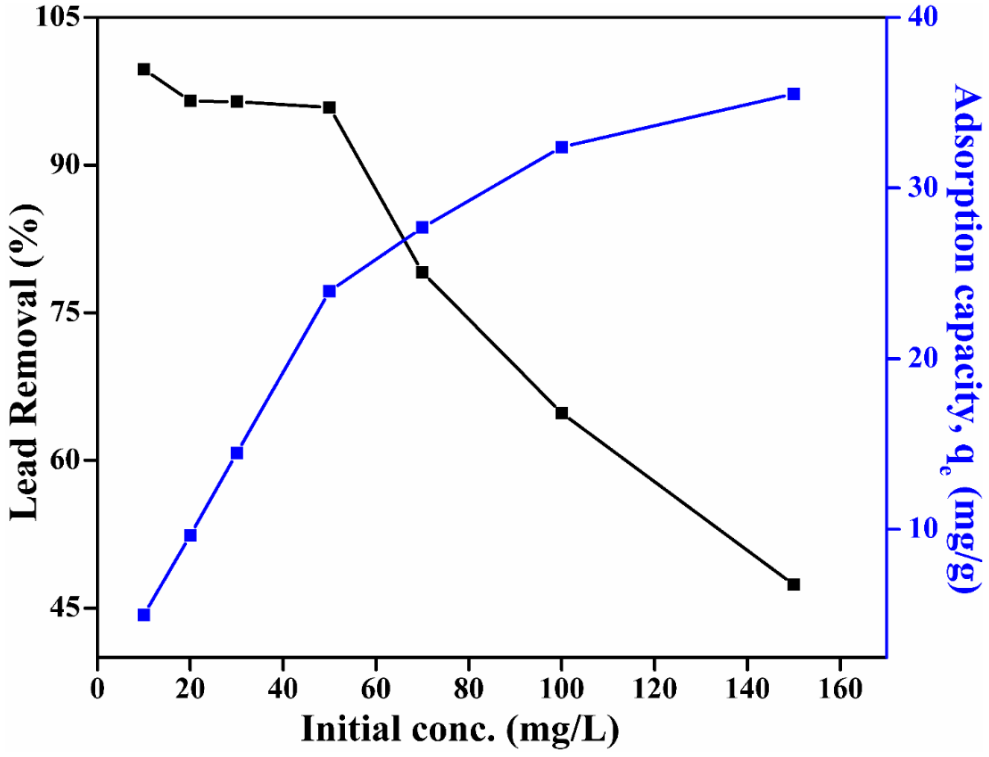

Fig. 7.27 Concentrations effect on Pb (II) ions removal and uptake capacity with CuO nanoparticles.

7.3.3.6 Temperature effect and thermodynamic study

The temperature dependence adsorption and its thermodynamic studied was carried out at three different temperatures 25, 35 and 45 ºC on CuO nanoparticles based adsorbent, while fixed all other parameters manually optimized such as pH 6, adsorbent dose 2.0 g/L, Pb (II) ions concentration 50 mg/L and contact time 180 min. The results show that with increase the temperature from 25 to 45 ºC, the percentage adsorption of Pb (II) ions increased from 83 to 94% indicating endothermic behaviour of adsorption process. The thermodynamic parameters such as Gibb's free energy change (ΔG), enthalpy change (ΔH) and entropy change (ΔS) for adsorption process was calculated using equations (3), (4) and (5). The results are summarized in **Table 7.8**. Positive ΔH value indicates the endothermic behaviour of Pb (II) ions adsorption and negative values of ΔG concluded the spontaneous nature of adsorption **[328].** The low value of ΔS indicates that no significant change in entropy occur during adsorption experiments **[329].** Also, the positive ΔS value reflects the increase in randomness of metal ion in solid-solution interaction during adsorption and also indicates the occurrence of ion replacement reactions. The value of ΔH (14.60 kJ/mol^{-1}) indicated that the adsorption of Pb (II) ions on CuO nanoparticles is physico-chemical adsorption rather than a pure physical or chemical, as heats of chemisorption generally lie into a range of 80–200 kJ/mol.

Table. 7.8 Thermodynamics parameters for the Pb (II) ions adsorption onto CuO nanoparticles.

Temperature (K)	ΔH (kJ/mol)	ΔS (kJ/mol/K)	ΔG (kJ/mol)
298	14.60	0.144	–43.150
308			–44.599
318			–46.047

7.3.3.7 Kinetics of Adsorption

The order of the reaction and the rate constant value can be find out from the kinetics adsorption data. The adsorptive removal of Pb (II) ions from aqueous solution on adsorbent can be explained on the basis of kinetics models and observed the rate controlling mechanism of adsorption process such as chemical reaction, diffusion control and mass transfer. The kinetic of lead adsorption onto CuO nanoparticles was evaluated by three models viz. pseudo first-

order, pseudo second-order and intraparticle diffusion models and the results are given in **Fig. 7.28, 7.29 and 7.30**. The pseudo first-order equation assumes that the bindings are originated from physical adsorption and given in **eq. (6).** The pseudo second-order model gives chemical adsorption (chemisorption) and given in **eq. (7)**. In addition to this, the intraparticle diffusion model was applied to identify the diffusion mechanism as given in **eq. (8)**. The initial adsorption rate was find out using the $h = k_2 Q_e^2$. The linearized results are represented in **Table. 7.9**.

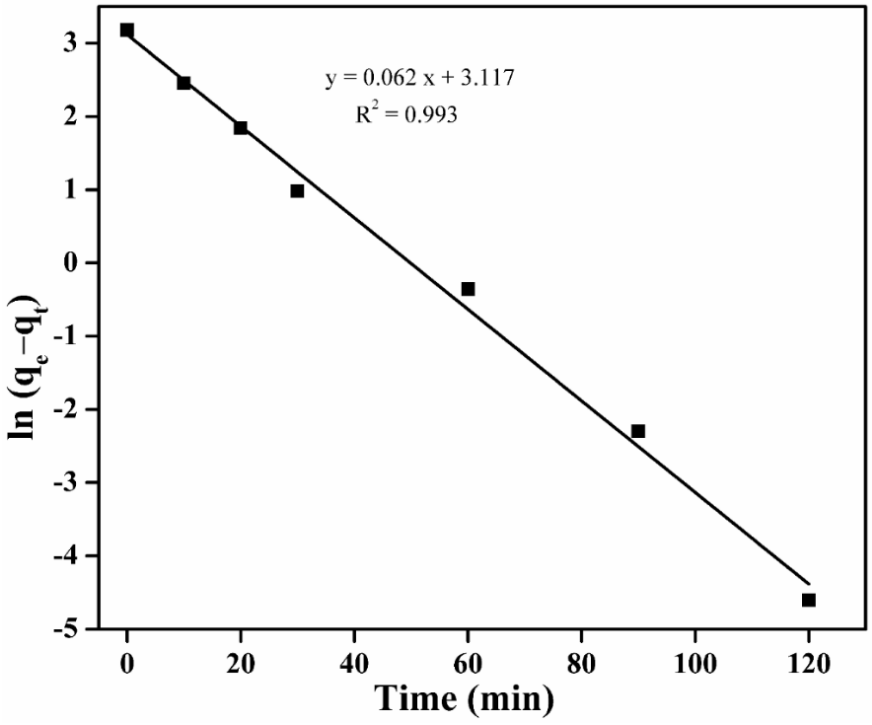

Fig. 7.28 Pseudo first–order kinetic model for Pb (II) ions adsorption onto CuO nanoparticles.

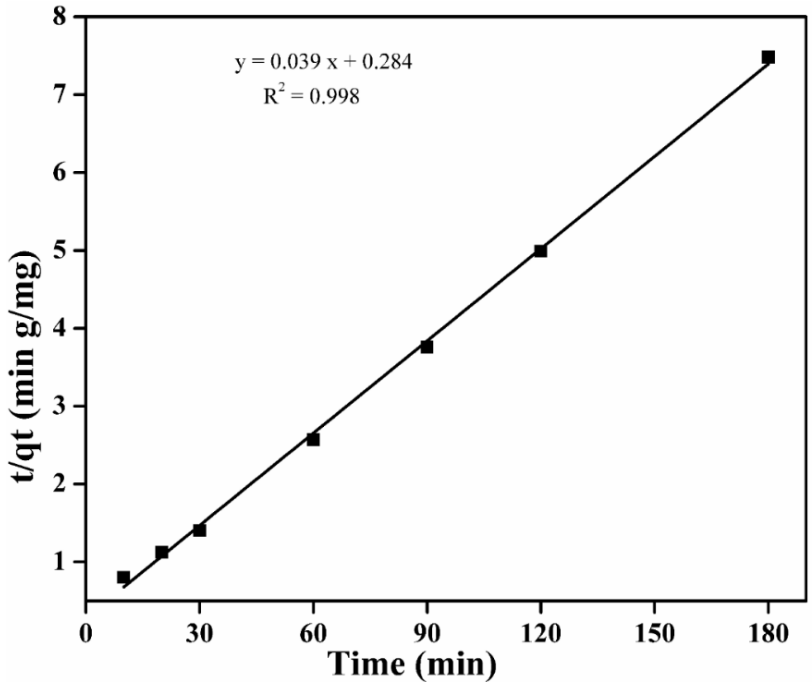

Fig. 7.29 Pseudo second–order kinetic model for Pb (II) ions adsorption onto CuO nanoparticles.

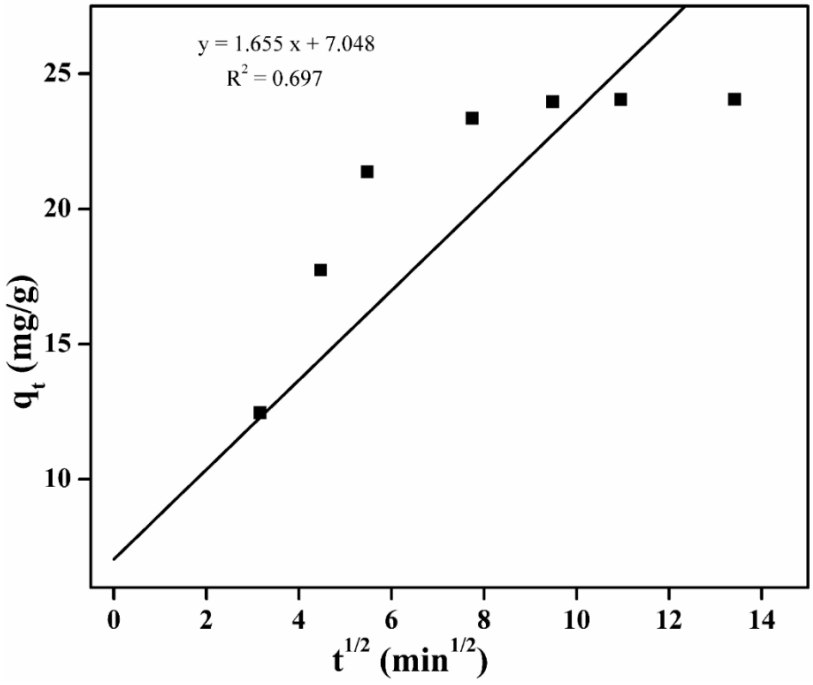

Fig. 7.30 Interparticle diffusion model for Pb (II) ions adsorption onto CuO nanoparticles.

Table. 7.9 Coefficients studies of kinetic models for the Pb (II) ions adsorption over CuO nanoparticles.

Kinetics models	CuO nanoparticles
Kinetic study and model parameters	
Pseudo first-order model	
R^2	0.993
Q_e (mg/g)	22.578
k_1 (min^{-1})	0.0625
Pseudo second-order model	
R^2	0.998
Q_e (mg/g)	25.641
k_2 (g/mg min)	0.00535
h (mg/g min	3.517
Intraparticle diffusion model	
R^2	0.697
k_i	1.655
C	7.048

By comparing the correlation coefficients (R^2), the kinetics results indicate that the adsorption of Pb (II) ions is controlled by pseudo second-order model (R^2 = 0.998) rather than pseudo first-order (R = 0.993) and intraparticle diffusion (R^2 = 0.697) model, which indicates that the Pb (II) ions adsorption process occur due to chemisorption. The assumption behind the pseudo-second-order model is that the rate-limiting step may be chemisorption involving valence forces through sharing or exchange of electrons between adsorbent and adsorbate **[304, 307].**

7.3.3.8 Adsorption isotherm

Adsorption isotherm is important parameter to describe the interaction of solutes towards sorbent surface. Here, two isotherm models were used for the isotherm studies viz.: Langmuir (**eq. 9**) and Freundlich (**eq. 10**) isotherm models by varying the initial Pb (II) ions concentration from 10 to 150 mg/L which are given in **Fig. 7.31** and **7.32**. From these, Langmuir constants Q_o and K_L were calculated and are listed in **Table 7.10**.

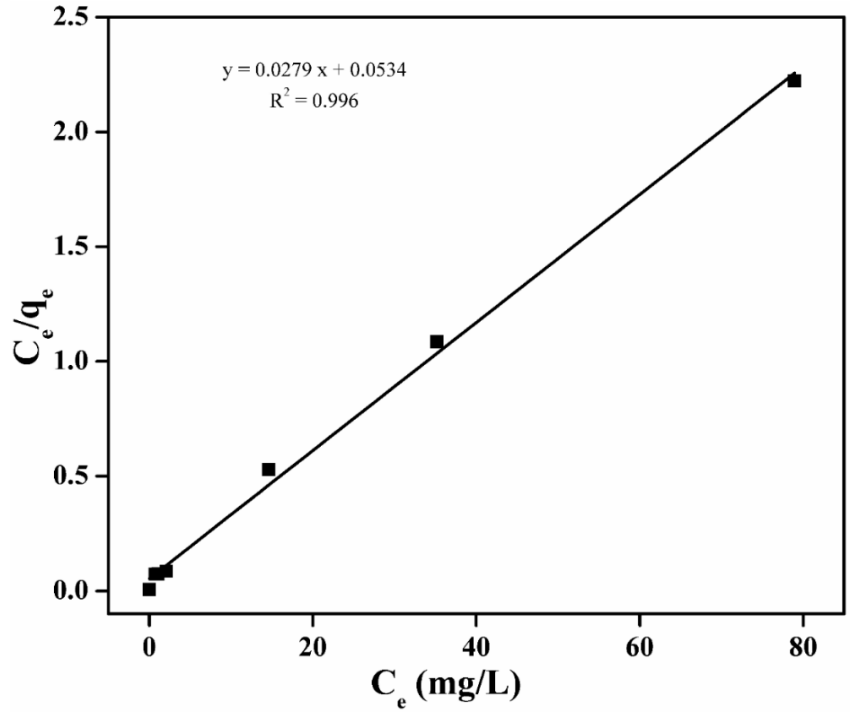

Fig. 7.31 Langmuir isotherm for Pb (II) ions adsorption onto CuO nanoparticles.

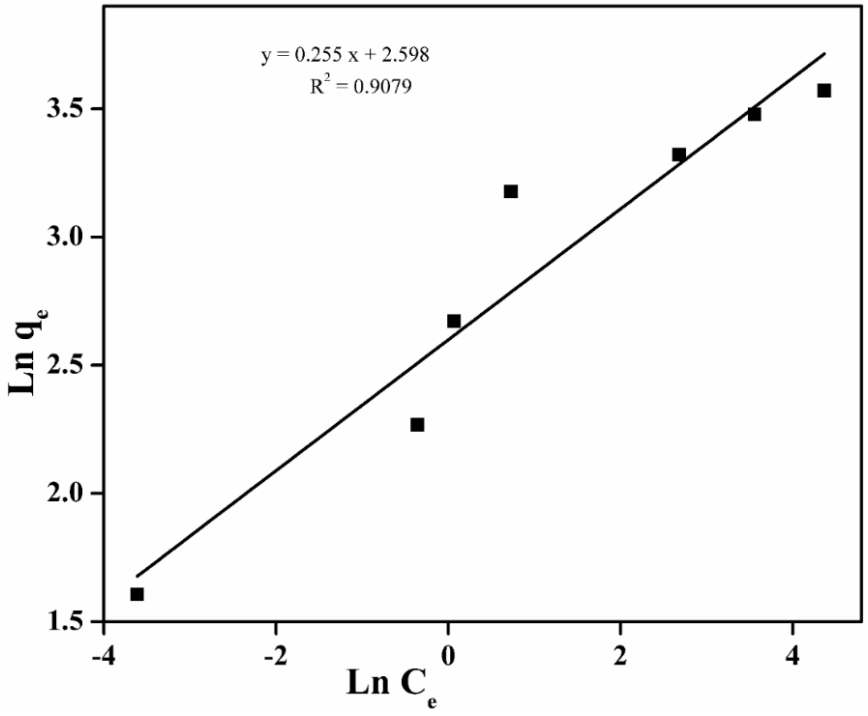

Fig. 7.32 Freundlich isotherm for Pb (II) ions adsorption onto CuO nanoparticles.

Table. 7.10 Coefficients studies of isotherm models for the Pb (II) ions adsorption over CuO nanoparticles at different temperatures.

Isotherm	Parameters	25 ºC	35 ºC	45 ºC
Langmuir	Q_e (mg/g)	37.027	38.461	39.680
	K_L (L/mg)	0.509	0.465	0.743
	R^2	0.998	0.996	0.996
	R_L	0.012	0.014	0.008
Freundlich	n	3.921	4.149	5.102
	K_F (mg/g)(L/mg)$^{1/n}$	13.436	14.805	17.637
	R^2	0.907	0.921	0.928

To determine the effect of adsorption isotherm, another important parameter R_L, a dimensionless constant which referred to as separation factor or equilibrium parameter is defined from the **eq. 10**. Here, R_L value was 0.0182 for Pb (II) ions adsorption which is in between 0 and 1, indicating favourable adsorption.

The Freundlich isotherm model exhibits an empirical relationship which describes the heterogeneity of sorbent surface and reflects as multilayer adsorption. The linearized form of Freundlich isotherm is given in **eq. 11**. The values of Freundlich constants are given in **Table 7.10**. Both the isotherm experiments were carried out at room temperature.

Based on the higher values of correlation coefficients R^2, the adsorption data depicted better by the Langmuir isotherm model than the Freundlich isotherm model. Fitness of Langmuir isotherm model exhibits that the adsorption of Pb (II) ions on the surface of CuO nanoparticles was monolayer and adsorption energy was uniformly distributed over the adsorbent surface.

A comparison was carried out of the adsorption capacity for Pb (II) ions removal by other adsorbents with current synthesized CuO nanoparticles and is shown in **Table 7.11**. The high adsorption capacity within a short contact time of this study revealed that magnetron sputtered CuO nanoparticles could be a promising adsorbent for Pb (II) ions removal.

Table. 7.11 A comparative study of various adsorption capacities for Pb (II) ions.

Adsorbent	Adsorption capacity (mg/g)	References
Acid activated bentonite	8.92	**[330]**
activated carbon	21.38	**[331]**
Thiol-functionalized cellulosic biomass	28.67	**[332]**
Poly2-hydroxyethyl methacrylate (PHEMA)	3.037	**[333]**
Copolymer 2-hydroxyethyl methacrylate with monomer methyl methacrylate P(MMAHEMA)	31.447	**[333]**
Multi-walled carbon nanotubes	17.5	**[334]**
Bamboo charcoal	25.0	**[335]**
Coir	18.9	**[336]**
Fly ash	15.08	**[337]**
Oryza sativa L. husk	8.6	**[338]**
Sawdust	3.19	**[339]**
CuO nanoparticles	3.31	**[340]**
Magnetron sputtered CuO nanoparticles	37.027	(Current study)

7.3.4 Conclusion

The CuO nanoparticles have been synthesized using magnetron sputtering, a novel physical vapor deposition technique and then characterized by XRD, Raman, FT−IR, FE−SEM, TEM and N_2−BET techniques which confirm the formation of monoclinic phase with high purity and narrow size distribution. The CuO nanoparticles were found to be excellent candidates for removal of Pb (II) ions from aqueous solutions. The optimum conditions for the lead removal were found to be: pH of 6, adsorbent dose of 2.0 g/L and Pb (II) ions concentration of 50 mg/L at room temperature. The positive ΔH (14.60) and negative ΔG values indicate the endothermic behavior and spontaneous nature of adsorption process, respectively. The adsorption process was found to be physicochemical adsorption rather than a pure physical or chemical one with the positive ΔS value which indicates the increase in randomness of metal ions in solid-solution interface during adsorption. The adsorption of Pb (II) ions follows pseudo-second order kinetics. The adsorption isotherm follows the Langmuir isotherm model and gives 37.027 mg/g adsorption efficiency of the adsorbent for the lead at room temperature.

CHAPTER 8

CONCLUSIONS AND FUTURE SCOPE

The main objective of the present work was to synthesize high purity metal oxides nanostructures for the decontamination of chemical warfare agent and removal of heavy metal ions from aqueous solution. Four types of nanostructures namely copper oxide, tungsten oxide, zirconium oxide and manganese oxide were synthesized by using DC reactive magnetron sputtering technique. The following is a brief summary and conclusions made based on the results obtained on the aforementioned coatings. The suggestions for the future work are proposed at the end.

8.1 Synthesis of sputter deposited CuO nanoparticles for the Decontamination of 2–Chloro Ethyl Ethyl Sulphide (CEES)

The copper oxide nanoparticles were synthesized using reactive sputtering technique at the sputtering parameters of working pressure 10 mTorr, gas ratio of argon and oxygen 40:10, power 80 W at −194 ºC temperature to deposite optimum particles size. Thereafter, the obtained nanoparticles were annealed at different temperatures to obtained different size nanoparticles. These nanoparticles were used to decontaminate 2–chloro ethyl ethyl sulphide (CEES), a well known simulant of sulphur mustard (HD). The decontamination reactions exhibited first order steady state (predominantly hydrolysis) behavior. The rate constant (0.434 h^{-1}) value for the decontamination of CEES over CuO nanoparticles was found to be maximum for as–deposited nanoparticles.

8.2 CuO nanoparticles: sputtering based synthesis and their structural, morphological and thermal studies

The nanoparticles were synthesized at various sputtering pressure and then characterized by different characterization techniques. The XRD results indicates purely crystalline monoclinic phase and the average crystallite size was found to be increased from 6 nm to 13 nm with increasing sputtering pressure from 10 mTorr to 50 mTorr. Raman spectrum confirmed the monoclinic phase of synthesized nanoparticles. FE–SEM and TEM results indicate the

aggregates small nanoparticles having size range in XRD data. The TG data indicates the weight loss only due to physisorbed water.

8.3 Synthesis of WO_3 nanoparticles for the degradation of 2-chloro ethyl ethyl sulphide and dimethyl methyl phosphonate

WO_3 nanoparticles were synthesized at 30 mTorr base pressure, 40:10 ratio of argon and oxygen, power 80 W at −194 ºC temperature. After synthesis, these nanoparticles were annealed at various temperatures to obtained different size. Thereafter, these different size nanoparticles were used to degrade 2−chloro ethyl ethyl sulphide (CEES) and dimethyl methyl phosphonate (DMMP). The decontamination reactions exhibited pseudo first order steady state (predominantly hydrolysis) with rate constant (k) and half life ($t_{1/2}$) values 0.143–0.109 h^{-1} and 4.82–6.49 h for CEES and 0.018–0.010 h^{-1} and 36.87–66.65 h for DMMP with increase in particle size, respectively.

8.4 6.4 Power effect on structural and thermal properties of magnetron sputtered WO_3 Nanoparticles

The nanoparticles were synthesized at different sputtering pressure and then characterized by various techniques. The XRD gives amorphous nature of the WO_3 nanoparticles but SAED shows the crystalline nature which was confirmed by Raman spectrum, gives monoclinic phase of WO_3 nanoparticles. The particle size was found to be in the increasing form (2−6 nm) with increasing sputtering power. TG analysis shows the weight loss occur only due to loss of physisorption water.

8.5 ZrO_2 nanoparticles: A good decontaminating agent for 2−chloro ethyl ethyl sulphide and dimethyl methyl phosphonate

ZrO_2 nanoparticles were synthesized using 90 W sputtering power, 30 mTorr base pressure and 40:5 ratio of argon and oxygen. These nanoparticles were annealed at different annealing temperature and then used as decontaminating agent to degrade 2−chloro ethyl ethyl sulphide (CEES) and dimethyl methyl phosphonate (DMMP). The nanoparticles destroy these agents by forming non−toxic hydrolysis and elimination products. The reactions show pseudo first order kinetic behavior with rate constant values 0.178–0.107 h^{-1} and 0.034–0.015 h^{-1} for CEES and

DMMP, respectively with increase in particle size. Also, as−deposited nanoparticles exhibited best decontamination results over annealed nanoparticles.

8.6 Synthesis and characterization of new magnetron sputtered manganese oxide nanostructures– application for Decontamination of 2–choloro ethyl ethyl sulphide and dimethyl methyl phosphonate

Reactive sorbent composed of aggregates MnO_2 nanoparticles and nanorods (nanostructures) were synthesized using reactive magnetron sputtering technique and then studied the decontamination reactions of CEES and DMMP with these nanostructures. These MnO_2 nanostructures destroy the agents (predominantly through hydrolysis reactions) by pseudo first order kinetic reaction with rate constant and half life value 0.267 h^{-1} and 2.58 h for CEES, also 0.068 h^{-1} and 10.10 h for DMMP, respectively.

8.7 CuO nanoparticles applications for the removal of Cr (VI) ions from aqueous solution

Copper oxide nanoparticles were synthesized at 20 mTorr working pressure using reactive magnetron sputtering technique and then characterized by various techniques which confirm the formation of monoclinic phase with high purity and narrow size distribution. These CuO nanoparticles were found to be an effective adsorbent for the removal of Cr (VI) ions from water. The pH 3, adsorbent dose of 1.6 g/L and Cr (VI) ions concentration of 20 mg/L were found the optimized conditions for the Cr (VI) ions removal. Thermodynamic studies show the feasible, endothermic and spontaneous nature of adsorption process. The adsorption follows pseudo−second order kinetics. The isotherm data well fits to Langmuir model and give adsorption efficiency of 15.62 mg/g which confirms monolayer adsorption over the CuO nanoparticles surface.

8.8 Adsorptive removal of Pb (II) ions from aqueous solution using CuO nanoparticles synthesized by sputtering method

The CuO nanoparticles were synthesized at 30 mTorr working pressure using magnetron sputtering technique and then characterized by different techniques which confirm the formation of single monoclinic phase with high purity. The sputtered deposited CuO nanoparticles were found to be excellent adsorbent for the removal of Pb (II) ions from water.

The optimum conditions for the lead removal were found to be: pH of 6, adsorbent dose of 2.0 g/L and Pb (II) ions concentration of 50 mg/L at room temperature. The positive ΔH (14.60) and negative ΔG (−43.25, −44.599, −46.047) values indicate the endothermic behavior and spontaneous nature of adsorption process, respectively. The adsorption was found to be physicochemical rather than a pure physical or chemical one with the positive ΔS (0.144) value which indicates the increase in randomness of metal ions in solid−solution interface during adsorption. The adsorption of Pb (II) ions follows pseudo−second order kinetics. The adsorption isotherm follows the Langmuir isotherm model and gives 37.027 mg/g adsorption efficiency.

8.9 Suggestions for Future Work

Based on the present work carried out on the investigation of nanostructures such as copper oxide, tungsten oxide, zirconium oxide and manganese oxide, following recommendations for the future work are proposed.

- Other metal oxides can be synthesized for the decontamination of chemical warfare agents.
- Decontamination of other chemical warfare agents can be examined using currently synthesized nanostructures materials.
- The investigation of the photocatalytic properties of the CuO and WO_3 nanoparticles can be examined.
- MnO_2 nanostructures can be used in the application of solar cell capacitor and energy storage media.
- The investigation of the sensing properties of the synthesized materials can be examined.
- Catalytic properties of the synthesized metal oxides in the different reactions can be examined.
- Other heavy metal ions such as As (III) and As (V), Cd (II), Hg (II) can be removed from aqueous water using different metal oxides nanostructures.
- The other nanostructures materials such as ZnO, MgO can be synthesized for the removal of heavy metal ions from water.

References

[1] W. . Eckert, “Mass death by gas or chemical poisoning. A historical perspective,” *Am. J. Forensic Med. Pathol.*, vol. 12, pp. 119–125, 1991.

[2] B. Riley, “The toxicology and treatmet of injuries from chemical warfare agents,” *Curr. Anaesth. Crit. Care*, vol. 14, pp. 149–154, 2003.

[3] T. Okumura, N. Takasu, S. Ishimatsu, S. Miyanoki, A. Mitsuhashi, K. Kumada, K. Tanaka, and S. Hinohara, “Report on 640 victims of the Tokyo subway sarin attack.,” *Ann. Emerg. Med.*, vol. 28, pp. 129–135, 1996.

[4] T. AT, “Overview of sarin terrorist attacks on Japan. Am Chem Soc Symp Ser. 745 (2000) 304-307,” *J. am. chem. soc. symp ser.*, vol. 745, pp. 304–307, 2000.

[5] J. Bajgar, J. Fusek, J. Kassa, K. Kuca, and D. Jun, “Chemical aspects of pharmacological prophylaxis against nerve agent poisoning,” *Curr. Med. Chem.*, vol. 16, pp. 2977–2986, 2009.

[6] J. Bajgar, “Organophosphates / Nerve Agent Poisoning: Mechanism of Action, Diagnosis, Prophylaxis, and treatment,” *Adv. Clin. Chem.*, vol. 38, pp. 151–216, 2004.

[7] R. C. Malhotra, K. Ganesan, K. Sugendran, and R. V. Swamy, “Chemistry and toxicology of sulphur mustard - a review,” *Def. Sci. J.*, vol. 49, pp. 97–116, 1999.

[8] B. Papirmeister, C. L. Gross, H. L. Meier, J. P. Petrali, and J. B. Johnson, “Molecular basis for mustard-induced vesication,” *Fundam. Appl. Toxicol.*, vol. 5, pp. 134–149, 1985.

[9] M. P. Shakarjian, D. E. Heck, J. P. Gray, P. J. Sinko, M. K. Gordon, R. P. Casillas, N. D. Heindel, D. R. Gerecke, D. L. Laskin, and J. D. Laskin, “Mechanisms mediating the vesicant actions of sulfur mustard after cutaneous exposure,” *Toxicol. Sci.*, vol. 114, pp. 5–19, 2009.

[10] T. Clark and T. Stephenson, “Effects of Chemical Addition on Aerobic Biological Treatment of Municipal Wastewater,” *Environ. Technol.*, vol. 19, pp. 579–590, 1998.

[11] S. K. Raza and D. K. Jaiswal, “Mechanism of Cyanide Toxicity and Efficacy Jaiswal of its Antidotes,” *Def. Sci. J.*, vol. 44, pp. 331–340, 1994.

[12] S.A. Cucinell, “Review of the toxicity of long-term phosgene exposure,” *Arch. Environ. Heal.*, vol. 28, pp. 272 – 275, 1974.

[13] G. P. Wheeler, *Studies related to the mechanisms of action of cytotoxic alkylating agents: A review*, vol. 22. 1962.

[14] V. Meyer, *Weitere studien zur kennthis der thiophengruppe*, vol. 19. 1886.

[15] P. D. Barlett and C. G. Swain, "Kinetics of hydrolysis and displacement reactions of beta, beta1- dichlorodiethyl sulfide (mustard gas) and of beta-chloro-betar-hydroxy diethyl sulfide (mustard chlorohydrin)," *J. Am. Chem. Soc.*, vol. 71, pp. 1406–1415, 1949.

[16] Y. C. Yang, J. R. Ward, J. R. B. Wilson, and J. S. W. Winterle, "On the activation energy for the hydrolysis of bis-(2-chloroethyl) sulfide II. Hermochimica. Acta," *Hemochimica acta*, vol. 114, pp. 313–317, 1987.

[17] F. L. Hsu, L. L. Szafraniec, W. T. Beaudry, and Y.C. Yang, "Oxidation of sulphur mustard to sulphoxides by dirnethylsulfoxide," *J. Org. Chem.*, vol. 55, pp. 4153–4155, 1990.

[18] Y. Yang, L. L. Szafraniec, and W. T. Beaudry, "A comparision of the oxidative reactivities of Mustard (2,2"-dichlorodiethyl sulfide) and Bivalent sulfides," *J.Org. Chem.*, vol. 55, pp. 3664–3666, 1990.

[19] J. Emsley and D.Hall, "The Chemistry of Phosphorus Harper & Row.pdf." pp. 502–508, 1976.

[20] "20. Organophosphorus Poisons.pdf." .

[21] H. P. Benschop and L. P. A. D. Jong, "Nerve Agent Stereoisomers : Analysis , Isolation , and Toxicology," *Acc. Chem. Res.*, vol. 21, pp. 368–374, 1988.

[22] R. Helmer and I. Hespandol, "Water pollution control-guide to the use of water quality management principles. Londan: E&FN Spon (1997)."

[23] "United Nations world water development report UNRSCO. Water for people for life (2015). Available at http://www.unesco.org/new/en/natural sciences/environment/water/wwap/wwdr/2015-water-for-a-sustainable-world/."

[24] "World water council. Home WWC/Water cricis. Available at http://www.worldwatercouncil.org/."

[25] J. D. Zuane, "Handbook of drinking water quality. New York Van Nostrand Reinhold (1997)." .

[26] B. Koziorowski and J. Kucharski, "Industrial waste disposal. Oxford pergamon Press (1972)." .

[27] R. A. Conway and R. D. Ross, "Handbook of industrial waste disposal. New York: Van Nostrand Reinhold (1980).," p. 1980, 1980.

[28] J.W. Moore, “Inorganic contaminants of surface water res. And monitoring priorities,” *New York Springer-Verlag*, p. 1991, 1991.

[29] F. Caturla, J. M. Martin-Martinez, M. Molina-Sabio, F. Rodriguez-Reinoso, and R. Torregrosa, “Adsorption of substituted phenols on activated carbon,” *J. Colloid Interface Sci.*, vol. 124, pp. 528–534, 1984.

[30] M. Fingas, M. Penner, G. Silasi, and F. Colbourne, “Treatment of intracerebral hemorrhage in rats with 12 h, 3 days and 6 days of selective brain hypothermia.,” *Exp. Neurol.*, vol. 219, pp. 156–162, 2009.

[31] P. C. Nicholas, *Handbook of water and wastewater treatment technologies*. 2002.

[32] S. Wellert, H. Inh, A. H.J., and T. H. Richardt, “Decontamination of chemical warfare agents using perchloroethylene IHF-H2O based microemulsions, welling and extraction properties on realistic surface,” *Colloid. polym. sci.*, pp. 417–426, 2008.

[33] Y. Yang, J. A. Baker, and J. R. Ward, “Decontamination of Chemical Warfare Agents,” *chem. Rev.*, vol. 92, pp. 1729–1743, 1992.

[34] “Y. Yang, L.L. Szafraniec, W.T. Beaudry, F.A. Davis, On Simulating the Oxidation Reactivities of HD and VX. In Proceedings of the 1988 US. Army CRDEC Scientific Conference on Chemical Defense Research, CRDEC-SP-013, US. Army CRDEC Aberdeen Proving Ground, ,” vol. I, p. 1989, 1989.

[35] R. L. Gustafson and A. E. Martell, “The half life of GD hydrolysis at pH= 10 an 25 oc is 12 min at an ionic streangth,” *Chem. Soc.*, vol. 84, pp. 2316–2323, 1962.

[36] J. Eptein, V. E. Bauer, M. Saxe, and M. M. Demek, “The hypochlorite anion wan reported to catalyze the hydrolysis of GB by complexing with the phosphoryl group, J. Am. Chem. SOC. 78 (1966) 4088-4071.,” *J.Am. Chem. SOC.*, vol. 78, pp. 4071–4088, 1966.

[37] L. L. Szafraniec and W. T. Beaudry, “Reactions of Chemical warfare agents with DS2: Product identification by NMR II. 2 chlororthyl sulfides,” *Ph.D thesis*, 1993.

[38] D. B. Mawhinney, J. A. Rossin, K. Gerhart, and J. John T. Yates, “Adsorption and reaction of 2-Chloroethylethyl Sulfide with Al2O3 Surfaces,” *Langmuir*, vol. 15, pp. 4789–4795, 1999.

[39] G. W. Wagner, P. W. Bartram, O. Koper, and K. J. Klabunde, “Reactions of VX , GD , and HD with Nanosize MgO,” *J. Phys. Chem. B*, no. 410, pp. 3225–3228, 1999.

[40] P. W. B. Bartram and George W. Wagner, “DECONTAMINATION OF CHEMICAL

WARFARE AGENTS USING ACTIVATED ALUMINUM OXIDE," *Pat. number 5689038*, 1997.

[41] S. M. Kanan and C. P. Tripp, "An infrared study of adsorbed organophosphonates on silica: A prefiltering strategy for the detection of nerve agents on metal oxide sensors," *Langmuir*, vol. 17, pp. 2213–2218, 2001.

[42] N. Nemerow and A. Das Gupta, "Industrial and Hazardous Wastes Treatment. Van Nostrand Reinhold, New York (1991)."

[43] L. B. Franklin, "wastewater engineering: treatment, disposal and reuse. Mc Graw-Hill, Inc. New York (1991)."

[44] A. A. Latifossglu, G. Surucu, and M. Evirgen, "Improvement of the dewaterability of Ferric sludge produced from chemical treatment of wastewaters," *Water Pollut. IV Model. Meas., Predict.*, vol. 4th Int. C, pp. 733 – 742, 1997.

[45] A. R. Pendashteh, A. Fakhru'l-Razi, T. G. Chuah, A. . D. Radiah, S. S. Madaeni, and Z. A. Zurina, "Biological treatment of produced water in a sequencing batch reactor by a consortium of isolated halophilic microorganisms.," *Environ. Technol.*, vol. 31, pp. 1229–39, 2010.

[46] B.P. Robert, "Method for desalinating salt-containing water, single-effect or multiple-effect distillation apparatus and modular element suitable for a single-effect or multiple-effect distillation apparatus," in *PCT int. appl. WO1998025679 A1 (App. No. PCT/NL*, 1998, vol. A1.

[47] A. G. Zinkus, W. D. Byers, and W. W. Doerr, "Identify Appropriate Water Reclamat ' ion Technologies," *Water reuse*, vol. 20, pp. 19–32, 1998.

[48] F. van der Ham, G. J. Witkamp, J. de Graauw, and G. M. van Rosmalen, "Eutectic freeze crystallization: Application to process streams and waste water purification," *Chem. Eng. Process. Process Intensif.*, vol. 37, pp. 207–213, 1998.

[49] R. J. Bigda, "Consider Fenton's Chemistry for Wastewater Treatment," *Chem. Eng. Prog.*, vol. 89, pp. 62 – 66, 1995.

[50] P. R. Gogate and A. B. Pandit, "A review of imperative technologies for wastewater treatment I: Oxidation technologies at ambient conditions," *Adv. Environ. Res.*, vol. 8, pp. 501–551, 2004.

[51] P. Bautista, A. F. Mohedano, J. A. Casas, J. A. Zazo, and J. J. Rodriguez, "An overview of the application of Fenton oxidation to industrial wastewaters treatment," *J. Chem.*

Technol. Biotechnol., vol. 83, pp. 1323–1338, 2008.

[52] C. Comninellis, A. Kapalka, S. Malato, S. A. Parsons, I. Poulios, and and D. Mantzavinos, "advanced oxidation processes for water treatment: advances and trends for R&D," *J. Chem. Technol. Biotechnol.*, vol. 83, pp. 769–776, 2008.

[53] I. A. Balcıoğlu and M. Ötker, "Treatment of pharmaceutical wastewater containing antibiotics by O 3 and O 3/H 2 O 2 processes," *Chemosphere*, vol. 50, pp. 85–95, 2003.

[54] W. Gernjak, T. Krutzler, A. Glaser, S. Malato, J. Caceres, R. Bauer, and A. R. Fernandez-Alba, "Photo-Fenton treatment of water containing natural phenolic compounds," *Chemosphere*, vol. 50, pp. 71–78, 2003.

[55] S. Esplugas, D. M. Bila, L. G. T. Krause, and M. Dezotti, "Ozonation and advanced oxidation technologies to remove endocrine disrupting chemicals (EDCs) and pharmaceuticals and personal care products (PPCPs) in water effluents," *J. Hazard. Mater.*, vol. 149, pp. 631–642, 2007.

[56] J. A. Herrera Melian, J. M. Dona Rodriguez, A. Viera Suarez, E. Tello Rend??n, C. Valdes Do Campo, J. Arana, and J. Perez Pena, "The photocatalytic disinfection of urban waste waters," *Chemosphere*, vol. 41, pp. 323–327, 2000.

[57] K. M. Parida, K. H. Reddy, S. Martha, D. P. Das, and N. Biswal, "Fabrication of nanocrystalline LaFeO3: An efficient sol-gel auto-combustion assisted visible light responsive photocatalyst for water decomposition," *Int. J. Hydrogen Energy*, vol. 35, pp. 12161–12168, 2010.

[58] L. F. Greenlee, D. F. Lawler, B. D. Freeman, B. Marrot, and P. Moulin, "Reverse osmosis desalination: Water sources, technology, and today's challenges," *Water Res.*, vol. 43, pp. 2317–2348, 2009.

[59] E. Diamadopoulos, K. Megalou, M. Georgiou, and N. Gizgis, "Coagulation and precipitation as post-treatment of anaerobically treated primary municipal wastewater.," *Water Env. Res.*, vol. 79, pp. 131–139, 2007.

[60] T. Xu, "Ion exchange membranes: State of their development and perspective," *J. Memb. Sci.*, vol. 263, pp. 1–29, 2005.

[61] E. Naffrechoux, S. Chanoux, C. Petrier, and J. Suptil, "Sonochemical and photochemical oxidation of organic matter," *Ultrason. sonochemistry*, vol. 7, pp. 255–259, 2000.

[62] V. K. Gupta and Imran Ali, "Water Treatment: Low-Cost Alternatives to Carbon Adsorbents, Encyclopedia of Surface and Colloid Science, (edited by Hubbard A.),

Marcel Dekker, Inc., New York," vol. 1, pp. 136–166, 2002.

[63] M. Y. A. Mollah, P. Morkovsky, J. A. G. Gomes, M. Kesmez, J. Parga, and D. L. Cocke, "Fundamentals, present and future perspectives of electrocoagulation," *J. Hazard. Mater.*, vol. B114, pp. 199–210, 2004.

[64] X. Tongwen, "Electrodialysis processes with bipolar membranes (EDBM) in environmental protection - A review," *Resour. Conserv. Recycl.*, vol. 37, pp. 1–22, 2002.

[65] P. J. M. Carrott, M. M. L. Ribeiro Carrott, I. P. P. Cansado, and J. M. V Nabais, "Reference data for the adsorption of benzene on carbon materials," *Carbon N. Y.*, vol. 38, pp. 465–474, 2000.

[66] Dabrowski Andrewes, "Adsorption: from theory to practice," *Adv. colloid interface Sci.*, vol. 93, pp. 135–224, 2001.

[67] J. H. Boer and B. G. Linsen, "Physical and chemical aspects of adsorbents and catalysts, Academic Press, London (1970)."

[68] W. K. Backhaus, E. Klumpp, H.-D. Narres, and M. J. Schwuger, "Adsorption of 2,4-Dichlorophenol on Montmorillonite and Silica: Influence of Nonionic Surfactants," *J. Colloid Interface Sci.*, vol. 242, pp. 6–13, 2001.

[69] Y. Kim, C. Kim, S. Rengaraj, and J. Yi, "Arsenic Removal Using Mesoporous Alumina Prepared via a Templating Method," *Environ. Sci. Technol.*, vol. 38, pp. 924–931, 2004.

[70] C. Gabaldón Marzal, P., Ferrer, J., Seco, A., "Single and competitive adsorption of Cd and Zn ont a granular activated carbon," *Water Res.*, vol. 30, pp. 3050–3060, 1996.

[71] I. Ali, V. K. Gupta, and H. Y. Aboul-Enein, "Chiral resolution of some environmental pollutants by capillary electrophoresis," *Electrophoresis*, vol. 132–146, pp. 132–146, 2003.

[72] E. Lorenc-Grabowska and G. Gryglewicz, "Adsorption characteristics of Congo Red on coal-based mesoporous activated carbon," *Dye. Pigment.*, vol. 74, pp. 34–40, 2007.

[73] J. Y. Hu, T. Aizawa, Y. Ookubo, T. Morita, and Y. Magara, "Adsorptive characteristics of ionogenic aromatic pesticides in water on powdered activated carbon," *Water Res.*, vol. 32, pp. 2593–2600, 1998.

[74] A. N. Malhas, R. A. Abuknesha, and R. G. Price, "Removal of detergents from protein extracts using activated charcoal prior to immunological analysis," *J. Immunol. Methods*, vol. 264, pp. 37–43, 2002.

[75] J. L. Sotelo, G. Ovejero, J. A. Delgado, and I. Mart??nez, "Comparison of adsorption

equilibrium and kinetics of four chlorinated organics from water onto GAC," *Water Res.*, vol. 36, pp. 599–608, 2002.

[76] X. Zhang and R. A. Minear, "Formation, adsorption and separation of high molecular weight disinfection byproducts resulting from chlorination of aquatic humic substances," *Water Res.*, vol. 40, pp. 221–230, 2006.

[77] I. Pikaar, A. A. Koelmans, and P. C. M. van Noort, "Sorption of organic compounds to activated carbons. Evaluation of isotherm models," *Chemosphere*, vol. 65, pp. 2343–2351, 2006.

[78] C. A. Toles, W. E. Marshall, and M. M. Johns, "Phosphoric Acid Activation of Nutshells for Metal and Organic Remediation: Process Optimization," *J. Chem. Technol. Biotechnol.*, vol. 72, pp. 252–263, 1998.

[79] M. Soleimani and T. Kaghazchi, "Activated Hard Shell of Apricot Stones: A Promising Adsorbent in Gold Recovery," *Chinese J. Chem. Eng.*, vol. 16, pp. 112–118, 2008.

[80] Y. Kawahara, K. Yamamoto, H. Wakisaka, K. Izutsu, M. Shioya, T. Sakai, Y. Takahara, and N. Ishibashi, "Carbonaceous adsorbents produced from coffee lees," *J. Mater. Sci.*, vol. 44, pp. 1137–1139, 2009.

[81] D. Nityanandi and C. V. Subbhuraam, "Kinetics and thermodynamic of adsorption of chromium(VI) from aqueous solution using puresorbe," *J. Hazard. Mater.*, vol. 170, pp. 876–882, 2009.

[82] C. A. Toles and W. E. Marshall, "Copper ion removal by almond shell carbons and commercial carbons: batch and column studies," *Sep. Sci. Technol.*, vol. 37, pp. 2369–2383, 2002.

[83] K. Nyazi, A.Yaacoubi, A. Baçaoui, C. Bennouna, A. Dahbi, J. Rivera-utrilla, and C. M.-Castilla, "Preparation and characterization of new adsorbent materials from the olive waster," *J. Phys. IV Fr.*, vol. 123, pp. 121–124, 2005.

[84] V. K. Gupta, A. Mittal, A. Malviya, and J. Mittal, "Adsorption of carmoisine A from wastewater using waste materials-Bottom ash and deoiled soya," *J. Colloid Interface Sci.*, vol. 335, pp. 24–33, 2009.

[85] V. K. Gupta, R. Jain, S. Varshney, and V. K. Saini, "Removal of Reactofix Navy Blue 2 GFN from aqueous solutions using adsorption techniques," *J. Colloid Interface Sci.*, vol. 307, pp. 326–332, 2007.

[86] W. T. Tsai, C. Y. Chang, S. Y. Wang, C. F. Chang, S. F. Chien, and H. F. Sun,

"Utilization of Agricultural Waste Corn Cob for the Preparation of Carbon Adsorbent," *J. Environ. Sci. Heal. Part B*, vol. 36, pp. 677–686, 2001.

[87] M. P. Elizalde-Gonzalez, J. Mattusch, and R. Wennrich, "Chemically modified maize cobs waste with enhanced adsorption properties upon methyl orange and arsenic," *Bioresour. Technol.*, vol. 99, pp. 5134–5139, 2008.

[88] B. S. Girgis, L.B. Khalil, and T.A.M. Tawfik, "Activated Carbon from Sugar Cane Bagasse by Carbonization in the Presence of Inorganic Acids," *J. Chem. Technol. Biotechnol.*, vol. 61, pp. 87–92, 1994.

[89] C. Namasivayam and D. Sangeetha, "Recycling of agricultural solid waste, coir pith: Removal of anions, heavy metals, organics and dyes from water by adsorption onto ZnCl2 activated coir pith carbon," *J. Hazard. Mater.*, vol. B135, pp. 449–452, 2006.

[90] B. Benguella and H. Benaissa, "Cadmium removal from aqueous solutions by chitin : kinetic and equilibrium studies," *Water Res.*, vol. 36, pp. 2463–2474, 2002.

[91] Y. Fu and T. Vıraraghavan, "Removal of Congo Red from an aqueous solution by Fungus Aspergillus niger," *Adv. Environ. Res.*, vol. 7, pp. 239–247, 2002.

[92] Q. Sun and L. Yang, "The adsorption of basic dyes from aqueous solution on modified peat – resin particle," *Water Res.*, vol. 37, pp. 1535–1544, 2003.

[93] M. I. Baraton and Eds, "Synthesis, Functionalization and surface Treatment of nanoparticles, American scientific Publishers, Los Angeles, USA, (2003)."

[94] A. Champi, A. B. Aguilar, M. Camilo, and M. Quintana, "Influence of the Iron Oxide Nanoparticles on the Electro-optical Properties of Graphite and Few-layers Graphene," *Mater. Today Proc.*, vol. 3S, pp. S214–S220, 2016.

[95] D. Mohan and C. U. Pittman, "Arsenic removal from water/wastewater using adsorbents-A critical review," *J. Hazard. Mater.*, vol. 142, pp. 1–53, 2007.

[96] G. K. Prasad, "Decontamination of 2 chloro ethyl phenyl sulphide using mixed metal oxide nanocrystals," *J. Sci. Ind. Res. (India).*, vol. 69, pp. 835–840, 2010.

[97] G. K. Prasad, T. H. Mahato, B. Singh, P. Pandey, A. N. Rao, K. Ganesan, and R. Vijayraghavan, "Decontamination of Sulfur Mustard on Manganese Oxide Nanostructures," *AIChE J.*, vol. 53, pp. 1562–1567, 2007.

[98] C. Suryanarayna, "Nanocrystalline materials" Int. Mater. Rev. 40, 41 (1995)." .

[99] K. Lu and J. Lu, "Nanostructured surface layer on metallic materials induced by surface mechanical attrition treatment," *Mater. Sci. Eng. A*, vol. 375–377, pp. 38–45, 2004.

[100] S. Anandan, T. Sivasankar, and T. Lana-Villarreal, “Synthesis of TiO2/WO3 nanoparticles via sonochemical approach for the photocatalytic degradation of methylene blue under visible light illumination,” *Ultrason. Sonochem.*, vol. 21, pp. 1964–1968, 2014.

[101] S. Anandan, X. Wen, and S. Yang, “Room temperature growth of CuO nanorod arrays on copper and their application as a cathode in dye-sensitized solar cells,” *Mater. Chem. Phys.*, vol. 93, pp. 35–40, 2005.

[102] C. B. Almquist and P. Biswas, “Role of Synthesis Method and Particle Size of Nanostructured TiO2 on Its Photoactivity,” *J. Catal.*, vol. 212, pp. 145–156, 2002.

[103] A. K. Gupta and M. Gupta, “Synthesis and surface engineering of iron oxide nanoparticles for biomedical applications,” *Biomaterials*, vol. 26, pp. 3995–4021, 2005.

[104] T.-J. Huang and D.-H. Tsai, “CO Oxidation Behavior of Copper and Copper Oxides,” *Catal. Letters*, vol. 87, pp. 173–178, 2003.

[105] J. Kukkola, M. Mohl, A. R. Leino, J. M??klin, N. Halonen, A. Shchukarev, Z. Konya, H. Jantunen, and K. Kordas, “Room temperature hydrogen sensors based on metal decorated WO3 nanowires,” *Sensors Actuators, B Chem.*, vol. 186, pp. 90–95, 2013.

[106] J. Zheng, J. T. Petty, and R. M. Dickson, “High quantum yield blue emission from water-soluble Au 8 nanodots,” *J. Am. Chem. Soc.*, vol. 125, pp. 7780–7781, 2003.

[107] K.J. Klabunde, *Free atoms, clusters, and nanoscale particles (Academic press, San Diego, CA)*. 1994.

[108] S. Mohan, Y. Singh, D. K. Verma, and S. H. Hasan, “Synthesis of CuO nanoparticles through green route using Citrus limon juice and its application as nanosorbent for Cr(VI) remediation: Process optimization with RSM and ANN-GA based model,” *Process Saf. Environ. Prot.*, vol. 96, pp. 156–166, 2015.

[109] C. A. Martinson and K. J. Reddy, “Adsorption of arsenic(III) and arsenic(V) by cupric oxide nanoparticles,” *J. Colloid Interface Sci.*, vol. 336, pp. 406–411, 2009.

[110] J. G. Ekerdt, K. J. Klabunde, J. R. Shapley, J. M. White, and J. Yates, J. T., “Surface Chemistry of Organophosphorus Compunds,” *J. Phys. Chem.*, vol. 92, pp. 6182–6188, 1988.

[111] T. H. Mahato, G. K. Prasad, B. Singh, J. Acharya, A. R. Srivastava, and R. Vijayaraghavan, “Nanocrystalline zinc oxide for the decontamination of sarin,” *J. Hazard. Mater.*, vol. 165, pp. 928–932, 2009.

[112] R. Vijayalakshmi and V. Rajendran, “Synthesis and characterization of nano-TiO2 via different methods,” *Sch. Res. Libr.*, vol. 4, pp. 1183–1190, 2012.

[113] T. H. Mahato, G. K. Prasad, B. Singh, K. Batra, and K. Ganesan, “Mesoporous manganese oxide nanobelts for decontamination of sarin, sulphur mustard and chloro ethyl ethyl sulphide,” *Microporous Mesoporous Mater.*, vol. 132, pp. 15–21, 2010.

[114] H. Wang, J. Z. Xu, J. J. Zhu, and H. Y. Chen, “Preparation of CuO nanoparticles by microwave irradiation,” *J. Cryst. Growth*, vol. 244, pp. 88–94, 2002.

[115] M. Salavati-Niasari and F. Davar, “Synthesis of copper and copper(I) oxide nanoparticles by thermal decomposition of a new precursor,” *Mater. Lett.*, vol. 63, pp. 441–443, 2009.

[116] R. V. Kumar, R. Elgamiel, and Y. Diamant, “Sonochemical preparation and characterization of nanocrystalline copper oxide embedded in poly (vinyl alcohol) and its effect on crystal growth of copper oxide,” *Langmuir*, vol. 17, pp. 1406–1410, 2001.

[117] X. P. Gao, J. L. Bao, G. L. Pan, H. Y. Zhu, P. X. Huang, F. Wu, and D. Y. Song, “Preparation and Electrochemical Performance of Polycrystalline and Single Crystalline CuO Nanorods as Anode Materials for Li Ion Battery,” *J. Phys. Chem. B*, vol. 108, pp. 5547–5551, 2004.

[118] P. Kong and a Kawczak, “Plasma synthesis of nanoparticles for nanocomposite energy applications,” *8th World Congr. Enabling Technol. New Mark. Nanocomposites 2008*, 2008.

[119] G. Saito and T. Akiyama, “Nanomaterial Synthesis Using Plasma Generation in Liquid,” *J. Nanomater.*, vol. 2015, pp. 1–21, 2015.

[120] S. Perla, “FLAME SYNTHESIS OF CARBON-NANOSTRUCTURES A Thesis Submitted to the Graduate Faculty of the Louisiana State University and Agricultural and Mechanical College in partial fulfillment of the requirements for the degree of Master of Science in Mechanical Engi,” *Thesis*, no. December, 2005.

[121] M. Nazari, N. Ghasemi, H. Maddah, and M. M. Motlagh, “Synthesis and characterization of maghemite nanopowders by chemical precipitation method,” *J. Nanostructure Chem.*, vol. 4, p. 99, 2014.

[122] M. A. Bratescu, N. Saito, and O. Takai, “Redox reactions in liquid plasma during iron oxide and oxide-hydroxide nanoparticles synthesis,” *Curr. Appl. Phys.*, vol. 11, pp. S30–S34, 2011.

[123] T. Iwasaki, K. Kosaka, T. Yabuuchi, S. Watano, T. Yanagida, and T. Kawai, “Novel mechanochemical process for synthesis of magnetite nanoparticles using coprecipitation method,” *Adv. Powder Technol.*, vol. 20, pp. 521–528, 2009.

[124] K. B. Podbolotov and E. M. Dyatlova, “Phase- and structure-formation processes during self-propagating high-temperature synthesis in the system Al - MgCO 3 - SiO 2 - C,” *Glas. Ceram.*, vol. 66, pp. 332–336, 2009.

[125] G. M. Medine, V. Zaikovskii, and K. J. Klabunde, “Synthesis and adsorption properties of intimately intermingled mixed metal oxide nanoparticles,” *J. Mater. Chem.*, vol. 14, p. 757, 2004.

[126] M. Verma, R. Chandra, and V. K. Gupta, “Synthesis and characterization of magnetron sputtered ZrO2 nanoparticles: Decontamination of 2-choloro ethyl ethyl sulphide and dimethyl methyl phosphonate,” *J. Environ. Chem. Eng.*, vol. 4, pp. 219–229, 2016.

[127] H. Zeng, X. W. Du, S. C. Singh, S. A. Kulinich, S. Yang, J. He, and W. Cai, “Nanomaterials via laser ablation/irradiation in liquid: A review,” *Adv. Funct. Mater.*, vol. 22, pp. 1333–1353, 2012.

[128] H. Ellision, “Handbook of chemical and biological warfare agents (CRCpress LLC, USA) 1991, 21-361.”

[129] A. Michalkova, M. Ilchenko, L. Gorb, and J. Leszczynski, “Theoretical Study of the Adsorption and Decomposition of Sarin on Magnesium Oxide,” *J. Phys. Chem. B*, vol. 108, pp. 5294–5303, 2004.

[130] G. W. Wagner, O. B. Koper, E. Lucas, S. Decker, and K. J. Klabunde, “Reactions of VX, GD, and HD with Nanosize CaO: Autocatalytic Dehydrohalogenation of HD,” *J. Phys. Chem. B*, vol. 104, pp. 5118–5123, 2000.

[131] A. Saxena, A. Sharma, A. K. Srivastava, B. Singh, P. K. Gutch, and R. P. Semwal, “Kinetics of adsorption of sulfurmustard on Al2O3 nanoparticles with and without impregnants,” *J. wiley Intersci.*, vol. 84, pp. 1860–1872, 2009.

[132] A. Saxena, A. K. Srivastava, B. Singh, A. K. Gupta, M. V. S. Suryanarayana, and P. Pandey, “Kinetics of adsorptive removal of DEClP and GB on impregnated Al2O3 nanoparticles,” *J. Hazard. Mater.*, vol. 175, pp. 795–801, 2010.

[133] M. T. Naseri, M. Sarabadani, D. Ashrafi, H. Saeidian, and M. Babri, “Photoassisted and photocatalytic degradation of sulfur mustard using TiO2 nanoparticles and polyoxometalates,” *Environ. Sci. Pollut. Res.*, vol. 20, pp. 907–916, 2013.

[134] G. K. Prasad, P. V. R. K. Ramacharyulu, B. Singh, K. Batra, A. R. Srivastava, K. Ganesan, and R. Vijayaraghavan, "Sun light assisted photocatalytic decontamination of sulfur mustard using ZnO nanoparticles," *J. Mol. Catal. A Chem.*, vol. 349, pp. 55–62, 2011.

[135] G. K. Prasad, T. H. Mahato, P. Pandey, B. Singh, M. V. S. Suryanarayana, A. Saxena, and K. Shekhar, "Reactive sorbent based on manganese oxide nanotubes and nanosheets for the decontamination of 2-chloro-ethyl ethyl sulphide," *Microporous Mesoporous Mater.*, vol. 106, pp. 256–261, 2007.

[136] V. Stengl, V. Houskova, S. Bakardjieva, N. Murafa, M. Marikova, F. Oplustil, and T. Nemec, "Zirconium doped nano-dispersed oxides of Fe, Al and Zn for destruction of warfare agents," *Mater. Charact.*, vol. 61, pp. 1080–1088, 2010.

[137] T. H. Mahato, B. Singh, A. K. Srivastava, G. K. Prasad, A. R. Srivastava, K. Ganesan, and R. Vijayaraghavan, "Effect of calcinations temperature of CuO nanoparticle on the kinetics of decontamination and decontamination products of sulphur mustard," *J. Hazard. Mater.*, vol. 192, pp. 1890–1895, 2011.

[138] B. Singh, T. H. Mahato, A. K. Srivastava, G. K. Prasad, K. Ganesan, R. Vijayaraghavan, and R. Jain, "Significance of porous structure on degradatin of 2 2??? dichloro diethyl sulphide and 2 chloroethyl ethyl sulphide on the surface of vanadium oxide nanostructure," *J. Hazard. Mater.*, vol. 190, pp. 1053–1057, 2011.

[139] B. Aurian-Blajeni and M. M. Boucher, "Interaction of dimethyl methylphosphonate with metal oxides," *Langmuir*, vol. 5, pp. 170–174, 1989.

[140] S. Chandra Shekar, K. Soni, R. Bunkar, M. Sharma, B. Singh, M. V. S. Suryanarayana, and R. Vijayaraghavan, "Vapor phase catalytic degradation of bis(2-chloroethyl) ether on supported vanadia-titania catalyst," *Appl. Catal. B Environ.*, vol. 103, pp. 11–20, 2011.

[141] J. Praveen Kumar, G. K. Prasad, P. V. R. K. Ramacharyulu, P. Garg, and K. Ganesan, "Mesoporous CuO-ZnO binary metal oxide nanocomposite for decontamination of sulfur mustard," *Mater. Chem. Phys.*, vol. 142, pp. 484–490, 2013.

[142] G. K. Prasad, P. V. R. K. Ramacharyulu, K. Batra, B. Singh, A. R. Srivastava, K. Ganesan, and R. Vijayaraghavan, "Decontamination of Yperite using mesoporous mixed metal oxide nanocrystals," *J. Hazard. Mater.*, vol. 183, pp. 847–852, 2010.

[143] M. SATO, T. KANBAYASHI, N. KOBAYASHI, and Y. SHIMA, "Hydroxyl Groups on

Silica, Alumina, and Silica-Alumina Catalysts," *J. Catal.*, vol. 7, pp. 342–351, 1967.

[144] M. Templeton and W. H. Weinberg, "Decomposition of phosphonate esters adsorbed on aluminum oxide," *J. Am. Chem. Soc.*, vol. 107, pp. 774–779, 1985.

[145] Y. Li, J. R. Schlup, and K. J. Klabunde, "Fourier Transform Infrared Photoacoustic Spectroscopy Study of the Adsorption of Organophosphorus Compounds," *Langmuir*, vol. 7, pp. 1394–1399, 1991.

[146] S. T. Lin and K. J. Klabunde, "Thermally activated magnesium oxide surface chemistry. Adsorption and decomposition of phosphorus compounds," *Langmuir*, vol. 1, pp. 600–605, 1985.

[147] G. W. Wagner, L. R. Procell, R. J. O'Connor, S. Munavalli, C. L. Carnes, P. N. Kapoor, and K. J. Klabunde, "Reactions of VX, GB, GD, and HD with nanosize AL2O3. Formation of aluminophosphonates," *J. Am. Chem. Soc.*, vol. 123, pp. 1636–1644, 2001.

[148] Y. C. Yang, L. L. Szafraniec, W. T. Beaudry, and C. a Bunton, "Perhydrolysis of Nerve Agent VX," *J. Org. Chem.*, vol. 58, pp. 6964–6965, 1993.

[149] Y. C. Yang, "Chemical detoxification of nerve agent VX," *Acc. Chem. Res.*, vol. 32, pp. 109–115, 1999.

[150] G. K. Prasad, T. H. Mahato, B. Singh, K. Ganesan, P. Pandey, and K. Sekhar, "Detoxification reactions of sulphur mustard on the surface of zinc oxide nanosized rods," *J. Hazard. Mater.*, vol. 149, pp. 460–464, 2007.

[151] A. Saxena, B. Singh, A. K. Srivastava, M. V. S. Suryanarayana, K. Ganesan, R. Vijayaraghavan, and K. K. Dwivedi, "Al2O3 nanoparticles with and without polyoxometalates as reactive sorbents for the removal of sulphur mustard," *Microporous Mesoporous Mater.*, vol. 115, pp. 364–375, 2008.

[152] Y. C. Yang, L. L. Szafraniec, T. B. William, and J. R. Wa, "Kinetics and mechanism of the hydrolysis of 2-chloroethyl sulfides," *J. Org. Chem.*, vol. 53, pp. 3293–3297, 1988.

[153] G. K. Prasad, B. Singh, K. Ganesan, A. Batra, T. Kumeria, P. K. Gutch, and R. Vijayaraghavan, "Modified titania nanotubes for decontamination of sulphur mustard," *J. Hazard. Mater.*, vol. 167, pp. 1192–1197, 2009.

[154] A. Kleinhammes, G. W. Wagner, H. Kulkarni, Y. Jia, Q. Zhang, L. C. Qin, and Y. Wu, "Decontamination of 2-chloroethyl ethylsulfide using titanate nanoscrolls," *Chem. Phys. Lett.*, vol. 411, pp. 81–85, 2005.

[155] T. H. Mahato, G. K. Prasad, B. Singh, A. R. Srivastava, K. Ganesan, J. Acharya, and R.

Vijayaraghavan, “Reactions of sulphur mustard and sarin on V1.02O2.98 nanotubes,” *J. Hazard. Mater.*, vol. 166, pp. 1545–1549, 2009.

[156] K. Tanabe, M. Misono, Y. Ono, and H. Hattori, “New Solid Acids and Bases: Their Catalytic Properties, Elsevier, 1989.”

[157] H. Tang, Z. Cheng, H. Zhu, G. Zuo, and M. Zhang, “Effect of acid and base sites on the degradation of sulfur mustard over several typical oxides,” *Appl. Catal. B Environ.*, vol. 79, pp. 323–333, 2008.

[158] H. Fan, L. Yang, W. Hua, X. Wu, Z. Wu, S. Xie, and B. Zou, “Controlled synthesis of monodispersed CuO nanocrystal,” *Nanotechnology*, vol. 15, pp. 37–42, 2004.

[159] S. M. Kanan, Z. Lu, and C. P. Tripp, “A Comparative Study of the Adsorption of Chloro- and Non-Chloro-Containing Organophosphorus Compounds on WO 3,” *J. Phys. Chem. B*, vol. 106, pp. 9576–9580, 2002.

[160] R. I. Hegde and J. M. White, “Interaction of dimethyl methylphosphonate with oxidized iron and the effect of coadsorbed water,” *Appl. Surf. Sci.*, vol. 28, pp. 1–10, 1987.

[161] S. R. Segal, L. Cao, S. L. Suib, X. Tang, and S. Satyapal, “Thermal Decomposition of Dimethyl Methylphosphonate over Manganese Oxide Catalysts,” *J. Catal.*, vol. 198, pp. 66–76, 2001.

[162] J. Zhou, K. Varazo, J. . Reddic, M. . Myrick, and D. A. Chen, “Decomposition of dimethyl methylphosphonate on TiO2(110): principal component analysis applied to X-ray photoelectron spectroscopy,” *Anal. Chim. Acta*, vol. 496, pp. 289–300, 2003.

[163] V. M. Bermudez, “Effect of humidity on the interaction of dimethyl methylphosphonate (DMMP) vapor with SiO2 and Al2O3 surfaces, studied using infrared attenuated total reflection spectroscopy,” *Langmuir*, vol. 26, pp. 18144–18154, 2010.

[164] M. B. Mitchell, V. N. Sheinker, and E. A. Mintz, “Adsorption and Decomposition of Dimethyl Methylphosphonate on Metal Oxides,” *J. Phys. Chem. B*, vol. 101, pp. 11192–11203, 1997.

[165] A. R. Wilmsmeyer, J. Uzarski, P. J. Barrie, and J. R. Morris, “Interactions and binding energies of dimethyl methylphosphonate and dimethyl chlorophosphate with amorphous silica,” *Langmuir*, vol. 28, pp. 10962–10967, 2012.

[166] C. LX, S. SR, S. SL, X. Tang, and S. Satyapal, “Thermocatalytic oxidation of dimethyl methylphosphonate on supported metal oxides,” *J. Catal.*, vol. 194, pp. 61–70, 2000.

[167] S. Ma, J. Zhou, Y. C. Kang, J. E. Reddic, and D. A. Chen, “Dimethyl

methylphosphonate decomposition on Cu surfaces: Supported Cu nanoclusters and films on TiO2 (110)," *Langmuir*, vol. 20, pp. 9686–9694, 2004.

[168] J. V. Stark, D. G. Park, I. Lagadic, and K. J. Klabunde, "Nanoscale Metal Oxide Particles/Clusters as Chemical Reagents. Unique Surface Chemistry on Magnesium Oxide As Shown by Enhanced Adsorption of Acid Gases (Sulfur Dioxide and Carbon Dioxide) and Pressure Dependence," *Chem. Mater.*, vol. 8, pp. 1904–1912, 1996.

[169] S. P. Decker, J. S. Klabunde, and K. J. Klabunde, "Catalyzed Destructive Adsorption of Environmental Toxins with Nanocrystalline Metal Oxides . Compounds," *Environ. Sci. Technol.*, vol. 36, pp. 762–768, 2002.

[170] D. A. Panayotov and J. R. Morris, "Uptake of a chemical warfare agent simulant (DMMP) on TiO 2: Reactive adsorption and active site poisoning," *Langmuir*, vol. 25, pp. 3652–3658, 2009.

[171] L. A. Patil, A. R. Bari, M. D. Shinde, V. Deo, and M. P. Kaushik, "Detection of dimethyl methyl phosphonate - A simulant of sarin: The highly toxic chemical warfare - Using platinum activated nanocrystalline ZnO thick films," *Sensors Actuators, B Chem.*, vol. 161, pp. 372–380, 2012.

[172] D. A. Chen, J. S. Ratliff, X. Hu, W. O. Gordon, S. D. Senanayake, and D. R. Mullins, "Dimethyl methylphosphonate decomposition on fully oxidized and partially reduced ceria thin films," *Surf. Sci.*, vol. 604, pp. 574–587, 2010.

[173] Y. Li, O. Koper, M. Atteya, and K. J. Klabunde, "Adsorption and Decomposition of Organophosphorus Compounds on Nanoscale Metal Oxid Particles. In Situ GC-MS Studies of Pulsed Microreactions over Magnesium Oxide," *Chem. Mater.*, vol. 4, pp. 323–330, 1992.

[174] V. N. Sheinker and M. B. Mitchell, "Quantitative study of the decomposition of dimethyl methylphosphonate (DMMP) on metal oxides at room temperature and above," *Chem. Mater.*, vol. 14, pp. 1257–1268, 2002.

[175] M. K. Templeton and W. H. Weinberg, "Adsorption and Decomposition of dimethyl methylphosphonate on aluminium oxide surface," *J. Am. Chem. Soc.*, vol. 107, pp. 97–108, 1985.

[176] D. A. Trubitsyn and A. V. Vorontsov, "Experimental study of dimethyl methylphosphonate decomposition over anatase TiO2," *J. Phys. Chem. B*, vol. 109, pp. 21884–21892, 2005.

[177] M. B. Mitchell, V. N. Sheinker, W. W. Cox, E. N. Gatimu, and A. B. Tesfamichael, "The Room Temperature Decomposition Mechanism of Dimethyl Methylphosphonate (DMMP) on Alumina-Supported Cerium Oxide − Participation of Nano-Sized Cerium Oxide Domains," *J. Phys. Chem. B*, vol. 108, pp. 1634–1645, 2004.

[178] M. B. Mitchell, V. N. Sheinker, A. B. Tesfamichael, E. N. Gatimu, and M. Nunley, "Decomposition of dimethyl methylphosphonate (DMMP) on supported cerium and iron co-impregnated oxides at room temperature," *J. Phys. Chem. B*, vol. 107, pp. 580–586, 2003.

[179] T. N. Obee and S. Satyapal, "Photocatalytic decomposition of DMMP on titania," *J. Photochem. Photobiol. A Chem.*, vol. 118, pp. 45–51, 1998.

[180] S. M. Kanan and C. P. Tripp, "Prefiltering strategies for metal oxide based sensors: The use of chemical displacers to selectively dislodge adsorbed organophosphonates from silica surfaces," *Langmuir*, vol. 18, pp. 722–728, 2002.

[181] M. A. Henderson, T. Jin, and J. M. White, "A TPD/AES Study of the Interaction of Dimethyl methylphosphonate with α- Fe2O3 and SiO2," *J.Phys.Chem.*, vol. 2, pp. 4607–4611, 1986.

[182] L. Li, M. Fan, R. C. Brown, J. (Hans) Van Leeuwen, J. Wang, W. Wang, Y. Song, and P. Zhang, "Synthesis, Properties, and Environmental Applications of Nanoscale Iron-Based Materials: A Review," *Crit. Rev. Environ. Sci. Technol.*, vol. 36, pp. 405–431, 2006.

[183] B. L. Cushing, V. L. Kolesnichenko, and C. J. O. Connor, "Recent Advances in the Liquid-Phase Syntheses of Inorganic Nanoparticles Recent Advances in the Liquid-Phase Syntheses of Inorganic Nanoparticles," *Chem. Rev.*, vol. 104, pp. 3893–3946, 2004.

[184] J. Park, K. J. An, Y. S. Hwang, J.G. Park, H. J. Noh, J. Y. Kim, J. H. Park, N. M. Hwang, and T. Hyeon, "Ultra-large-scale syntheses of monodisperse nanocrystals," *Nat. Mater.*, vol. 3, pp. 891 – 895, 2004.

[185] X. Wang, J. Zhuang, Q. Peng, and Y. Li, "A general strategy for nanocrystal synthesis," *Nature*, vol. 437, pp. 121–124, 2005.

[186] M. Fan, T. Boonfueng, Y. Xu, L. Axe, and T. A. Tyson, "Modeling Pb sorption to microporous amorphous oxides as discrete particles and coatings," *J. Colloid Interface Sci.*, vol. 281, pp. 39–48, 2005.

[187] J. Pakarinen, R. Koivula, M. Laatikainen, K. Laatikainen, E. Paatero, and R. Harjula, "Nanoporous manganese oxides as environmental protective materials-Effect of Ca and Mg on metals sorption," *J. Hazard. Mater.*, vol. 180, pp. 234–240, 2010.

[188] M. Ghaedi, K. Niknam, A. Shokrollahi, E. Niknam, H. R. Rajabi, and M. Soylak, "Flame atomic absorption spectrometric determination of trace amounts of heavy metal ions after solid phase extraction using modified sodium dodecyl sulfate coated on alumina," *J. Hazard. Mater.*, vol. 155, pp. 121–127, 2008.

[189] A. Afkhami, M. Saber-Tehrani, and H. Bagheri, "Simultaneous removal of heavy-metal ions in wastewater samples using nano-alumina modified with 2,4-dinitrophenylhydrazine," *J. Hazard. Mater.*, vol. 181, pp. 836–844, 2010.

[190] X. Wang, W. Cai, Y. Lin, G. Wang, and C. Liang, "Mass production of micro/nanostructured porous ZnO plates and their strong structurally enhanced and selective adsorption performance for environmental remediation," *J. Mater. Chem.*, vol. 20, pp. 8582–8590, 2010.

[191] C. Gao, W. Zhang, H. Li, L. Lang, and Z. Xu, "Controllable fabrication of mesoporous MgO with various morphologies and their absorption performance for toxic pollutants in water," *Cryst. Growth Des.*, vol. 8, pp. 3785–3790, 2008.

[192] K. J. Reddy, "Method for removing arsenic from water, 2007, US Patent, 7, 235,179." .

[193] K. J. Reddy and V. Attili, "In: Eighth International Conference on the Biogeochemistry of Trace Elements, Adelaide (2005)."

[194] A. Goswami, P. K. Raul, and M. K. Purkait, "Arsenic adsorption using copper (II) oxide nanoparticles," *Chem. Eng. Res. Des.*, vol. 90, pp. 1387–1396, 2012.

[195] L. Arfaoui, S. Kouass, H. Dhaouadi, R. Jebali, and F. Touati, "Characterization and adsorption performance of Pb(II) on CuO nanorods synthesized by the hydrothermal method," *Mater. Res. Bull.*, vol. 70, pp. 284–290, 2015.

[196] A. A. Farghali, M. Bahgat, A. Enaiet Allah, and M. H. Khedr, "Adsorption of Pb(II) ions from aqueous solutions using copper oxide nanostructures," *Beni-Suef Univ. J. Basic Appl. Sci.*, vol. 2, pp. 61–71, 2013.

[197] F. C. Powell, H. O. Joseph, and J. M. B. (editors), "'Vapor Deposition'. The Electrochemical Society series. New York: Wiley, 1966."

[198] S. Gohil, R. Banerjee, S. Bose, and P. Ayyub, "Influence of synthesis conditions on the nanostructure of immiscible copper-silver alloy thin films," *Scr. Mater.*, vol. 58, pp.

842–845, 2008.

[199] N. Laegreid and G. K. Wehner, “Sputtering yields of metals for ar+ and ne+ ions with energies from 50 to 600 ev,” *J. Appl. Phys.*, vol. 32, pp. 365–369, 1961.

[200] D. Rosenberg and G. K. Wehner, “Sputtering Yields for Low Energy He+-, Kr+-, and Xe+-Ion Bombardment,” *J. Appl. Phys.*, vol. 33, pp. 1842–1845, 1962.

[201] Y. Yamamura, N. Matsunami, and N. Itoh, “Theoretical studies on an empirical formula for sputtering yield at normal incidence,” *Radiat. Eff.*, vol. 71, pp. 65–86, 1983.

[202] M. Ohring, “The Materials Science of Thin Films, Academic Press Inc, San Diego (1992).” .

[203] W. D. Sproula, D. J. Christieb, and D. C. Carterb, “Control of reactive sputtering processes,” *Thin Solid Films*, vol. 491, pp. 1–17, 2005.

[204] W. D. Westwood, S. M. Rossnagel, and J. J. Cuomo, “Reactive Sputter Deposition Handbook of Plasma Processing Technology: Fundamentals, Etching, Deposition and Surface Interactions, eds,” *Noyes Publ. New Jersey*, 1990.

[205] B. D. Cullity, *Elements Of X Ray Diffraction*. 1978.

[206] I. R. Lewis and H. Edward, “Handbook of Raman Spectroscopy: From the Research Laboratory to the Process Line, CRC Press, 2001,” p. 2001, 2001.

[207] D. Noble, “FT-IR SPECTROSCOPY, Anal. Chem. 1995, 67, 381A.” .

[208] S. L. Fleger, J. W. Heckman, J. Karen, and L. Klomparens, “Scanning and Transmission Electron Microscopy- An Introductio n”, Oxford University Press, New York, 1993,” p. 1993, 1993.

[209] D. B. Williams and C. B. Carter, “Transmission Electron Microscopy, 2nd Ed., Springer, 2009.” .

[210] W. W. Wendlandt, “Thermal Methods of Analysis, John Wiley & Sons, Inc., 2nd Ed., New York 1974.”

[211] S. C. Stout, S. C. Larsen, and V. H. Grassian, “Adsorption, desorption and thermal oxidation of 2-CEES on nanocrystalline zeolites,” *Microporous Mesoporous Mater.*, vol. 100, pp. 77–86, 2007.

[212] A. Saxena, A. K. Srivastava, B. Singh, and A. Goyal, “Removal of sulphur mustard, sarin and simulants on impregnated silica nanoparticles,” *J. Hazard. Mater.*, vol. 211–212, pp. 226–232, 2012.

[213] B. Singh, A. Saxena, A. K. Nigam, K. Ganesan, and P. Pandey, “Impregnated silica

nanoparticles for the reactive removal of sulphur mustard from solutions," *J. Hazard. Mater.*, vol. 161, pp. 933–940, 2009.

[214] J. A. Rodriguez and M. F. Garcia, "Synthesis, Properties, and Applications of Oxide Nanomaterials, John Wiley and Sons, New York, 2007."

[215] M. Winter, D. Hamal, X. Yang, H. Kwen, D. Jones, S. Rajagopalan, and K. J. Klabunde, "Defining reactivity of solid sorbents: What is the most appropriate metric?," *Chem. Mater.*, vol. 21, pp. 2367–2374, 2009.

[216] C. L. Carnes, P. N. Kapoor, and K. J. Klabunde, "Synthesis , Characterization , and Adsorption Studies of Nanocrystalline Aluminum Oxide and a Bimetallic Nanocrystalline Aluminum Oxide / Magnesium Oxide," *Chem. Mater.*, vol. 14, pp. 2922–2929, 2002.

[217] K. Phiwdang, S. Suphankij, W. Mekprasart, and W. Pecharapa, "Synthesis of CuO nanoparticles by precipitation method using different precursors," *Energy Procedia*, vol. 34, pp. 740–745, 2013.

[218] P. Mallick and S. Sahu, "Structure, Microstructure and Optical Absorption Analysis of CuO Nanoparticles Synthesized by Sol-Gel Route," *Nanosci. Nanotechnol.*, vol. 2, pp. 71–74, 2012.

[219] A. El-Trass, H. Elshamy, I. El-Mehasseb, and M. El-Kemary, "CuO nanoparticles: Synthesis, characterization, optical properties and interaction with amino acids," *Appl. Surf. Sci.*, vol. 258, pp. 2997–3001, 2012.

[220] R. Chandra, P. Taneja, J. John, P. Ayyub, G. . Dey, and S. K. Kulshreshtha, "Synthesis and TEM study of nanoparticles and nanocrystalline thin films of silver by high pressure sputtering," *NanoStructured Mater.*, vol. 11, pp. 1171–1179, 1999.

[221] A. K. Chawla and R. Chandra, "Synthesis and structural characterization of nanostructured copper," *J. Nanoparticle Res.*, vol. 11, pp. 297–302, 2009.

[222] X. Gu, J. Ge, H. Zhang, A. Auroux, and J. Shen, "Structural, redox and acid-base properties of V2O5/CeO2 catalysts," *Thermochim. Acta*, vol. 451, pp. 84–93, 2006.

[223] V. Chawla, R. Jayaganthan, and R. Chandra, "Influence of Sputtering Pressure on the Structure and Mechanical Properties of Nanocomposite Ti-Si-N Thin Films," *J. Mater. Sci. Technol.*, vol. 26, pp. 673–678, 2010.

[224] J. Pal, M. Ganguly, S. Dutta, C. Mondal, Y. Negishi, and T. Pal, "Hierarchical Au–CuO nanocomposite from redox transformation reaction for surface enhanced Raman

scattering and clock reaction," *CrystEngComm*, vol. 16, pp. 883–893, 2014.

[225] C. Tamuly, I. Saikia, M. Hazarika, and M. R. Das, "Reduction of aromatic nitro compounds catalyzed by biogenic CuO nanoparticles," *RSC Adv.*, no. 95, pp. 53229–53236, 2014.

[226] Q. Yu, H. Huang, R. Chen, P. Wang, H. Yang, M. Gao, X. Peng, and Z. Ye, "Synthesis of CuO nanowalnuts and nanoribbons from aqueous solution and their catalytic and electrochemical properties," *Nanoscale*, vol. 4, pp. 2613–2620, 2012.

[227] W. Wang, L. Wang, H. Shi, and Y. Liang, "A room temperature chemical route for large scale synthesis of sub-15 nm ultralong CuO nanowires with strong size effect and enhanced photocatalytic activity," *CrystEngComm*, vol. 14, pp. 5914–5922, 2012.

[228] V. Stengl, T. M. Grygar, J. Bludska, F. Oplustil, and T. Nemec, "Mesoporous iron-manganese oxides for sulphur mustard and soman degradation," *Mater. Res. Bull.*, vol. 47, pp. 4291–4299, 2012.

[229] A. Khaleel, W. Li, and K. J. Klabunde, "Nanocrystals as stoichiometric reagents with unique surface chemistry. New adsorbents for air purification," *Nanostructured Mater.*, vol. 12, pp. 463–466, 1999.

[230] V. Štengl, D. Králová, F. Opluštil, and T. Němec, "Mesoporous manganese oxide for warfare agents degradation," *Microporous Mesoporous Mater.*, vol. 156, pp. 224–232, 2012.

[231] G. W. Wagner, P. W. Bartram, O. Koper, and K. J. Klabunde, "Reactions of VX , GD , and HD with Nanosize MgO," *J. Phys. Chem. B*, vol. 104, pp. 5118–5123, 2000.

[232] D. B. Mawhinney, J. A. Rossin, K. Gerhart, and J. T. Y. Jr., "Adsorption and reaction of 2 chlororthylethyl sulfide with Al2O3 surfaces," *Langmuir*, vol. 15, pp. 4789–4796, 1999.

[233] C.-P. Li, F. Lin, R. M. Richards, C. Engtrakul, R. C. Tenent, and C. a. Wolden, "The influence of sol–gel processing on the electrochromic properties of mesoporous WO3 films produced by ultrasonic spray deposition," *Sol. Energy Mater. Sol. Cells*, vol. 121, pp. 163–170, 2014.

[234] C. Pang, J. Luo, Z. Guo, M. Guo, and T. Hou, "Inhibition of tungsten particle growth during reduction of V-doped WO3 nanoparticles prepared by co-precipitation method," *Int. J. Refract. Met. Hard Mater.*, vol. 28, pp. 343–348, 2010.

[235] T. A. Nguyen, S. Park, J. B. Kim, T. K. Kim, G. H. Seong, J. Choo, and Y. S. Kim,

"Polycrystalline tungsten oxide nanofibers for gas-sensing applications," *Sensors Actuators, B Chem.*, vol. 160, pp. 549–554, 2011.

[236] D. B. Hernandez-Uresti, D. Sanchez-Mart??nez, A. Mart??nez-De La Cruz, S. Sepulveda-Guzm??n, and L. M. Torres-Martinez, "Characterization and photocatalytic properties of hexagonal and monoclinic WO3 prepared via microwave-assisted hydrothermal synthesis," *Ceram. Int.*, vol. 40, pp. 4767–4775, 2014.

[237] R. Chandra, P. Taneja, J. John, P. Ayyub, G. K. Dey, and S. K. Kulshreshtha, "Synthesis and TEM study of nanoparticles and nanocrystalline thin films of silver by high pressure sputtering," *Nanostructured Mater.*, vol. 11, pp. 1171–1179, 1999.

[238] X. Zhang, X. Lu, Y. Shen, J. Han, L. Yuan, L. Gong, Z. Xu, X. Bai, M. Wei, Y. Tong, Y. Gao, J. Chen, J. Zhou, and Z. L. Wang, "Three-dimensional WO3 nanostructures on carbon paper: photoelectrochemical property and visible light driven photocatalysis.," *Chem. Commun. (Camb).*, vol. 47, pp. 5804–5806, 2011.

[239] K. NONAKA, A. TAKASE, and K. MIYAKAWA, "Raman spectra of sol-gel-derived tungsten oxides," *J. Mater. Sci. Lett.*, vol. 12, pp. 274–277, 1993.

[240] C. G. Granqvist, "Electrochromic tungsten oxide: Review of progress 1993-1998," *Sol. Energy Mater. Sol. Cells*, vol. 60, pp. 201–262, 2000.

[241] D. S??nchez-Mart??nez, A. Mart??nez-De La Cruz, and E. L??pez-Cu??llar, "Synthesis of WO3 nanoparticles by citric acid-assisted precipitation and evaluation of their photocatalytic properties," *Mater. Res. Bull.*, vol. 48, no. 2, pp. 691–697, 2013.

[242] A. Martinez-de la Cruz, D. S. Martinez, and E. L. Cuellar, "Synthesis and characterization of WO3 nanoparticles prepared by the precipitation method: Evaluation of photocatalytic activity under vis-irradiation," *Solid State Sci.*, vol. 12, pp. 88–94, 2010.

[243] J. Cao, B. Luo, H. Lin, B. Xu, and S. Chen, "Thermodecomposition synthesis of WO3/H2WO4 heterostructures with enhanced visible light photocatalytic properties," *Appl. Catal., B*, vol. 111–112, pp. 288–296, 2012.

[244] S. Supothina, P. Seeharaj, S. Yoriya, and M. Sriyudthsak, "Synthesis of tungsten oxide nanoparticles by acid precipitation method," *Ceram. Int.*, vol. 33, pp. 931–936, 2007.

[245] S. Rajagopalan, O. Koper, S. Decker, and K. J. Klabunde, "Nanocrystaline metal oxide as destructive adsorbents for organophosphorus compound at room temperature," *Chem. Eur. J.*, vol. 8, pp. 2602 – 2607, 2002.

[246] A. Saxena, B. Singh, A. Sharma, V. Dubey, R. P. Semwal, M. V. S. Suryanarayana, V. K. Rao, and K. Sekhar, "Adsorption of dimethyl methylphosphonate on metal impregnated carbons under static conditions," *J. Hazard. Mater.*, vol. 134, pp. 104–111, 2006.

[247] V. Stengl, T. M. Grygar, J. Bludska, F. Oplustill, and T. Nemec, "Mesoporous iron-manganese oxides for sulphur mustard and soman degradation," *Mater. Res. Bull.*, vol. 47, pp. 4291–4299, 2012.

[248] B. M. Smith, "Catalytic methods for the destruction of chemical warfare agents under ambient conditions.," *Chem. Soc. Rev.*, vol. 37, pp. 470–478, 2008.

[249] M. M. Khin, a. S. Nair, V. J. Babu, R. Murugan, and S. Ramakrishna, "A review on nanomaterials for environmental remediation," *Energy Environ. Sci.*, vol. 5, p. 8075, 2012.

[250] G. W. Wagner, P. W. Bartram, O. Koper, and K. J. Klabunde, "Reactions of VX , GD , and HD with Nanosize MgO," *J. Phys. Chem. B*, vol. 103, pp. 3225–3228, 1999.

[251] K. J. Klabunde, J. Stark, O. Koper, C. Mohs, D. G. Park, S. Decker, Y. Jiang, I. Lagadic, and D. Zhang, "Nanocrystals as stochiometric reagents with unique surface chemistry," *J. Phys. Chem.*, vol. 100, pp. 12142–12153, 1996.

[252] G. Y. Guo and Y. L. Chen, "A nearly pure monoclinic nanocrystalline zirconia," *J. Solid State Chem.*, vol. 178, pp. 1675–1682, 2005.

[253] M. Jafarpour, E. Rezapour, M. Ghahramaninezhad, and A. Rezaeifard, "A novel protocol for selective synthesis of monoclinic zirconia nanoparticles as a heterogeneous catalyst for condensation of 1,2-diamines with 1,2-dicarbonyl compounds," *New J. Chem.*, vol. 38, p. 676, 2014.

[254] L. Kumari, G. H. Du, W. Z. Li, R. S. Vennila, S. K. Saxena, and D. Z. Wang, "Synthesis, microstructure and optical characterization of zirconium oxide nanostructures," *Ceram. Int.*, vol. 35, no. 6, pp. 2401–2408, 2009.

[255] L. Bai, F. Wyrwalski, C. Machut, P. Roussel, E. Monflier, and A. Ponchel, "Hydroxypropyl-β-cyclodextrin as a versatile additive for the formation of metastable tetragonal zirconia exhibiting high thermal stability," *CrystEngComm*, vol. 15, p. 2076, 2013.

[256] N. Zink, F. Emmerling, T. Häger, M. Panthöfer, M. N. Tahir, U. Kolb, and W. Tremel, "Low temperature synthesis of monodisperse nanoscaled ZrO2 with a large specific

surface area.," *Dalton Trans.*, vol. 42, pp. 432–40, 2013.

[257] E. K. Goharshadi and M. Hadadian, "Effect of calcination temperature on structural, vibrational, optical, and rheological properties of zirconia nanoparticles," *Ceram. Int.*, vol. 38, pp. 1771–1777, 2012.

[258] L. Li and W. Wang, "Synthesis and characterization of monoclinic ZrO2 nanorods by a novel and simple precursor thermal decomposition approach," *Solid State Commun.*, vol. 127, pp. 639–643, 2003.

[259] L. Shi, K. C. Tin, and N. B. Wong, "Thermal stability of zirconia membranes," *J. Mater. Sci.*, vol. 34, pp. 3367–3374, 1999.

[260] E. L. Fuller and R. B. Gammage, "Heats of Immersion in the Zirconium Oxid+Water System," *J. Phys. Chem.*, vol. 76, pp. 1497–1502, 1972.

[261] D. T. Livey, "J. Am. Ceram. Soc., P. Murray 29 (1956) 369." .

[262] F. Chen, Q. Hong, G.-Q. Xu, T. S. A. Hor, and S. Shen, "Characterization of nano-crystalline ZrO2 synthesized via reactive plasma processing," *PhD Propos.*, vol. 88, pp. 2649–2651, 2015.

[263] W. Li, H. Huang, H. Li, W. Zhang, and Haichao Liu, "Stopped-flow studies of the mechanisms of ozone-alkene reactions in the gas phase: tetramethylethylene," *Langmuir*, vol. 24, pp. 8353–8366, 2008.

[264] M. Verma, R. Chandra, and V. K. Gupta, "Synthesis of magnetron sputtered WO<inf>3</inf> nanoparticles-degradation of 2-chloroethyl ethyl sulfide and dimethyl methyl phosphonate," *J. Colloid Interface Sci.*, vol. 453, pp. 60–68, 2015.

[265] M. Verma, V. K. Gupta, V. Dave, R. Chandra, and G. K. Prasad, "Synthesis of sputter deposited CuO nanoparticles and their use for decontamination of 2-chloroethyl ethyl sulfide (CEES)," *J. Colloid Interface Sci.*, vol. 438, pp. 102–109, 2015.

[266] D. B. Mawhinney, J. A. Rossin, K. Gerhart, and J. John T. Yates, "Adsorption and Reaction of 2-Chloroethylethyl Sulfide with Al2O3Surfaces," *Langmuir*, vol. 15, pp. 4789–4795, 1999.

[267] G. K. Prasad, P. V. R. K. Ramacharyulu, K. Batra, B. Singh, a R. Srivastava, K. Ganesan, and R. Vijayaraghavan, "Decontamination of Yperite using mesoporous mixed metal oxide nanocrystals.," *J. Hazard. Mater.*, vol. 183, pp. 847–52, 2010.

[268] A. Saxena, B. Singh, A. Sharma, V. Dubey, R. P. Semwal, M. V. S. Suryanarayana, V. K. Rao, and K. Sekhar, "Adsorption of dimethyl methylphosphonate on metal

impregnated carbons under static conditions," *J. Hazard. Mater.*, vol. B134, pp. 104–111, 2006.

[269] N. Sharma and R. Kakkar, "Recent advancements on warfare agents/metal oxides surface chemistry and their simulation study," *Adv. Mater. Lett.*, vol. 4, pp. 508–521, 2013.

[270] G. W. Wagner, O. B. Koper, E. Lucas, S. Decker, and K. J. Klabunde, "Reactions of VX , GD , and HD with Nanosize CaO: Autocatalytic Dehydrohalogenation of HD," *J. Phys. Chem. B*, vol. 104, pp. 5118–5123, 2000.

[271] T. Gao, M. Glerup, F. Krumeich, R. Nesper, H. Fjellvâg, and P. Norby, "Microstructures and spectroscopic properties of cryptomelane-type manganese dioxide nanofibers," *J. Phys. Chem. C*, vol. 112, pp. 13134–13140, 2008.

[272] M. Wei, Y. Konishi, H. Zhou, H. Sugihara, and Hironori Arakawa, "Synthesis of single-crystal manganese dioxide nanowires by a soft chemical process, 16 (2005) 245 – 249," *Nanotechnology*, vol. 16, pp. 245–249, 2005.

[273] L. Qu, C. He, Y. Yang, Y. He, and Z. Liu, "Hydrothermal synthesis of alumina nanotubes templated by anionic surfactant," *Mater. Lett.*, vol. 59, pp. 4034–4037, 2005.

[274] S. H. Maron and C. F. Prutton, "Principles of Physical Chemistry, 4th ed. New Delhi, India: Amerind Publishing, 1972:548 – 592."

[275] L. K.J., "New York McGraw-Hill," *Chem. Kinet.*, 1950.

[276] T. Kasuga, M. Hiramatsu, A. Hoson, T. Sekino, and K. Niihara, "Formation of Titanium Oxide Nanotube," *Langmuir*, vol. 14, pp. 3160–3163, 1998.

[277] A. Roy, A. K. Srivastava, B. Singh, T. H. Mahato, D. Shah, and A. K. Halve, "Kinetics of degradation of sulfur mustard and sarin simulants on HKUST-1 metal organic framework," *Dalton Trans.*, vol. 41, p. 12346, 2012.

[278] G. W. Wagner, L. R. Procell, R. J. O'Connor, S. Munavalli, C. L. Carnes, P. N. Kapoor, and K. J. Klabunde, "Reactions of VX, GB, GD, and HD with nanosize AL2O3. Formation of aluminophosphonates," *J. Am. Chem. Soc.*, vol. 123, no. 8, pp. 1636–1644, 2001.

[279] H. Yan, L. Yang, Z. Yang, H. Yang, A. Li, and R. Cheng, "Preparation of chitosan/poly(acrylic acid) magnetic composite microspheres and applications in the removal of copper(II) ions from aqueous solutions," *J. Hazard. Mater.*, vol. 229–230, pp. 371–380, 2012.

[280] M. Bansal, D. Singh, and V. K. Garg, "A comparative study for the removal of hexavalent chromium from aqueous solution by agriculture wastes' carbons," *J. Hazard. Mater.*, vol. 171, pp. 83–92, 2009.

[281] Ö. Gerçel and H. F. Gerçel, "Adsorption of lead(II) ions from aqueous solutions by activated carbon prepared from biomass plant material of Euphorbia rigida," *Chem. Eng. J.*, vol. 132, pp. 289–297, 2007.

[282] R. J. Kieber and G. R. Helz, "Indirect photoreduction of aqueous chromium (VI)," *Environ. Sci. Technol.*, vol. 26, pp. 307–312, 1992.

[283] V. K. Gupta, A. K. Jain, and G. Maheshwari, "Aluminum(III) selective potentiometric sensor based on morin in poly(vinyl chloride) matrix.," *Talanta*, vol. 72, pp. 1469–1473, 2007.

[284] S. Rengaraj, K. Yeon, and S. Moon, "Removal of chromium from water and wastewater by ion exchange resins," *J. Hazard. Mater.*, vol. 87, pp. 273–287, 2001.

[285] S. Doyurum and A. Çelik, "Pb(II) and Cd(II) removal from aqueous solutions by olive cake," *J. Hazard. Mater.*, vol. B138, pp. 22–28, 2006.

[286] C. A. Kozlowski and W. Walkowiak, "Removal of chromium(VI) from aqueous solutions by polymer inclusion membranes," *Water Res.*, vol. 36, pp. 4870–4876, 2002.

[287] V. K. Gupta, A. Rastogi, and A. Nayak, "Adsorption studies on the removal of hexavalent chromium from aqueous solution using a low cost fertilizer industry waste material," *J. Colloid Interface Sci.*, vol. 342, pp. 135–141, 2010.

[288] A. Baran, E. Biçak, Ş. H. Baysal, and S. Önal, "Comparative studies on the adsorption of Cr(VI) ions on to various sorbents," *Bioresour. Technol.*, vol. 98, pp. 661–665, 2006.

[289] W. Liu, J. Zhang, C. Zhang, Y. Wang, and Y. Li, "Adsorptive removal of Cr (VI) by Fe-modified activated carbon prepared from Trapa natans husk," *Chem. Eng. J.*, vol. 162, pp. 677–684, 2010.

[290] G. Lv, Z. Li, W. T. Jiang, C. Ackley, N. Fenske, and N. Demarco, "Removal of Cr(VI) from water using Fe(II)-modified natural zeolite," *Chem. Eng. Res. Des.*, vol. 92, pp. 384–390, 2014.

[291] A. Mittal, D. Kaur, A. Malviya, J. Mittal, and V. K. Gupta, "Adsorption studies on the removal of coloring agent phenol red from wastewater using waste materials as adsorbents," *J. Colloid Interface Sci.*, vol. 337, pp. 345–354, 2009.

[292] A. Mittal, J. Mittal, A. Malviya, and V. K. Gupta, "Adsorptive removal of hazardous

anionic dye ‘Congo red’ from wastewater using waste materials and recovery by desorption,” *J. Colloid Interface Sci.*, vol. 340, pp. 16–26, 2009.

[293] Y. Liu, Q. Li, S. Gao, and J. K. Shang, “Exceptional As(III) sorption capacity by highly porous magnesium oxide nanoflakes made from hydrothermal synthesis,” *J. Am. Ceram. Soc.*, vol. 94, pp. 217–223, 2011.

[294] M. E. Argun, S. Dursun, C. Ozdemir, and M. Karatas, “Heavy metal adsorption by modified oak sawdust: Thermodynamics and kinetics,” *J. Hazard. Mater.*, vol. 141, pp. 77–85, 2007.

[295] K. Anupam, S. Dutta, C. Bhattacharjee, and S. Datta, “Adsorptive removal of chromium (VI) from aqueous solution over powdered activated carbon: Optimisation through response surface methodology,” *Chem. Eng. J.*, vol. 173, pp. 135–143, 2011.

[296] Y. Wu, J. Zhang, X. J. Jin, J. M. Gao, and Q. Zhao, “Study of Cr(VI) adsorption onto nitrogen-enriched activated carbon from waste medium density fiberboard,” *Wood Sci. Technol.*, vol. 48, pp. 713–725, 2014.

[297] Z. A. AL-Othman, R. Ali, and M. Naushad, “Hexavalent chromium removal from aqueous medium by activated carbon prepared from peanut shell: Adsorption kinetics, equilibrium and thermodynamic studies,” *Chem. Eng. J.*, vol. 184, pp. 238–247, 2012.

[298] D. K. Verma, S. H. Hasan, D. Ranjan, and R. M. Banik, “Modified biomass of Phanerochaete chrysosporium immobilized on luffa sponge for biosorption of hexavalent chromium,” *Int. J. Environ. Sci. Technol.*, vol. 11, pp. 1927–1938, 2014.

[299] H. D. Choi, W. S. Jung, J. M. Cho, B. G. Ryu, J. S. Yang, and K. Baek, “Adsorption of Cr(VI) onto cationic surfactant-modified activated carbon,” *J. Hazard. Mater.*, vol. 166, pp. 642–646, 2009.

[300] M. Barkat, D. Nibou, S. Chegrouche, and A. Mellah, “Kinetics and thermodynamics studies of chromium(VI) ions adsorption onto activated carbon from aqueous solutions,” *Chem. Eng. Process.*, vol. 48, pp. 38–47, 2009.

[301] and P. N. T. Singh, Vinay K., “Removal and recovery of chromium (VI) from industrial waste water,” *J. Chem. Technol. Biotechnol.*, vol. 69, pp. 376–382, 1997.

[302] Y. S. Ho and G. McKay, “Pseudo-second order model for sorption processes,” *Process Biochem.*, vol. 34, pp. 451–465, 1999.

[303] W. J. Weber and J. C. Morris, “Kinetics of Adsorption on carbon from Solution,” *j. sanit. eng. div.*, vol. 89, pp. 31–60, 1963.

[304] H. Qiu, L. Lv, B. Pan, Q. Zhang, W. Zhang, and Q. Zhang, "Critical review in adsorption kinetic models," *J. Zhejiang Univ. Sci. A*, vol. 10, pp. 716–724, 2009.

[305] E. Demirbas, N. Dizge, M. T. Sulak, and M. Kobya, "Adsorption kinetics and equilibrium of copper from aqueous solutions using hazelnut shell activated carbon," *Chem. Eng. J.*, vol. 148, pp. 480–487, 2009.

[306] Irving Langmuir, "The adsorption of gases on glass, mica and platinum," *ges.*, vol. 16, pp. 1361–1403, 1918.

[307] R. H. Kenneth, L. C. Eagleton, A. Acrivos, and T. Vermeulen, "PORE-AND SOLID-DIFFUSION KINETICS IN FIXED-BED ADSORPTION UNDER CONSTANT-PATTERN CONDITIONS," *I E C Fundam.*, vol. 5, pp. 212–223, 1966.

[308] M. L. Paul, J. Samuel, S. B. Das, S. Swaroop, N. Chandrasekaran, and A. Mukherjee, "Studies on Cr (VI) Removal from Aqueous Solutions by Nanoalumina," *Ind. Eng. Chem. Res.*, vol. 51, pp. 15242–15250, 2012.

[309] H. M. F. Freundlich, "Über die adsorption in lösungen. Z. Phys. Chem. 57." pp. 385–470, 1906.

[310] N. K. Hamadi, Xiao Dong Chen, M. M. Farid, and M. G. Q. Lu, "Adsorption kinetics for the removal of chromium(VI) from aqueous solution by adsorbents derived from used tyres and sawdust," *Chem. Eng. J.*, vol. 84, pp. 95–105, 2001.

[311] C. Selomulya, V. Meeyoo, and R. Amal, "Mechanisms of Cr (VI) removal from water by various types of activated carbons," *J. Chem. Technol. Biotechnol.*, vol. 74, pp. 111–122, 1999.

[312] S. Li, X. Lu, Y. Xue, J. Lei, T. Zheng, and C. Wang, "Fabrication of polypyrrole/graphene oxide composite nanosheets and their applications for Cr(VI) removal in aqueous solution," *PLoS One*, vol. 7, pp. 1–7, 2012.

[313] M. Dakiky, M. Khamis, a Manassra, and M. Mer'eb, "Selective adsorption of chromium (VI) in industrial wastewater using low-cost abundantly available adsorbents," *Adv. Environ. Res.*, vol. 6, pp. 533–540, 2002.

[314] P. K. Ghosh, "Hexavalent chromium [Cr(VI)] removal by acid modified waste activated carbons," *J. Hazard. Mater.*, vol. 171, pp. 116–122, 2009.

[315] M. H. Dehghani, M. M. Taher, A. K. Bajpai, B. Heibati, I. Tyagi, M. Asif, S. Agarwal, and V. K. Gupta, "Removal of noxious Cr (VI) ions using single-walled carbon nanotubes and multi-walled carbon nanotubes," *Chem. Eng. J.*, vol. 279, pp. 344–352,

2015.

[316] L. Sun, Z. Yuan, W. Gong, L. Zhang, Z. Xu, G. Su, and D. Han, “The mechanism study of trace Cr(VI) removal from water using Fe0 nanorods modified with chitosan in porous anodic alumina,” *Appl. Surf. Sci.*, vol. 328, pp. 606–613, 2015.

[317] S. S. Liu, Y. Z. Chen, L. De Zhang, G. M. Hua, W. Xu, N. Li, and Y. Zhang, “Enhanced removal of trace Cr(VI) ions from aqueous solution by titanium oxide-Ag composite adsorbents,” *J. Hazard. Mater.*, vol. 190, pp. 723–728, 2011.

[318] H. Wang, Y. G. Liu, G. M. Zeng, X. J. Hu, X. Hu, T. T. Li, H. Y. Li, Y. Q. Wang, and L. H. Jiang, “Grafting of β-cyclodextrin to magnetic graphene oxide via ethylenediamine and application for Cr(VI) removal,” *Carbohydr. Polym.*, vol. 113, pp. 166–173, 2014.

[319] R. Dubey, J. Bajpai, and a. K. Bajpai, “Green synthesis of graphene sand composite (GSC) as novel adsorbent for efficient removal of Cr (VI) ions from aqueous solution,” *J. Water Process Eng.*, vol. 5, pp. 83–94, 2015.

[320] H. D. Choi, W. S. Jung, J. M. Cho, B. G. Ryu, J. S. Yang, and K. Baek, “Adsorption of Cr(VI) onto cationic surfactant-modified activated carbon,” *J. Hazard. Mater.*, vol. 166, pp. 642–646, 2009.

[321] N. K. Hamadi, X. Dong, M. M. Farid, and M. G. Q. Lu, “Adsorption kinetics for the removal of chromium (VI) from aqueous solution by adsorbents derived from used tyres and sawdust,” *Chem. Eng. J.*, vol. 84, pp. 95–105, 2001.

[322] C. Selomulya, V. Meeyoo, and R. Amal, “Mechanisms of Cr (VI) removal from water by various types of activated carbons,” *J. Chem. Technol. Biotechnol.*, vol. 122, pp. 111–122, 1999.

[323] M. U. Dakiky, M. Khamis, A. Manassra, and M. Mer, “Selective adsorption of chromium ž VI / in industrial wastewater using low-cost abundantly available adsorbents,” *Adv. environmantal Res.*, vol. 6, pp. 533–540, 2002.

[324] P. K. Ghosh, “Hexavalent chromium [Cr(VI)] removal by acid modified waste activated carbons,” *J. Hazard. Mater.*, vol. 171, pp. 116–122, 2009.

[325] R. Y. Stefanova, “Removal of metal ions from water solutions by iron/cobalt oxide coated keramzite,” *J. Environ. Sci. Heal. Part A Tox. Hazard. Subst. Environ. Eng.*, vol. 36, pp. 1287 – 1302, 2001.

[326] S. Hasan, T. K. Ghosh, D. S. Viswanath, and V. M. Boddu, “Dispersion of chitosan on perlite for enhancement of copper(II) adsorption capacity,” *J. Hazard. Mater.*, vol. 152,

pp. 826–837, 2008.

[327] S. Liu, J. Pan, J. Cao, X. Dai, M. Meng, R. Wu, J. Yao, and Y. Yan, “Simultaneous removal of Pb(II) and 2,4,6-trichlorophenol by a hierarchical porous PU@PDA@MSNs sponge with reversible ‘shape memory’ effect,” *Chem. Eng. J.*, vol. 284, pp. 10–20, 2016.

[328] C. Xiong, C. Yao, L. Wang, and J. Ke, “Adsorption behavior of Cd(II) from aqueous solutions onto gel-type weak acid resin,” *Hydrometallurgy*, vol. 98, pp. 318–324, 2009.

[329] L. Zeng, “Arsenic adsorption from aqueous solutions on an Fe (III)-Si binary oxide adsorbent,” *Water Qual. Res. J. Canada*, vol. 39, pp. 267–275, 2004.

[330] E. Eren, B. Afsin, and Y. Onal, “Removal of lead ions by acid activated and manganese oxide-coated bentonite,” *J. Hazard. Mater.*, vol. 161, pp. 677–685, 2009.

[331] G. Mckay, H. S. Blair, and J. R. Gardener, “Adsorption of dyes on chitin. I. Equilibrium studies,” *J. Appl. Polym. Sci.*, vol. 27, pp. 3043 – 3057, 1982.

[332] A. Bée, D. Talbot, S. Abramson, and V. Dupuis, “Magnetic alginate beads for Pb(II) ions removal from wastewater,” *J. Colloid Interface Sci.*, vol. 362, pp. 486–492, 2011.

[333] O. Moradi, M. Aghaie, K. Zare, M. Monajjemi, and H. Aghaie, “The study of adsorption characteristics Cu2+ and Pb2+ ions onto PHEMA and P(MMA-HEMA) surfaces from aqueous single solution,” *J. Hazard. Mater.*, vol. 170, pp. 673–679, 2009.

[334] D. K. Venkata Ramana, J. S. Yu, and K. Seshaiah, “Silver nanoparticles deposited multiwalled carbon nanotubes for removal of Cu(II) and Cd(II) from water: Surface, kinetic, equilibrium, and thermal adsorption properties,” *Chem. Eng. J.*, vol. 223, pp. 806–815, 2013.

[335] Y. Wang, X. Wang, X. Wang, M. Liu, Z. Wu, L. Yang, S. Xia, and J. Zhao, “Adsorption of Pb(II) from aqueous solution to Ni-doped bamboo charcoal,” *J. Ind. Eng. Chem.*, vol. 19, pp. 353–359, 2013.

[336] K. Conrad and H. C. Bruun Hansen, “Sorption of zinc and lead on coir.,” *Bioresour. Technol.*, vol. 98, pp. 89–97, 2007.

[337] H. Cho, D. Oh, and K. Kim, “A study on removal characteristics of heavy metals from aqueous solution by fly ash,” *J. Hazard. Mater.*, vol. B127, pp. 187 – 195, 2005.

[338] M. M. D. Zulkali, A. L. Ahmad, and N. H. Norulakmal, “L. husk as heavy metal adsorbent: Optimization with lead as model solution,” *Bioresour. Technol.*, vol. 97, pp. 21–25, 2006.

[339] B. Yu, Y. Zhang, A. Shukla, S. S. Shukla, and K. L. Dorris, “The removal of heavy metals from aqueous solutions by sawdust adsorption--removal of lead and comparison of its adsorption with copper.,” *J. Hazard. Mater.*, vol. B84, pp. 83–94, 2001.

[340] P. K. Raul, S. Senapati, A. K. Sahoo, I. M. Umlong, R. R. Devi, A. J. Thakur, and V. Veer, “CuO nanorods: a potential and efficient adsorbent in water purification,” *RSC Adv.*, vol. 4, pp. 40580–40587, 2014.